



TECHNISCHE
UNIVERSITÄT
WIEN
Vienna University of Technology

GEOWISSENSCHAFTLICHE MITTEILUNGEN

Heft Nr. 90, 2012

Tidal excitation of Earth rotation observed by VLBI and GNSS

Sigrid Böhm

Veröffentlichung des Departments für Geodäsie und Geoinformation
ISSN 1811-8380

Schriftenreihe der Studienrichtung VERMESSUNG UND GEOINFORMATION



TECHNISCHE
UNIVERSITÄT
WIEN
Vienna University of Technology

GEOWISSENSCHAFTLICHE MITTEILUNGEN

Heft Nr. 90, 2012

Tidal excitation of Earth rotation observed by VLBI and GNSS

Sigrid Böhm

Veröffentlichung des Departments für Geodäsie und Geoinformation
ISSN 1811-8380

Schriftenreihe der Studienrichtung VERMESSUNG UND GEOINFORMATION

2012

Published by the Department of Geodesy and Geoinformation
of the Vienna University of Technology
Gußhausstraße 27-29
1040 Vienna, Austria

Responsible for this issue: Prof. Dr. Johannes Böhm
Printed by: Grafisches Zentrum HTU GmbH

The digital version of the full document with colored figures is available online:
<http://www.ub.tuwien.ac.at/diss/AC07814286.pdf>

Die Kosten für den Druck wurden vom Department für Geodäsie und Geoinformation übernommen.

Diese Arbeit wurde an der Fakultät für Mathematik und Geoinformation der Technischen Universität
Wien zur Erlangung des akademischen Grades einer Doktorin der technischen Wissenschaften
eingereicht.

Begutachter:

Prof. Dr. Harald Schuh
Department für Geodäsie und Geoinformation der Technischen Universität Wien
Gußhausstraße 27-29, 1040 Wien, Österreich
Department 1 „Geodäsie und Fernerkundung“, Deutsches Geoforschungszentrum GFZ
Telegrafenberg, 14473 Potsdam, Deutschland

Prof. Dr. Aleksander Brzeziński
Fakultät für Geodäsie und Kartographie der Technischen Universität Warschau
pl. Politechniki 1, 00-661 Warschau, Polen
Weltraumforschungszentrum der Polnischen Akademie der Wissenschaften
ul. Bartycka 18A, 00-716 Warschau, Polen

Tag der mündlichen Prüfung: 25.10.2012

Auflage: 80 Stück

ISSN 1811-8380

Acknowledgments

I wish to express my sincere gratitude to my supervisor Harald Schuh. He gave the initial ideas for this dissertation and granted me at the same time a great degree of freedom in the realization. I appreciate his encouragement to present my work at numerous international conferences, where I did not only gain fresh thoughts for my research, but also had a lot of nice encounters with colleagues from all over the world.

I am truly indebted and thankful to my co-supervisor Robert Weber who was always there to enlighten my understanding of Global Navigation Satellite Systems and guide me through the pitfalls of the Bernese Software. I am grateful for his interest in my work and his helpful and accurate comments on this thesis.

I would like to thank Aleksander Brzeziński for accepting the assessment of this dissertation, for motivating me to employ the complex demodulation technique for my studies, and for the cordial cooperation.

This thesis would be less complete without the initiative of Johannes Böhm to develop the Vienna VLBI Software. I am obliged to him and all colleagues who contributed to the evolution of VieVS and thereby supported my work. Special thanks in this respect go to Hana Krásná for providing the brilliant global solution module. I am further grateful to Lucia Plank and to Johannes Böhm for several valuable discussions on scientific problems and for proofreading this work or parts of it.

The help of a special person, who significantly contributed to the improvement of the most important parts of the thesis, is deeply appreciated.

Many nice colleagues have accompanied me during my studies at the research group of Advanced Geodesy and assisted my research by providing a friendly and pleasant atmosphere to work in. I owe particular thankfulness to all my officemates of the last years, who always were a source of inspiration in one way or another.

It is a great pleasure to express my heartfelt gratitude to my husband Herbert Böhm, my family, and my friends, for their love, their patience, and their solidarity. I am especially thankful for their understanding and the tacit acceptance of my almost chronic lack of time in the last months.

I appreciate the establishment, preprocessing and complimentary allocation of VLBI and GNSS observation data by the International VLBI Service for Geodesy and Astrometry and the International GNSS Service.

Finally, I acknowledge the Austrian Academy of Sciences for awarding me a DOC-fFORTE grant. This work was furthermore supported by the Austrian Science Fund (FWF): projects P23143-N21 and P24813-N29.

Abstract

Detailed descriptions of Earth rotation variability, based on a profound geophysical background, are required to ensure the precision and reliability of statements and parameters derived from space geodetic observations. Vice versa, the availability of highly accurate time series of Earth rotation parameters (ERP) allows to draw conclusions about global dynamic processes and interactions in system Earth and enables the evaluation and improvement of geophysical models. Both aspects are treated in the present dissertation with respect to tidal excitation of Earth rotation from subdiurnal to annual periods.

The model for diurnal and subdiurnal ocean tidal effects on polar motion and universal time (UT1) which is currently recommended by the IERS (International Earth Rotation and Reference Systems Service) has been derived from an already outdated ocean tide model and is suspected to negatively influence GPS (Global Positioning System) orbit determination and, in special cases, the analysis of VLBI (Very Long Baseline Interferometry) observations. The explicit knowledge of the ocean tidal contribution to Earth rotation variations is furthermore essential to study other high-frequency influences, such as thermal tides of atmosphere and oceans and the effect of the lunisolar torque on the triaxial Earth, denominated libration. The objectives of this work regarding high-frequency tidal phenomena are to identify deficiencies of the conventional ocean tidal ERP model, to examine alternatives, and to investigate the potential benefit of a combined analysis of GPS with the Russian Global Navigation Satellite System (GNSS) GLONASS.

The second central subject of this thesis concerns the long-period tidal variations in UT1. These are referred to as zonal tidal variations and comprise the effects of solid Earth tides (elastic and anelastic Earth response) and long-period ocean tides. Appropriate models are important for the prediction of UT1 and thus for real-time applications and navigation tasks. The research assignments in this respect are to employ VLBI and GNSS observations of UT1, first, in order to assess whether the conventional model for zonal tidal variations represents the observational evidence, and second, in order to investigate the achievable precision of the zonal response coefficient κ . This is a proportionality factor to transfer tidal potential amplitudes to zonal tidal amplitudes in UT1, which characterizes the response properties of the Earth-ocean-system.

Zonal as well as high-frequency variations are derived by least-squares adjustment from VLBI- and GNSS-based ERP time series with adapted resolution. For extracting short-period tidal signal from VLBI, the complex demodulation technique and the direct determination of tidal terms within a global solution are applied additionally.

The examination of the IERS Conventions (2010) model for ocean tidal ERP variations reveals significant deficiencies of most of the major model terms, concerning polar motion as well as UT1. Corresponding Earth rotation variations derived from the recent ocean tide model TPXO7.2 agree slightly better with the observed ERP. In contrast to the conventional model, polar motion residuals to TPXO7.2 are further reduced by application of the libration corrections. The benefit

of a combined GPS+GLONASS solution cannot be proved, owing to the small number (7%) of available GLONASS observations during the inspected time period (2008–2008.6). Different combinations of geophysical models for the excitation (atmospheric, non-tidal oceanic) of the thermal S_1 component show mutual disagreement and, moreover, none of the compared model combinations is capable of explaining the observed S_1 residuals.

The IERS Conventions (2010) model for zonal tidal variations is in good accordance with UT1 and derived LOD (length of day) observations. The main deficit of the previous conventional model (IERS Conventions, 2003) is confirmed to be the negligence of a dynamic ocean tide for fortnightly and monthly constituents. Conspicuous peaks in the LOD residual spectrum at the semiannual and annual periods can be attributed to the contribution of upper zonal winds, not contained in the atmosphere angular momentum data used for preprocessing. At present, the zonal response coefficient κ can be determined from the empirical fortnightly and monthly zonal terms with a precision of 0.3%.

The revision of the conventional model for high-frequency ocean tidal excitation of Earth rotation is strongly recommended. It is clearly demonstrated in the present work, that a re-computation on the basis of a more recent ocean tide model decreases the residuals, but to a minor degree. The inclusion of a harmonic model of the thermal S_1 ocean tide to a standard ocean tidal ERP model is not advised unless the presented discrepancies of geophysical models are explained. Updating the current conventional model for zonal tidal UT1 variations is not necessary from the observational point of view. Yet, in view of the now achievable precision of the zonal response coefficient, a modern model for the elastic solid Earth response would certainly facilitate the quantification of mantle anelasticity by means of observations.

Kurzfassung

Eine präzise Beschreibung des Rotationsverhaltens der Erde, die auf geophysikalischen Grundlagen beruht, ist unabdingbar für die Präzision und Zuverlässigkeit der aus Beobachtungen geodätischer Weltraumverfahren abgeleiteten Aussagen und Parameter. Umgekehrt ermöglicht die Verfügbarkeit hochgenauer Zeitreihen der Erdrotationsparameter (ERP) Erkenntnisse über globale dynamische Prozesse und Wechselwirkungen im System Erde und erlaubt die Evaluierung und Verbesserung von Modellen, die diese beschreiben. Beide Aspekte werden in der vorliegenden Dissertation hinsichtlich des Einflusses der Gezeiten auf die Erdrotation im Periodenbereich von einigen Stunden bis zu einem Jahr behandelt.

Das vom IERS (International Earth Rotation and Reference Systems Service) empfohlene Modell für tägliche und sub-tägliche Effekte der Ozeangezeiten auf Polbewegung und Weltzeit (UT1) basiert auf einem inzwischen überholten Ozeangezeitenmodell. Es besteht die Vermutung, dass dadurch die Bahnbestimmung des GPS (Global Positioning System), sowie, unter bestimmten Gegebenheiten, auch die Analyse von Beobachtungen der VLBI (Very Long Baseline Interferometry), negativ beeinflusst werden. Die exakte Kenntnis des Beitrags der Ozeangezeiten zu Erdrotationsschwankungen ist ferner essentiell für die Erforschung anderer hochfrequenter Einflüsse, wie der thermischen Gezeiten der Atmosphäre und Ozeane und die Auswirkungen des lunisolaren Drehmoments auf die triaxiale Figur der Erde, genannt Libration. Die Ziele dieser Arbeit bezüglich hochfrequenter Gezeitenphänomene sind, die Mängel des konventionellen ERP-Ozeangezeitenmodells aufzuzeigen, Alternativen zu erkunden, und den potentiellen Vorteil einer kombinierten Analyse von GPS mit dem russischen GNSS (Global Navigation Satellite System) GLONASS zu untersuchen.

Die zweite zentrale Fragestellung dieser Doktorarbeit betrifft langperiodische gezeitenbedingte Schwankungen der Weltzeit. Sie werden als zonale gezeitenbedingte Variationen bezeichnet und umfassen die Effekte der festen Erdgezeiten (elastische und anelastische Reaktion des Erdkörpers) und langperiodischer Ozeangezeiten. Entsprechende Modelle sind wichtig für die Prädiktion von UT1 und somit für Echtzeitanwendungen und Navigationsaufgaben. Anhand von UT1-Beobachtungen der Verfahren VLBI und GNSS wird beurteilt, ob das konventionelle Modell der zonalen gezeitenbedingten Variationen die empirisch ermittelten Schwankungen ausreichend genau repräsentiert. Des Weiteren wird erforscht, mit welcher Unsicherheit der zonale Reaktionskoeffizient κ aus den Beobachtungen bestimmt werden kann. Dieser Koeffizient beschreibt den Zusammenhang zwischen Amplituden des Gezeitenpotentials und Amplituden des zonalen Gezeitensignals in UT1 und charakterisiert damit die Reaktionseigenschaften des Erde-Ozean-Systems.

Die Komponenten der gezeitenbedingten Schwingungen werden durch Ausgleichung nach der Methode der kleinsten Quadrate aus VLBI- und GNSS-ERP-Zeitreihen mit geeigneter Auflösung ermittelt. Zur Ableitung der hochfrequenten Gezeitensignale aus VLBI kommen außerdem

das Verfahren der komplexen Demodulation und die direkte Schätzung der harmonischen Koeffizienten innerhalb einer globalen Lösung zum Einsatz.

Die Analyse der Erdrotationsschwankungen im Hinblick auf kurzperiodische Ozeangezeiten offenbart signifikante Mängel des Modells der neuesten IERS Conventions (2010) bezüglich der meisten Hauptterme, sowohl in der Polbewegung als auch in UT1. Entsprechende unter Verwendung des aktuellen Ozeangezeitenmodells TPXO7.2 durchgeführte ERP-Prädiktionen stimmen etwas besser mit beobachteten ERP überein. Im Gegensatz zum konventionellen Modell werden durch Anbringen der Librationskorrekturen auch die Polbewegungsresiduen zu TPXO7.2 weiter verringert. Der Vorteil einer kombinierten GPS+GLONASS Lösung kann, aufgrund der geringen Anzahl (7%) verfügbarer GLONASS Daten im Beobachtungszeitraum (2008–2008.6), nicht bewiesen werden. Verschiedene Kombinationen geophysikalischer Modelle für die Anregung der thermischen S_1 -Komponente (atmosphärische, nicht-gezeitenbedingte ozeanische) lassen im Vergleich keine einheitlichen Tendenzen erkennen; zudem sind die beobachteten S_1 -Residuen durch keine der herangezogenen Modellkombinationen zu begründen.

Das in den IERS Conventions (2010) propagierte Modell für den Effekt der zonalen Gezeiten weist gute Übereinstimmungen mit gemessenen UT1- und abgeleiteten LOD- (length of day) Werten auf. Als wesentlicher Nachteil des Vorgängermodells (IERS Conventions, 2003) wird die Vernachlässigung einer dynamischen Ozeantide für halbmonatliche und monatliche Komponenten bestätigt. Auffällige Spitzenwerte des LOD-Residuenspektrums zu halbjährlichen und jährlichen Perioden sind auf den Beitrag zonaler Winde in der oberen Atmosphäre zurückzuführen, der in den zur Datenreduktion verwendeten atmosphärischen Drehimpulsfunktionen nicht berücksichtigt ist. Der zonale Reaktionskoeffizient κ kann aus den empirischen halbmonatlichen und monatlichen zonalen Termen gegenwärtig auf 0.3% genau bestimmt werden.

Das konventionelle Modell der hochfrequenten Anregung der Erdrotation durch Ozeangezeiten sollte zweifellos revidiert werden. Wie in der vorliegenden Arbeit deutlich dargestellt wird, reduziert die Neuberechnung auf Basis eines neueren Gezeitenmodells die vorhandenen Abweichungen, allerdings nur in geringem Maße. Die Einbeziehung eines harmonischen Modells der thermischen S_1 -Ozeantide in ein Standardmodell zur Vorhersage der ozeangezeitenbedingten ERP ist nicht zu empfehlen, solange offenkundige Diskrepanzen zwischen den geophysikalischen Modellen bestehen.

Eine Aktualisierung des konventionellen Modells für zonale UT1-Variationen ist, vom Standpunkt der Beobachtungen aus, nicht zwingend notwendig. Angesichts der nun erreichbaren Genauigkeit in der Bestimmung des zonalen Reaktionskoeffizienten, würde ein modernes Modell des elastischen Anteils der festen Erdgezeiten jedoch mit Sicherheit die Quantifizierung des anelastischen Verhaltens anhand von Beobachtungen voranbringen.

Contents

1	Introduction	1
1.1	Earth rotation variability	1
1.2	Hunting for the sub-millimeter – GGOS objectives	2
1.3	Aims and outline of the present study	3
2	Rotational dynamics of a deformable Earth	7
2.1	Geodetic reference systems and frames	7
2.1.1	Celestial reference frame	7
2.1.2	Terrestrial reference frame	8
2.1.3	Transformation concepts and Earth orientation parameters	8
2.2	Fundamental relations	11
2.2.1	Equations of motion	11
2.2.2	Modeling geophysical excitation	14
2.2.3	Connection between theoretical and observed axes	15
2.3	Compilation of the major effects on Earth rotation	16
2.3.1	Axis orientation	17
2.3.2	Rotation speed	18
3	Tides and Earth rotation	21
3.1	Tidal force	21
3.1.1	Tidal potential expansions	22
3.1.2	Fundamental astronomical arguments	24
3.2	Solid Earth tides	27
3.2.1	Impact of zonal deformation on Earth rotation	28
3.2.2	The zonal response coefficient of the Earth-ocean-system	29
3.2.3	Theoretical models of zonal tidal Earth rotation variations	31
3.3	Ocean tides	34
3.3.1	Ocean tide models	35
3.3.2	Tidal analysis	37
3.3.3	Ocean tidal angular momentum	41
3.3.4	Earth rotation variations from ocean tide models	42

3.4	Tides in the atmosphere	44
4	Earth rotation variations from Very Long Baseline Interferometry	47
4.1	Observation equation and error sources	48
4.2	Determination of Earth orientation parameters	51
4.2.1	Partial derivatives and a priori information	52
4.2.2	Parametrization	53
4.2.3	Datum definition and correlation issues	54
4.3	Estimation of Earth rotation parameter long-time series	57
4.3.1	OCCAM solution	59
4.3.2	VieVS solution	61
4.4	Estimation of demodulated Earth rotation parameters	62
4.4.1	Alternative ERP parametrization	63
4.4.2	Processing and time series characteristics	64
4.5	Direct estimation of tidal ERP variations	66
4.5.1	Formulation and partial derivatives	67
4.5.2	Processing and solution characteristics	68
5	Earth rotation variations from Global Navigation Satellite Systems	71
5.1	Observation equation and error sources	72
5.2	Determination of Earth orientation parameters	73
5.2.1	Partial derivatives and estimability of EOP	74
5.2.2	Datum definition and correlation issues	76
5.3	Estimation of Earth rotation parameters using Bernese Software	76
5.3.1	GPS-only campaign (2005–2007)	77
5.3.2	GPS+GLONASS campaign (2008–2008.6)	79
6	Modeled and observed tidal Earth rotation variations	85
6.1	Time series analysis – recovery of harmonic signals	85
6.1.1	Short-period variations from highly resolved ERP	86
6.1.2	Short-period variations from demodulated ERP	88
6.1.3	Zonal tidal variations from UT1 and LOD	89
6.1.4	Estimation of the zonal response coefficient from VLBI observations	93
6.2	Derivation of ocean tidal ERP models	95
6.2.1	Diurnal and semidiurnal ocean tidal ERP models based on TPXO7.2 and HAMTIDE11a	95
6.2.2	Monthly and fortnightly ocean tidal ERP model based on TPXO7.2	97
6.3	Comparison of empirical and semi-empirical models – diurnal and subdiurnal tidal band	99
6.3.1	Retrograde diurnal polar motion	99
6.3.2	GNSS solutions	102

6.3.3	VLBI solutions	105
6.3.4	Assessment of ocean tidal ERP models	110
6.4	Comparison of empirical and theoretical models – long-period tidal band	118
6.4.1	Mutual agreement of empirical models	119
6.4.2	Assessment of zonal tidal UT1/LOD models	123
6.4.3	Results for the zonal response coefficient	127
7	Summary, conclusions, and future prospects	131
7.1	Discussion of short-period polar motion and UT1 variations	132
7.2	Discussion of long-period UT1 and LOD variations	134
A	Tables	137
A.1	Orthotide formalism	137
A.2	Tidal ERP coefficients	137
A.3	Root mean square of tidal coefficients differences	143
B	Figures	145
B.1	Empirical high-frequency ERP terms	145
B.2	Empirical zonal tidal UT1/LOD terms	149
List of Figures		151
List of Tables		153
Acronyms		155
Bibliography		157

Chapter 1

Introduction

The surface of the Earth is constantly moving and changing its appearance, periodically as well as permanently. The periodic deformations are predominantly products of tidal forces, exerted by the Moon and Sun, and the rotation of the Earth. Tides of the solid Earth have a magnitude of several tens of centimeters, whereas ocean tides can reach heights of several meters (mostly due to the presence of the continents and resonance effects in ocean basins). Tidal phenomena continuously affect directly or indirectly all kinds of global and also local geodetic observations, geometric as well as gravimetric ones. Mass displacements due to tidal height variations and relative particle motion due to tidal current flows cause significant changes in the Earth rotation speed and can alter the direction of the rotation axis. The variability of both the Earth rotation speed and the direction of the rotation axis again has considerable consequences for the observation of the positions of objects in space and stations on the Earth surface. Accordingly, the explicit knowledge of Earth rotation irregularities, whatever source of excitation they have, is substantial for all tasks of precise positioning and navigation relying on space observations. As to geodesy that applies in particular for the space techniques, VLBI (Very Long Baseline Interferometry), GNSS (Global Navigation Satellite System), SLR, and LLR (Satellite and Lunar Laser Ranging) and DORIS (Doppler Orbitography and Radiopositioning Integrated by Satellite). On the one hand these space geodetic techniques partially depend on information about the spatio-temporal relation between positions on Earth and in space and on the other hand they as well observe and furnish such information. The space geodetic observations thus play a key role in Earth rotation research and vice versa independent and realistic models of Earth rotation variability can considerably improve the results of space geodesy.

1.1 Earth rotation variability

The Earth is not rotating uniformly. Its rotation speed shows a long-term negative trend and undergoes periodic and irregular fluctuations. Moreover, the direction of the rotation axis is stable neither with respect to space nor with respect to the Earth surface. The variability of the rotational behavior is, inter alia, due to the fact that the Earth is not a rigid body, but a

dynamic system partly covered by oceans and enveloped by an atmosphere. A deformable Earth can change the moments of inertia and must, because of the conservation of angular momentum, accordingly change the rotation speed. Similarly, a variation in the angular momentum of geophysical fluids, like oceans or atmosphere, will lead to a complementary variation in the angular momentum of the solid Earth, since the total angular momentum of the whole Earth system is conserved (in the absence of external torques, which are disregarded for this simplified explanation). These mechanisms, surface mass redistributions, relative motions, and also internal processes, do not only affect the magnitude of the rotation vector, but also its direction mainly the one w.r.t. the Earth, referred to as polar motion. Besides the direct effect on polar motion, geophysical processes are also responsible for exciting the Earth's most prominent free oscillation, known as Chandler wobble. This free oscillation, induced by the misalignment of the axis of rotation with the figure axis of the Earth, represents the largest component of polar motion. In combination with an annual oscillation (predominantly caused by atmospheric pressure changes) the total polar motion can reach up to 9 m at the Earth surface (understood as maximum deviation from a mean value). Converted to the length of the circular arc at the equator which is traversed in a certain time, the variations of the Earth rotation speed can reach even considerably larger amplitudes, amounting to several tens of meters at very long periods.

Changes in the rotation speed are conventionally specified either as deviation of universal time (UT1) from atomic time (universal time coordinated - UTC) or as excess over the nominal length of one day (24 hours), shortly length of day or LOD, respectively. In contrast to polar motion which represents the direction of the Earth axis w.r.t. the crust, motions of the axis w.r.t. the star background are termed precession and nutation.

The precession, which was known already in ancient Greece, is by far the largest effect in the variation of the Earth rotation vector. It is a circular motion of the Earth's rotation pole around the pole of the ecliptic (the orbital plane of the Earth) with a velocity of around 600 m per year if visualized on the Earth surface. The Earth, being an oblate spheroid as a first approximation, reacts like a symmetric gyroscope to the torques exerted by Moon and Sun, leading to this evasive movement of the rotation axis with a period of almost 26000 years. Precession is superposed by smaller effects with much shorter periods, having the same physical cause, which are called nutations. The major nutation component has a period of 18.6 years (corresponding to one revolution of the lunar ascending node) and a magnitude of approximately 280 m if projected on the Earth surface. A review on Earth rotation variability and associated terms and definitions is given for example in Seitz & Schuh (2010) or more briefly in Schuh & Böhm (2011).

1.2 Hunting for the sub-millimeter – GGOS objectives

The Global Geodetic Observing System GGOS is a central constituent of the International Association of Geodesy (IAG). GGOS works with all IAG components integrating different geodetic measurement techniques, models and approaches in order to provide the three basic observables

of global geodesy and their variations, the geometrical shape, gravity field and rotation of the Earth (Plag & Pearlman, 2009). These three pillars are the framework geodetic reference frames are built on. With the allocation of precise and stable coordinate frames GGOS provides the metrological basis for Earth observation. The relevance of Earth observations goes far beyond the scholarly interest. Monitoring, understanding and possible prediction of dynamic processes – especially under the influence of global change – are of vital interest for global society in various aspects. The global sea level is one such example which literally rises or falls with the reference it is gauged on. In other words, the interpretation of geodynamic processes is very often based on rather weak signals and trends, which is why a profound reference is crucial to ensure the reliability of the results. In view of target quantities of sometimes comparatively small magnitudes on the one hand and considering the increasing technical capabilities of the observation methods on the other hand, the ambitious goals of GGOS are to provide variations in the fundamental parameters with an accuracy of 1–0.1 ppb. Expressed in terms of station coordinates this implies about 1–2 mm accuracy for station positions and 0.1–0.3 mm/year for station velocities. These numbers correspond to the future objectives for terrestrial reference frame determination of the IVS (International VLBI Service for Geodesy and Astrometry) (Schuh *et al.*, 2002). Since the three pillars of geodesy are intrinsically linked to each other, the demand for utmost accuracy in each of them, leading to highly accurate and reliable end products – the geodetic reference frames, becomes obvious. Geodetic reference frames rely on parameters which are derived from the observations of space geodetic techniques. The robustness and precision of the analysis of space geodetic observations is therefore of great importance for reference frame realization. Precise knowledge of Earth rotation variability is one subject of specific interest.

1.3 Aims and outline of the present study

The irregularities of Earth rotation are partly predicted by theoretical or semi-empirical models and partly they have to be monitored by means of space geodetic techniques. The transformation between space-fixed and Earth-fixed reference systems, which essentially accounts for all phenomena of Earth orientation variability mentioned before (precession-nutation, polar motion, changes of the rotation speed), is an integral part of the observation equations of space geodetic techniques. Effects of precession-nutation are almost completely represented by a model. Offsets to this model as well as quantities specifying polar motion and changes of the rotation speed are denominated Earth orientation parameters (EOP). The subgroup of only the latter two effects is referred to as Earth rotation parameters (ERP). The EOP represent the rather unpredictable part of Earth orientation variability, which should therefore be estimated within the analysis of space geodetic observations, if possible. However, in many cases the estimation of EOP is either not feasible for all of the parameters or impossible at all. This is valid e.g. for spacecraft navigation, where most accurate predictions of the EOP are required. Such missions cannot wait for the post-processing results based on the observations of space geodetic techniques, their plan-

ning and realization necessitate adequate models to extrapolate the EOP into the future. This is one of three main rationales behind the efforts to provide best possible models of Earth rotation variations. The second is the importance for space geodetic data processing itself: Since the analysis of those observations is usually based on least-squares procedures, a most precise functional model and therein appropriate a priori EOP models are essential. This fact becomes evident especially in cases where not all or even none of the parameters of Earth orientation can be estimated within the data analysis, but have to be fixed to a priori values. Last but not least, models of Earth rotation variations comprise information about the properties of the fluids exciting them, as well as parameters characterizing the shape or rheology of the Earth. Proper Earth rotation models in combination with precise observations thus permit valuable conclusions about Earth system dynamics.

The present dissertation is devoted to tidal excitation of Earth rotation, observed by VLBI and GNSS. In the past, the tidal phenomena, having a well-known periodic behavior, were either considered as well predictable or their impact on Earth rotation was too small to be taken into account or even to be detected. In the last decades first the accuracy of the measurements has increased considerably and second the time span of available observations of good quality now fairly exceeds 18.6 years, which is the longest period of the important tidal signals. Consequently, studies of tidal signals in Earth rotation observations are now particularly effective, on the one hand, but on the other hand deficiencies in the tidal EOP models can have significant and undesirable influence on the results of the data analysis. For example, the present conventional model for the effect of diurnal and subdiurnal ocean tides, which is used as standard to infer high-frequency a priori polar motion and UT1 information, is suspected to cause problems particularly in GPS (Global Positioning System) orbit determination. Another important conventional model, relevant for the prediction of UT1, reproduces the effects of long-period solid Earth tides and ocean tides on the rotation speed. These are summarized under the term zonal tidal variations.

The main aims of this work are to scrutinize and validate these conventional tidal Earth rotation models on the basis of observations from VLBI and GNSS. Furthermore, different methods to estimate in particular diurnal and subdiurnal tidal variations are investigated. In this respect the possible benefit of a combined analysis of GPS and GLONASS (the Russian GNSS) observations is examined as well. Besides the technical, observational aspects, this thesis also aims at inspecting the geophysical findings and modeling possibilities in the areas of solid Earth and ocean tides. The research objective is thus a combination of evaluation and enhancement of the performance of models for tidally induced Earth rotation variations. In terms of comparison with space geodetic observations the emphasis is placed on high-frequency ocean tidal effects in polar motion and UT1 as well as on long-period UT1 variations. Long-period variations due to ocean tides in polar motion are touched only with respect to geophysical modeling. Zonal tidal UT1 variations extracted from the space geodetic observations can be utilized to determine a kind of rheological parameter, the so-called zonal response coefficient of the Earth-ocean-system κ . This coefficient can provide conclusions about the response of solid Earth and oceans to tidal forcing.

A subordinate yet not insignificant task of this work is to estimate as to which precision the zonal response coefficient can be determined at present.

After this preface, the thesis continues with the description of the theoretical framework split to two chapters. Chapter 2 gives information about the definition and realization of geodetic reference systems and the transition between them. Furthermore the basic equations for modeling the Earth's rotational motion and the geophysical excitation of Earth rotation are provided, closing with a compilation of the most important phenomena affecting the direction of the Earth axis and rotation speed.

The third chapter is dedicated to tides and their interaction with Earth rotation. At first the generation of the tidal force and its representation in the form of tidal potential expansions are explained. This is followed by three sections that deal with specification and modeling of solid Earth tides, ocean tides and atmosphere tides as well as with their impact on Earth rotation.

Chapters 4 and 5 are in between theory and practice, as they treat the observation of Earth rotation variations by means of VLBI and GNSS. In both chapters the basic observation equations of the respective technique are addressed just as the realization and limitations of the determination of parameters describing Earth orientation.

The VLBI chapter comprises moreover explications about estimating tidal Earth rotation variations with three different methods which were employed to derive several different time series and solutions. Exemplary results and the characteristics of these solutions are also presented within this part.

Aside from covering the general background of EOP observation with GNSS, Chapter 5 refers to the practical calculation of time series and the processing strategies followed in two main campaigns.

Observed Earth rotation variations are analyzed and compared to one another and to geophysical models in Chapter 6, which is composed of four sections. The first section discusses the extraction of tidal signal from time series separately for short- and long-period variations. The second section is an excursus to geophysical modeling – it reports about the derivation of polar motion and UT1 excitation from ocean tide models and allocates the results for diurnal and semidiurnal as well as monthly and fortnightly tidal waves. Finally all results are assembled and juxtaposed to theoretical, empirical and semi-empirical models in the last two sections, independently for high- and low-frequency variations.

The closing Chapter 7 summarizes the findings of this thesis, states the conclusions and gives an outlook to future work and challenges related to this topic.

Chapter 2

Rotational dynamics of a deformable Earth

The real Earth is not a rigid body, it has a layered structure, its solid parts are of ductile material and more than two thirds of its surface are covered by oceans. Considering the Earth as deformable has several consequences for the description of its rotational behavior and makes it a particular intricate task to attach reference frames to the Earth crust.

2.1 Geodetic reference systems and frames

Monitoring the orientation of the Earth axis in space and w.r.t. the Earth surface relies on the definition and establishment of adequate reference frames. The realization of a space-fixed coordinate system is called celestial reference frame (CRF), the realization of a body- or Earth-fixed coordinate system is referred to as terrestrial reference frame (TRF). Constitution and maintenance of conventional reference frames belong to the core tasks of the International Earth Rotation and Reference Systems Service (IERS).

2.1.1 Celestial reference frame

The ICRF2 (International Celestial Reference Frame 2; Fey *et al.* (2009)) is the current conventional space-fixed coordinate frame. ICRF2 is the second realization of the International Celestial Reference System (ICRS; Arias *et al.*, 1995) at radio frequencies. The first realization is commonly referred to as ICRF (Ma *et al.*, 1998), hereafter as ICRF1 to place a clear distinction. According to the recommendations of the International Astronomical Union (IAU), the origin of the celestial reference system is at the barycenter of our Solar System. The directions of its axes are fixed relative to distant extragalactic radio sources, with the ICRS pole aligned with the J2000.0 direction defined by the previous conventional IAU models for precession (Lieske *et al.*, 1977) and nutation (Seidelmann, 1982). The ICRS is an equatorial system with the lead angle called right ascension counted from 0 to 24 hours, counterclockwise. The distance an-

gle is denominated declination and counted from 0 to 90 degrees towards north and from 0 to -90 degrees towards south. The origin of right ascensions and datum plane of the ICRS realization are aligned and consistent with the previously used vernal equinox and equator at the standard epoch J2000. However, the positions of the 295 defining sources of ICRF2 are not epoch-dependent. ICRF2 is stated to have a noise floor of around $40 \mu\text{as}$ and an axis stability of approximately $10 \mu\text{as}$, making the second realization about 5-6 times more accurate and twice as stable as ICRF1 (Fey *et al.*, 2009).

2.1.2 Terrestrial reference frame

The International Terrestrial Reference System (ITRS) is geocentric, with the origin defined at the center of mass of the whole Earth, including oceans and atmosphere. It is a cartesian coordinate system, having the orientation of the previous BIH (Bureau International de l'Heure) system at the epoch 1984.0 (IERS Conventions, 2010, Ch. 4). The ITRS pole coincides approximately with the position of the mean rotation pole at the beginning of the 20th century, while the origin of longitudes corresponds roughly to the Greenwich meridian.

The realization of the ITRS consists of estimated coordinates and velocities of a set of stations on the Earth surface, observed by VLBI, SLR, LLR, GNSS and DORIS. The current specification of the conventional ITRS realization is named ITRF2008 (International Terrestrial Reference Frame 2008; Altamimi *et al.*, 2011). ITRF2008 is the twelfth in the line of ITRF, which started with ITRF88. The time evolution of the orientation of the ITRF is ensured by imposing a no-net-rotation condition on the horizontal tectonic motions over the whole Earth. A TRF refers to a specified epoch and can be related to other TRF versions with a set of seven parameters (three rotations, three translations and a scale) and their temporal derivatives. ITRF is a crust-based frame, providing regularized conventional tide-free station coordinates at a time t . The instantaneous position of a point anchored on the crust, $\mathbf{X}(t)$, can be obtained according to the following model:

$$\mathbf{X}(t) = \mathbf{X}_0 + \dot{\mathbf{X}} \cdot (t - t_0) + \sum_i \Delta\mathbf{X}_i(t). \quad (2.1)$$

\mathbf{X}_0 and $\dot{\mathbf{X}}$ are the coordinates and velocities given in the TRF solution, referring to epoch t_0 . The $\Delta\mathbf{X}_i(t)$ are appropriate corrections, mostly for the short term deformation of the crust at the epoch of interest, as it is caused for example by solid Earth tides or loading effects. The ITRF2008 positions refer to the epoch 2005.0. The accuracies of origin and scale of ITRF2008 are believed to be at the level of 1 cm and 1.2 ppb (8 mm at the equator), respectively (Altamimi *et al.*, 2011).

2.1.3 Transformation concepts and Earth orientation parameters

Earth orientation parameters are the elements defining in real terms the transformation between space-fixed, but geocentric, and Earth-fixed reference frames. These are, two angles describing the orientation of a preassigned reference direction w.r.t. to the CRF, precession-nutation,

two angles representing the motion of this reference axis in the TRF, polar motion, and one angle providing the actual phase of rotation of the TRF w.r.t. the CRF, namely an Earth rotation angle. The choice of the reference axis is actually not forced by the observation conditions, but somewhat arbitrary. The axis, precession-nutation models are calculated for, can be any, such as the rotation axis, the angular momentum or even the figure axis, as long as polar motion is defined accordingly and local geophysical motions are taken into account (Seidelmann, 1982). The conventional reference direction is the axis of the Celestial Intermediate Pole (CIP). It corresponds to neither of the previously mentioned physical axes but can be mathematically transferred to any of them. The observations of all space-based techniques, which use a conventional precession-nutation model within the respective parameter estimation, refer to the CIP. Commonly the term rotation axis is used (also in the introduction to this thesis) when speaking about the observation of Earth rotation variations. Technically, though, the space-geodetic techniques do not observe the motion of the instantaneous rotation vector, but the motion of the CIP (refer to last part of this section for additional details).

The transition from celestial to terrestrial coordinates or vice versa is defined by a sequence of rotations. Since no translations are involved, the initial coordinates have to be geocentric in both cases. To convert from a barycentric system, as the ICRS, to a geocentric system, corrections for aberration and parallax effects have to be applied.

There are two commonly used transformation concepts, both of which are specified between the so-called Geocentric Celestial Reference System (GCRS – oriented as the ICRS) and the ITRS. The older concept, based on the vernal equinox, as the nodal point defined by ecliptic and equator, is still in use, but shall not be elaborated here (see IERS Conventions (1996) for further information). The IERS recommends to apply the transformation, based on the so-called Non-Rotating Origin (NRO), according to IAU Resolutions 2000 and 2006 (IERS Conventions, 2010, Ch. 5):

$$\mathbf{r}_{\text{GCRS}}(t) = \underbrace{\mathbf{R}_3(-E) \cdot \mathbf{R}_2(-d) \cdot \mathbf{R}_3(E+s)}_{\mathbf{Q}(t)} \cdot \underbrace{\mathbf{R}_3(-\text{ERA})}_{\mathbf{R}(t)} \cdot \underbrace{\mathbf{R}_3(-s') \cdot \mathbf{R}_2(x_p) \cdot \mathbf{R}_1(y_p)}_{\mathbf{W}(t)} \cdot \mathbf{r}_{\text{ITRS}}(t) \quad (2.2)$$

with $\mathbf{R}_i(\alpha)$ being a rotation matrix around axis i about the angle α and $E = \arctan Y/X$ and $d = \arcsin Y/E$. Equation (2.2) provides the instruction for transforming a vector \mathbf{r} given at a time t in the ITRS to the GCRS with a special order of rotation matrices. The ‘wobble’ matrix $\mathbf{W}(t)$ specifies the terrestrial motion of the CIP through the pole coordinates x_p and y_p . The small quantity s' , which is a function of the pole coordinates, locates the TIO (Terrestrial Intermediate Origin) on the equator of the CIP. The TIO and its celestial counterpart, the CIO (Celestial Intermediate Origin), realize the concept of the NRO (Capitaine *et al.*, 1986) and can be understood as a kind of prime meridian in the respective intermediate system. The Earth rotation matrix $\mathbf{R}(t)$ contains the angle between TIO and CIO measured along the equator of the CIP, the so-called ‘Earth Rotation Angle’ (ERA). Universal time 1 (UT1), which is the Earth rotation phase indicator in common use, is related to ERA by linear proportionality. The celestial transformation part

is effected by the precession-nutation matrix $Q(t)$, where the coordinates of the CIP w.r.t. the GCRS, X and Y , enter implicitly and the angle s serves as the CIO locator. This transformation concept is also designated CIO based, in contrast to equinox based, because the CIO somehow takes the role of the equinox in the new transformation concept. In the notation of the CIO based transformation, the five quantities $\{x_p, y_p, dUT1, X, Y\}$ are referred to as EOP. Wherein dUT1 equals UT1–UTC. In fact, it is also common practice to express the irregularities in the rotation rate as excess length of day, or shortly LOD, and regard this parameter as belonging to the EOP as well. The equinox based transformation contained separate precession and nutation matrices and nutation was represented as nutation in longitude $\Delta\psi$ and in obliquity $\Delta\epsilon$. The corresponding Earth orientation parameters were therefore $\{x_p, y_p, dUT1, \Delta\psi, \Delta\epsilon\}$. The nutation angles are usually composed from two parts: the major part, which is calculated from a conventional nutation model and a residual unpredictable part, which is observable by means of VLBI (also LLR). These additional fractions, $\{\delta X, \delta Y\}$ in the CIO based notation and $\{\delta\Delta\psi, \delta\Delta\epsilon\}$ in the equinox based notation, are denominated celestial pole offsets. The subset of the EOP, comprising only the terrestrial rotation components, i.e. the pole coordinates x_p and y_p and dUT1, or also LOD, respectively, are referred to as Earth rotation parameters (ERP). Polar motion, dUT1, LOD and celestial pole offsets are disseminated as continuous time series with daily resolution by the IERS. The conventional precession-nutation model, recommended by the IAU and the IERS, is the IAU 2006/2000 precession-nutation model (IERS Conventions, 2010, Ch. 5).

The CIP frequency conventions

Owing to tradition and also convenience, a transformation, which could be conducted using only three Eulerian angles, is in Earth rotation implemented using five angles. This leads to the fact that polar motion and nutation are kinematically connected and intercommunicable.

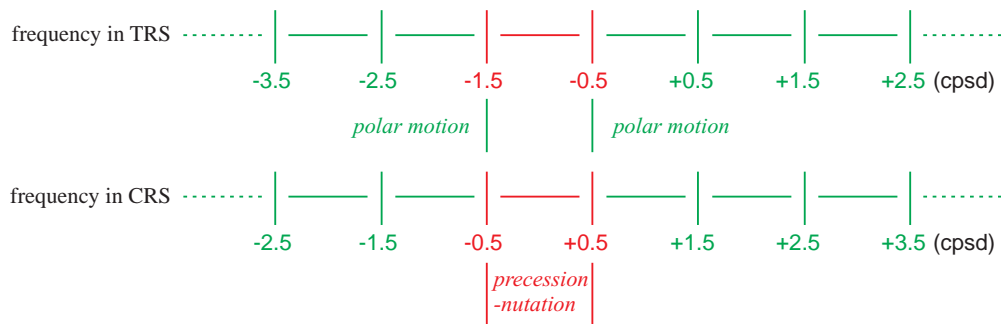


Figure 2.1: Conventional frequency separation between the terrestrial (top) and the celestial (bottom) motion of the CIP. The shift of 1 cpsd is a consequence of the diurnal rotation of the TRS w.r.t. the CRS. (The graphic is redrawn, following the IERS Conventions, 2010, Ch. 5)

In order to handle arising ambiguities the CIP was defined including a conventional frequency separation. This convention assigns all terms with periods longer than ± 2 sidereal days in the GCRS to the celestial motion (precession-nutation) of the CIP, viewed in the TRS these are

retrograde periods of $-2/3$ to -2 sidereal days. Retrograde means opposite to the sense of Earth rotation (marked by a minus sign), in contrast to prograde, signifying in the sense of Earth rotation (indicated by a plus sign). All variations with periods shorter than ± 2 sidereal days in the GCRS, corresponding to high frequency retrograde terms over -1.5 cpsd (cycles per sidereal day) and below -0.5 cpsd, as well as all prograde terms in the TRS, are belonging to the terrestrial motion (polar motion) of the CIP. Figure 2.1 illustrates the frequency conventions for the motion of the CIP, according to IERS Conventions (2010, Ch. 5).

2.2 Fundamental relations

The present work deals with tidal, i.e. geophysical, effects on Earth rotation. Geophysical phenomena take effect predominantly in the terrestrial part of Earth rotation, described by polar motion and dUT1 or LOD (ERP). The following paragraphs therefore provide the basic formalism for modeling geophysical effects and relating modeled Earth rotation variations to observed ERP.

2.2.1 Equations of motion

The dynamical equation of motion, representing the rotational behavior of a non-rigid Earth w.r.t. a terrestrial coordinate system, is the so-called Liouville equation (e.g. Moritz & Mueller, 1987; Munk & MacDonald, 1975). The Equation (2.3) balances changes in the Earth angular momentum \mathbf{H} and external torques \mathbf{L} . The angular momentum of a deformable Earth is dependent on changes of the Earth's figure, expressed in the tensor of inertia \mathbf{C} , relative angular momentum \mathbf{h} , induced by relative particle motion, and variations in the Earth rotation vector $\boldsymbol{\omega}$. The subsequent explications largely follow Moritz & Mueller (1987).

$$\underbrace{\frac{d}{dt}(\mathbf{C}(t)\boldsymbol{\omega}(t) + \mathbf{h}(t))}_{\frac{d}{dt}\mathbf{H}(t)} + \boldsymbol{\omega}(t) \times \underbrace{(\mathbf{C}(t)\boldsymbol{\omega}(t) + \mathbf{h}(t))}_{\mathbf{H}(t)} = \mathbf{L}(t). \quad (2.3)$$

The body-fixed reference frame, wherein the equations are formulated, is assumed to be a Tisserand mean-mantle frame (Tisserand, 1891). A Tisserand mean-mantle frame is defined such that velocities of relative motions of the crust or mantle are globally minimized in a least-squares sense. This implies that the relative angular momentum contributions $\mathbf{h}(t)$ are engendered solely by relative motions in the atmosphere, the oceans and the core.

The tensor of inertia \mathbf{C} is a function of the mass distribution of a body and is calculated by three-dimensional integration over all mass elements dM . Using index notation (implies summation over equal indices) and the Kronecker delta δ_{ij} it can be written, according to Moritz & Mueller (1987):

$$\mathbf{C}_{ij} = \iiint (x_k x_k \delta_{ij} - x_i x_j) dM \quad \text{with} \quad \delta_{ij} = \begin{cases} 0 & \text{for } i \neq j \\ 1 & \text{for } i = j \end{cases}. \quad (2.4)$$

The relative angular momentum is generally derived by integrating the cross product of the position vectors \mathbf{r} and velocity vectors $\dot{\mathbf{r}}$ of the mass elements:

$$\mathbf{h}(t) = \iiint \mathbf{r}(t) \times \dot{\mathbf{r}}(t) dM . \quad (2.5)$$

In order to express its temporal variability, the inertia tensor is composed of two parts (2.6). A constant part \mathbf{C}_0 , which is a diagonal matrix containing the principal moments of inertia of the Earth in an undeformed state, and a time variable part $\mathbf{c}(t)$, reflecting the deviations from the equilibrium state. The moments of inertia are denominated A , B and C . If rotational symmetry is assumed the equatorial moments of inertia are equal ($A=B$).

$$\mathbf{C}(t) = \begin{bmatrix} A & 0 & 0 \\ 0 & A & 0 \\ 0 & 0 & C \end{bmatrix} + \begin{bmatrix} c_{11}(t) & c_{12}(t) & c_{13}(t) \\ c_{12}(t) & c_{22}(t) & c_{23}(t) \\ c_{13}(t) & c_{23}(t) & c_{33}(t) \end{bmatrix} . \quad (2.6)$$

As the Earth is not rotating regularly around the vertical axis of the body-fixed reference system, the rotation vector $\boldsymbol{\omega}$ is split up into two vectors as well. The constant vector $\boldsymbol{\omega}_0$ represents an undeformed mean state, i.e. rotation around the z-axis of the TRS with a constant angular velocity Ω , and the elements m_1, m_2 and m_3 of vector $\delta\boldsymbol{\omega}(t)$ express the deviations from uniform rotation, hence the polar motion of the rotation axis and changes of the rotation speed.

$$\boldsymbol{\omega}(t) = \begin{bmatrix} 0 \\ 0 \\ \Omega \end{bmatrix} + \begin{bmatrix} m_1(t) \\ m_2(t) \\ m_3(t) \end{bmatrix} \Omega . \quad (2.7)$$

By substituting Equations (2.6) and (2.7) into the Liouville equation (2.3) and neglecting the squares, products and higher powers of the elements of \mathbf{c} and $\delta\boldsymbol{\omega}$ (linearization), the so-called Euler-Liouville equations (2.8) are obtained (Moritz & Mueller, 1987):

$$\begin{aligned} A\Omega\dot{m}_1(t) + (C - A)\Omega^2 m_2(t) + \Omega\dot{c}_{13}(t) - \Omega^2 c_{23}(t) + \dot{h}_1(t) - \Omega h_2(t) &= L_1(t) , \\ A\Omega\dot{m}_2(t) + (C - A)\Omega^2 m_1(t) + \Omega\dot{c}_{23}(t) + \Omega^2 c_{13}(t) + \dot{h}_2(t) + \Omega h_1(t) &= L_2(t) , \\ C\Omega\dot{m}_3(t) + \dot{c}_{33}(t)\Omega + \dot{h}_3(t) &= L_3(t) . \end{aligned} \quad (2.8)$$

If all variables that do not belong to the rotation vector are assembled in the three quantities ψ_1 , ψ_2 and ψ_3 , named excitation functions, and $\sigma_E = \frac{C-A}{A}\Omega$ is substituted, the equations of motion reduce to

$$\dot{m}_1(t)/\sigma_E + m_2(t) = \psi_2(t) , \quad \dot{m}_2(t)/\sigma_E - m_1(t) = -\psi_1(t) , \quad (2.9)$$

$$\dot{m}_3(t) = \dot{\psi}_3(t) \quad (2.10)$$

with the excitation functions

$$\begin{aligned}
 \psi_1(t) &= (\Omega^2 c_{13}(t) + \Omega \dot{c}_{23}(t) + \Omega h_1(t) + \dot{h}_2(t) - L_2(t)) / (C - A) \Omega^2, \\
 \psi_2(t) &= (\Omega^2 c_{23}(t) - \Omega \dot{c}_{13}(t) + \Omega h_2(t) - \dot{h}_1(t) + L_1(t)) / (C - A) \Omega^2, \\
 \dot{\psi}_3(t) &= (-\Omega \dot{c}_{33}(t) - \dot{h}_3(t) + L_3(t)) / C \Omega.
 \end{aligned} \tag{2.11}$$

The solutions of the equations of motion (2.9) and (2.10) yield the deviations from uniform rotation around the z-axis of the terrestrial coordinate system, namely variations of the angular velocity

$$m_3(t) = \psi_3(t) + \text{const.} \tag{2.12}$$

and polar motion

$$\hat{m}(t) = e^{i\sigma_E t} \left[\hat{m}(0) - i\sigma_E \int_0^t \hat{\psi}(\tau) e^{-i\sigma_E \tau} d\tau \right], \tag{2.13}$$

where polar motion components and equatorial excitation functions are written in complex notation, $\hat{m} = m_1 + im_2$ and $\hat{\psi} = \psi_1 + i\psi_2$, with the imaginary unit $i = \sqrt{-1}$ (Lambeck, 1980; Moritz & Mueller, 1987; Munk & MacDonald, 1975).

Except for the external torque L , the excitation functions ψ_i contain variable elements which describe the perturbation from rigid body rotation. Changes in the inertia tensor, represented by the c_{ij} can be induced by mass redistribution, due to tidal and centrifugal forces, variations in the atmosphere and oceans or internal processes. Relative angular momentum h_i is generated mainly by atmospheric and oceanic circulation. In the absence of external torques and geophysical excitation, Equation (2.13) produces the free mode of a rigid Earth, which is a circular motion with the Euler period of about 304 days ($2\pi/\sigma_E$). For a completely elastic Earth, without oceans and atmosphere, the frequency of the free mode turns into the theoretical Chandler frequency of about 430 days. It is determined by the elastic response of the Earth to tidal and centrifugal forcing, represented by the second degree Love number k_2 and the so-called secular Love number k_s . The (elastic) Chandler frequency can be expressed in terms of the Euler frequency

$$\sigma_C(\text{elastic}) = \sigma_E \frac{1 - \frac{k}{k_s}}{1 + \frac{k}{k_s} \frac{\sigma_E}{\Omega}} \quad \text{with} \quad k_s = \frac{3G(C - A)}{\Omega^2 R^5}, \tag{2.14}$$

where R denotes the mean Earth radius and G is the gravitational constant (Moritz & Mueller, 1987). The Chandler wobble of the real Earth is a damped oscillation with a complex frequency, usually written in dependence of its observed period T_C and a quality factor Q (Zharkov *et al.*, 1996):

$$\hat{\sigma}_C = \frac{2\pi}{T_C} \left(1 + \frac{i}{2Q} \right). \tag{2.15}$$

Widely recognized and employed values are 433 days for the Chandler period and a Q of 179, estimated by Wilson & Vicente (1990).

If appropriate time series of mass variations and relative angular momentum are available a solution of the non-linearized Liouville equation by means of numerical integration is feasible. Such an approach was successfully applied by Seitz (2004) and Seitz *et al.* (2004), in particular for the investigation of atmospheric and oceanic excitation of polar motion. A slightly modified calculus, which allows a more component-wise examination of different effects and a practicable comparison to geodetic observations, shall be described in Section 2.2.2.

2.2.2 Modeling geophysical excitation

The utilization of the excitation functions (2.11) entails the difficulty that it requires knowledge about the temporal derivatives of the inertia increments c_{ij} and angular momenta h_i of geophysical processes. In practice these are not readily available, but would have to be calculated by numerical differentiation, implicating rather high uncertainty. The concept of the excitation functions was transformed and adapted to a more applicable formalism, known as angular momentum functions (AMF), e.g. by Barnes *et al.* (1983). The basic angular momentum functions for a rigid Earth with oceans and atmosphere read

$$\chi_1(t) = \frac{\Omega c_{13}(t) + h_1(t)}{(C - A)\Omega}, \quad \chi_2(t) = \frac{\Omega c_{23}(t) + h_2(t)}{(C - A)\Omega}, \quad (2.16)$$

$$\chi_3(t) = \frac{\Omega c_{33}(t) + h_3(t)}{C\Omega}. \quad (2.17)$$

Equations (2.16) and (2.17) are referred to as equatorial and axial angular momentum functions, respectively (note, that the AMF do not comprise the components of the torque L). As it is the case also for the excitation functions and the angular momentum in general, the angular momentum functions can be split into a mass term and a motion term. The mass term contains the inertia variations c_{ij} , caused by mass displacements on the Earth surface or inside the Earth. Mass displacements within particle flows, where one mass element is replaced by another after its dislocation, generate relative angular momenta h_i , forming the motion part. The angular momentum functions can be extended to consider the consequences of geophysical excitation on the real Earth. The so-called effective angular momentum functions (EAMF), as given in Gross (2007), account for a deformable Earth with an anelastic mantle, the effects of a fluid core, the presence of oceans, load and rotational deformation. Introducing the complex quantities $\hat{\chi} = \chi_1 + i\chi_2$, $\hat{c} = c_{13} + ic_{23}$ and $\hat{h} = h_1 + ih_2$ and the average equatorial moment of inertia $A' = \frac{A+B}{2}$, the equatorial and axial EAMF can be written

$$\hat{\chi}(t) = \frac{1.100 \cdot \hat{c}(t)}{(C - A')} + \frac{1.608 \cdot \hat{h}(t)}{\Omega \cdot (C - A')} = \hat{\chi}^{\text{mass}} + \hat{\chi}^{\text{motion}}, \quad (2.18)$$

$$\chi_3(t) = 0.748 \frac{c_{33}(t)}{C_m} + 0.997 \frac{h_3(t)}{C_m \Omega} = \chi_3^{\text{mass}} + \chi_3^{\text{motion}}. \quad (2.19)$$

The numerical scaling coefficients derive from a composition of different parameters characterizing the Earth's response to loading, core-mantle coupling etc. and depend on the adopted Earth model. The parameters and the numerical values which yield the coefficients given above are quoted in Gross (2007). The equations of motion expressed in terms of angular momentum functions, using the observed Chandler frequency $\hat{\sigma}_C$ (2.15) then become

$$\hat{m}(t) + \frac{i}{\hat{\sigma}_C} \dot{\hat{m}}(t) = \hat{\chi}(t) - \frac{i}{\Omega} \dot{\hat{\chi}}(t), \quad (2.20)$$

$$m_3(t) = -\chi_3(t). \quad (2.21)$$

Formulae (2.18)–(2.21) are valid for the study of Earth rotation changes that occur on time scales considerably longer than one day (Gross, 2007). Diurnal and subdiurnal effects require special attendance, because of the free core nutation (FCN) resonance in the diurnal band. The FCN is another free oscillation of the Earth, originating from the misalignment of the rotation axes of the outer core and the mantle. It is a retrograde motion with a period of about 430 days in the celestial frame, corresponding to a retrograde quasi-diurnal motion as viewed in the terrestrial frame. Explanations on the treatment of daily and subdaily polar motion excitation are provided in Gross (1993) and Brzeziński (1994).

Angular momentum functions are usually applied for modeling and investigating geophysical excitation within the so-called angular momentum approach. This is one of two equivalently valid formulations for modeling global dynamic processes and their impact on Earth rotation. In the angular momentum approach, the Earth with oceans and atmosphere is considered as one closed system, the total angular momentum of which is conserved. If one of the subsystems, such as the atmosphere, undergoes a change of its associated angular momentum, the solid Earth experiences a coincident variation of its proper angular momentum, leading to a corresponding variation of the Earth rotation vector. Only lunisolar and planetary tidal forces are modeled as external torques. The alternative, called torque approach, regards the primary components of the system Earth, atmosphere and oceans, as extra-terrestrial as well. Thus the rate of change of the angular momentum of the solid Earth is related to the torques arising at the boundary surfaces of the system components as a consequence of the presence and motion of the respective geophysical fluid (Barnes *et al.*, 1983).

2.2.3 Connection between theoretical and observed axes

The rotational behavior of the Earth is formulated, in the above-given relations, in terms of the instantaneous rotation axis. As stated in Section 2.1.3, the space geodetic techniques do not observe the rotation axis, but the axis of the CIP and the variations of Earth rotation are reported as Earth orientation parameters. Hence an interconnection between the elements

of the rotation vector and the EOP is needed, to facilitate the comparison of observed Earth rotation variations with geophysical excitation. The derivations to establish this connection were furnished by Brzeziński (1992) and also by Gross (1992). The EOP disseminated by the IERS are consistent with the ITRF, which is realized as a Tisserand mean-mantle frame, according to Altamimi *et al.* (2011). Thus the preconditions for the application of the equations of motion, formulated in such a frame, together with the observed Earth rotation parameters are fulfilled. Writing the total reported polar motion in complex notation as $\hat{p} = x_p - iy_p$ the connection between the terrestrial motion of the CIP and the instantaneous rotation pole can be given

$$\hat{m}(t) = \hat{p}(t) - \frac{i}{\Omega} \dot{\hat{p}}(t). \quad (2.22)$$

The relation of a reported perturbation \hat{p} of the CIP axis to a small excitation $\hat{\chi}$ is deduced considering Equation (2.20)

$$\hat{\chi}(t) = \hat{p}(t) + \frac{i}{\hat{\sigma}_C} \dot{\hat{p}}(t). \quad (2.23)$$

For axial excitation we find the following relation (2.24) to reported LOD values ΔLOD or $d\text{UT1}$, where LOD_0 designates the nominal length of the day of 86400 seconds. To comply with rigorous nomenclature the reported values of LOD variations would have to be denominated ΔLOD , because they represent the excess of the actual length of the solar day as measured from Earth rotation observation to the nominal length of the day. It is common practice though to simply use LOD when actually ΔLOD is meant and the naming applied in this work will abide by that custom. The standard unit of excess LOD is seconds per nominal day (24 h). In the following only time units (s, ms or μs) are used for LOD, but in contrast to UT1, these are understood as time per nominal day. Since the LOD units are nowhere in this work referred to another time period than the day, ‘per day’ or ‘/d’ is omitted in the labels.

$$\chi_3(t) = \frac{\Delta\text{LOD}(t)}{\text{LOD}_0} = - \frac{d}{dt} d\text{UT1}(t). \quad (2.24)$$

2.3 Compilation of the major effects on Earth rotation

This section outlines the main parts composing measured Earth rotation variations, so as to enable the assessment and classification of the tidal effects, which are the master subject of the present work, among the other existing influences. The phenomena determining the dynamics of the Earth’s rotational motion can be categorized according to their causes and also commensurate with the temporal characteristics of their occurrence. With this in mind we can distinguish between variations which are caused by the direct action of external gravitational torques exerted on pronounced features of the Earth figure by other celestial bodies and fluctuations excited by geophysical processes. The latter can again be subdivided into tidal and non-tidal variations. Tidal effects are classified as high-frequency or short-period variations if their repeat cycle is at

least once per day and as low-frequency or long-period variations with periods of several days to years. Non-tidal excitation encompasses secular, decadal, interannual, seasonal, intraseasonal and also episodic events. Besides Earth rotation variations induced by gravitational or geophysical effects there is the third category of the Earth's free modes, most prominent, the Chandler wobble and the free core nutation. Their nature is rather determined by special rotational properties of the Earth's mantle and core than by any effect but they are consistently excited by geophysical effects. For a comprehensive treatment of Earth rotation effects refer to the reviews by Eubanks (1993) and Gross (2007).

2.3.1 Axis orientation

The spectrum of variations in the orientation of the CIP axis is divided into a celestial part and a terrestrial part, as defined in Section 2.1.3. The conventional frequency separation for the CIP leads to the somewhat strange effect, that variations produced by the same phenomenon are partly attributed to polar motion and partly to precession-nutation. Figure 2.1 infers that this is the case for terrestrial motions in the retrograde diurnal frequency band. Another consequence of the CIP convention is that variations which are actually of geodynamic nature, such as those excited by solid Earth tides, are assigned to precession-nutation. Vice versa, high-frequent astronomical nutations, i.e. responses to external gravitational forces, belong to polar motion.

The major portion of the celestial motion is caused by extra-terrestrial torques exerted by the Moon, the Sun and the planets upon the equatorial bulge of the Earth. As the forces generating them, these nutational motions are periodical, covering tidal harmonics from periods of a few days to 18.6 years. Small diurnal and semidiurnal 'nutations', originating from the effect of (mainly) the lunisolar torque on the non-axisymmetric figure of the Earth, are absorbed to long-period polar motion and diurnal polar motion. This signal is also termed polar libration (Chao *et al.*, 1991). The terrestrial motion of the Earth rotation axis also experiences forced perturbations due to the action of the external gravitational torques manifesting themselves as quasi-diurnal retrograde polar motion. Adhering to the CIP definition, these terms, the so-called Oppolzer terms, do not show up in the terrestrial motion of the CIP, but are fully represented by the nutation model.

Figure 2.2 illustrates the composition of polar motion and indicates the narrow band where nutation frequencies are located w.r.t. the terrestrial frame. In addition, phenomena such as the FCN or the effect of the solid Earth tides, which actually belong to the celestial CIP motion, are pointed out as well. Since the solid Earth tides' influence is shifted to nutation, the ocean tides clearly dominate the high-frequency excitation of polar motion. The effects of polar libration and atmosphere tides are already one order of magnitude smaller. The largest polar motion component is the Chandler wobble, though with a very variable amplitude, which can even reach almost zero. The second largest signal is an annual wobble excited for the most part by seasonal pressure variations in the atmosphere. Other contributions to polar motion excitation on time scales from several days to decadal come from changes of the ocean bottom pressure,

2.3 Compilation of the major effects on Earth rotation

ocean currents and winds. Strictly periodic variations in these bands are induced by long-period ocean tides with the main constituents being fortnightly, monthly, semi-annual, annual and at 18.6 years.

Further changes in the axis direction, not included in Figure 2.2, are a secular drift of the pole predominantly due to post-glacial rebound, aftereffects of episodic events like earthquakes, and also the possible impact of continental hydrology.

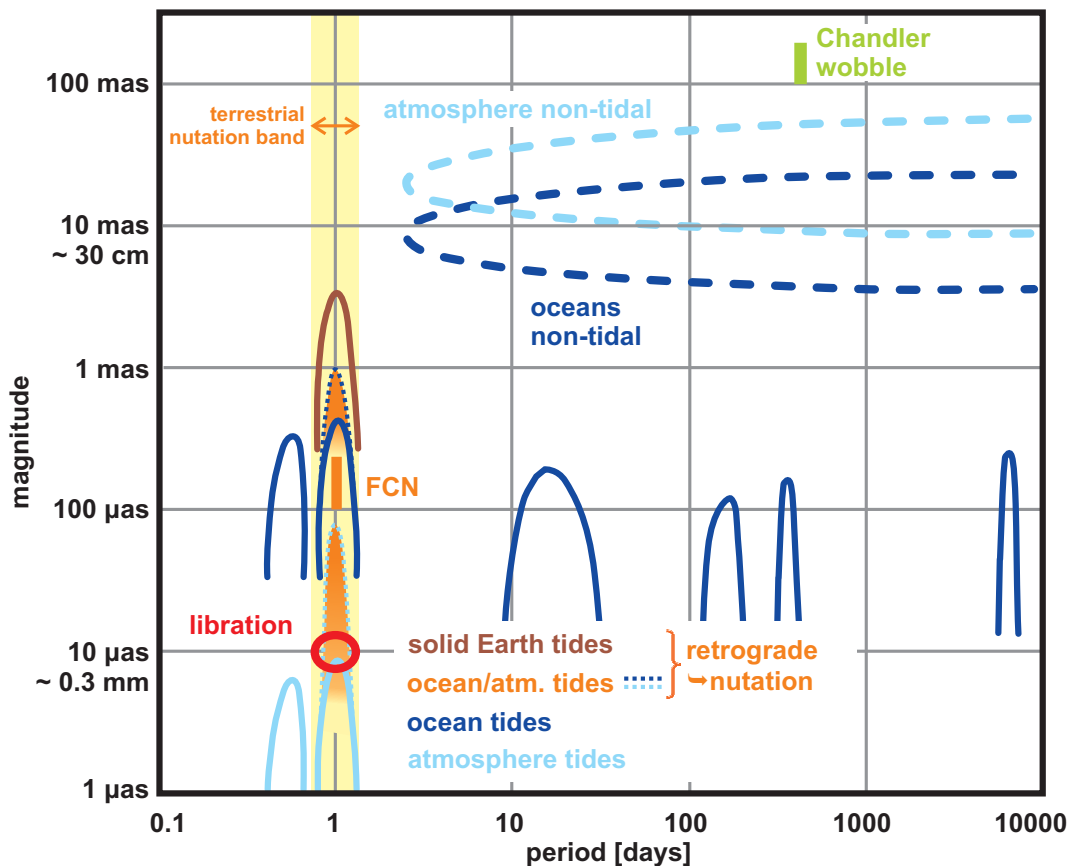


Figure 2.2: Signal components of polar motion. (The figure is an adaption of <ftp://gemini.gsfc.nasa.gov/pub/core/fig2.ps>)

2.3.2 Rotation speed

Breaking down the effects that contribute to variations of the rotation speed is straightforward, because we do not have to deal with spatial, but only temporal variations and none of the Earth's resonances is repeatedly influencing the angular velocity. Fluctuations of the rotation speed can be expressed either as variations in LOD or in UT1. UT1 is an integral quantity, while LOD is the rate of change of dUT1. This relation implies that different factors will have different effects on the two parameters depending on the frequency of the excitation.

Secular variations of the spin rate are reasonably represented by LOD. The secular increase of LOD by 1.8 ms per century (Morrison & Stevenson, 2001) is primarily induced by tidal friction.

This is the deceleration of Earth rotation caused by gravitational torques acting on the tidal bulge. The formation of the flood bulge is slightly retarded due to friction in solid Earth and oceans. For this reason, the Earth's rotation leads the deformation to being always ahead of the direction to the tide generating body, rendering it a point of action for the tidal forces. This effect is mainly connected with the semidiurnal tides or more precisely with the associated tidal displacements of oceans and solid Earth corresponding to the sectorial spherical harmonics of degree two (see first paragraph of Section 3.2).

The non-linear effects in the speed of rotation on time scales from few hours to decadal are presented in terms of UT1 in Figure 2.3. In order to get an idea of the magnitude of the same effects in LOD, the UT1 amplitudes should be multiplied by the nominal length of day of 86400 s and the angular frequency of the respective phenomenon. However, this relation holds only for harmonic or quasi-harmonic variations and is not applicable on strongly irregular fluctuations.

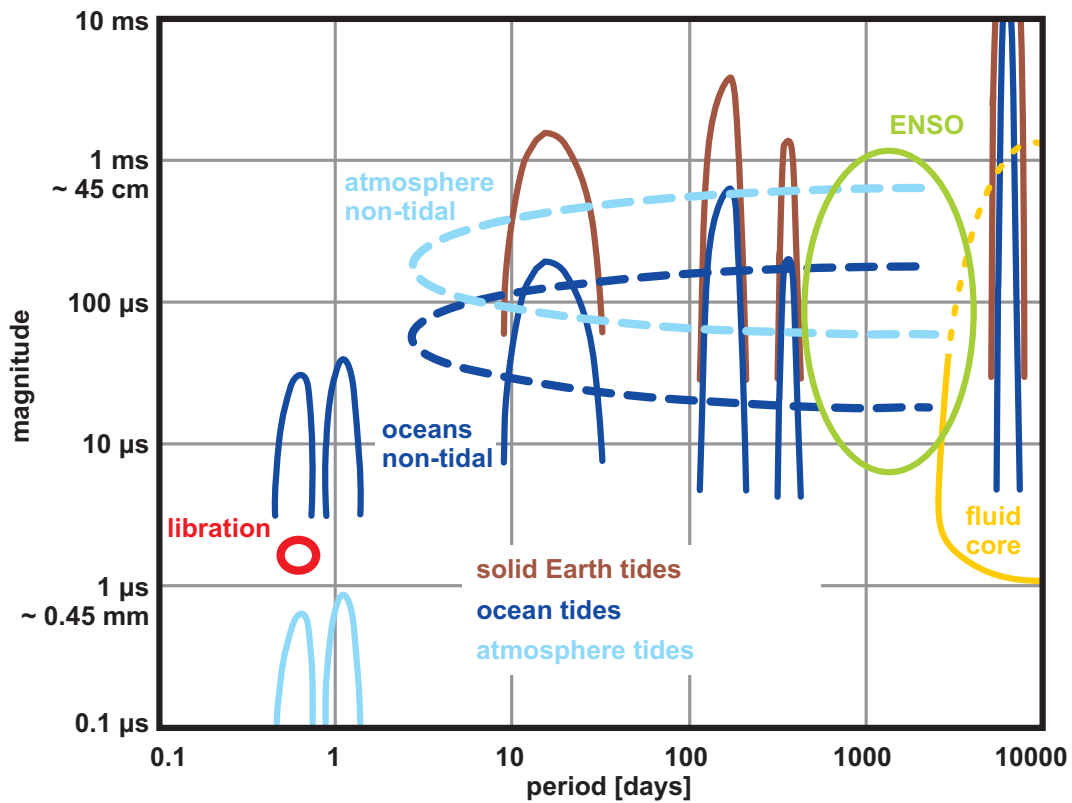


Figure 2.3: Signal components of universal time. (The figure is an adaption of <ftp://gemini.gsfc.nasa.gov/pub/core/fig1.ps>)

As in the polar motion spectrum, the ocean tidal effects are the largest components in the high-frequency domain, outnumbering libration and the influence of tides in the atmosphere by one order of magnitude. In contrast to their influence on the axis orientation, the solid Earth tides do not have diurnal effects, but induce long-period UT1 variations, which dominate the excitation budget. At the same tidal periods, markedly smaller variations due to long-period ocean tides

2.3 Compilation of the major effects on Earth rotation

are present. The tidal signals are partially superposed or even covered by atmospheric excitation, predominately effected by zonal winds. Non-tidal mass redistribution and current flows in the oceans contribute to UT1 variability as well, yet to a lesser extent. A specific atmosphere and ocean interaction, occurring every two to seven years, is called El Niño Southern Oscillation (ENSO). Depending on its intensity, the climate phenomenon can leave significant footprints in Earth rotation. At decadal time scales tidal terms are potentially swamped by fairly aperiodic and unpredictable effects of the core (the uncertainty of the magnitude in universal time is indicated by the dotted upper part of the curve).

Chapter 3

Tides and Earth rotation

Tides are periodical deformations of the solid or fluid parts of a celestial body which are caused by the interplay of centrifugal and spatially varying gravitational forces arising from the presence and motions of other celestial bodies. These forces, called tidal forces, the associated torques, acting on special features of the Earth, as well as the tidal deformations are the major contributors to periodic Earth rotation variations. Detailed information about tidal phenomena in general and their relation to Earth rotation can be found in the standard works e.g. by Melchior (1983) and Wilhelm *et al.* (1997), also Agnew (2007).

3.1 Tidal force

The tidal force f_t sensed by a point mass m is a differential force resulting from the difference of the gravitational acceleration due to the attraction of a celestial object a_{cel} and the acceleration of the Earth center of mass in inertial space a_0 :

$$\mathbf{f}_t = m \cdot (\mathbf{a}_{\text{cel}} - \mathbf{a}_0). \quad (3.1)$$

The tidal acceleration vectors can be expressed using Newton's law of gravitation:

$$\mathbf{a}_t = \mathbf{a}_{\text{cel}} - \mathbf{a}_0 = \frac{GM_{\text{cel}}}{d^2} \frac{\mathbf{d}}{d} - \frac{GM_{\text{cel}}}{r_{\text{cel}}^2} \frac{\mathbf{r}}{r}. \quad (3.2)$$

The acceleration of the Earth center of mass corresponds to the centrifugal acceleration experienced by an observer on the Earth. It depends on the distance r_{cel} from the Earth center of mass to the tide raising body with the mass M_{cel} and has the same magnitude in every surface point, whereas the gravitational acceleration varies with the distance d from the surface point A to the celestial body. The resultants of gravitational and centrifugal force at each point of the globe constitute a tidal force envelope with two alternate bulges, as delineated in Figure 3.1. The tidal force field is very conveniently represented by the tidal potential V_t , where $\mathbf{f}_t = \text{grad}V_t$ describes the tidal force effect on a unit mass. Defining the condition $V_t = 0$ at the Earth center of mass

(i.e. for $d = r_{\text{cel}}$), we get Equation (3.3), with the Earth radius R and the angle at center ψ (e.g. Torge, 2001, Ch. 3):

$$V_t = GM_{\text{cel}} \left(\frac{1}{d} - \frac{1}{r} - \frac{R \cos \psi}{r_{\text{cel}}^2} \right). \quad (3.3)$$

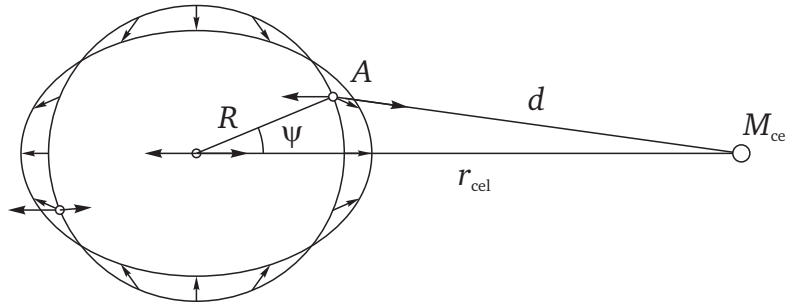


Figure 3.1: Tidal force.

3.1.1 Tidal potential expansions

The reciprocal distance $1/d = (R^2 + r_{\text{cel}}^2 - 2Rr_{\text{cel}} \cos \psi)^{-1/2}$ in Equation (3.3) is advantageously expanded into a series of spherical harmonics, with $P_n(\cos \psi)$ being the Legendre polynomials.

$$V_t = GM_{\text{cel}} \sum_{n=2}^{\infty} \frac{R^n}{r_{\text{cel}}^{n+1}} P_n(\cos \psi). \quad (3.4)$$

Since the summands for degree zero and one and the two last terms in braces of Equation (3.3) cancel each other, the expansion (3.4) starts at degree two. The degree two terms contain about 98% of the total tidal potential. For that reason and also because the inertia tensor is sensitive only to degree two deformations, the tidal potential expansion will be restricted to degree two here.

The spherical distance ψ between the surface point A and the tracing point P of the celestial body may be represented using the spherical coordinates $(\theta, \lambda), (\theta', \lambda')$

$$\cos \psi = \cos \theta \cos \theta' + \sin \theta \sin \theta' \cos(\lambda' - \lambda) \quad (3.5)$$

as depicted in Figure 3.2. Application of (3.5) to the Legendre polynomials $P_n(\cos \psi)$ yields the addition theorem for spherical harmonics which allows the decomposition of $P_n(\cos \psi)$ into Legendre polynomials P_n and associated Legendre functions P_{nm} as functions of the spherical coordinates of point A and P (refer to e.g. Hofmann-Wellenhof & Moritz, 2005, p. 26).

Subsequently, the tidal potential of degree two can be split up in three parts: (1) a zonal part (3.6), including only latitude dependent terms and representing therefore all the low-frequency

components of the tidal spectrum, with periods from a few days to several years, (2) a tesseral part (3.7), which is also dependent on the longitude of the tide raising body λ' and thus describes diurnally varying tidal forcing, and finally (3) a sectorial part (3.8), which has nearly semidiurnal periods as it is a function of $2\lambda'$.

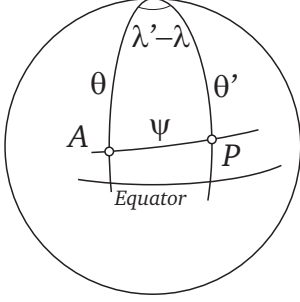


Figure 3.2: Spherical triangle.

Equations (3.6)–(3.8) hold of course for the tidal potential due to any celestial body. The total tidal potential taking effect at the Earth surface is then simply the sum of the individual potential fields of each tide generating body. For most cases only the effects of Moon and Sun are considered, since the tidal influence of the nearest planets Venus, Mars and Jupiter is already four orders of magnitude smaller (Torre, 2001).

$$V_{t20} = GM_{\text{cel}} \frac{R^2}{r_{\text{cel}}^3} P_{20}(\cos \theta) P_{20}(\cos \theta'), \quad (3.6)$$

$$V_{t21} = \frac{1}{3} GM_{\text{cel}} \frac{R^2}{r_{\text{cel}}^3} P_{21}(\cos \theta) P_{21}(\cos \theta') \cos(\lambda - \lambda'), \quad (3.7)$$

$$V_{t22} = \frac{1}{12} GM_{\text{cel}} \frac{R^2}{r_{\text{cel}}^3} P_{22}(\cos \theta) P_{22}(\cos \theta') \cos 2(\lambda - \lambda'). \quad (3.8)$$

The associated Legendre functions for degree two are

$$P_{20}(\cos \theta) = \frac{3}{2} \cos^2 \theta - \frac{1}{2}, \quad P_{21}(\cos \theta) = 3 \sin \theta \cos \theta, \quad P_{22}(\cos \theta) = 3 \sin^2 \theta. \quad (3.9)$$

The terrestrial coordinates (θ', λ') of the celestial bodies and their distances r_{cel} from the Earth show a fairly complicated time dependence and need to be calculated for the intervals of interest from precise ephemeris, such as the DE 421, provided by the Jet Propulsion Laboratory (JPL) in California (Folkner *et al.*, 2009). Alternatively, the orbits of the celestial objects can be expanded in harmonic series, the arguments of which are varying smoothly with time. In this way the tidal potential is represented in frequency domain as a sum of an actually arbitrary number of spectral components. Modern tidal potential catalogues inclose several thousands of such spectral components, so-called partial tides (e.g. Büllfeld, 1985; Hartmann & Wenzel, 1995; Roosbeek, 1996; Tamura, 1987; Xi, 1989). The first harmonic development of the tide generating potential was derived by Doodson (1921), who also defined the six variables, still in use for the description of the lunar and solar ephemeris (see Section 3.1.2). Apart from precision and computation methods, the tidal potential catalogues differ in the way the tidal amplitudes are specified. Doodson (1921) defined the amplitudes to be dimensionless, which was adopted also by Roosbeek (1996), while Hartmann & Wenzel (1995) tabulated amplitudes in units of the potential [m^2/s^2], and Cartwright & Tayler (1971) provided equivalent tide heights [m]. Factors for the conversion of the amplitudes from one convention to the others can be found in Chapter 6 of the IERS Conventions (2010). Using Hartmann & Wenzel convention, the tidal

potential expansion of degree two is expressed as

$$V_{t2m}(r, \theta, \lambda) = \sum_{m=0}^2 \left(\frac{r}{a_E} \right)^2 \bar{P}_{2m}(\cos \theta) \sum_i \left[C_i^{2m}(t) \cos(m\lambda + \alpha_i(t)) + S_i^{2m}(t) \sin(m\lambda + \alpha_i(t)) \right] \quad (3.10)$$

with the semi-major axis of the Earth's mean ellipsoid, denoted a_E . Equation (3.10) yields the tidal potential for a site on Earth with the spherical coordinates (r, θ, λ) . The time dependent coefficients

$$C_i^{2m}(t) = C0_i^{2m} + t \cdot C1_i^{2m} \quad \text{and} \quad S_i^{2m}(t) = S0_i^{2m} + t \cdot S1_i^{2m} \quad (3.11)$$

are composed from potential coefficients $C0_i^{2m}$ and $S0_i^{2m}$ given in [m^2/s^2] and linear drift coefficients $C1_i^{2m}$ and $S1_i^{2m}$ with the dimension [m^2/s^2 per Julian century]. The time t is accordingly introduced in Julian centuries counted from the epoch J2000 (refer to IERS Conventions, 2010, Ch. 5., for further explanation). The \bar{P}_{2m} are fully normalized Legendre functions of degree two

$$\bar{P}_{20}(\cos \theta) = \sqrt{\frac{5}{4}}(3 \cos^2 \theta - 1), \quad \bar{P}_{21}(\cos \theta) = \sqrt{15} \sin \theta \cos \theta, \quad \bar{P}_{22}(\cos \theta) = \sqrt{\frac{15}{4}} \sin^2 \theta. \quad (3.12)$$

The varying terrestrial positions of the tide generating bodies (θ', λ') are represented by series expansions of their orbital elements and are contained implicitly in the time dependent angle arguments $\alpha_i(t)$, the concept and calculation of which is described in the next section.

3.1.2 Fundamental astronomical arguments

Conjointly with the first harmonic development of the tidal potential Doodson (1921) identified six elements, characterizing the mutual positions of the Moon, the Sun and the Earth. Two of these so-called Doodson variables reflect the apparent motion of the Sun, three describe the Moon's orbit and the mean lunar time τ relates to the local observer through the hour angle of the Moon H . The definitions of the variables, the conventional symbols and their periods are summarized in Table 3.1.

The angle argument $\alpha_i(t)$ of a partial tide i as used in (3.10) is constituted as a linear combination of the six variables arg_j multiplied with respective integers k_{ij}

$$\alpha_i(t) = \sum_{j=1}^6 k_{ij} \cdot arg_j(t) \quad \text{with} \quad k_{i1} = m. \quad (3.13)$$

The fundamental variables $arg_j(t)$ are given as polynomials in time (e.g. Simon *et al.*, 1994). Doodson used a set of six numbers $(d_1 d_2 d_3, d_4 d_5 d_6)$, called the argument number or later also Doodson number, to uniquely specify a tidal wave with the argument α . It is related to the integer

Table 3.1: Doodson variables arg_j (following Table 2.6 in Beutler *et al.*, 2005).

Symbol	Period	Definition
$\tau = 180^\circ + H$	24 ^h 50 ^m	mean lunar time
s	27.32 days	mean longitude of the Moon
h	1 year	mean longitude of the Sun
p	8.85 years	mean longitude of the lunar perigee
$N' = -\Omega$	18.61 years	negative mean longitude of ascending lunar node
p_S	20940 years	mean longitude of solar perigee
$t = \tau + s - h$	24 ^h 00 ^m	mean solar time
$\tau + s = t + h$	23 ^h 56 ^m	mean sidereal time

multipliers k_j as follows

$$\alpha = \underbrace{d_1}_{k_1} \tau + \underbrace{(d_2 - 5)}_{k_2} s + \underbrace{(d_3 - 5)}_{k_3} h + \underbrace{(d_4 - 5)}_{k_4} p + \underbrace{(d_5 - 5)}_{k_5} N' + \underbrace{(d_6 - 5)}_{k_6} p_S. \quad (3.14)$$

All terms with the same d_1 constitute a species. The different species are separated from each other by about one cycle per lunar day. Terms with the same $(d_1 d_2)$ form a group, the groups are separated by one cycle per month. Ensembles $(d_1 d_2 d_3)$ represent a so-called constituent, with one cycle per year separation. A value $d_5 \neq 5$ supplies nodal modulation to a constituent (Cartwright, 1977).

Doodson's choice of fundamental arguments is commonly used in the areas of tidal potential and tides, but there are also other possible ensembles of astronomical arguments to represent the lunar and solar orbit characteristics as a combination of spectral components. The so-called Delaunay arguments shall be explicitly mentioned here, because they are conventionally applied in nutation theory and also for other Earth rotation models related to tidal effects (see Table 3.2). Numerical expressions for the Delaunay variables are quoted in Chapter 5 of the IERS Conventions (2010) or also in Simon *et al.* (1994).

Table 3.2: Delaunay variables ARG_j (following Table 2.6 in Beutler *et al.*, 2005).

Symbol	Period	Definition
l	27.53 days	mean anomaly of the Moon
l'	365.26 days	mean anomaly of the Sun
F	27.21 days	argument of latitude of the Moon
D	29.53 days	mean elongation of the Moon from the Sun
Ω	18.61 years	mean longitude of ascending lunar node
$\text{GMST} + \pi$	23 ^h 56 ^m	Greenwich Mean Sidereal Time + π

3.1 Tidal force

The arguments of the individual waves are as well built from linear combinations of the Delaunay variables ARG_j using corresponding integer multipliers K_{ij}

$$\alpha_i(t) = \sum_{j=1}^6 K_{ij} \cdot ARG_j(t). \quad (3.15)$$

The integer multipliers of both argument types can be very conveniently transformed from one representation to the other by a linear transformation according to Gipson (1996).

$$K_{ij} = k2K \cdot k_{ij} \quad \text{and} \quad k_{ij} = k2K^{-1} \cdot K_{ij} \quad \text{with} \quad k2K = \begin{pmatrix} 0 & 0 & 0 & -1 & 0 & 0 \\ 0 & 0 & 0 & 0 & 0 & -1 \\ -1 & 1 & 1 & 1 & 0 & 1 \\ 0 & 0 & -1 & 0 & 0 & -1 \\ -1 & 1 & 1 & 1 & -1 & 1 \\ 1 & 0 & 0 & 0 & 0 & 0 \end{pmatrix}. \quad (3.16)$$

A choice of principal waves of the tidal potential is provided in Tables 3.3 and 3.4.

Table 3.3: Selected tidal waves – long-period components (The potential amplitudes are taken from the Hartmann & Wenzel (1995) tidal potential catalogue and transformed to heights in mm).

Symbol	Doodson Nr.	Argument	Period [days]	Amplitude [mm]	Origin M/S
M_0	055.555	–	permanent	215	M
S_0	055.555	–	permanent	100	S
	055.565	N'	6798	28	M
Sa	056.554	$(h - p_S)$	365.26	5	S
Ssa	057.555	$2h$	182.62	31	S
Sta	058.554	$2h + (h - p_S)$	121.75	2	S
Msm	063.655	$(s - 2h + p)$	31.81	7	M
Mm	065.455	$(s - p)$	27.56	35	M
MSf	073.555	$2(s - h)$	14.77	6	M
Mf	075.555	$2s$	13.66	67	M
Mf'	075.565	$2s + N'$	13.63	28	M
$Mstm$	083.655	$2s + (s - 2h + p)$	9.56	2	M
Mtm	085.455	$2s + (s - p)$	9.13	13	M
Mtm'	085.465	$2s + (s - p) + N'$	9.12	5	M
$Msqm$	093.555	$2s + 2(s - h)$	7.10	2	M

Table 3.4: Selected tidal waves – short-period components (The potential amplitudes are taken from the Hartmann & Wenzel (1995) tidal potential catalogue and transformed to heights in mm).

Symbol	Doodson Nr.	Argument	Period [hours]	Amplitude [mm]	Origin M/S
$2Q_1$	125.755	$(\tau - s) - 2(s - p)$	28.01	6	M
σ_1	127.555	$(\tau - s) - 2(s - h)$	27.85	8	M
Q'_1	135.645	$(\tau - s) - (s - p) - N'$	26.87	9	M
Q_1	135.655	$(\tau - s) - (s - p)$	26.87	50	M
ρ_1	137.455	$(\tau - s) - (s - 2h + p)$	26.72	10	M
O'_1	145.545	$(\tau - s) - N'$	25.82	49	M
O_1	145.555	$(\tau - s)$	25.82	262	M
	155.455	$(\tau - s) + (s - p)$	24.85	7	M
M_1	155.655	$(\tau + s) - (s - p)$	24.83	21	M
π_1	162.556	$(t - h) - (h - p_s)$	24.13	7	S
P_1	163.555	$(t - h)$	24.07	122	S
S_1	164.556	$(t + h) - (h - p_s)$	24.00	3	S
K_1^m	165.555	$(\tau + s)$	23.93	252	M
K_1^s	165.555	$(t + h)$	23.93	117	S
K'_1	165.565	$(\tau + s) + N'$	23.93	50	M
J_1	175.455	$(\tau + s) + (s - p)$	23.10	21	M
OO_1	185.555	$\tau + 3s$	22.31	11	M
OO'_1	185.565	$\tau + 3s + N'$	22.30	7	M
$2N_2$	225.855	$2\tau - 3(s - p)$	12.91	16	M
μ_2	237.555	$2\tau - 2(s - h)$	12.87	19	M
N_2	245.655	$2\tau - (s - p)$	12.66	121	M
ν_2	247.455	$2\tau - (s - 2h + p)$	12.63	23	M
M'_2	255.545	$2\tau - N'$	12.42	24	M
M_2	255.555	2τ	12.42	632	M
L_2	265.455	$2\tau - (s - p)$	12.19	18	M
T_2	272.556	$2t - (h - p_s)$	12.02	17	S
S_2	273.555	$2t$	12.00	294	S
K_2^m	275.555	$2(\tau + s)$	11.97	55	M
K_2^s	275.555	$2(t + h)$	11.97	25	S
K'_2	275.565	$2(\tau + s) + N'$	11.97	24	M
M_3	355.555	3τ	8.28	8	M

3.2 Solid Earth tides

Solid Earth tides, also denoted body tides, are periodic deformations of the solid Earth due to the action of the tidal forces. Similar to the tidal potential the tidal deformation can be represented by spherical harmonics. In case of the solid Earth tides the geometry of the agitation is

virtually mapped to the geometry of the deformation. That means the long-period zonal tidal potential causes long-period zonal deformations of the solid Earth, the quasi-diurnal tesseral tidal potential generates quasi-diurnal tesseral deformations and the semidiurnal sectorial tidal potential raises semidiurnal sectorial body tides. Each of these deformation kinds influences Earth

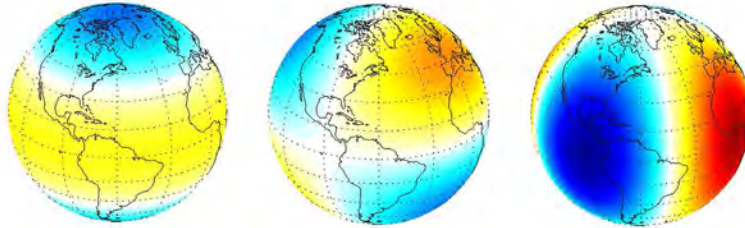


Figure 3.3: Zonal, tesseral and sectorial deformation of degree two.

rotation in a different way, as it is readily understandable from looking at their characteristic shapes. The three types of spherical harmonics of degree two are depicted in Figure 3.3. A zonal type deformation changes the polar moment of inertia, leading to a corresponding change of the rotation speed (conservation of angular momentum presupposed), hence it produces universal time or length of day variations. A tesseral deformation is asymmetric to the equatorial plane, it causes deviation moments in the inertia tensor and is therefore obviously capable of tilting the Earth axis, i.e. exciting polar motion. The sectorial deformation does not have a direct effect, but contributes indirectly to the deceleration of the Earth rotation through tidal friction. The topic of this thesis are periodic tidal phenomena in rotation rate and polar motion. The solid Earth tide effect on polar motion occurs in the retrograde diurnal period band and is attributed to precession-nutation on account of the CIP frequency convention, as mentioned in Chapter 2. For this reasons, interrelations of diurnal and semidiurnal body tides with Earth rotation will not be elaborated further, instead the focus is put on the zonal tidal perturbations of the rotation speed.

3.2.1 Impact of zonal deformation on Earth rotation

The influence of an external potential on the Earth figure and rotational behavior is strongly constrained by the adopted Earth model. A basic simple model to start with is a homogeneously elastic Earth without oceans. The elementary formula for investigating variations of the rotation speed is the third of the Euler-Liouville equations (2.8). The subsequent equations follow the derivations of Moritz & Mueller (1987), but can be found in different notations also in Munk & MacDonald (1975) or Lambeck (1980). When assuming rotational symmetry and Tisserand axes, the axial component of the torque L_3 and the relative angular momentum h_3 vanish. The equation then reduces to

$$C\Omega\dot{m}_3(t) + \Omega\dot{c}_{33}(t) = 0 . \quad (3.17)$$

Integration gives

$$m_3(t) = -\frac{c_{33}(t)}{C}. \quad (3.18)$$

Equation (3.18) relates a change in the rotation speed m_3 to a distortion of the polar moment of inertia c_{33} . For elastic deformation it can be shown that the trace of the inertia tensor is invariant (Moritz & Mueller, 1987). This yields a relation between a change in the inertia moment c_{33} and a perturbation of the Earth's gravitational potential δV_{20} at the planet surface:

$$\delta V_{20}(t) = -\frac{3}{2} \frac{G}{R^3} P_{20}(\cos \theta) c_{33}(t). \quad (3.19)$$

The change of the gravitational potential due to the tidal deformation is directly proportional to the perturbing potential, in this case the zonal tidal potential of degree two. The proportionality factor is the elastic Love number of degree two k_2 . A variation of the geopotential due to the zonal tidal deformation can thus be written

$$\delta V_{20}(t) = k_2 \cdot a_t^{20}(t) P_{20}(\cos \theta), \quad (3.20)$$

where a_t^{20} represents the time variable coefficient of the zonal tidal potential. It is straightforward to compare Equations (3.19) and (3.20) to express the variations of the inertia tensor element c_{33} in terms of the time dependent tidal potential coefficient and deduce the resulting variation of the angular velocity:

$$m_3(t) = k_2 \cdot \frac{2}{3} \frac{R^3}{GC} \cdot a_t^{20}(t). \quad (3.21)$$

Considering Equations (2.21) and (2.24) we get for the zonal tidal variation of the length of day δLOD

$$\delta \text{LOD}(t) = -k_2 \cdot \text{LOD}_0 \frac{2}{3} \frac{R^3}{GC} \cdot a_t^{20}(t). \quad (3.22)$$

That holds of course only for a rotationally symmetric, completely elastic solid Earth. Consequences of a fluid core, oceans, and deviations from elastic behavior will be outlined in the next section.

3.2.2 The zonal response coefficient of the Earth-ocean-system

Agnew & Farrell (1978) introduced an extension to the concept of the Love number k_2 , which they denominated the zonal response coefficient of the Earth-ocean-system κ . It is a frequency dependent, complex coefficient that allows for a response of the Earth to zonal tidal forcing, taking into account effects of ocean tides, a fluid core and mantle anelasticity. Equation (3.22) is accordingly rewritten in frequency domain, with the second degree Love number replaced by

the zonal response coefficient:

$$\delta\text{LOD}(\sigma_\ell) = -\kappa(\sigma_\ell) \cdot \text{LOD}_0 \frac{2}{3} \frac{R^3}{GC} \cdot A_t^{20}(\sigma_\ell). \quad (3.23)$$

Equation (3.23) is valid for each tidal spectral component of frequency σ_ℓ , belonging to a fundamental argument $\alpha_\ell = \sigma_\ell t + \beta_\ell$. The $A_t^{20}(\sigma_\ell)$ are the corresponding zonal tidal potential amplitudes from a trigonometric series expansion, such as (3.10). When calculating amplitudes of LOD variations using a tidal potential catalogue, care has to be taken regarding additional multiplication factors and the type of Legendre functions that were applied in the derivation of the catalogue – the amplitudes $A_t^{20}(\sigma_\ell)$ need to be adapted correspondingly.

Considering relation (2.24), the amplitudes of zonal tidal variations in universal time can be deduced by integration:

$$\delta\text{UT1}(\sigma_\ell) = \kappa(\sigma_\ell) \cdot \frac{1}{i\sigma_\ell} \frac{2}{3} \frac{R^3}{GC} \cdot A_t^{20}(\sigma_\ell). \quad (3.24)$$

Time series of the zonal tidal contribution to LOD or dUT1 are obtained from

$$\delta\text{LOD}(t) = \sum_{\ell} \delta\text{LOD}(\sigma_\ell) \cdot e^{i\alpha_\ell(t)} \quad (3.25)$$

or

$$\delta\text{UT1}(t) = \sum_{\ell} \delta\text{UT1}(\sigma_\ell) \cdot e^{i\alpha_\ell(t)} = -\frac{1}{\text{LOD}_0} \sum_{\ell} \frac{1}{i\sigma_\ell} \delta\text{LOD}(\sigma_\ell) \cdot e^{i\alpha_\ell(t)}, \quad (3.26)$$

where actually only the real part of the expansion is considered. A comparison of Equations (3.25) and (3.26) illustrates an important, universally valid, relation between LOD variations and UT1 variations: the LOD amplitude is divided by the nominal length of day times the frequency of the variation and the phase is retarded by $\pi/2$.

The rather simple proportionality of the tidal potential amplitudes to the LOD changes induced by the corresponding tidal deformations, obviously offers two modeling options. Either special values for κ are assumed on the basis of a certain Earth response to model resulting LOD variations or observed LOD variations are used to constrain the response parameter, i.e. the rheological properties of the Earth. However, the comparison of modeled and observed variations bears the challenge to properly separate different effects, inherent in the LOD or UT1 observations. Within the zonal tidal spectrum there are large nearly harmonic fluctuations excited by atmospheric wind and pressure variations (cf. Figure 2.3), which should be removed from the observations before estimating tidal amplitudes. Throughout the evolution of Earth rotation research many authors have investigated and exploited the relation between variations of the rotation rate and rheological parameters of the Earth using astronomical and space geodetic observations (e.g. Chao *et al.*, 1995; Defraigne & Smits, 1999; Dickman & Nam, 1995, 1998; Hefty,

1982; Hefty & Capitaine, 1990; Merriam, 1984; Nam & Dickman, 1990; Robertson *et al.*, 1994; Woolard, 1959; Yoder *et al.*, 1981).

Depending on the presumed Earth model some possible values for κ can be given. According to Chao *et al.* (1995), for a spherically symmetric Earth without oceans, κ would have the value of the (static) Love number $k_2 \approx 0.3$. An equilibrium ocean would increase the value by 16%, whereas a completely decoupled fluid core would decrease it by about 11%, leading to a total approximated value of $\kappa \approx 0.315$. If the oceans are additionally considered to have a dynamic response and furthermore time dependent core-mantle coupling and mantle anelasticity are assumed, then the zonal response coefficient becomes frequency dependent and a phase lag is introduced, making it complex-valued. At this point it should be noted that although this section is entitled ‘Solid Earth tides’, also effects of zonal ocean tide components are treated here, since the concept of the response coefficient permits the inclusion of those effects. Another reason is that they appear at the same tidal periods as the body tides and are usually treated together in conventional models for zonal tidal variations.

3.2.3 Theoretical models of zonal tidal Earth rotation variations

A major mission of this thesis is the validation of theoretical or semi-empirical models for the prediction of tidally induced irregularities of Earth rotation. The composition and background of the conventional models, which are inspected, are not always obvious and shall therefore be explained in more detail. The model adopted for the first published recommendations of the IERS, the IERS Standards (1989), was computed by Yoder *et al.* (1981). In the IERS Conventions (2003), the model was exchanged for a more modern calculation of the effect by De-fraigne & Smits (1999). Since the publication of the recent IERS Conventions (2010), the model of Yoder *et al.* (1981) is again the basis of the conventional model for zonal tidal effects on UT1, for reasons described in Gross (2009).

Yoder *et al.* (1981) derived their model using a similar concept as in Equation (3.24). Instead of κ they used as a proportionality or respectively scaling factor, the quantity k/C^* . With k being an effective Love number — conceptionally in fact nothing else than κ — and the dimensionless polar moment of inertia $C^* = C/M_E R_e$, where M_E and R_e are the Mass and equatorial radius of the Earth. Tidal variations in UT1 were calculated as follows

$$\delta\text{UT1}(t) = -\frac{k}{C^*} \cdot \text{LOD}_0 \int \frac{M_{\text{cel}}}{M_E} \frac{R_e^3}{r_{\text{cel}}^3(t)} \left(\frac{1}{3} - \sin^2 \delta(t) \right) dt . \quad (3.27)$$

The variable declination δ and distance r_{cel} of the tide raising body were actually expressed by series expansions that are represented using Delaunay variables. In the end, this equals then again to a spectral decomposition of the tidal potential and the finally computed variations were

therefore given in terms of amplitudes $\delta\text{UT1}(\sigma_\ell)$

$$\delta\text{UT1}(t) = \frac{k}{C^*} \cdot \sum_{\ell} \delta\text{UT1}(\sigma_\ell) \cdot \sin(\alpha_\ell(t)). \quad (3.28)$$

The actual fine tuning of the model was accomplished by a careful examination of possible values for the scaling factor. Yoder *et al.*'s final recommendation is a value of 0.944 for k/C^* , which includes the effects of an equilibrium ocean tide, a decoupled fluid core and rotational deformation. The value is composed like this: the basis is a bulk Love number $k_2 = 0.301$; it is increased by 0.040 due to the ocean tides, according to Dahlen (1976); Yoder *et al.* (1981) found that k_2 is decreased by 0.064 if the fluid core is rotationally decoupled from the mantle and C^* is then accordingly replaced by the moment of inertia of the mantle $C_m^* = 0.293$; the total fraction is finally reduced by 2% to consider the small effect of rotational deformation. The model does not account for mantle anelasticity or ocean tides departing from equilibrium.

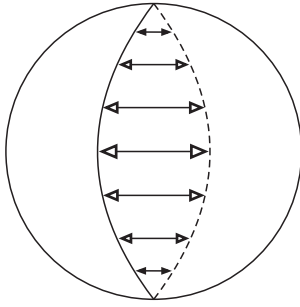


Figure 3.4: Toroidal oscillation of degree one (following Kertz, 1995).

they act along concentric circles. Spherical surfaces are thereby distorted as if they consisted of an elastic skin (Moritz & Mueller, 1987). Hence the toroidal displacement vector $\tau_1^0(\sigma)$ represents an infinitesimal change of the rotational velocity, generated by a tidal potential of degree two order zero with the frequency σ . Following Defraigne & Smits (1999) the norm of the vector corresponds to the length of the circular arc at the Earth surface and can thus be linked to a variation of UT1:

$$\tau_1^0(\sigma) = \mu_s e^{i(\sigma t + \beta)} \hat{\mathbf{z}} \times \mathbf{r} \quad \implies \quad \delta\text{UT1}(\sigma) = \frac{\mu_s}{\Omega} e^{i(\sigma t + \beta)}, \quad (3.29)$$

where μ_s is the angle of the rotation, σ and β are the frequency and phase of the potential, \mathbf{r} is the position vector at the surface, and $\hat{\mathbf{z}}$ represents the polar axis of the reference system.

Defraigne & Smits (1999) presented their results in portions, investigating different effects. In general they based their computations on an Earth structure provided by the Preliminary Reference Earth Model (PREM, Dziewonski & Anderson, 1981) and external forcing as given

in the RATGP95 tidal potential series of Roosbeek (1996). The seismic velocity and density distribution in the Earth interior of PREM are illustrated in Figure 3.5.

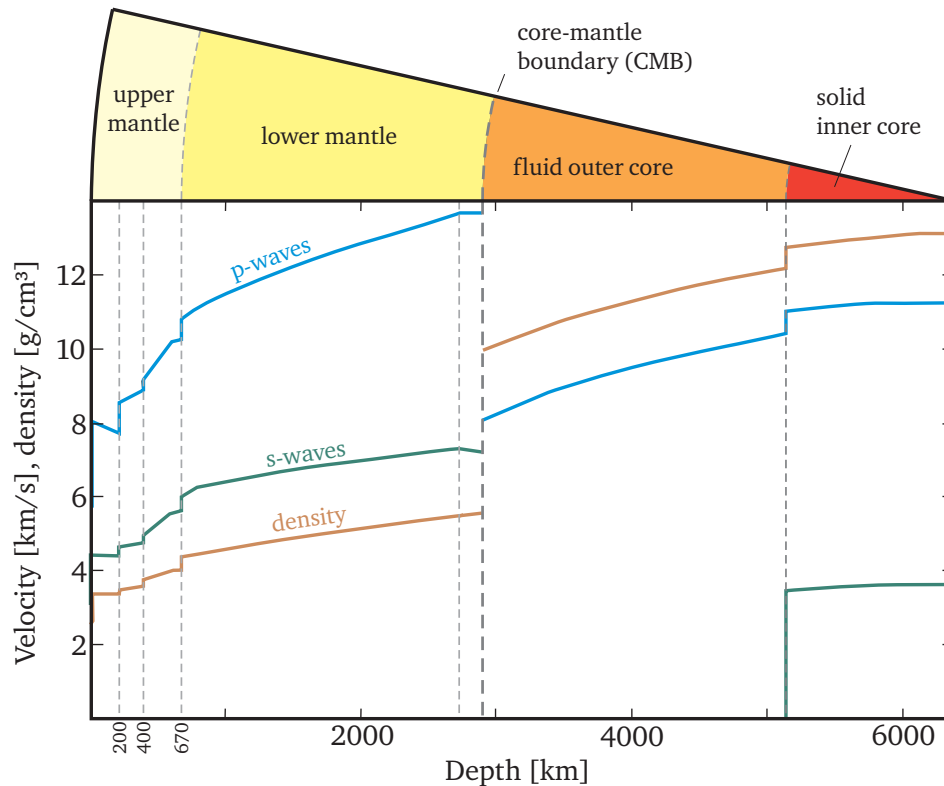


Figure 3.5: Seismic velocity and density in the Earth – Preliminary Reference Earth Model PREM (Dziewonski & Anderson, 1981).

The first results were two sets of UT1 and LOD amplitudes for the 11 major tidal terms from 6.86 days to 18.6 years, calculated for an elastic solid Earth with decoupled core. One set was derived for an Earth in hydrostatic equilibrium and the second ensemble considered the effect of a non-hydrostatic structure. The differences between the hydrostatic and the non-hydrostatic amplitudes were less than 0.1 percent and were thus considered negligible. Using Equation (3.23) or (3.24) and the potential amplitudes of RATGP95, the zonal response coefficient corresponding to the stated amplitudes can be deduced. Defraigne & Smits (1999) obtained a κ value of 0.2362 for an elastic, oceanless Earth with core-mantle decoupling. The κ for the same conditions calculated from the results of Yoder *et al.* (1981) would be 0.2678. Apparently the transfer function for the response of an Earth with such properties to tidal forcing is not frequency dependent, as the value is the same for all constituents. The reason for the difference between the two models should be mostly the use of different initial Earth models. Yoder *et al.* based their adopted values for the Love number on the older Earth model 1066A (Gilbert & Dziewonski, 1975).

As a further result they gave the effect of mantle anelasticity on the UT1 variations for the five major terms from fortnightly to the 18.6 years period, for different assumptions of the frequency dependence. The attenuation factor Q and the shear and bulk moduli, which enter into the

transfer function computation, depend on the frequency according to σ^α , where α is the anelastic parameter. In the paper, Defraigne & Smits gave preference to an anelasticity model with $\alpha = 0.15$ and a reference period of 200 s. In terms of κ the effect is about 0.01 e.g. for the semiannual tide, it decreases with the frequency. The IERS Conventions (2003) model, which is taken as a reference model in this thesis, uses the basic model, with non-hydrostatic Earth structure and in addition accounts for anelasticity and an equilibrium ocean. Anelasticity is considered applying the same α and reference period σ_{ref}^{-1} as Defraigne & Smits (1999), but those values are applied to an anelasticity law for the Love number k_2 stated in Chapter 6 of the IERS Conventions (2003). This relation is written here in terms of the enhancement of κ due to an anelastic mantle:

$$\hat{\kappa}_{\text{an}} = -5.796 \cdot 10^{-4} \left\{ \cot \frac{\alpha\pi}{2} \left[1 - \left(\frac{\sigma_{\text{ref}}}{\sigma} \right)^\alpha \right] + i \left(\frac{\sigma_{\text{ref}}}{\sigma} \right)^\alpha \right\}. \quad (3.30)$$

Equation (3.30) contains also a complex part, hence it introduces an out-of-phase part to κ and to the resulting UT1 and LOD variations. Defraigne & Smits (1999) also investigated the effects of dynamic ocean tides and provided results for corrected κ values from two different ocean models. Because of the disagreement of these ocean corrections from the dynamic models, a constant admittance of 0.044 was applied in the final IERS2003 model of the zonal tidal variations.

The present IERS2010 model was suggested by Gross (2009). It is based on the model of Yoder *et al.* (1981) with the recommended value of 0.94 for k/c^* , considering elastic solid Earth tides plus an equilibrium ocean tide. The effect of the anelastic body tide was inferred according to Wahr & Bergen (1986) and the influence of a dynamic ocean behavior was included for the fortnightly and monthly ocean tide, extracted from Kantha *et al.* (1998).

3.3 Ocean tides

Ocean tides are the reaction of the ocean water to external tidal forcing in combination with several other effects. In contrast to the solid Earth tides, the forming of the ocean tides is not only dominated by the tidal potential but influenced by many other factors, such as the Coriolis force, friction, viscosity, distribution of the land masses, sea floor topography and even the differential solar heating.

The most simple tidal theory, which neglects all the last-mentioned effects, is the so-called equilibrium theory, going back to Isaac Newton. This theory states that the sea surface coincides at all times with a gravitational equipotential. It is also called the theory of static tides, because it assumes that the flood bulges are formed until an equilibrium state between pressure gradients and tidal force is reached, then the water displacements stop and the tidal deformation of the sea remains unchanged and fixed in the direction to the tide raising body. An equilibrium tide does not exhibit any currents, it is a pure mass displacement without relative motions. The equilibrium theory provides a rather good approximation for long periods, but does not hold at all for diurnal and semidiurnal periods.

Pierre-Simon Laplace founded the dynamic theory of ocean tides. He postulated that instead

of stationary tidal bulges the tidal forces would induce flood waves. According to the dynamic theory, the tide height and arrival time is highly dependent also on the ocean depth and topography (friction effects) and the morphology and free oscillations of ocean basins (resonance effects). In contrast to equilibrium tides, the dynamic tides are accompanied by significant water flows, namely flood and ebb currents.

Since ocean tides extensively deviate from equilibrium, their shape and time of occurrence are fairly complex. The geographical pattern of the ocean tides therefore does not correspond to the geometry of the exciting potential as in the case of the body tides. A spherical harmonic expansion of the ocean tidal deformation field features zonal, tesseral and sectorial terms with all kinds of periods. As a consequence, ocean tides excite LOD variations and polar motion with diurnal and subdiurnal periods as well as with long periods. Earth rotation fluctuations due to ocean tides are thus estimated and predicted on the basis of ocean tide models. The ocean tide quantities of interest are thereby the varying tidal elevations as well as the tidal current velocities. The latter being particularly important when dealing with diurnal and subdiurnal tides, which show a behavior deviating significantly from equilibrium, as pointed out by Baader *et al.* (1983) and Brosche *et al.* (1989).

3.3.1 Ocean tide models

Regarding general assumptions about the ocean circulation we have to distinguish between barotropic and baroclinic tide models. Barotropic flow is independent of depth and is in balance with, or results from, a sea surface slope. That means it occurs when the levels of constant pressure in the ocean are always parallel to the surfaces of constant density. Unlike barotropic flow, baroclinic flow results from the density distribution in the ocean and arises when levels of constant pressure are inclined to surfaces of constant density. The corresponding current velocity is in this case depth-dependent (refer to Stewart, 2008, for further information). The relations for the calculation of the ocean tide influence on Earth rotation, that are given in the subsequent sections, imply the use of barotropic tide models.

In respect of the computation there are basically three types of ocean tide models. Hydrodynamic models are constructed solving equations of fluid dynamics fed with physical parameters about the ocean state. Meteorological observation data is often used to drive such models, but they do not make use of sea surface observations. Hydrodynamic models where information from tide gauges or satellite altimetry is introduced are called assimilation models. The third group are purely empirical tide models, which do not involve any physical equations, but are calculated solely from observations of sea surface changes. A priori, empirical ocean tide models deliver only the ocean tide heights, but no current velocities.

The ocean response to the tide generating potential is commonly represented individually for each tidal wave i by the tide height $\zeta_i(\theta, \lambda, t)$, dependent on position (θ, λ) and time t . In terms of frequency the ocean tides equal the solid Earth tides, but they differ in phase, due to the more complex nature of the ocean tides. The tide heights can be given on a global grid, as amplitude

and phase or as in-phase and quadrature coefficients. Another option is the use of spherical harmonics for the description of the tidal elevation field. In both cases cosine is the base function and phase lags are used in the tidal argument, which is built according to the convention of Doodson & Warburg (1941). The spherical harmonic representation reads

$$\zeta_i(\theta, \lambda, t) = \sum_{n=0}^{\infty} \sum_{m=0}^n \sum_{+}^{-} D_{nm,i}^{\pm} \cos\left(\alpha_i(t) + \chi_i \pm m\lambda - \psi_{nm,i}^{\pm}\right) P_{nm}(\cos\theta) \quad (3.31)$$

with amplitudes D_{nm}^+ , D_{nm}^- and phases ψ_{nm}^+ , ψ_{nm}^- . In tidal literature the quantities with a plus sign are called 'prograde', meaning in the direction of the tide raising body (westward), the negatively labeled quantities are called 'retrograde' (eastward).¹ The previously used tidal argument α_i is extended here with an additional angle χ_i that enables the use of cosine functions with always positive amplitudes. This is the so-called Doodson-Warburg phase correction, it depends on the sign of the corresponding potential coefficient C_i^{nm} or S_i^{nm} (the rule given here is valid for the potential coefficients provided in Hartmann & Wenzel convention):

$$\chi = \begin{cases} -90^\circ & \text{for } C^{21}, S^{21} > 0, \\ 0 & \text{for } C^{20}, S^{20} < 0 \text{ and } C^{22}, S^{22} > 0, \\ +90^\circ & \text{for } C^{21}, S^{21} < 0, \\ +180^\circ & \text{for } C^{20}, S^{20} > 0 \text{ and } C^{22}, S^{22} < 0 \text{ and } C^{33}, S^{33} < 0. \end{cases} \quad (3.32)$$

The grid-wise ocean tide representation is written as

$$\zeta_i(\theta, \lambda, t) = f_i^m(t) \left[z_{1i}(\theta, \lambda) \cos\left(\alpha_i(t) + \chi_i + u_i^m(t)\right) + z_{2i}(\theta, \lambda) \sin\left(\alpha_i(t) + \chi_i + u_i^m(t)\right) \right], \quad (3.33)$$

where z_1 and z_2 are the in-phase and quadrature tidal coefficients at each grid node with the spherical coordinates (θ, λ) . The parameters f_i^m and u_i^m are optional so-called nodal corrections, which account for the modulation of the principal lunar tides by the 18.6 years revolution of the lunar ascending node and the 8.85 years revolution of the Moon's perigee. If an ocean tide model would provide a complete harmonic analysis of the tidal elevation field, including all significant minor tides and side lobes, these nodal corrections would be obsolete. Usually the time intervals of observations of tidal height fluctuations are too short to estimate and separate adjacent waves. Standard models that use empirical data therefore consist of the major tidal constituents only, which are then to be adapted using the nodal corrections. The influence of other minor tides can be inferred by means of admittance assumptions. The tidal admittance is the relationship between the observed tidal height and the tidal potential for a given frequency σ . The admittance $Z(\sigma)$ is assumed to be a slowly varying function of frequency, relating the 'input' signal, the tidal potential $V_t(\sigma)$ to the 'output' signal, the tidal elevation $\zeta(\sigma)$ according

¹Note that this notation is opposite to the definition of pro- and retrograde used in Earth rotation.

to $Z(\sigma) = \zeta(\sigma)/V_t(\sigma)$. Since the admittances of the major tides are known they can be used to interpolate the admittances of minor tides introducing their known frequencies.

The current velocities, relevant for Earth rotation studies, are provided as East and North components u_i and v_i in the same form as the tide heights, for each tidal wave i , either on a global grid or as spherical harmonic coefficients. Figure 3.6 shows the diurnal and semidiurnal constituents of the ocean tide model TPXO7.1 (Egbert & Erofeeva, 2002). The currents are represented as so-called volume transport, which is the current velocity multiplied by the ocean depth.

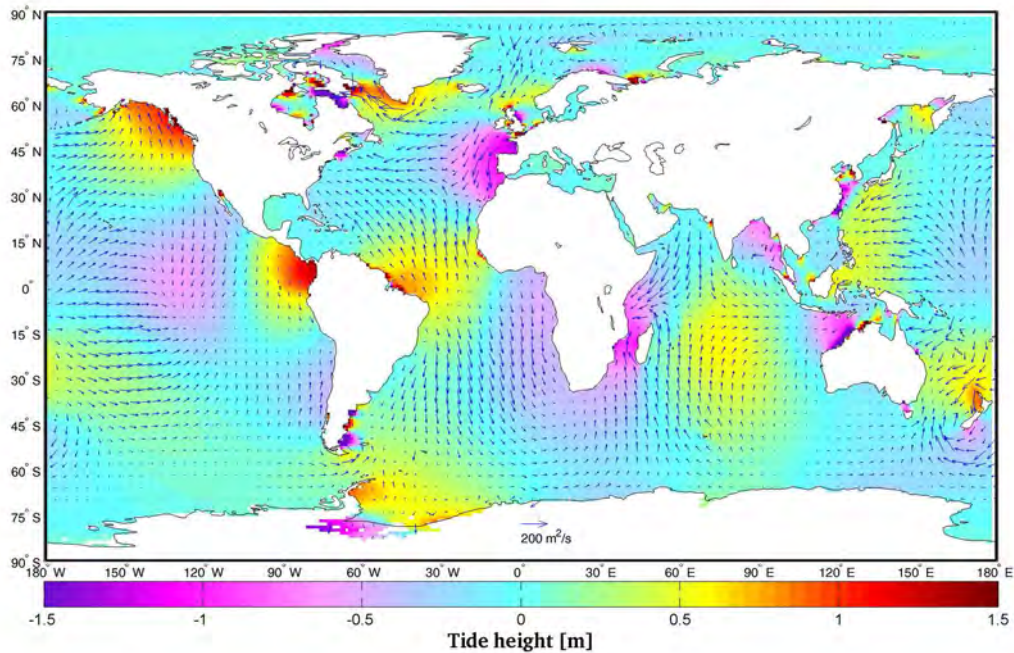


Figure 3.6: Ocean tide heights and volume transports evaluated from TPXO7.1 (Egbert & Erofeeva, 2002) evaluated at an arbitrary day, 20 h UTC: the colorbar gives the tidal elevation in meters, the arrows represent volume transport in m^2/s .

3.3.2 Tidal analysis

Due to the fact that the prediction of Earth rotation variations induced by ocean tides, resembles tidal analysis in various aspects, some remarks about the main analysis methods shall be given here. Tidal analysis generally amounts to a least-squares fit of sea level observations with the unknown parameters depending on the approach. Most prominent are the harmonic analysis and the response method.

Harmonic analysis is based on the assumption that the tidal variations can be represented by

a finite number N of harmonic terms:

$$\zeta(\theta, \lambda, t) = \sum_{i=1}^N Z_i(\theta, \lambda) \cos(\sigma_i t - \delta_i(\theta, \lambda)) , \quad (3.34)$$

where $Z_i(\theta, \lambda)$ is an amplitude, $\delta_i(\theta, \lambda)$ is the phase lag on the equilibrium tide at Greenwich and σ_i is the frequency of the harmonic term i (Pugh, 1996). The unknown amplitudes and phase lags for each node (θ, λ) are estimated by solving a linear system with the measured tidal height variations ζ as observations. As in the model representations (3.31) and (3.33), the argument $\sigma_i t = \alpha_i(t)$ is built from a linear combination of the six Doodson variables (3.13). The number of estimable terms depends strongly on the length of the observed time series. In general, analysis of a month of data can only determine independently those terms which belong to different groups, i.e. which are separated by at least one cycle per month. An observation period of one year allows for the separation of different constituents. The amplitude and phase affecting nodal modulations can be considered in the equation system by introducing the nodal correction factors f^m and u^m as in Equation (3.33). It is standard in tidal analysis to use the Doodson-Warburg phase correction χ , yet it is omitted in this section for the sake of readability. If the data period is too short to resolve certain constituents, their effect can be accounted for by condition equations or constraints. Commonly the amplitude ratio and phase lag of the weaker term are related to the amplitude and phase of the stronger term. In case there is no data reference of a station for these relationships, the relations from the forcing function or the tidal admittance, respectively, may be taken (Pugh, 1996).

Optionally, the harmonic analysis can be conducted in a spherical harmonic representation. The expressions $Z_i \cos \delta_i$ and $Z_i \sin \delta_i$ are then developed into spherical harmonics:

$$\begin{aligned} Z_i(\theta, \lambda) \cos \delta_i(\theta, \lambda) &= \sum_{n=0}^{\infty} \sum_{m=0}^n (a_{nm,i} \cos m\lambda + b_{nm,i} \sin m\lambda) P_{nm}(\cos \theta) , \\ Z_i(\theta, \lambda) \sin \delta_i(\theta, \lambda) &= \sum_{n=0}^{\infty} \sum_{m=0}^n (c_{nm,i} \cos m\lambda + d_{nm,i} \sin m\lambda) P_{nm}(\cos \theta) . \end{aligned} \quad (3.35)$$

The coefficients a_{nm} , b_{nm} , c_{nm} and d_{nm} are connected to the amplitudes D_{nm}^{\pm} and phases ψ_{nm}^{\pm} , already introduced in the previous section, in the following way:

$$\begin{aligned} D_{nm,i}^{\pm} \sin \psi_{nm,i}^{\pm} &= \frac{1}{2} (a_{nm,i} \mp d_{nm,i}) , \\ D_{nm,i}^{\pm} \cos \psi_{nm,i}^{\pm} &= \frac{1}{2} (c_{nm,i} \pm b_{nm,i}) . \end{aligned} \quad (3.36)$$

Disadvantages of the harmonic analysis are the dependence on the observation time span, which determines the resolvability of the constituents and the fact that a quite high number of parameters is needed to adequately describe the total variance of the sea surface. An alternative technique, the so-called response method (introduced by Munk & Cartwright, 1966), is indepen-

dent of the available data length and can accommodate slightly more of the total variance with less than half of the harmonic parameters (Pugh, 1996). The principle of the response method is to predict the tide height at a time t as a weighted sum of past and present values of the potential,

$$\zeta(t) = \sum_s w(s) V_t(t - \tau_s) \quad (3.37)$$

with the weights $w(s)$ at increment s and time steps $\tau_s = s\Delta t$. The weights represent the response of the sea level to the input forcing function V_t . Munk & Cartwright (1966) expressed the response formalism, using a spherical harmonic expansion of the tidal potential with the time dependent real and imaginary coefficients $a_t^{nm}(t)$ and $b_t^{nm}(t)$:

$$\zeta(t) = \sum_{n=0}^{\infty} \sum_{m=0}^n \sum_s [w_1^{nm}(s) a_t^{nm}(t - \tau_s) + w_2^{nm}(s) b_t^{nm}(t - \tau_s)] . \quad (3.38)$$

The prediction weights $w^{nm}(s) = w_1^{nm}(s) + iw_2^{nm}(s)$ can be estimated by least-squares adjustment for any ocean site. The established default time step Δt for τ_s is 48 hours. The approach can be problematic, because pairs of terms, such as $a_t(t)$, $a_t(t - \Delta t)$, are not orthogonal, leading to an ill conditioned normal equation matrix in the adjustment. To overcome this deficiency Groves & Reynolds (1975) suggested a modified formalism where the time functions in (3.38) are replaced by a sequence of orthogonal functions that are themselves derived from the time functions (Cartwright & Ray, 1990). These are called orthotide functions P_ℓ^{nm} and Q_ℓ^{nm} and are calculated as follows

$$\begin{aligned} P_0(t) &= p_{00} a_t(t), \\ P_1(t) &= p_{10} a_t(t) - p_{11} a_t^+(t), \\ P_2(t) &= p_{20} a_t(t) - p_{21} a_t^+(t) + q_{21} b_t^-(t), \\ Q_0(t) &= p_{00} b_t(t), \\ Q_1(t) &= p_{10} b_t(t) - p_{11} b_t^+(t), \\ Q_2(t) &= p_{20} b_t(t) - p_{21} b_t^+(t) - q_{21} a_t^-(t), \end{aligned} \quad (3.39)$$

with

$$\begin{aligned} a_t^\pm(t) &= a_t(t + \Delta t) \pm a_t(t - \Delta t), \\ b_t^\pm(t) &= b_t(t + \Delta t) \pm b_t(t - \Delta t). \end{aligned} \quad (3.40)$$

All quantities are actually valid for a certain degree n and order m , but the indices are dropped here to preserve the readability. The $p_{\ell k}$ and $q_{\ell k}$ are constants computed from the harmonic expansion of the tidal potential coefficients. Numerical values for the diurnal and semidiurnal harmonics are listed in Table A.1 of Appendix A. Using the orthogonal functions and restricting

to degree 2 and orders 1 and 2 (diurnal and semidiurnal tides), Equation (3.38) is reformulated:

$$\zeta(t) = \sum_{m=1}^2 \sum_{\ell=0}^2 [U_{\ell}^m P_{\ell}^m(t) + V_{\ell}^m Q_{\ell}^m(t)] . \quad (3.41)$$

The orthoweights U_{ℓ}^m and V_{ℓ}^m , representing the tidal variation at one location, are again retrieved by least-squares adjustment. They can be easily transferred to the in-phase and quadrature tidal harmonic coefficients z_1 and z_2 by means of the tidal admittances $X(\sigma)$ and $Y(\sigma)$ for each frequency σ :

$$\begin{aligned} z_1(\sigma) &= (-1)^m A_t(\sigma) X(\sigma) , \\ z_2(\sigma) &= -(-1)^m A_t(\sigma) Y(\sigma) , \end{aligned} \quad (3.42)$$

where $A_t(\sigma)$ is the tidal potential amplitude at frequency σ and the admittances are (following Matsumoto *et al.*, 1995):

$$\begin{aligned} X(\sigma) &= p_{00} U_0 + [p_{10} - p_{11} 2 \cos(\sigma \Delta t)] U_1 \\ &\quad + [p_{20} - p_{21} 2 \cos(\sigma \Delta t) + q_{21} 2 \sin(\sigma \Delta t)] U_2 , \end{aligned} \quad (3.43)$$

$$\begin{aligned} Y(\sigma) &= p_{00} V_0 + [p_{10} - p_{11} 2 \cos(\sigma \Delta t)] V_1 \\ &\quad + [p_{20} - p_{21} 2 \cos(\sigma \Delta t) + q_{21} 2 \sin(\sigma \Delta t)] V_2 . \end{aligned} \quad (3.44)$$

Figure 3.7 displays the orthotide functions of the diurnal and semidiurnal period bands for ten days in October 2006.

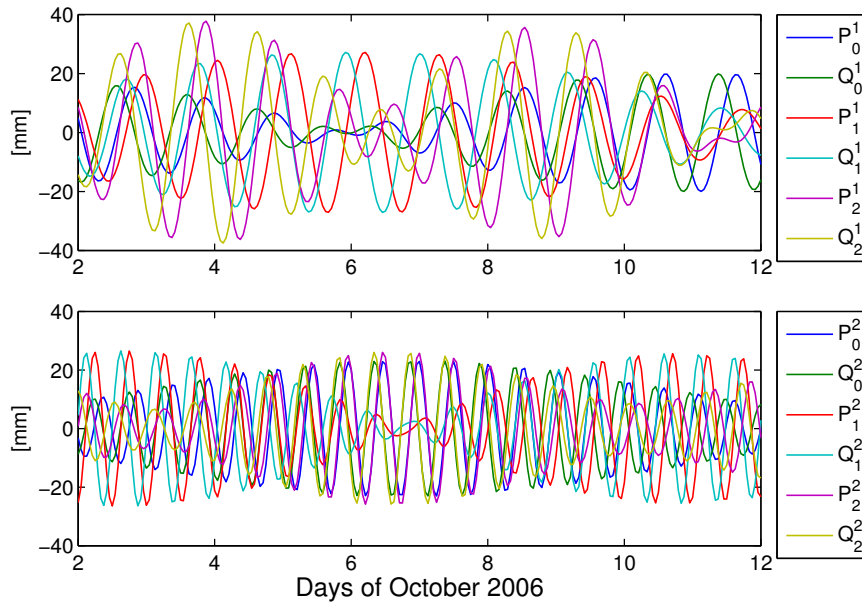


Figure 3.7: Orthotide functions of the diurnal (top) and semidiurnal (bottom) band.

3.3.3 Ocean tidal angular momentum

In compliance with the angular momentum approach, a variation of the solid Earth's rotation due to ocean tides is deduced from angular momentum transfer. The periodically varying ocean tidal angular momentum (OTAM) induces a periodic change in the solid Earth angular momentum of the same magnitude but opposite sign. Thus the impact of ocean tides on Earth rotation is calculated via OTAM that is subsequently introduced to the angular momentum functions, under special considerations regarding nearly diurnal variations, that are framed in Section 3.3.4. OTAM can be split in two parts: a mass portion, arising from the mass displacements due to the tide height fluctuations and a motion part, driven by relative motions within the tidal currents.

We use a spherical coordinate system with the coordinate components and derivatives

$$\begin{aligned} x_1 &= r \cos \varphi \cos \lambda, & \dot{x}_1 &= -u \sin \lambda - v \sin \varphi \cos \lambda, \\ x_2 &= r \cos \varphi \sin \lambda, & \dot{x}_2 &= u \cos \lambda - v \sin \varphi \sin \lambda, \\ x_3 &= r \sin \varphi, & \dot{x}_3 &= v \cos \varphi, \end{aligned} \quad (3.45)$$

where r is the radius, φ and λ are latitude and longitude, and u and v are velocities along parallels (East) and meridians (North), respectively. Considering Equations (2.4) and (2.5) and limitation to first order quantities, the components of ocean tidal angular momentum for each tidal frequency σ can be written as

$$\begin{aligned} H_1^{\text{ot}}(\sigma) &= -R^4 \rho_{\text{oc}} \Omega \iint \zeta(\sigma) \cos^2 \varphi \sin \varphi \cos \lambda \, d\lambda \, d\varphi \\ &\quad + R^3 \rho_{\text{oc}} \iint D (v(\sigma) \sin \lambda - u(\sigma) \sin \varphi \cos \lambda) \cos \varphi \, d\lambda \, d\varphi, \end{aligned} \quad (3.46)$$

$$\begin{aligned} H_2^{\text{ot}}(\sigma) &= -R^4 \rho_{\text{oc}} \Omega \iint \zeta(\sigma) \cos^2 \varphi \sin \varphi \sin \lambda \, d\lambda \, d\varphi \\ &\quad - R^3 \rho_{\text{oc}} \iint D (v(\sigma) \cos \lambda + u(\sigma) \sin \varphi \sin \lambda) \cos \varphi \, d\lambda \, d\varphi, \end{aligned} \quad (3.47)$$

$$\begin{aligned} H_3^{\text{ot}}(\sigma) &= R^4 \rho_{\text{oc}} \Omega \iint \zeta(\sigma) \cos^3 \varphi \, d\lambda \, d\varphi \\ &\quad + R^3 \rho_{\text{oc}} \iint D u(\sigma) \cos^2 \varphi \, d\lambda \, d\varphi \end{aligned} \quad (3.48)$$

with the mean sea water density ρ_{oc} , the undisturbed water depth D and Ω being once more the mean angular velocity of the Earth (cf. e.g. Chao & Ray, 1997; Ray *et al.*, 1994; Seiler, 1991; Wunsch & Seiler, 1992). The first part of Equations (3.46)–(3.48), the mass term, is constituted by the ocean tidal inertia increments, whereas the second part, the motion term, represents relative angular momentum. The double integral in the equations extends over the

ocean surface

$$\iint (\dots) d\lambda d\varphi = \int_{-\frac{\pi}{2}}^{\frac{\pi}{2}} \int_0^{2\pi} (\dots) d\lambda d\varphi . \quad (3.49)$$

Tidal elevations and current velocities are generally provided by the ocean tide models, with the exception that purely empirical models do not implicitly output the tidal currents, as mentioned in the previous section. Potentially the tide models also come with the undisturbed water depth, otherwise D can be retrieved from publicly available global bathymetric charts, such as GEBCO (General Bathymetric Chart of the Oceans, web site: www.gebco.net). The average density of the sea water ρ_{oc} is assumed to vary no more than about 2% from a value of 1035 kg/m^3 (Gill, 1982).

3.3.4 Earth rotation variations from ocean tide models

Diurnal and semidiurnal ocean tides are the most important drivers of short-period variations in LOD and polar motion. Hence this section expands on the transfer from OTAM to ERP variations, particularly with regard to high-frequency tidal signal. However, the quoted formalism is equally applicable to long-period tides, even though those do not necessitate special handling. In fact, for modeling high-frequency LOD excitation the relations given in Sections 2.2.2 and 2.2.3 are readily employable. Just in case of polar motion the FCN resonance has to be taken into account additionally, because the periodic forcing by the main ocean tides is near the terrestrial frequency of the FCN. A general scheme for the derivation of high-frequency ERP variations from parameters of an ocean tide model is displayed in Figure 3.8.

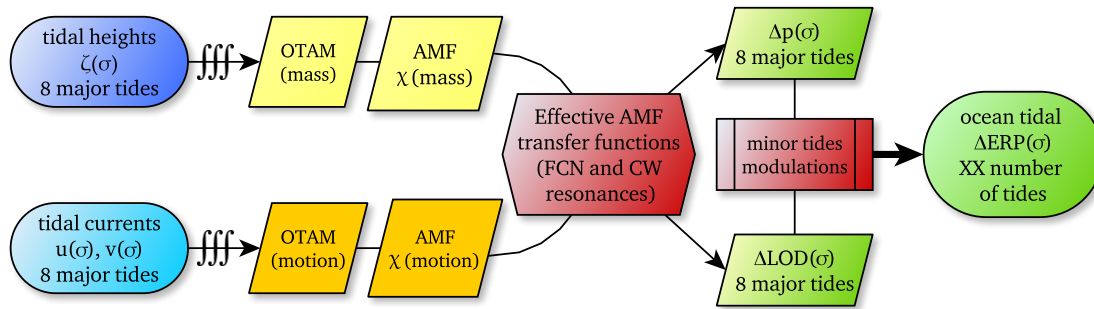


Figure 3.8: Ocean tide model \Rightarrow ERP variations.

Ocean tide models provide at least for the eight major constituents ($Q_1, O_1, P_1, K_1, N_2, M_2, S_2, K_2$) the tidal heights and current velocities as in-phase and quadrature coefficients. These are globally integrated according to Equations (3.46)–(3.48) to obtain mass and motion parts of OTAM for each tidal wave of frequency σ . The OTAM components are the input for equatorial and axial angular momentum functions or effective AMF, respectively, if a non-rigid Earth model is assumed. As it is a kind of standard procedure,

the OTAM to polar motion transfer including resonance effects, as suggested by Gross (1993), shall be quoted here:

$$\begin{aligned} \delta\hat{p}(\sigma) = & \left[2.554 \cdot 10^{-4} \frac{\Omega}{\sigma_{\text{NDFW}} - \sigma} + 2.686 \cdot 10^{-3} \frac{\Omega}{\hat{\sigma}_{\text{C}} - \sigma} \right] \frac{3G\hat{c}(\sigma)}{\Omega^2 R^5} \\ & + \left[6.170 \cdot 10^{-4} \frac{\Omega}{\sigma_{\text{NDFW}} - \sigma} + 1.124 \frac{\Omega}{\hat{\sigma}_{\text{C}} - \sigma} \right] \frac{\hat{h}(\sigma)}{A\Omega}. \end{aligned} \quad (3.50)$$

A formula for LOD variations derives from the combination of Equations (2.19) and (2.24):

$$\delta\text{LOD}(\sigma) = \text{LOD}_0 \left[0.748 \frac{c_{33}(\sigma)}{C_m} + 0.997 \frac{h_3(\sigma)}{C_m \Omega} \right]. \quad (3.51)$$

Equations (3.50) and (3.51) contain the rotational angular momentum components implicitly as variations of the corresponding increments of the Earth inertia tensor \mathbf{C}

$$c_{13} = \frac{H_1^{\text{ot}}(\text{mass})}{\Omega}, \quad c_{23} = \frac{H_2^{\text{ot}}(\text{mass})}{\Omega}, \quad c_{33} = \frac{H_3^{\text{ot}}(\text{mass})}{\Omega} \quad \text{with} \quad \hat{c} = c_{13} + ic_{23}$$

and the relative angular momentum components directly as parts of the corresponding vector $\mathbf{h} = (h_1 h_2 h_3)$ with $\hat{h} = h_1 + ih_2$. G is as before the gravitational constant, A stands for the equatorial moment of inertia, C_m for the axial moment of inertia of the mantle and $\hat{\sigma}_{\text{C}}$ is the complex frequency of the Chandler wobble (CW). With respect to the terrestrial reference frame the FCN is called Nearly Diurnal Free Wobble (NDFW), hence the terrestrial FCN frequency is denominated σ_{NDFW} in Equation (3.50). The whole procedure of ERP model development can be essentially executed in the frequency domain, provided that the input parameters are given as harmonic functions. The periodicity of the ocean tides is mapped one to one to the ocean tidal angular momentum and consequently to the ocean tidal Earth rotation variations. Assuming the eight major constituents as input would therefore yield eight amplitudes and phases of polar motion and LOD variations each.

The present conventional model for the high-frequency ocean tidal ERP variations contains 71 harmonic terms (cf. IERS Conventions, 2010, Ch. 8), but it is as well based on an ocean tide model that gives only the eight major tides. In the IERS Conventions (1996), a first version of the model for subdaily ocean tidal effects on ERP was given for these eight major ocean tides as time dependent sine and cosine amplitudes for polar motion, UT1, LOD and rotation speed. These eight terms were taken from a publication by Chao *et al.* (1996) and correspond to the Model C quoted in that article. The Earth rotation variations of the Model C are based on ocean tidal angular momentum calculated from the ocean tide model TPXO.2 (Egbert *et al.*, 1994). TPXO.2 is a hydrodynamic model with observations from the satellite altimetry mission TOPEX/Poseidon assimilated. The influence of minor tides and nodal modulations was considered in a later version of the ERP model by using the above described orthotide formalism. The final model with 71 terms was assembled in a two-stage process: the basic eight terms plus nodal corrections and

minor tides were considered in the calculation of the 12 so-called orthoweights. In combination with the orthotide functions and constant coefficients these 12 weights could be used directly as a model, which can be evaluated for polar motion or LOD/UT1 for any time of interest. If the expression of the tidal ERP model as harmonic functions is preferred, there is the option to translate the orthoweights to sine and cosine coefficients by means of their relation with the tidal potential (see Section 3.3.2). In case of the conventional model the orthotide functions were simply evaluated for a long time span and 71 harmonic coefficients were fitted to the time series.

3.4 Tides in the atmosphere

Moon and Sun exert gravitational attraction also on the mass particles of the atmosphere, but the ground pressure amplitudes of gravitational tides are fairly below meteorological noise (Brzeziński *et al.*, 2002). From long time series of weather data it was as yet only possible to detect signal of the M_2 and O_1 waves. Much stronger tide-like patterns in atmospheric pressure and wind are created by the differential heating of the Sun. The solar radiation cycle is determined predominantly by the diurnal rotation and the annual revolution of the Earth around the Sun. Accordingly, the basic periods of the so-called thermal or radiational tides are one solar day and one tropical year. Furthermore, several harmonics with positive and negative integer multiples of the original frequencies are generated due to the geophysical diversity of the ground (e.g. ocean-land distribution, topography, humidity, clouds, vegetation, ...). Because of their coherence with the gravitational waves, the thermal tides carry the same labels. As the solar diurnal and semidiurnal astronomical constituents for instance, the diurnal and semidiurnal radiational waves are denominated S_1 and S_2 . All diurnal and subdiurnal thermal tides exhibit also seasonal modulations, this means that their amplitudes and phases are varying with seasonal periods. It is worth noting that effects of the atmospheric tides or of the solar radiation are as well present in the ocean tidal signal. These effects emerge when admittances to the gravitational tidal potential are evaluated from sea level observations. Small anomalies can then be found near one and two cycles per solar day and one cycle per year (Cartwright, 1977). Partly, these variations can be attributed to direct heating and cooling of the ocean surface and onshore winds associated with the heating and cooling of the coastal land, and to some extent the anomalies are caused by coupling with the tides of the atmosphere through surface pressure. Due to this coupling mechanism, the solar constituents of empirical or semi-empirical ocean tide models will always contain a fraction caused by atmospheric tides. Standard models represent the diurnal and subdiurnal sea surface variations with the eight major tides, among those the semidiurnal S_2 tide. According to Pugh (1996) about 10–20% of the S_2 amplitude is not of gravitational but of radiational origin. When comparing geodetic excitation (Earth rotation data) to geophysical excitation inferred from geophysical data, this coupling of oceanic and atmospheric tides should always be kept in mind, in order to avoid multiple consideration of the same phenomenon.

Effect of atmosphere tides on Earth rotation

As for the non-tidal atmospheric effects, the influence of the atmosphere tides on Earth rotation can be assessed from purely physical general circulation models or numerical weather data provided by global weather services. The two most well-known centers allocating such data, are the United States National Center for Environmental Predictions (NCEP) and the European Centre for Medium-Range Weather Forecasts (ECMWF).

Similar to the ocean tides, the Earth rotation excitation by the atmosphere can be expressed by the angular momentum functions or effective angular momentum functions, respectively. The formalism to derive the atmospheric angular momentum components is very much alike the procedure given in Section 3.3.3 for the ocean tides and shall not be quoted here. It can be found for example in Appendix A of Brzeziński *et al.* (2002). The crucial parameter for the evaluation of the mass term is the surface pressure. The calculation of the motion term requires wind velocities in East and North components for different height levels. Understandably, the mass term is often called pressure term and the motion term is named wind term, in the context of atmospheric excitation.

The study of atmospheric diurnal and subdiurnal tides necessitates of course also the consideration of the FCN resonance in the diurnal retrograde period band. The essential formalism given in Section 3.3.4 for the ocean tides is applicable to atmospheric high-frequency variations as well. Alternatively, the handling of the resonance problem is described also by Brzeziński (1994). Another issue in the computation of atmospheric AMF is the handling of angular momentum transfer above the oceans. At present there are two modeling options: the inverted barometer (shortly IB) assumption and the non-IB assumption. The IB hypothesis states that the ocean surface yields to a change in the atmospheric pressure and absorbs in that way a pressure variation. A non-IB reaction of the ocean would be the direct transfer of the surface pressure change to the sea floor, where it manifests itself as ocean bottom pressure. The consequence of accepting the IB assumption is a reduction of the magnitude of the AMF pressure term. The IB model is widely agreed to be valid for long periods and deep water areas. For diurnal and subdiurnal variations, Brzeziński *et al.* (2002) conclude that it fails, because the IB correction deteriorates the agreement of the atmospheric excitation with geodetic data. A more extensive description of atmospheric effects on Earth rotation is provided e.g. in Schindelegger *et al.* (2013).

As to the size of atmospheric tidal effects on ERP, Brzeziński *et al.* (2002) and also Brzeziński *et al.* (2004) estimate the diurnal and semidiurnal (S_1, S_2) contribution to below 10 μs for polar motion and to about 5 μs for LOD. Still, the estimation of the semidiurnal harmonics is rather uncertain, since the temporal resolution of the available numerical weather data is by default only six hours. Atmospheric excitation from numerical weather data with higher resolution (hourly), provided for the limited period of the special VLBI campaign CONT08, was investigated by Schindelegger *et al.* (2011). The high-resolution angular momentum functions showed a decrease in the spectral power compared to angular momentum functions with six-

3.4 Tides in the atmosphere

hourly resolution which was attributed to a significant counteraction of pressure and wind terms on short time scales.

Chapter 4

Earth rotation variations from Very Long Baseline Interferometry

While the preceding chapters give the theoretical framework of Earth rotation and treat the causes and consequences of tidal phenomena, the present and following chapters deal with the observation of Earth rotation variability by means of space geodetic techniques. The first measurement system, to be treated in this chapter, is the geodetic VLBI. It is one of the most important techniques for Earth rotation monitoring as it grants access to the full set of Earth orientation parameters, nutation offsets, dUT1 and polar motion. Since a complete description of the functionality would go beyond the scope of this thesis, only an outline of the VLBI system with special focus on the aspects relevant for Earth rotation observation shall be given.

VLBI is based on the simultaneous observation of the microwave signal emitted by an extragalactic radio source, e.g. so-called quasars, at two stations on the Earth surface, which are usually several hundred to several thousand kilometers apart. This observation configuration is designated a baseline. As the name very long baseline interferometry tells, the technique uses the physical principle of wave interference. But in contrast to a conventional interferometer, where the superposition of the waves happens quasi instantaneously, the interference is established mathematically in post-processing mode. In order to realize this, the radio telescopes are connected with very precise and stable atomic clocks and recording devices. To first approximation the signal comes in as a plane wavefront and reaches the receivers of the two distant sites at different times. The two signal pieces are tagged with timestamps and recorded on magnetic disks (formerly on magnetic tapes). The hard disks are then transported to a special processing unit, the correlator, where the signals are cross-correlated, i.e. shifted in phase until constructive interference is accomplished. Together with the time tag information this process renders the fundamental VLBI observable, the difference of the radio signal arrival times at the two stations, also called 'delay'. The observing frequencies of geodetic VLBI belong to the S and X band and are 2.3 and 8.4 GHz, respectively. A sketch of the measurement concept is shown in Figure 4.1. The picture illustrates only a single baseline configuration, whereas routine VLBI experiments are carried out within a network of four to eight globally distributed stations on average. A soli-

tary VLBI experiment is denominated a session. The number and distribution of the telescopes participating in such a session depends of course on the purpose. That can be a densification of the celestial reference frame, monitoring of Earth rotation, determination of global or regional reference frames or plate motions and so forth. The method allows for the determination of a variety of parameters, all of which are related either to the radio source, or the terrestrial position of the site, or to the signal path in between. In fact almost any parameter that appears in the observation equation can be solved for within a least-squares adjustment procedure, as long as there is a sufficient number of observations. The geodetic prime quantities are certainly the coordinates of the radio sources, the station positions and velocities and the Earth orientation parameters.

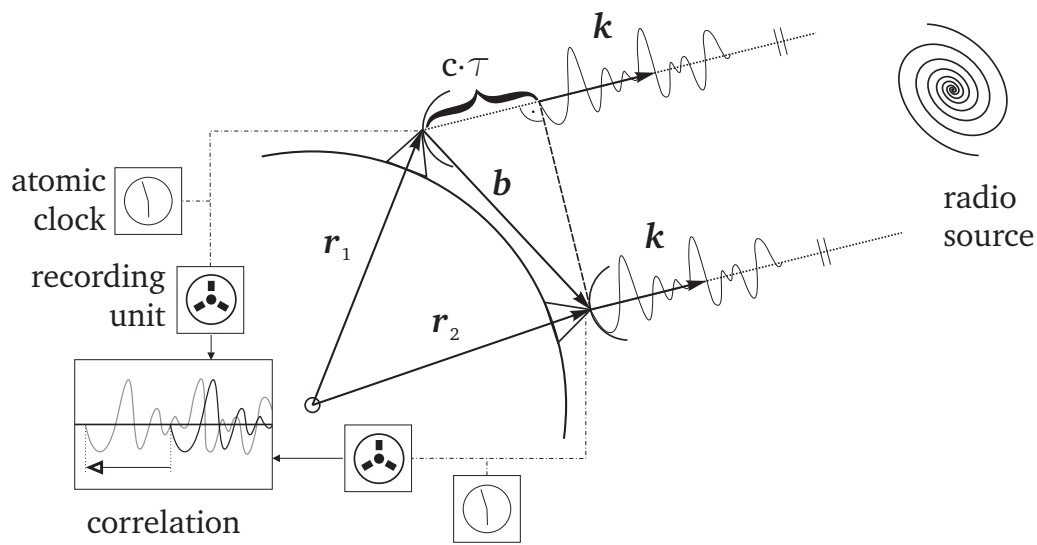


Figure 4.1: Basic principle of VLBI observation.

4.1 Observation equation and error sources

The basic observation equation of VLBI can be virtually deduced from Figure 4.1, as it is fairly simple. It contains only three variables, the baseline vector \mathbf{b} , the unit vector in source direction \mathbf{k} and the delay τ , as well as the constant velocity of light c (cf. Schuh, 1987):

$$\tau = - \frac{\mathbf{b} \cdot \mathbf{k}}{c}. \quad (4.1)$$

The equation can be just as well quoted with a positive sign (e.g. Tesmer, 2004), because the sign depends only on the definition of the delay. In the representation used here, the delay convention is: $\tau = t_2 - t_1$, with the signal arrival times t_1 and t_2 at station 1 and 2 as depicted in Figure 4.1. The delay depends essentially on the distance between the two telescopes $|\mathbf{b}| = |\mathbf{r}_2 - \mathbf{r}_1|$ corresponding to the baseline length, on the orientation of the baseline with re-

spect to the quasar and on the properties of the medium where the signal is traveling through. These quantities themselves are subject to variations determined by a multitude of factors. Most prominent is the variation of the station positions with respect to the radio source due to Earth rotation. For solving the observation equation the baseline vector and the source vector have to be represented in the same coordinate system. Yet, as explained in Chapter 2, the coordinates of the stations and so the baseline vector are given in the TRF, while the source positions are provided in the CRF. Hence the introduction of the transformation from TRF to CRF (Equation 2.2) is a crucial extension of Equation 4.1:

$$\tau = - \frac{k_{\text{CRF}}}{c} \cdot \mathbf{Q} \cdot \mathbf{R} \cdot \mathbf{W} \cdot \mathbf{b}_{\text{TRF}} . \quad (4.2)$$

In practical processing of VLBI observations, Equation (4.2), which actually constitutes the functional model of the adjustment procedure, needs to be further extended to consider all effects that influence the delay. However, details in terms of additional equations, thus the complete delay model, will not be given in this section. For further particulars on the formulas refer to standard literature, e.g. the seminal paper by Sovers *et al.* (1998) or the IERS Conventions (2010) and references therein. Recent general and also detailed information on the VLBI system and analysis can be found in Schuh & Behrend (2012) and Schuh & Böhm (2013).

Effects on VLBI observations

VLBI experiments are conventionally interpreted and processed using the principles of least-squares adjustment. Such procedures require very accurate initial values or theoretical models, respectively. Given that the delay is the basic observable of VLBI the whole a priori model is called the delay model. Following Sovers *et al.* (1998), the effects on VLBI observations can be assigned to three different sections of the delay model. These are a geometric, an instrumental and an atmospheric delay model part.

The geometric delay comprises modeling of the wavefront shape, a so-called retarded baseline correction and relativistic effects, as well as all corrections regarding telescope location and deformation, and issues related to the orientation and position of the baseline w.r.t. the barycenter of the solar system.

The calculation of the theoretical delay starts with the correction of the baseline vector, represented in the TRF, for station dependent effects. Tectonic plate motion shifts the site positions predominantly horizontally and is usually modeled as a linear process. Deviations from the linear motion can occur locally or also regionally due to episodic events such as earthquakes. Stations in affected regions need special attention, when indicated. In areas which were covered by large glacier shields during the last ice age, the stations exhibit yearly uplift rates of several millimeters due to post-glacial rebound. Periodic crustal deformations are of tidal origin. Among them, the solid Earth tides have the largest magnitudes reaching up to 50 cm. A secondary tidal effect is the so-called pole tide. It is a deformation of the Earth crust due to an additional centrifugal po-

tential, caused by the misalignment of the rotation axis and the Earth's figure axis. The pole tide is thus dependent on polar motion. Even though being partially kilometers inland, observation sites can also be significantly affected by the elastic response of the Earth to ocean tidal loading. Minor site displacements are generated by atmospheric pressure changes and non-tidal ocean, ocean pole tide, hydrological and snow loading.

The reference points of the VLBI sites are defined at a physical or virtual intersection of the antenna axes. For this reason a reference marker is not only influenced by deformation of the ground but also by the deformation of the antenna itself. The latter can be produced by thermal expansion of the material or in case of large telescopes by gravitational attraction of the mass of the dish.

After the correction for all these station dependent effects, the baseline vector is rotated to the geocentric space-fixed reference frame. To finally match the coordinates of the sources which are given in the solar system barycentric (SSB) frame, the baseline is converted by Lorentz transformation taking account of the consequences of special relativity. The time delay for the passage of the wave front from station 1 to station 2 is then calculated in the SSB coordinate and the barycentric coordinate time (TCB) frame. At this step the implications of the real receiver to wave front geometry are considered. The signal is eventually modeled as a curved wave front (for sources within our solar system), and the rotation of the Earth and hence of the baseline during the signal propagation time from the first station to the second station is introduced to the delay model. The latter measure is the already mentioned retarded baseline correction. Another relativistic effect, though belonging to general relativity, is imposed via the so-called gravitational delay. It expresses the retardation of a signal propagating in a gravitational potential (Earth, Sun, planets) relative to its travel time. The geometric delay part in TCB is finally obtained, which is subsequently back-transformed to the TT (Terrestrial Time) frame. A further correction to the geometric delay would be the consideration of the radio source structure, the conventional application of which is currently discussed.

Instrumental delay consists mainly of components due to station clock instabilities, but contains also for example a cable calibration fraction. The frequency standards at the stations are normally not synchronized. Therefore it is standard procedure to set one preferably stable instrument as reference clock and to model the behavior of the other(s) relative to this reference. The clock model is for instance a quadratic polynom in time valid for the whole session. Such atomic clocks can also exhibit large jumps, which are termed clock breaks in processing. If a clock break occurs, a new clock function has to be estimated starting from the time of the jump and the corresponding clock is certainly not apt to serve as a reference.

Atmospheric delay is one of the most sensitive and unpredictable parts of the VLBI model. However, the atmospheric delay has two contributions, one of which is actually easy to handle. Related to signal propagation we have to distinguish between tropospheric and ionospheric effects.

The ionosphere is the upper part of the Earth atmosphere, starting at about 80 km and migrating into interplanetary space, which contains charged particles, i.e. electrons and ions. The

usually employed VLBI observable, the group delay, experiences a signal advance or an additive delay, when traveling through the ionosphere. For microwaves the ionosphere is a dispersive medium, that means signal propagation speed is frequency dependent. This property allows to eliminate the ionospheric refraction by dual-frequency calibration. As mentioned before, geodetic VLBI experiments are carried out in S band and X band, permitting the calculation of a ionospheric correction. This can be applied to the measured delay and the effects of the ionosphere can otherwise be ignored in delay modeling.

In contrast, the troposphere is a non-dispersive medium and hence the distortion of the ray path in that layer has to be modeled and fully accounted for. The troposphere is the lower part of the Earth's atmosphere, up to about 10 km. All substantial processes related to weather, clouding and wind happen within this shell. With respect to a signal traveling in vacuum, the radio waves are delayed, bended and attenuated on the journey through the troposphere. The effective tropospheric path delay is a function of the refractivity integrated over the ray path. It is commonly split up into two parts, according to the dependence of the refractivity on different parameters. These parameters are essentially the partial pressure of dry air and the partial pressure of water vapor. The tropospheric delay is consequently composed of a hydrostatic and a wet portion. While the hydrostatic contribution can be computed rather accurately from surface pressure and station height and latitude, the wet part has to be estimated within the adjustment procedure. The element of uncertainty is thereby the distribution of the water vapor above the VLBI site. In general the tropospheric delay is first modeled in local zenith direction and then transferred to the slant delay by means of so-called mapping functions. The mapping functions account for the 'thickness' of the troposphere, but disregard possible horizontal inequalities. Such azimuthal asymmetries can be considered by additional estimation of horizontal tropospheric gradients. More detailed information about mapping functions and gradients in VLBI analysis can be found in Böhm & Schuh (2004) and in Böhm & Schuh (2007).

4.2 Determination of Earth orientation parameters

As explained in the previous section, unknown parameters are estimated within a common adjustment of all observations of a VLBI session. This is called a single session solution. Single session solutions allow the determination of parameters which are resolvable within the time interval of the session. For example it is not possible to estimate station velocities from one session with a duration of only 24 hours, as these are usually measured in meters per year. Station velocities belong to the so-called global parameters, which are determined accordingly in a so-called global solution. A global solution is obtained by accumulating the normal equation systems of single sessions covering the time span of several weeks, months or years, depending on the purpose of the solution. Parameters common to many sessions, such as station coordinates and velocities or source positions, are adjusted in one cast, whereas fast fluctuating parameters like tropospheric delays are reduced session-wise. The estimates of the reduced parameters cannot

be retrieved from the global solution. Yet it is possible to obtain the estimated session-wise values in a backward solution. Of course also varying quantities such as EOP can be estimated as global parameters. These are then stacked for common epochs determined by the observations of more than one session. However, this is only feasible for a limited time period, because the inversion of the normal equation matrix becomes computationally impracticable from a certain number of unknowns.

4.2.1 Partial derivatives and a priori information

This section shall shed light especially on the determination of Earth rotation parameters within single session solutions, assuming the approach known as Gauß-Markov model (cf. Niemeier, 2008, p. 137) as basic adjustment method. The general functional model reads

$$l + v = A\Delta x \quad (4.3)$$

with the reduced observation vector (observed minus computed) l and the vector of the residuals v on the left hand side, and the design matrix containing the partial derivatives A and the reduced vector of unknowns Δx on the right hand side. Determination of ERP demands for the derivation of the respective partial derivatives from the VLBI observation equation and the set up of these parameters as unknowns in estimation intervals to be specified. Equation (4.2) shows how the Earth orientation is embedded in the observation equation. The transformation from TRF to CRF is a sequence of rotation matrices which are functions of the EOP (see Equation 2.2). If the complete transformation matrix is denoted by Υ , the partial derivative w.r.t. any EOP, for example x_p , is

$$\frac{\partial \tau}{\partial x_p} = -\frac{k_{\text{CRF}}}{c} \cdot \frac{\partial \Upsilon}{\partial x_p} \cdot \mathbf{b}_{\text{TRF}}. \quad (4.4)$$

According to the chain rule this can be further broken down to

$$\frac{\partial \Upsilon}{\partial x_p} = \mathbf{Q} \cdot \mathbf{R} \cdot \frac{\partial \mathbf{W}}{\partial x_p} \quad \text{with} \quad \frac{\partial \mathbf{W}}{\partial x_p} = \mathbf{R}_3(-s') \cdot \frac{\partial \mathbf{R}_2(x_p)}{\partial x_p} \cdot \mathbf{R}_1(y_p), \quad (4.5)$$

and analogously for $\frac{\partial \tau}{\partial y_p}$. The angle s' , though being actually a function of the pole coordinates, can be regarded as constant multiplication factor in this context. In case of UT1 the partial is decomposed in two parts, since the rotation matrix \mathbf{R} actually involves the Earth rotation angle ERA and UT1 is deduced as a function of that angle

$$\frac{\partial \Upsilon}{\partial \text{UT1}} = \mathbf{Q} \cdot \frac{\partial \mathbf{R}_3(-\text{ERA})}{\partial \text{ERA}} \cdot \frac{\partial (\text{ERA})}{\partial \text{UT1}} \cdot \mathbf{W}. \quad (4.6)$$

The proportionality relation of UT1 to the Earth rotation angle can be found in Chapter 5 of the IERS Conventions (2010). In order to obtain the partials for the celestial pole offsets δX and δY

the matrix Q and the respective submatrices concerned with the parameter of interest have to be differentiated accordingly.

A usual prerequisite for the convergence of least-squares adjustment procedures is the availability of suitable a priori information. Initial values are needed for all parts of the functional model from station positions to Earth orientation parameters. Since the introduced a priori values determine the meaning of the estimated residuals, the composition of a priori EOP values will be examined more closely. It was already mentioned in Chapter 2 that the celestial coordinates of the CIP X and Y are formed predominantly by forced motions of gravitational origin which can be modeled and predicted quite well. Only a comparatively small, unpredictable part, represented by the celestial pole offsets, has to be imposed from observations. For polar motion and UT1 the situation is exactly the reverse, the major part of the signals is caused by a variety of unsteady, chiefly geophysical processes that cannot be accurately captured by models. These effects, generating polar motion and UT1 variations, are described in Section 2.3. In post-processing, a priori ERP values are taken therefore from observational time series provided by the IERS, e.g. the C04 series, derived from a combination of Earth rotation observations of different space geodetic techniques. However, IERS series contain smoothed daily values only and do not reproduce subdaily variations. The high-frequency fluctuations have to be taken into account by application of suitable models. At present it is standard to introduce diurnal and subdiurnal ERP variations due to ocean tides and libration, as recommended in the IERS Conventions (2010). Absolute ‘observed’ EOP values are hence constructed as follows

$$x_p(\text{observed}) = x_p(\text{C04}) + \underbrace{x_p(\text{ocean tides}) + x_p(\text{libration})}_{\text{a priori value}} + \Delta x_p(\text{estimated}), \quad (4.7)$$

$$X(\text{observed}) = X(\text{IAU2000/2006}) + \underbrace{\delta X(\text{C04})}_{\text{a priori value}} + \Delta X(\text{estimated}), \quad (4.8)$$

where x_p is stated exemplarily for all ERP and X for precession-nutation.

4.2.2 Parametrization

With regard to the two different VLBI software packages that were employed for the derivation of EOP variations in the course of this work, the two ways of parametrization that are used there shall now be surveyed briefly. The OCCAM software (Titov *et al.*, 2004) was developed based on the BVSS (Bonn-VLBI-Software-System, see e.g. Schuh, 1987) and refined inter alia at the Institute of Geodesy and Geophysics of the Vienna University of Technology (IGG), especially concerning the least-squares program branch using the Gauß-Markov model. This version of OCCAM is actually no longer maintained at IGG since the advent of the new Vienna VLBI Software VieVS which has been developed since 2008 (Böhm *et al.*, 2009). Figure 4.2 demonstrates the two approaches of parameter setup as implemented in OCCAM (left) and VieVS (right). OCCAM offers to estimate time dependent parameters either as continuous piecewise linear functions or

as discontinuous piecewise linear functions. With the first option, one offset is estimated at the beginning of the session and then only rates are solved for each interval. The second option permits the setup of offsets or offsets plus rates, where the offsets refer to the middle (blue) or to the beginning of the time intervals (green), respectively. As it is illustrated in the figure, the epochs of the parameters are determined by the time of the first observation of the session and the chosen parameter spacing. Figure 4.2 shows a parameter spacing of 6 hours as an example.

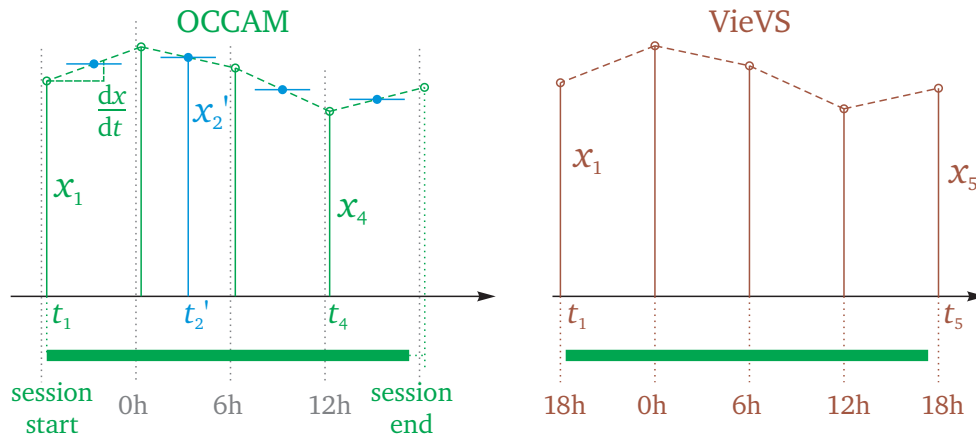


Figure 4.2: Setup of time dependent parameters in OCCAM and VieVS.

Routine VLBI experiments start around 18 h UTC and last 24 hours. In order to facilitate the combination of normal equations from different space geodetic techniques, VieVS incorporates the parametrization concept of piecewise linear offsets at integer hours or minutes of UTC (see also Teke *et al.*, 2012). The nodal points of the first and last offset therefore enclose the session as tightly as the selected estimation interval tolerates. To avoid singularities in cases where there are not enough observations in one estimation interval, relative constraints can be introduced between successive offsets. Choosing very tight constraints leads to one average value over the whole session regardless of the defined interval. The insertion of constraints is possible also in OCCAM for offsets as well as for rates.

4.2.3 Datum definition and correlation issues

Geodetic VLBI is a purely geometric technique that does not establish any physical relation to the center of mass of the Earth. The network stations constitute a polyhedron in space which is attached to the terrestrial reference frame by datum definition. A completely free solution of the station coordinates is at any rate not feasible, because it would leave a rank deficiency and inhibit the inversion of the normal equation matrix. Single VLBI sessions have a datum defect of six (three rotations, three translations), if station coordinates and EOP are estimated simultaneously. Source coordinates are commonly not estimated from single session solutions, but fixed to their catalogue positions. The estimation of EOP and parallel elimination of the datum deficiency can be realized by means of two options each with variations. One possibility is

to fix the coordinates of selected up to all station coordinates to the a priori values. The second approach is to model the datum realization as a seven-parameter Helmert transformation from a priori station positions (e.g. ITRF) to the estimated positions. The transformation comprises three rotations, three translations and a scale. In fact, in VLBI the scale is considered to be defined by the velocity of light and is therefore set constant. In order to remove the datum defect, the translations and rotations are minimized in a least-squares sense over the whole or parts of the network. This is called imposing no-net-translation (NNT) and no-net-rotation (NNR) conditions on the station positions.

The suitability of a VLBI session for the determination of EOP is determined in the first instance by the network configuration and in the second by the observation schedule. As a rule of thumb, UT1 estimation demands a large East-West extension, whereas for polar motion the North-South distribution is more important (Schuh, 2000). The influence of the geometry (and the weighting of the observations) is reflected in the correlation matrix of a session, representing the functional dependencies among the unknowns. The correlation matrix is calculated from the cofactor matrix of the unknown parameters $\mathbf{Q}_{xx} = (\mathbf{A}^T \mathbf{P} \mathbf{A})^{-1}$, with the weight matrix \mathbf{P} and the elements $q_{x_i x_j}$. The elements of the correlation matrix \mathbf{R}_{ij} are derived as

$$r_{ij} = \frac{q_{x_i x_j}}{\sqrt{q_{x_i x_i} \cdot q_{x_j x_j}}} . \quad (4.9)$$

Figure 4.3 displays as an example the observation networks and correlation matrices of two VLBI sessions designed for different purposes. The session labeled 08FEB06XA (left part of the figure) belongs to the IVS-OHIG program, which aims at tying together all sites in the southern hemisphere to determine an accurate regional TRF around the South Pole. It is actually not formed for the observation of EOP, which is expressed in the rather strong correlations between the different EOP and also between EOP and several coordinate components. Session 08AUG04XA (right part of the figure) in contrast, is designed for global TRF and EOP determination, indicated by the much more homogeneous distribution of the stations. Accordingly, the corresponding correlation matrix suggests an extensively independent estimability of EOP and station positions. The correlation matrices emanate from a processing setup with estimation of station coordinates using NNR/NNT conditions and diurnal EOP estimation interval.

Of course, the parameter correlations reflect only the mathematical connection but do not yield any information about the precision of the resulting EOP. To predict the EOP quality from the network geometry there are other measures, for example Malkin (2009) proposed the network volume as an indicator and found an average increase of the EOP accuracy with the volume of the polyhedron formed by the stations. The polyhedra spanned by the two example networks including their volumina are displayed in Figure 4.4.

Nevertheless, the correlation matrix can give valuable clues to the reliability and reasonability of the processing settings. This is demonstrated with regard to the separability of EOP in the

4.2 Determination of Earth orientation parameters

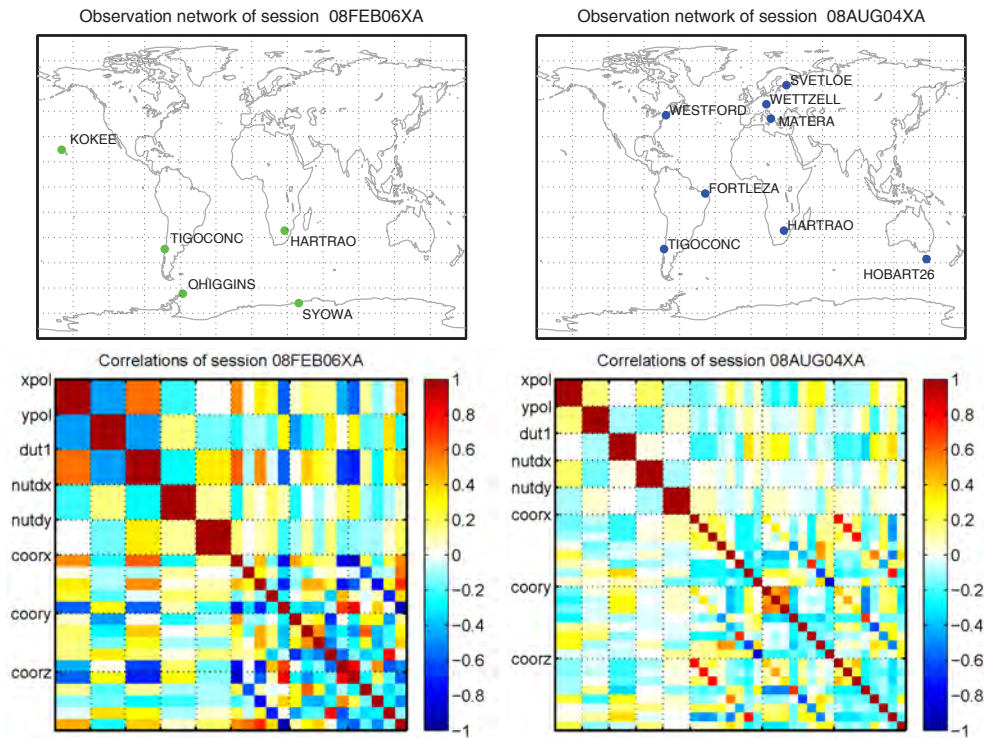


Figure 4.3: Station networks (top) and correlation matrices of EOP and station coordinates (bottom) of the VLBI sessions 08FEB06XA (left) and 08AUG04XA (right).

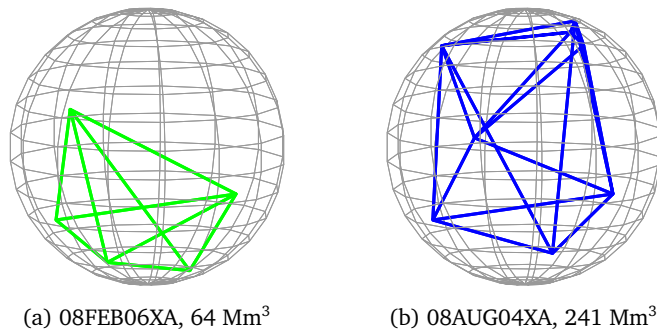


Figure 4.4: Polyhedra and volumina of the station networks.

case of subdaily parameter spacing, using the example of session 08AUG04XA. Two parametrization scenarios are evaluated for the resulting correlations which are illustrated in Figure 4.5. The left matrix is generated with an hourly estimation interval for polar motion and UT1 and simultaneous diurnal estimation of celestial pole offsets, i.e. nutation. It shows highly systematic correlations between the pole coordinates and the nutation parameters. These are a consequence of the transformation concept, where retrograde diurnal polar motion and precession-nutation are mathematically equivalent and are separated only by convention (see Section 2.1.3). Hence, the parallel estimation of subdiurnal polar motion and celestial pole offsets in time domain is

impracticable. If polar motion is set up with subdiurnal resolution, nutation has to be fixed to a priori values to decorrelate the parameters. This second scenario is represented by the matrix on the right side of Figure 4.5. The problem was pointed out and illustrated similarly by Tesmer *et al.* (2001).

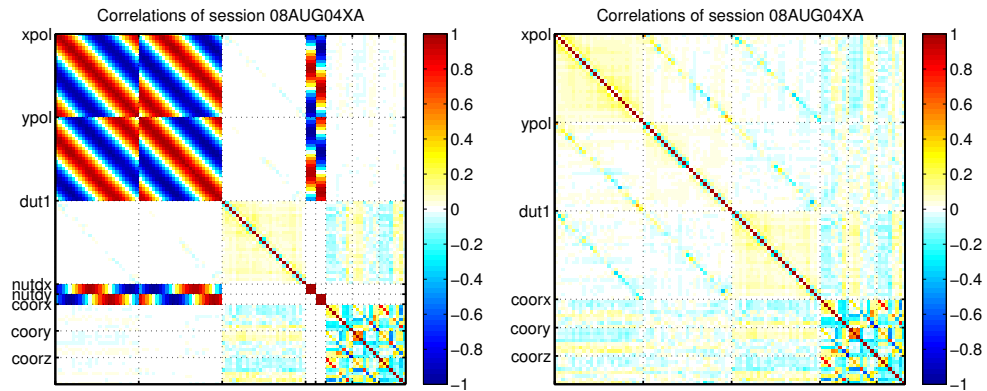


Figure 4.5: Correlation matrices (EOP and station coordinates) of the VLBI session 08AUG04XA with subdaily ERP sampling and simultaneous estimation (left) or fixing (right) of celestial pole offsets.

4.3 Estimation of Earth rotation parameter long-time series

The scientific rationale of the present work is the investigation of tidally induced Earth rotation variations observed by VLBI and also GNSS. As accentuated in Chapter 3, the period of the ascending lunar node's revolution of 18.6 years is the most important tidal modulation period, because it generates significant side lobes to the main constituents of the tidal spectrum. In order to separate two neighboring harmonic terms, at least one beat period of the two signals has to be observed. For a main tidal constituent and its side terms this beat period corresponds to 18.6 years. A constraint-free determination of these terms therefore necessitates EOP time series of at least that length. Geodetic VLBI can currently resort to more than 25 years of observations, qualified to be analyzed for such a purpose. Hence, the first task in heading towards the interpretation of Earth rotation variations from VLBI with respect to tidal excitation, is the estimation of ERP long-time series.

In the course of this study various different ERP time series were calculated with the two afore-mentioned software packages OCCAM and VieVS, differing in datum definition, resolution, transformation concept, parametrization and a priori models. The series were derived to examine zonal tidal variations in universal time on the one hand and diurnal and subdiurnal tidal variations in universal time and polar motion on the other hand.

In particular regarding the estimation of high-frequency variations in ERP some general comments concerning the processing strategy should be added: Subdaily harmonic oscillations can be

deduced from space geodetic observations in basically three different ways. The most rigorous approach is to formulate the harmonic functions already in the observation equation and estimate amplitudes and phases of the variations within a global solution (see Section 4.5). Another method, to be described in Section 4.4, is the application of the so-called complex demodulation technique, which requires an alternative parametrization of the ERP. And, finally, there is a multistage procedure, where the harmonic terms are estimated from highly resolved ERP time series. Recently, Artz *et al.* (2011) presented a kind of compromise procedure between the time series approach and the direct estimation of tidal terms in a global adjustment. They applied the transformation of normal equation systems, which contain highly resolved ERP, to normal equations representing the high-frequency signal as tidal amplitudes. In this way the estimation of an empirical tidal model from normal equations of different space geodetic techniques is facilitated.

As demonstrated in the last section, the calculation of polar motion with subdaily spacing precludes the simultaneous estimation of celestial pole offsets. This leaves three options for the processing: (1) celestial pole offsets can be set to zero, i.e. nutation is fixed to the nutation model, (2) nutation is fixed to the nutation model plus a priori celestial pole offsets from the IERS, e.g. C04, (3) nutation is fixed to the nutation model plus a priori celestial pole offsets that are estimated in a preliminary solution together with diurnal polar motion. Choice (1) and (2) both have the potential to introduce retrograde diurnal signal to the polar motion series, which is rather unlikely in case (3). Yet, option (3) calls for a duplicate processing of all sessions, a first run to determine the a priori nutation offsets and the second to derive the high-resolution ERP time series. All three possibilities were exploited in the frame of the present thesis, not least owing to disabilities and evolution of the employed software packages in certain respects.

An explicit difference between OCCAM and VieVS, which does not have large-scale effects on the EOP determination though, is the applied TRF/CRF transformation. While in OCCAM still the traditional equinox based transformation was used, VieVS incorporates already the NRO concept (cf. Section 2.1.3). More important distinctions between the softwares are the way of parametrization, treated in Section 4.2.2, and the datum definition facilities. OCCAM allowed the application of NNR/NNT conditions only for all stations of a network, whereas it is possible to exclude stations from the datum with VieVS.

In terms of long-time series we have to distinguish between ERP series generated for studying subdaily ERP variations, calculated with hourly resolution, and dUT1 series generated for studying the impact of the solid Earth and long-period ocean tides, which were usually derived with six hours resolution. The hourly time series are in general more noisy, but the high resolution is required in order to properly resolve semidiurnal or smaller periods. The estimation interval for the long-period tidal effects was chosen as a compromise between high sampling rate and noise level. The level of formal errors of the dUT1 results with six hours interval is approximately half of the formal error level of the hourly values.

Geodetic VLBI observations can be categorized into different groups of sessions, not all of which are suitable for the determination of Earth orientation parameters. The criteria for the suitability are: the observation network should be global, not local or regional, the network

should consist of at least three telescopes and the session should have more than 250 observations. Almost all sessions which do not meet these criteria are listed in a continuously updated textfile¹ provided by the IVS analysis coordinator. One exception are the so-called Intensive sessions, which are operating on a single baseline and for one hour only. Their aim is to estimate dUT1 once per day, primarily to support the prediction. The quality of the dUT1 estimates from the Intensives is of course not comparable to the quality of dUT1 from 24-hour sessions. In the present work, results from time series including Intensives are not shown, as their contribution is of minor advantage. Qualified 24-hour sessions are of course available neither continuously nor in perfectly regular time intervals. Consequently, VLBI-derived parameter series are not equally spaced and can have gaps of several days. Besides, the observation network, and hence the geometry, is varying from session to session and the total observation time is not uniformly distributed between all telescopes contributing to a long-time series. Figure 4.6 illustrates this displaying all baselines that were processed to derive one of the OCCAM solutions described below.

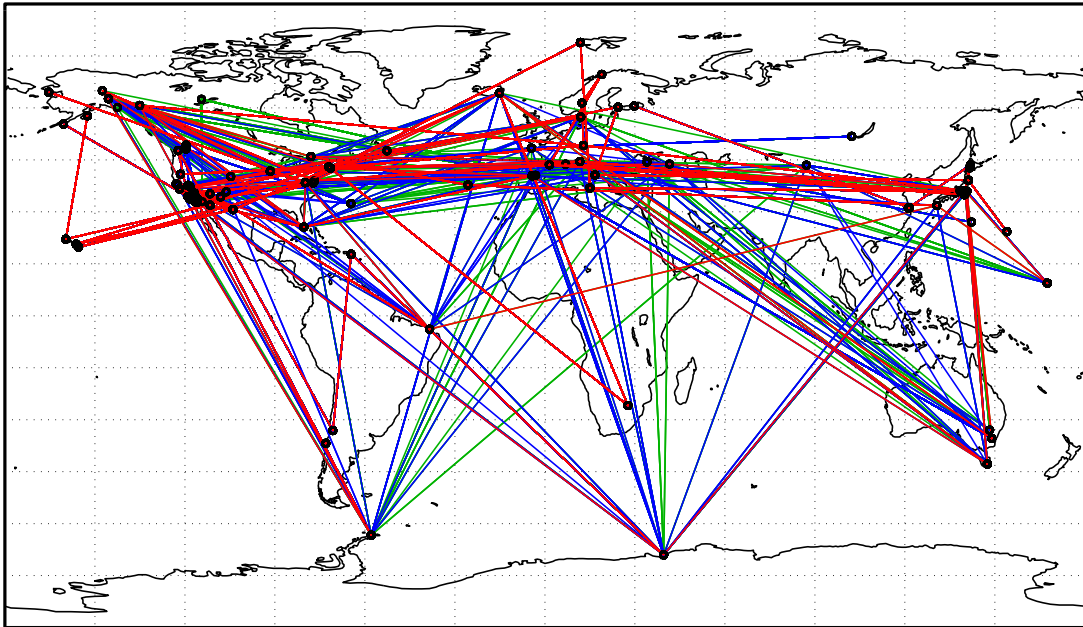


Figure 4.6: Global map of processed baselines (1984–2009). Baselines were observed: less than 10 times (green), between 10 and 100 times (blue), more than 100 times (red).

4.3.1 OCCAM solution

Four different ERP time series, which are consulted for further interpretation in Chapter 6, were calculated using the OCCAM software. Two of these series were estimated with hourly resolution and differ most notably w.r.t. the treatment of nutation, but also concerning the un-

¹<http://vlbi.geod.uni-bonn.de/IVS-AC/data/exclude.txt>

derlying TRF. The IGG07R04 (quoted in Table 4.1) is a reference frame calculated at IGG in Vienna as a successor of the TRF solution described in Heinkelmann *et al.* (2006). At the time of the derivation of the first series the software was not yet capable of introducing a priori celestial pole offsets, therefore nutation had to be fixed to the values of the nutation model due to previously explained reasons. This series is disposed here only to demonstrate how retrograde diurnal polar motion is introduced undesirably when residuals to the nutation model are not properly taken into account. For the production of the second series the software was modified to enable the consideration of a priori celestial pole offsets. This functionality was exploited also for the derivation of the time series with longer estimation interval. A time series with six and a time series with five hours resolution was created with otherwise the same processing settings. The purpose was to test whether an interval which is not an integer divisor of 24 hours would be beneficial for the amplitude estimation.

In all cases tropospheric zenith delays and gradients and station clocks were estimated as auxiliary parameters. Zenith delays were modeled as continuous piecewise linear functions with one offset and hourly rates. Tropospheric gradients were determined in six-hour intervals. The clocks were likewise modeled with one offset and hourly rates plus one quadratic term per clock. For all VLBI solutions including the ones derived with VieVS the Vienna Mapping Functions 1 – VMF1 (Böhm *et al.*, 2006b) were used for tropospheric modeling and ocean loading was considered on the basis of FES2004 (Letellier, 2004).

Table 4.1 provides an overview of the ERP relevant processing settings of the four above-mentioned time series. The solution names are composed of the name of the software and a token ‘sp’ for short-period and ‘lp’ for long-period to indicate the purpose the series were created for.

Table 4.1: Characteristics of the OCCAM solutions.

Parameter setup	OCCAMsp1	OCCAMsp2	OCCAMlp1a	OCCAMlp1b
CRF	ICRF Extension 2			
TRF	IGG07R04	ITRF2005		
Prec./Nut.	IAU2000A			
A priori EOP	IERS C04 05			
$\delta X, \delta Y$	not est.	fixed to IERS C04 05		
x_p, y_p	1-h interval		6-h int.	5-h int.
dUT1	1-h interval		6-h int.	5-h int.
Observation period	1984–2007.5		1984–2009	

4.3.2 VieVS solution

By means of the newly developed software VieVS highly resolved ERP time series and a six-hourly dUT1 time series were generated consistently using the same data and processing settings as far as possible. Those two solutions are listed in Table 4.2 as VieVSsp1 and VieVSlp1. In contrast to OCCAM, where the coordinates were fixed to ITRF2005, the VieVS software allows to impose NNR/NT conditions on selected datum stations. This option was applied for the two solutions mentioned already relative to the coordinates of the VTRF2008 (Böckmann *et al.*, 2010). Another difference to the OCCAM solutions is the handling of the celestial pole offsets. In the very first solution OCCAMsp1 the celestial pole offsets were not estimated, i.e. nutation was fixed to the nutation model, while for OCCAMsp2 it was fixed to the model plus celestial pole offsets from the IERS C04 05 EOP series. Before estimating VieVSsp1 a preliminary solution was run to calculate celestial pole offsets, as explained in the main part of this section – termed option (3) there. These values were then interpolated and reintroduced as a priori information. In case of VieVSlp1 only dUT1 was estimated with subdiurnal resolution, for which reason polar motion and celestial pole offsets could be calculated simultaneously with daily spacing. A third, again highly resolved, ERP time series (VieVSsp2) was finally computed w.r.t. the in-house terrestrial reference frame solution of IGG, VieTRF10a (Krásná *et al.*, 2012).

Table 4.2: Characteristics of the VieVS solutions.

Parameter setup	VieVSsp1	VieVSsp2	VieVSlp1
CRF	ICRF2		
TRF	VTRF2008	VieTRF10a	VTRF2008
Prec./Nut.	IAU2006/2000A		
A priori EOP	IERS C04 05	IERS C04 08	IERS C04 05
$\delta X, \delta Y$	fixed to pre-solution		24-h int.
x_p, y_p	1-h interval		24-h int.
dUT1	1-h interval		6-h int.
Observation period	1984–2010.5	1984–2011	1984–2010.5

As for the auxiliary parameters, tropospheric delays were estimated as piecewise linear offsets with 30 minutes resolution, as well as gradients every six hours. Clocks were modeled as hourly piecewise linear offsets, one rate and one quadratic term per clock. Daily EOP were always set up with very tight constraints in order to receive a mean over the whole session, whereas subdaily Earth rotation parameters were endowed with loose constraints just to prevent a singularity in the normal equation matrix in intervals of sparse observations.

To give an impression of the results, the high-frequency parts of the ‘sp’ ERP time series of

OCCAM and VieVS including their formal errors are contrasted with the ocean tidal ERP model of the IERS Conventions (2010) in Figure 4.7 for three days of the special VLBI campaign CONT05. The solutions were corrected either a priori or a posteriori for the influence of the polar and spin libration according to IERS Conventions (2010). It is discernible in the plot that OCCAM and VieVS parameters are estimated for different epochs due to the two ways of parameter setup, expatiated in Section 4.2.2. This difference in parametrization also explains values with larger errorbars at the session borders visible in the VieVS solutions. The estimation times are set to integer hours in VieVS, so the first or last estimate eventually rests upon very few observations only. The single time series differ predominantly in polar motion. Most probably this discrepancy originates from the different treatment of nutation which can cause retrograde diurnal polar motion that shows up in the x_p and y_p time series.

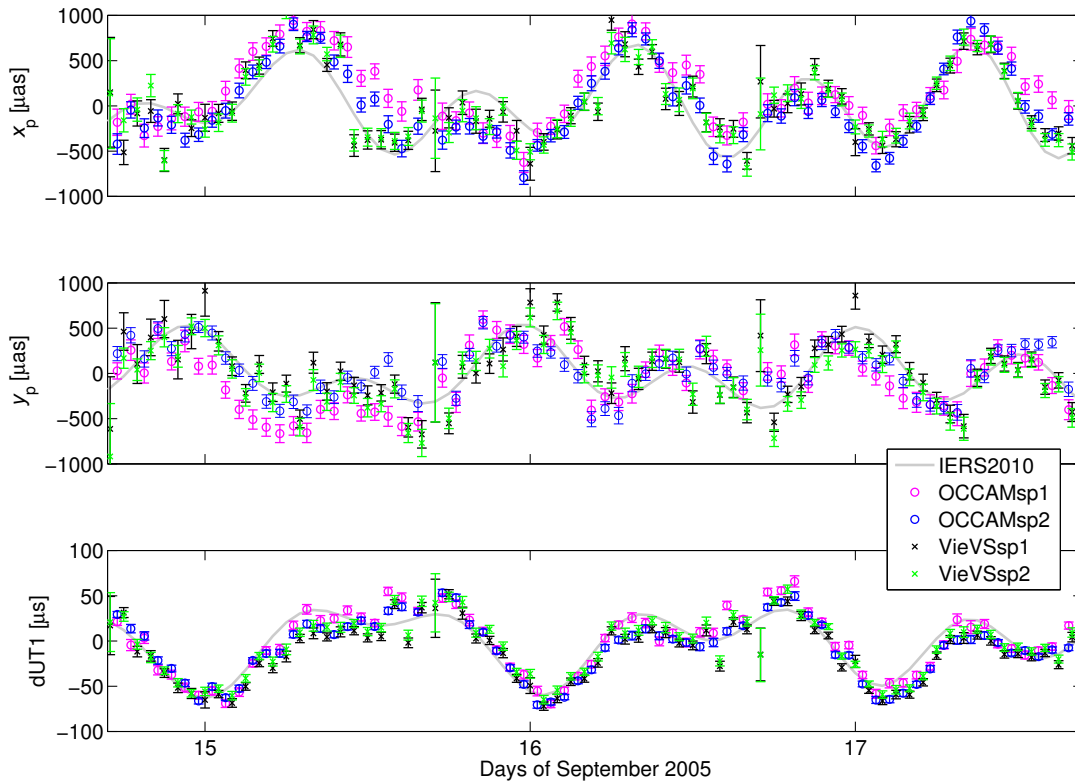


Figure 4.7: Comparison of the IERS2010 model for ocean tidal ERP variations with the high-frequency parts of the four different highly resolved ERP time series. Top: polar motion x_p , middle: polar motion y_p , bottom: dUT1.

4.4 Estimation of demodulated Earth rotation parameters

The so-called complex demodulation is a technique which transfers the spectral components of a high-frequency band to low frequencies, but retains the original amplitudes. In terms of

Earth rotation parameters this method allows to study subdaily phenomena with daily parameter spacing. Details about complex demodulation and its use for interpreting high-frequency geophysical excitation of Earth rotation are provided in Brzeziński (2012). The application to VLBI analysis is particularly explained in Böhm *et al.* (2011) and large parts of the section follow this publication. This approach can be either applied to time series or can be implemented already at the step of data processing. The idea of complex demodulation is the following: a time series is multiplied by the complex exponential $e^{-i\phi}$, where ϕ is the demodulation argument; the argument is time dependent and composed in linear form as $\phi = \Omega \cdot t + \text{const.}$, with the demodulation frequency Ω ; the derived demodulated time series is subsequently low-pass filtered or smoothed, respectively, to remove signal at or above the demodulation frequency Ω ; the procedure shifts the original spectral component at the center frequency Ω to infinity and its amplitude arises as an offset in the demodulated series; similarly, the original signal components close to the center frequency, σ_i , are mapped to low frequencies ($\sigma_i - \Omega$).

4.4.1 Alternative ERP parametrization

The features of the complex demodulation technique can be exploited for the estimation of diurnal and subdiurnal Earth rotation variations from VLBI with the coarse sampling of one day. The application of the method to VLBI analysis demands for a change of the Earth rotation parametrization. More precisely, the parametrization needs to be extended, as proposed originally by Herring & Dong (1994):

$$\begin{bmatrix} x_p(t) \\ y_p(t) \end{bmatrix} = \sum_{\substack{k=-K \\ k \neq -1}}^K \begin{bmatrix} x_k(t) \\ y_k(t) \end{bmatrix} \cos(k\phi(t)) + \begin{bmatrix} y_k(t) \\ -x_k(t) \end{bmatrix} \sin(k\phi(t)), \quad (4.10)$$

$$\text{dUT1}(t) = \sum_{k=0}^K u_k^c(t) \cos(k\phi(t)) + u_k^s(t) \sin(k\phi(t)). \quad (4.11)$$

In that way ERP are estimated already in demodulated form. The demodulation frequencies are integer multiples of the diurnal rotation frequency Ω . The diurnal rotation of the Earth can be conveniently expressed via Greenwich mean sidereal time (GMST), leading to a demodulation argument $\phi = \text{GMST} + \pi$. K is the number of frequency bands that are considered. The case $k = 0$ corresponds to the usual representation of polar motion and dUT1 and contains the low-frequency variations in this context. High-frequency polar motion is estimated separately for prograde and retrograde frequency bands. For $k = 1, 2, 3, \dots, K$ we obtain parameters representing the diurnal, semidiurnal, terdiurnal variations and so on. Theoretically, K can be chosen to an arbitrary integer number, but of course exceeding $K = 4$ is not very reasonable, as there are no geophysical excitation mechanisms acting on such short periods, which would be detectable by VLBI observation. In the experiments conducted for this thesis, K was limited to 4, the quarter-

diurnal band. The term $k = -1$ incorporates diurnal retrograde polar motion and is excluded in Equation (4.10), because from the point of view of mathematical formulation it would be exactly equivalent to estimating celestial pole offsets (Brzeziński & Capitaine, 1993).

The introduction of the alternative ERP parameters into the VLBI delay model is straightforward, anyhow it shall be outlined briefly. For the estimation of demodulated ERP parts of the software VieVS were modified in the frame of this work. Obviously the modifications are necessary already at the level of the design matrix setup, wherein the partial derivatives for polar motion and dUT1 ought to be adapted. Instead of one value per ERP quantity per epoch we now have to determine two parameters per quantity for each frequency band per epoch. Moreover, we can conclude from Equation (4.10) that the polar motion parameters x_k and y_k are both inherent in the x_p and in the y_p total polar motion components. The partial derivatives are therefore slightly more complicated than with the usual ERP representation (see Section 4.2.1). The polar motion matrix derivated e.g. for x_k reads

$$\frac{\partial \mathbf{W}}{\partial x_k} = \mathbf{R}_3(-s') \cdot \left[\frac{\partial \mathbf{R}_2(x_p)}{\partial x_p} \cdot \cos(k\phi) \cdot \mathbf{R}_1(y_p) + \mathbf{R}_2(x_p) \cdot \frac{\partial \mathbf{R}_1(y_p)}{\partial y_p} \cdot (-\sin(k\phi)) \right]. \quad (4.12)$$

The partials for the other demodulated parameters y_k , u_k^c and u_k^s can be derived likewise on the basis of Equations (4.5), (4.6), (4.10) and (4.11).

4.4.2 Processing and time series characteristics

In the preceding sections it is pointed out articulately that subdiurnal estimation of polar motion inhibits a parallel estimation of the celestial pole offsets. One clear advantage of the demodulation approach is the possibility to determine high-frequency ERP variations and celestial pole offsets at the same time. Since the high-frequency signal is mapped to low frequencies the variations are sufficiently represented using diurnal sampling. To underline this statement, the correlation matrix of the same session as in Figure 4.5, derived with the modified VieVS, is plotted in Figure 4.8. Despite of the simultaneous estimation of high-frequency polar motion components and celestial pole offsets there are no such systematic correlations present as in the left part of Figure 4.5. Some weak correlations are apparent, but these can be considered a result of the network configuration.

Demodulated Earth rotation parameters are at hand from three different processing runs, the settings of which are listed in Table 4.3 (the token ‘cd’ in the series names stands for complex demodulation). The first two solutions were derived on the basis of the same observation data as the standard ERP solution VieVSp1 described in the previous section. VieVScd1a and VieVScd1b are different only regarding the introduction of a priori high-frequency ERP models. For the generation of 1a no a priori model was applied, whereas in 1b the effects of ocean tides and libration are considered. This designed disparity was used to verify the correctness of the implementation and the approach in general, as discussed in detail in Böhm *et al.* (2011). Solution VieVScd2 corresponds to VieVSp2 in terms of observation data and other processing characteristics. One

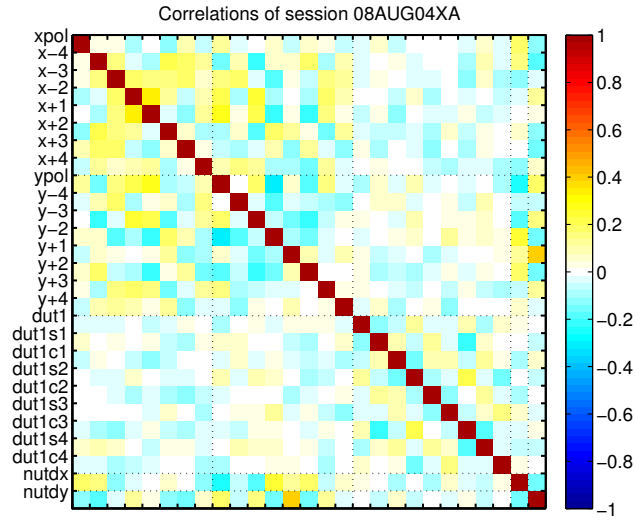


Figure 4.8: EOP correlation matrix for session 08AUG04XA with simultaneous estimation of daily demodulated ERP and daily celestial pole offsets.

commonality of all ‘cd’ series is that celestial pole offsets as well as demodulated ERP were estimated in 24-h intervals with very tight constraints. Because of the concept of piecewise linear offsets in VieVS this setup yields actually one mean value over the whole session. Consequently the estimates temporally refer to the mid of the session and not anymore to the integer hour epochs.

Figure 4.9 shows exemplarily demodulated dUT1 parameters of the solutions VieVScd1a and 1b for five years (2005–2010). The upper panel displays smoothed values of the in-phase component u_1^c and the lower panel contains the out-of-phase component u_1^s . The two series are juxtaposed here to visualize the functionality of the complex demodulation technique. Both exhibit the typical long-period variations inferred by the demodulation. VieVScd1a, plotted in gray, was calculated considering all high-frequency ERP models a priori, therefore the parameters represent only residual diurnal variations. For the processing of VieVScd1b, depicted in black, no such a priori model was applied and so the values represent the full signal that is seen by VLBI in the diurnal frequency band. As mentioned at the outset of the demodulation section, the amplitude of the spectral component which corresponds to the demodulation frequency appears as an offset in the demodulated time series. The demodulation frequency for the diurnal band is the diurnal rotation frequency and this is at the same time also the frequency of the K1 ocean tide. Since K1 is one of the largest terms in the spectrum its amplitude clearly shows up as an offset in the demodulated series, as illustrated in Figure 4.9.

The procedure for recovering harmonic signals from the demodulated Earth rotation parameters is demonstrated in Chapter 6.

Table 4.3: Characteristics of the demodulated ERP solutions.

Parameter setup	VieVScd1a	VieVScd1b	VieVScd2
CRF	ICRF2		
TRF	VTRF2008		VieTRF10a
Prec./Nut.	IAU2006/2000A		
A priori EOP	IERS C04 05		IERS C04 08
$\delta X, \delta Y$	24-h interval		
High-freq. ERP model	none	libration, ocean tides (IERS2010)	
x_k, y_k	24-h interval		
u_k^c, u_k^s	24-h interval		
Observation period	1984–2010.5		1984–2011

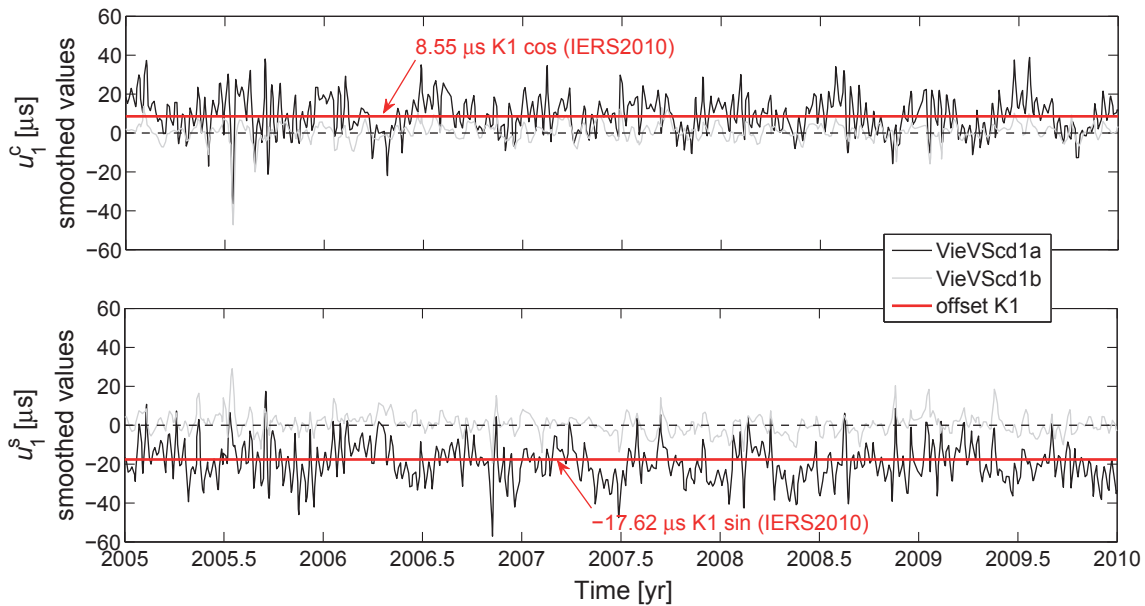


Figure 4.9: Smoothed demodulated diurnal dUT1 parameters u_k^c and u_k^s (2005–2010). The red lines show the magnitude of the cosine and sine terms of the K_1 tide (IERS2010), which show up as offsets in the black time series where no a priori high-frequency ERP model was applied.

4.5 Direct estimation of tidal ERP variations

To some extent the current section anticipates the explanations in Chapter 6 dealing with the determination of tidal variations from ERP observations. The whole present chapter describes how Earth rotation variations are observed by means of VLBI, but the subsequent treatment

of time series in order to derive harmonic coefficients of tidal signal is shifted to Chapter 6. However, in the direct approach the estimation of time series is skipped and the tidal amplitudes and phases are determined directly as part of the VLBI data analysis, hence it is treated in the analysis chapter. The implementation of this approach presumes the capability of the analysis software to run a global solution and implicates that partial derivatives of the parameters of interest have to be set up in the normal equation matrix of each single session solution. The public version of the VieVS global solution is qualified to estimate CRF, TRF and EOP. This version was extended for the estimation of short-period tidal terms in all ERP and for long-period tidal terms in dUT1. In the frame of this thesis only the implementation and the results for the short-period (subdaily) domain are treated further.

4.5.1 Formulation and partial derivatives

Tidal variations in Earth rotation are modeled as sum of sinusoidal functions. Instead of amplitudes and phases these are preferably expressed as in-phase and quadrature components, in order to provide linear equations for the least-squares adjustment. The frequency and phase reference for each tide i are represented by a tidal argument $\alpha_i(t)$ introduced in Section 3.1.2. In the field of Earth rotation it is common practice to build the angle argument using the Delaunay variables according to Equation (3.15). ERP variations at tidal periods for a number of N tides considered are then formulated as follows

$$\begin{aligned}\delta x_p(t) &= \sum_{i=1}^N -A_i^+ \cos(\alpha_i(t)) - A_i^- \cos(-\alpha_i(t)) + B_i^+ \sin(\alpha_i(t)) + B_i^- \sin(-\alpha_i(t)), \\ \delta y_p(t) &= \sum_{i=1}^N B_i^+ \cos(\alpha_i(t)) + B_i^- \cos(-\alpha_i(t)) + A_i^+ \sin(\alpha_i(t)) + A_i^- \sin(-\alpha_i(t)),\end{aligned}\tag{4.13}$$

$$\delta \text{UT1}(t) = \sum_{i=1}^N U_i^c \cos(\alpha_i(t)) + U_i^s \sin(\alpha_i(t)).\tag{4.14}$$

Polar motion is modeled as coherent two-dimensional process and therefore the tidally induced contributions δx_p and δy_p to polar motion are composed of prograde and retrograde coefficients A_i^+ , B_i^+ , A_i^- , B_i^- . Retrograde coefficients are associated with a retrograde angle argument that is opposite in sign to the prograde argument, this is indicated by a minus in the formulas (4.13). Tidal contributions to UT1 are represented by a cosine U_i^c and a sine U_i^s coefficient and are defined to be used with the prograde argument here.

Within the VLBI observation equation we now assume the ERP to be fragmented into a slowly varying part and high-frequency signals represented by harmonic functions as, e.g. for the x-component of polar motion $x_p(t) = x_{p0}(t) + \delta x_p(t)$. In practice the parameter setup for the ERP is kept as it is by default and the design matrix is extended for the partial derivatives of the

tidal coefficients. If we again resort to the example of polar motion, we can write the partial derivative, e.g. for the coefficient A_i^+ :

$$\frac{\partial W}{\partial A_i^+} = \mathbf{R}_3(-s') \cdot \left[\frac{\partial \mathbf{R}_2(x_p)}{\partial x_p} \cdot (-\cos(\alpha_i)) \cdot \mathbf{R}_1(y_p) + \mathbf{R}_2(x_p) \cdot \frac{\partial \mathbf{R}_1(y_p)}{\partial y_p} \cdot \sin(\alpha_i) \right]. \quad (4.15)$$

The partials for the remaining coefficients are constituted analogously.

It is certainly not reasonable to solve for these coefficients in a single session solution, by reason that the subdaily variations cannot be resolved with only 24 hours of observations. In the session-wise mode the parameters are solely set up and stored in normal equation systems. The normal equations covering an adequate time span are then accumulated in a global solution, wherein the tidal amplitudes can be estimated. The required length of the observation time depends of course on the periods, number and adjacency of the harmonic terms that shall be determined. With the objective to derive a constraint-free solution including major and minor tidal terms as well as their side bands the time period should span at least 18.6 years, as stated at the beginning of Section 4.3.

4.5.2 Processing and solution characteristics

There is only one set of directly estimated tidal ERP terms which are compared to the ensembles of terms derived with the other methods in Chapter 6. Regarding the processing settings this solution (denoted VieVSgs1 in the following) complies with the standard VieVSp2 and the demodulated VieVScd2 time series. The parameter setup is summarized in Table 4.4.

The ‘normal’ EOP were established with daily spacing and reduced session-wise in the global solution. That means offsets or trends to the smooth a priori EOP line (IERS C04) are absorbed to these daily values, which were also recovered later in a backwards solution. Similar to the demodulated series VieVScd2 all high-frequency ERP models were applied a priori, implicating that the estimated tidal terms are to be regarded as residuals to the a priori models. Simultaneously to the coefficients for 76 tidal frequencies, the station positions and velocities were estimated within the global solution using NNR/NNT conditions w.r.t. VieTRF10a.

Table 4.4: Characteristics of the VieVS global solution.

Parameter setup	VieVSgs1
CRF	ICRF2
TRF	VieTRF10a
Prec./Nut.	IAU2006/2000A
A priori EOP	IERS C04 08
$\delta X, \delta Y$	24-h int., reduced session-wise
High-freq. ERP model	libration, ocean tides (IERS2010)
x_p, y_p	24-h int., reduced session-wise
dUT1	24-h int., reduced session-wise
Observation period	1984–2011
A_i^+, B_i^+	33 semidiurnal, 43 diurnal
A_i^-, B_i^-	33 semidiurnal
U_i^c, U_i^s	33 semidiurnal, 43 diurnal

Chapter 5

Earth rotation variations from Global Navigation Satellite Systems

Global Navigation Satellite Systems are nowadays most important for the navigation of all kinds of vehicles on Earth and also for the tracking of other satellites in space. Owing to a globally distributed network of permanently observing stations, the GNSS contribute significantly to the realization of the terrestrial reference frame and provide fundamental input for the combined EOP series of the IERS. In contrast to VLBI, GNSS do not realize a space-fixed reference frame but are operating within a dynamical reference frame realized by the satellite orbits. The accuracy and estimability of GNSS derived parameters such as EOP is therefore bound to and limited by the quality of the orbit determination. Nutation offsets or universal time cannot be accessed directly by means of GNSS, nevertheless they are suited best for the precise estimation of polar motion due to the dense network of observing sites. Additionally, the derivatives of the inaccessible quantities, nutation rates and LOD, can be determined with high precision on short time scales. Yet, it should be noted that GNSS suffer from resonance and aliasing effects connected with the orbit repeat period and 24-h processing, which are particularly precarious when investigating periodic phenomena as the tides. Currently there are two GNSS relevant for Earth rotation observations, because they are operational with a sufficient number of satellites and worldwide tracking stations. The Global Positioning System (GPS) has the most significant impact due to the long observation record (more than 15 years) and the large number of active IGS (International GNSS Service) tracking stations (more than 350). In the last years also the Russian GLONASS (Globalnaja Nawigazionnaja Sputnikowaja Sistema) advanced to the full constellation and is continuously tracked by more than 150 receivers of the IGS network. The revolution period of the GPS satellites of 12 sidereal hours is in a deep 2:1 resonance with Earth rotation, bearing certain disadvantages for Earth rotation studies, especially regarding periods which are integer multiples of the orbital period. GLONASS satellites revolve the Earth in about 11.3 sidereal hours. A combined analysis of GPS and GLONASS should therefore mitigate the unfavorable resonance effects and be beneficial for the estimation of tidal terms in the tidal bands near the rotation frequency.

Just as for the VLBI technique a detailed description of the two GNSS, the functionality and the data analysis cannot be given in this thesis. The present chapter does only outline the principle, lists the basic influences and otherwise concentrates on the determination of Earth rotation parameters and the operational implementation. For more explicit information the interested reader is referred to standard literature, e.g. Seeber (2003) or Hofmann-Wellenhof *et al.* (2008).

GNSS is a microwave technique based on measuring signal travel time. Compared to VLBI, the measurement signal is emitted by artificial sources, frequency generators on board of the satellites. GPS and GLONASS satellites broadcast L-band signals which are located in the frequency range of 1.2–1.6 GHz. Basically, a frequency standard in the satellites and in the receiver both generate time tagged signals which are then correlated in the receiver to obtain the travel time and thus the distance between receiver and satellite. With respect to geometry, the observations to three satellites with known positions would be sufficient to accomplish a three-dimensional arc section in order to determine the receiver position. However, the receiver clocks are not perfectly synchronized with the system time. Consequently the measurement to at least a fourth satellite is required to estimate the clock error as unknown in addition to the three receiver coordinates. This principle of absolute positioning does not have high relevance for geodesy though.

GNSS transmit carrier phase signals of at least two different frequencies which are additionally modulated by special predefined codes. Geodetic receivers are in general able to track two or more frequencies and to process code as well as phase observations. For high-precision static geodetic applications, primarily the phase observations are used and analyzed in post-processing. In order to eliminate as many error sources as possible, relative positioning methods and linear combinations of the signals are employed. As mentioned before, details about GNSS analysis strategies will not be provided here, they can be found for example in the above stated publications or also in the user manual of the Bernese GNSS Software (Dach *et al.*, 2007).

5.1 Observation equation and error sources

The post-processing of GNSS data generally involves least-squares adjustment and/or Kalman filter procedures. Depending on the application, observation data of several stations and satellites are analyzed in a common adjustment using differential or zero-difference observations. The basic observables of GNSS are the code and carrier phase ranges. The undifferenced observation equation for a carrier phase measurement L_R^S from satellite S to receiver R can be written in metric units as

$$L_R^S(t_R) = \left| \mathbf{r}_R(t_R) - \mathbf{r}^S(t_R - \tau_R^S) \right| + c\delta t_R - c\delta t^S + \lambda \left(N_R^S + \alpha_R - \alpha^S \right) + \delta\rho_{\text{tro}} - \delta\rho_{\text{ion}} + \delta\rho_{\text{rel}} + \delta\rho_{\text{mul}} + \epsilon_R^S, \quad (5.1)$$

where all quantities refer to the signal reception time at the receiver, t_R . The vectors \mathbf{r}_R and \mathbf{r}^S contain the positions of the receiver at the time of reception t_R and of the satellite at the time of transmission, respectively. The norm of this difference vector is the geometrical distance between receiver and satellite and would correspond to the observed distance in case of error-free measurement conditions in vacuum. Under real conditions the signal is influenced by numerous effects which have to be accounted for in the observation equation inferring respective corrections.

The speed of light c multiplied by δt_R and δt^S represent the receiver and satellite clock corrections w.r.t. the GNSS system time in units of distance. The carrier phase observable provides only information about the phase shift which has to be completed by the integer number of full signal cycles between station and satellite, the so-called ambiguity N_R^S . Receiver and satellite specific phase biases are denoted α_R and α^S . These biases as well as the ambiguity parameters are multiplied by the carrier wavelength λ to transform them to range contributions.

When traveling through the atmosphere the GNSS signals are affected similar to the VLBI signals and have to be corrected for ionospheric $\delta\rho_{\text{ion}}$ and tropospheric $\delta\rho_{\text{tro}}$ effects. The first order ionospheric effects can be eliminated by means of two-frequency observations and forming appropriate linear combinations. The tropospheric delay needs to be modeled and, as for VLBI, the unpredictable wet part has to be estimated together with the other parameters within the adjustment.

Furthermore, a relativistic correction $\delta\rho_{\text{rel}}$ is necessary to account for the gravitational signal delay and consider a periodic variation of the satellite clock due to the eccentricity of the satellite orbits.

GNSS signals do not always arrive directly at the receiver but can be reflected from plane surfaces. Such signals of course do not carry the travel time information of the direct but of the deflected signal path, indicated here by a delay due to multipath, $\delta\rho_{\text{mul}}$. The quantity ϵ_R^S , finally, comprises unmodeled errors and measurement noise.

Since permanent GNSS stations are located on the Earth surface they are equally affected by deformation of the crust, such as Earth quakes, solid Earth tides, ocean loading and all other station dependent effects, already listed in Section 4.1. An additional fact that ought to be considered in GNSS analysis is the varying antenna phase center, i.e. the reference point, within the antenna on the ground and on board of the satellites. These phase center offsets and variations specific for each satellite and receiver antenna type have to be identified by calibration and are available from the IGS.

5.2 Determination of Earth orientation parameters

Determination or monitoring, respectively, of EOP by means of GNSS demands for a global network of permanent stations. Such a network of currently more than 350 sites tracking GPS and partly also GLONASS satellites is maintained by the IGS. Observation data as well as differ-

ent products (orbits, clocks, ERP, ...) are provided to the public free of charge at the IGS web portal (<http://igscb.jpl.nasa.gov>). The IGS network is tracking data continuously, but the observations are nevertheless binned to 24-h sessions and in a first step processed session-wise. The analysis of global GNSS networks is conveniently carried out using double-differences (differential observations between a pair of receivers and between a pair of satellites), because receiver and satellite clock errors are eliminated, yet more and more analysis centers and software packages already use zero-differences. In practice, the stations have to be thus connected by defining baselines. Analogous to VLBI analysis, the normal equations for the baselines can be collected and for instance adjusted in daily sessions. Thereby, station dependent parameters such as tropospheric delays are very often pre-eliminated and can be recovered, if necessary, in a backward solution. Station coordinates and ERP are estimated as global parameters. Optionally normal equations of seven days can be stacked and station coordinates and ERP are derived in more stable weekly solutions. As mentioned in Section 4.2.3 the geometry of the observation network is an important criterion for the quality of the derived Earth rotation parameters. GNSS is the most precise technique for the observation of polar motion owing to the rather widespread station distribution.

5.2.1 Partial derivatives and estimability of EOP

EOP are estimated in the frame of a common adjustment concurrently with other parameters, like station coordinates or satellite orbits. The transformation between terrestrial and celestial reference system and hence the EOP are inherent in the observation equation (5.1). In order to calculate the distance

$$\rho_R^S = \left| \mathbf{r}_R(t_R) - \mathbf{r}^S(t_R - \tau_R^S) \right|, \quad (5.2)$$

the positions of the receiver and the satellite have to be represented in the same reference system, as is usually not the case. The receiver positions are conventionally given in the TRF, while the satellite orbits are properly represented and interpolated in a space-fixed frame. If the CRS is chosen as the reference system of the observation equation, the station coordinates, originally given in the Earth-fixed system have to be transformed to the CRF according to Equation (2.2). Application to Equation (5.2) gives

$$\rho_R^S = \left| \mathbf{Q}(t_R) \cdot \mathbf{R}(t_R) \cdot \mathbf{W}(t_R) \cdot \mathbf{r}_{R,TRF}(t_R) - \mathbf{r}^S(t_R - \tau_R^S) \right|. \quad (5.3)$$

Setting up the design matrix requires the partial derivatives of the phase observation L_R^S w.r.t. the EOP. It is sufficient to take a closer look at the range term ρ_R^S , because the other correction terms of Equation (5.1) can be neglected for the calculation of the partials. Applying the chain

rule gives for example for x_p

$$\frac{\partial L_R^S}{\partial x_p} = \frac{\partial \rho_R^S}{\partial \mathbf{r}_{R,CRF}} \cdot \frac{\partial \mathbf{r}_{R,CRF}}{\partial x_p} . \quad (5.4)$$

The first partial on the right hand side yields the unit vector from the station to the satellite

$$\frac{\partial \rho_R^S}{\partial \mathbf{r}_{R,CRF}} = \frac{\mathbf{r}_{R,CRF}(t_R) - \mathbf{r}^S(t_R - \tau_R^S)}{\rho_R^S} = -\mathbf{e}_{R,CRF}^S . \quad (5.5)$$

Similar to Equation (4.5) the derivative of the receiver vector w.r.t. x_p reads

$$\frac{\partial \mathbf{r}_{R,CRF}}{\partial x_p} = \mathbf{Q} \cdot \mathbf{R} \cdot \mathbf{R}_3(-s') \cdot \frac{\partial \mathbf{R}_2(x_p)}{\partial x_p} \cdot \mathbf{R}_1(y_p) \cdot \mathbf{r}_{R,TRF} . \quad (5.6)$$

The partial derivatives for the other EOP could be deduced analogously. However, as mentioned in the introduction to this chapter, nutation offsets and dUT1 are not directly accessible with satellite techniques. The reason is an almost one-to-one correspondence between changes in the orbital elements of the satellites on one hand and the nutation angles and dUT1 on the other hand. Rothacher *et al.* (1999) published the relations visualizing that fact on the fundament of the equinox based transformation (see Section 2.1.3) with the nutation angles in obliquity $\delta\epsilon$ and longitude $\delta\psi$:

$$\Delta(\text{dUT1}) = -(\Delta\Omega + \cos i \cdot \Delta u_0) / \varrho , \quad (5.7)$$

$$\Delta\delta\epsilon = \cos\Omega \cdot \Delta i + \sin i \sin\Omega \cdot \Delta u_0 , \quad (5.8)$$

$$\Delta\delta\psi \cdot \sin\epsilon_0 = -\sin\Omega \cdot \Delta i + \sin i \cos\Omega \cdot \Delta u_0 \quad (5.9)$$

with

- Ω ... Right ascension of the ascending node of the satellite orbit
- i ... Inclination of the orbit w.r.t. the equator
- u ... Argument of latitude of the satellite
- u_0 ... u at the osculation epoch of the orbital elements
- ϵ_0 ... Mean obliquity of the ecliptic
- ϱ ... Ratio universal time to sidereal time ($\varrho \approx 1.0027379$)
- Δ ... Change of the respective quantity.

Equations (5.7)–(5.9) show that changes in universal time and changes in the nutation angles are directly linked to offsets of the orbital elements of the satellites. Hence dUT1, nutation offsets and satellite orbits may not be estimated simultaneously. Then again, it is possible to estimate the rates of dUT1 and nutation instead if the variations of the orbital elements can be adequately modeled. Nevertheless the estimated rates will have to be tied to some initial value determined by another technique, such as VLBI.

In terms of a priori EOP information the explanations given in Section 4.2.1 for VLBI are equally valid for GNSS processing, except that introducing polar and spin libration as a priori models was not possible in the version of the Bernese GNSS Software, which was used in the frame of this work. Moreover, instead of the IERS C04 series, the final ERP series of the Center for Orbit Determination in Europe (CODE) were employed consistently with the corresponding orbits.

5.2.2 Datum definition and correlation issues

In contrast to VLBI analysis, the correlation between the EOP and the station coordinates is not really an issue in processing a global GNSS network. Because of the more homogeneous and much denser allocation of the observation sites there is no such strong effect of the network geometry. Yet, the large extension of the network with partially very long baselines that have to be formed to bridge the oceans gives rise to a GNSS specific matter: the percentage of resolvable ambiguities decreases significantly with the length of the baseline. There is no real solution to this problem, it can be mitigated only by choosing the ambiguity resolution strategy with regard to the baseline length.

Concerning the datum definition, the options are the same as for VLBI analysis. All or a certain number of station coordinates can be fixed to the a priori values at the epoch or, more common, NNR conditions are imposed on the coordinates of selected datum stations. The counterpart to estimating the source coordinates, the satellite orbit determination opens up a very broad field of study going far beyond the scope of this thesis. So all GNSS calculations were performed taking the high-quality final orbits of the IGS analysis center CODE as a reference.

5.3 Estimation of Earth rotation parameters using Bernese Software

At the beginning of this section it is indicated to note that the ERP variations computed from GNSS in the frame of the present thesis cannot compete with the VLBI related findings in terms of observation length and diversity of approaches. The reason is very simple: processing of a global GNSS network is a huge effort, involving an immense number of observations, which can be handled by standard processors only for a limited time period. A re-processing of all available global data, which can be done in case of VLBI on a single PC within a few days, requires several weeks of computing time on a PC cluster, although the usable observations start only in 1994. The second re-processing of the full history of GPS data collected by the IGS global network is currently under way as a common effort of all IGS analysis centers. However, subdaily ERP will again not be among the public products resulting from this reanalysis.

By means of the Bernese GNSS Software Version 5.0 (Dach *et al.*, 2007) two separate processing campaigns were run. The first campaign spans the years 2005 and 2006 and involves only GPS observation data. The second campaign should serve to evaluate the contribution of GLONASS data and is not directly proximate to the first campaign, because the modernization

and upgrading of the GLONASS system started to become effective not until 2008. Since ERP were estimated once from GPS only and once from combined GPS+GLONASS data, this campaign necessitated almost the double processing effort, so the length of the time series is limited to 32 weeks of 2008. The station network, baselines and basic processing strategy employed for the two campaigns are outlined in the following sections. All parameter estimation was conducted on the basis of double-difference phase observations, code observations were used only for preprocessing and to some extent for ambiguity resolution.

5.3.1 GPS-only campaign (2005–2007)

The final ERP time series established within this campaign emerge from a kind of evolutionary process, in the course of which the processing network and settings were adapted and refined several times. In general, the time series were computed from the GPS observations of a subset of the IGS global tracking network. In the first attempts the processing network consisted of 80 carefully chosen, fairly stable stations which belonged to the IGB00 reference frame. The IGB00 reference frame is the IGS realization of ITRF2000. Later on, when the new ITRF2005 was adopted by the international community also the used processing network was adapted to the IGS version of the ITRF2005, which is called IGS05. The second operated processing network consists of 113 stations, belonging to IGS05. The latter was finally defined to be the effective one in the frame of this campaign. The network, including the used standard baseline configuration is shown in Figure 5.1. The red lines designate baselines up to 2000 km, which are accented here, because the ambiguity resolution is working best for baselines up to this length. Nevertheless it was necessary to incorporate also baselines exceeding 2000 km in order to form a worldwide network. For the second campaign, to be described in the next section, the ambiguity resolution strategy was actually chosen depending on the baseline length as a further refinement of the analysis.

The principal parameters of interest are the pole coordinates and LOD, which were estimated hourly for the study of short-period variations and every 6 hours for the investigation of long-period variations. The ERP were set up as continuous piecewise linear functions and were solved in weekly solutions. In Bernese Software the ERP are computed by default with respect to a subdaily ERP model for ocean tide effects. For this work the model recommended in the IERS Conventions (2003) was selected. The CODE final orbits were taken as orbit information and held fixed in the least-squares adjustment. For reasons of consistency, also the a priori ERP information of CODE was selected. The geodetic datum definition uses a minimum constraint solution, imposing a NNR condition on the station coordinates of the respective reference frame. In terms of currentness the so-called second order ionospheric correction (Kedar *et al.*, 2003) was implemented and all calculations were performed using absolute antenna phase center corrections. Site displacements due to ocean loading were taken into account with the FES2004 (Letellier, 2004) model and nutation was modeled using IAU2000A. The employed release of Bernese software was not ready to be used with VMF1, hence the provided Niell Mapping Func-

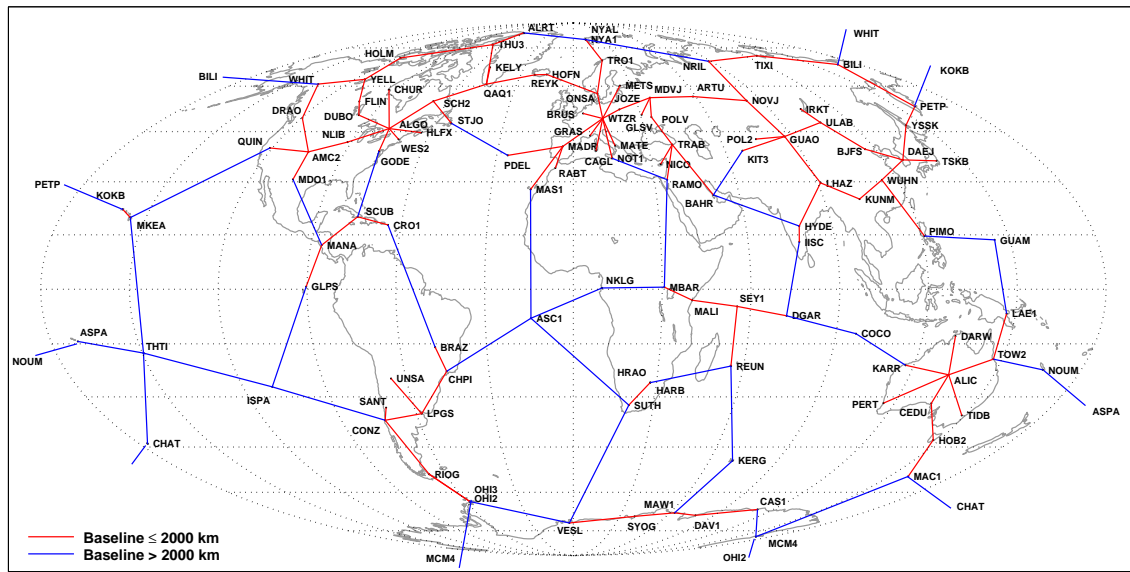


Figure 5.1: Network configuration, GPS-only campaign.

tion (Niell, 1996) was chosen instead. Troposphere parameters were estimated as piecewise linear functions, in 2-h intervals, complemented by troposphere gradients every 24 hours.

In the first instance four continuous ERP series covering only the year 2005 were generated with different solution strategies. Series A was estimated using the first network configuration and IGB00 reference frame. Series B0 was computed using the second network configuration (Figure 5.1) and IGS05. For series B1 the same geodetic datum definition as for series B0 was used, but a global ionospheric model (GIM) was introduced into the processing to enhance ambiguity resolution. The fourth series referred to as B2 is based on series B1, taking additionally into account the second order ionospheric correction (2IC).

The Figures 5.2 and 5.3 show the polar motion and LOD biases between comparable series. It is clearly visible that the largest differences arise from the reference frame switching (top diagram), where the average absolute deviation is 100 μ s in case of polar motion and 30 μ s in case of LOD. The introduction of the global ionosphere model still has an impact on the ERP estimation, as can be seen in the middle diagram, but the average absolute difference is only 35 μ s for polar motion and 10 μ s for LOD. The influence of the second order ionospheric correction reaches only 10 μ s in terms of polar motion and 1 μ s in terms of LOD on average (bottom diagram). The solution strategy for series B2, with the GIM and the second order ionospheric correction introduced, was adopted as the final one, because it satisfied best the state of knowledge. Two series using that processing strategy, one with hourly ERP and one with 6-h spacing, were then extended also to the full year 2006. For later comparisons these series are labeled GNSSsp1 and GNSSlp1, similar to the VLBI solutions.

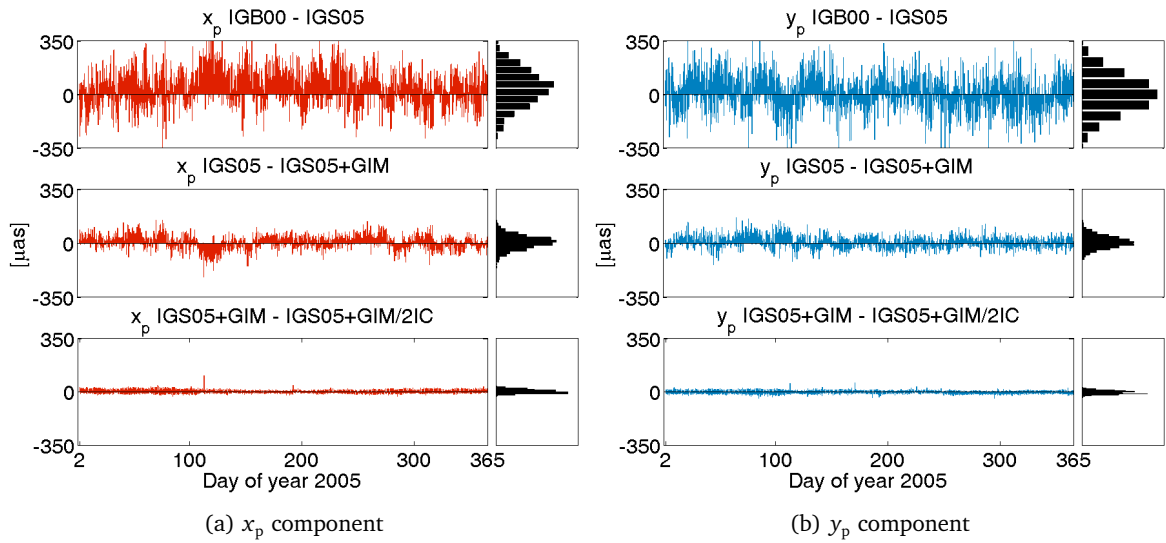


Figure 5.2: Polar motion biases between different GPS solutions. IGB00: station network of IGB00 reference frame, IGS05: station network of IGS05 reference frame, IGS05+GIM: IGS05 + use of global ionospheric maps (GIM), IGS05+GIM/2IC: IGS05+GIM + application of second order ionospheric correction.

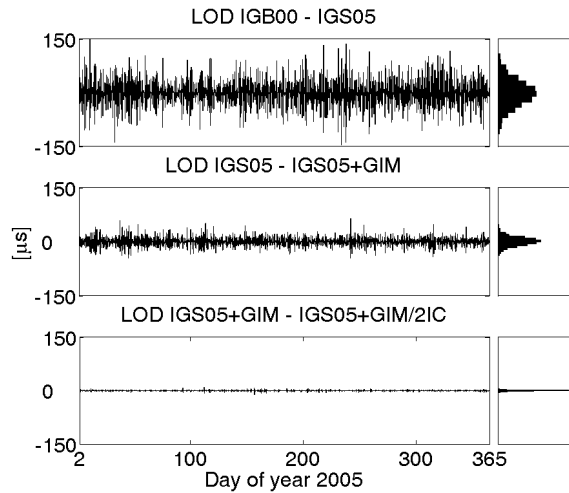


Figure 5.3: LOD biases between different GPS solutions. IGB00: station network of IGB00 reference frame, IGS05: station network of IGS05 reference frame, IGS05+GIM: IGS05 + use of global ionospheric maps (GIM), IGS05+GIM/2IC: IGS05+GIM + application of second order ionospheric correction. Note: the LOD units refer to the nominal day.

5.3.2 GPS+GLONASS campaign (2008–2008.6)

Combining GPS and GLONASS observations has great potential in particular for the investigation of diurnal and subdiurnal tides. As mentioned before, the GLONASS orbits do not exhibit the disadvantageous resonance with Earth rotation of the GPS satellites. Inclusion of GLONASS data to a combined GNSS solution is therefore supposed to diminish possible negative effects of this

resonance on the determination of the tidal terms at or around one sidereal day. The relations of the GNSS orbit periods with the main terms (Q_1 , O_1 , P_1 , K_1) of the diurnal tidal polar motion spectrum are illustrated in Figure 5.4. Apparently the twofold orbit repeat period of GLONASS is rather far apart from any prominent tidal constituent. The same holds for the, however not yet operable, European GALILEO system of which the revolution period is also integrated in the spectrum.

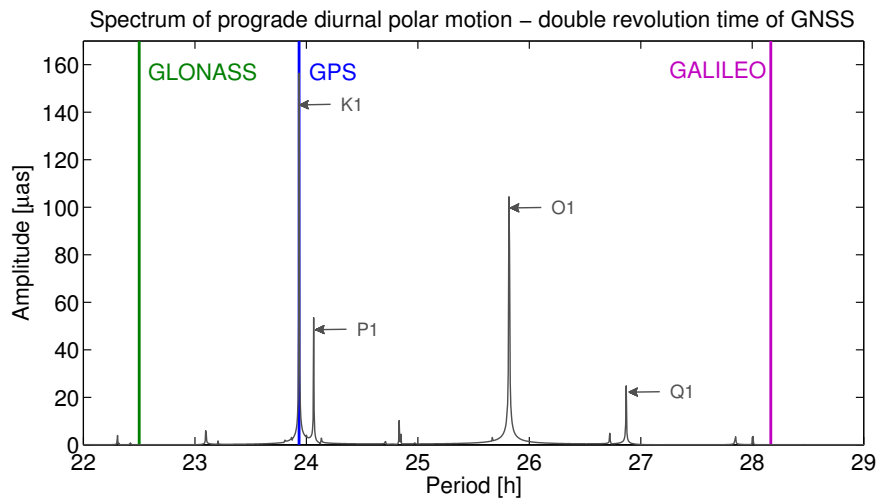


Figure 5.4: Spectrum of prograde diurnal polar motion compared to the double revolution time of different GNSS.

The primary intention of this second GNSS campaign was to test the capacity of the GPS+GLONASS combination with respect to the estimation of high-frequency Earth rotation variations. In the beginning of 2008 the GLONASS constellation comprised already 16 operational satellites and more than 50 stations of the IGS network were equipped with GPS and GLONASS receivers. Yet, the majority of those receivers was located in Europe.

All globally distributed GPS+GLONASS tracking stations of acceptable quality were integrated to the original processing network (Figure 5.1) and it was additionally supplemented with GLONASS baselines. The combined network configuration is presented in Figure 5.5, with GPS-only stations and baselines displayed in blue and those combining GPS and GLONASS shown in green. The network consists of around 120 sites in total, of which around one fourth are capable of observing GLONASS satellites as well.

In the course of the network rearrangement also the processing strategy was amended in two aspects. First the choice of the ambiguity resolution method was adapted to the length of the respective baseline. Up to a baseline length of 2000 km the so-called QIF (Quasi Ionosphere-Free) algorithm was applied, which allows to directly resolve L_1 and L_2 ambiguities making use of the ionosphere-free linear combination concept. Longer baselines were processed deploying the wide-lane technique based on the Melbourne-Wübbena linear combination and involving also the code observations. Further information on these ambiguity resolution approaches and

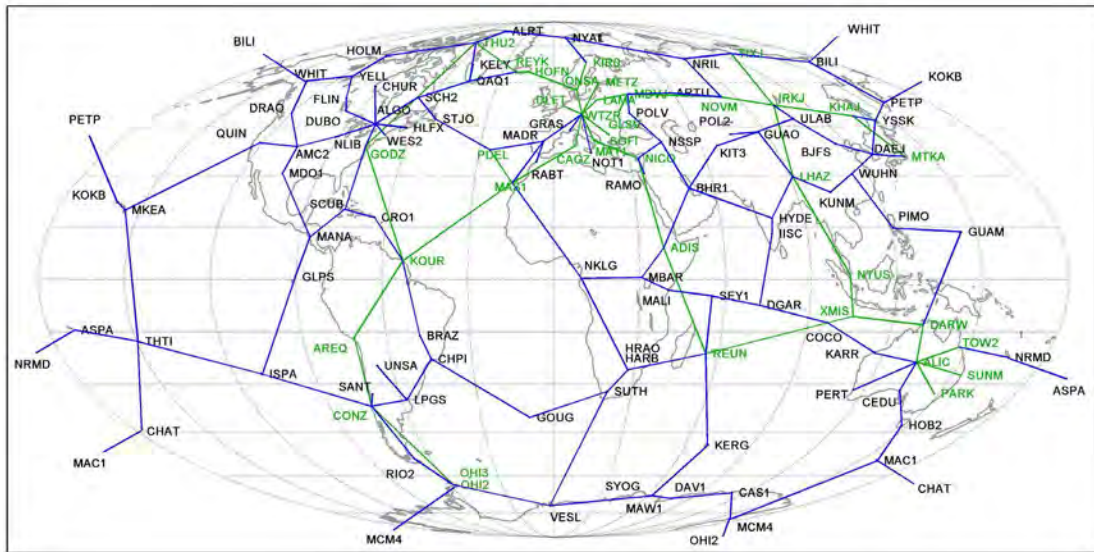


Figure 5.5: Network configuration, GPS+GLONASS campaign. Blue: GPS-only, green: GPS+GLONASS.

corresponding literature are given in Dach *et al.* (2007).

The second improvement regards the estimation of troposphere parameters and in that especially the mapping functions. In order to become more consistent with the VLBI processing, the Global Mapping Function (GMF: Böhm *et al.*, 2006a) was implemented into Bernese GNSS Software. GMF is an empirical mapping function based on the same numerical weather model data as VMF1. Comparisons with radiosonde data and the application in GPS and VLBI analysis have proven VMF1 to be the most accurate mapping function that is currently available globally for the whole history of VLBI and GPS observations (Böhm *et al.*, 2008). According to Böhm *et al.* (2008) it is recommended to use GMF, rather than NMF (Niell Mapping Function), since it is consistent with VMF1 and, in contrast to the latter, it can be implemented to the analysis programs quite effortlessly. Figure 5.6 shows the coordinate differences appearing in the station network at an exemplary day, 2nd of January 2008, when GMF is applied instead of NMF. Horizontal changes are in the range of a few millimeters, while changes of the station height can reach more than one centimeter at stations in the Antarctica. The latter ones cannot be clearly discerned in the figure, because the colorbar was fixed to ± 7 mm.

Other ‘virtual’ station motions are observed when weekly coordinate solutions from GPS-only to GPS+GLONASS scenarios are compared, as plotted for GPS-week 1460 (first GPS-week of January 2008) in Figure 5.7. In this case the height seems to be less affected, but horizontal changes with some systematic character are noticed. Although the coordinate shifts are small they are expected to map to the Earth rotation parameters via the NNR condition imposed on the TRF. ERP were estimated within this campaign exclusively in hourly intervals to conduce to the investigation of the high-frequency effects. The treatment of auxiliary parameters and the

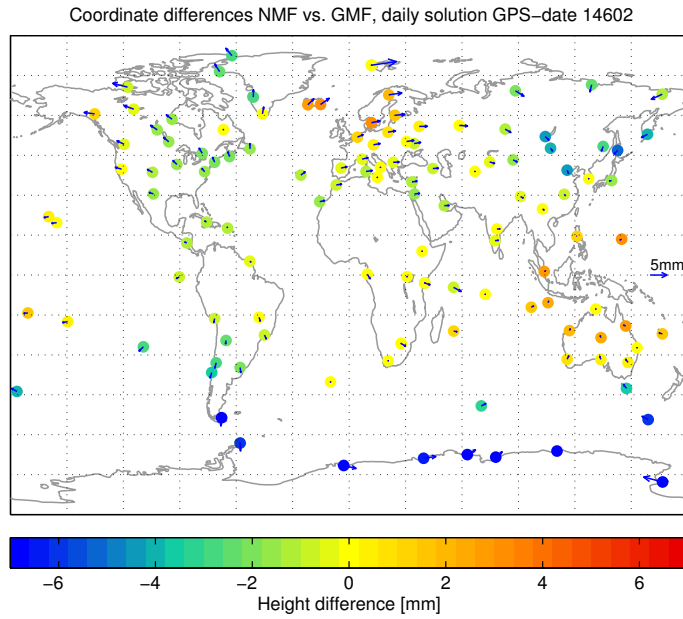


Figure 5.6: Differences in station coordinates when using GMF instead of NMF for GPS-only processing (daily solution for 2nd of January 2008). Horizontal changes are indicated by arrows; vertical changes are color-coded according to the given colorbar.

selection of basic models are equivalent to the previous campaign.

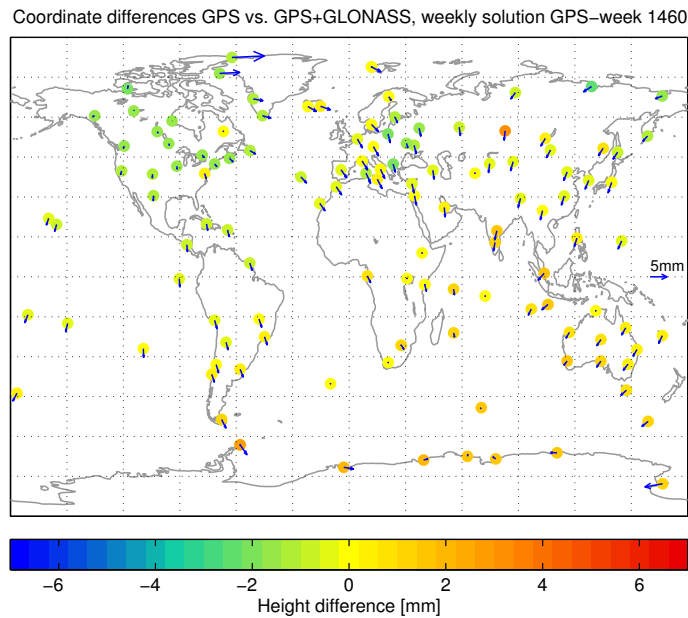


Figure 5.7: Differences in station coordinates for a GPS-only compared to a GPS+GLONASS scenario (weekly solution for GPS-week 1460). Horizontal changes are indicated by arrows; vertical changes are color-coded according to the given colorbar.

The resulting ERP differences between the GPS-only and the combined GPS+GLONASS solution are shown in Figure 5.8 for the whole observation period of the campaign. For polar motion the deviations are largely within a level of $\pm 100 \mu\text{s}$. LOD differences are inside a range of $\pm 150 \mu\text{s}$. Interestingly the combined solution appears to have larger impact on LOD estimation than on the polar motion estimates. However, there is no obvious reason for this discrepancy to be stated here, as this issue was not further investigated in the frame of this work.

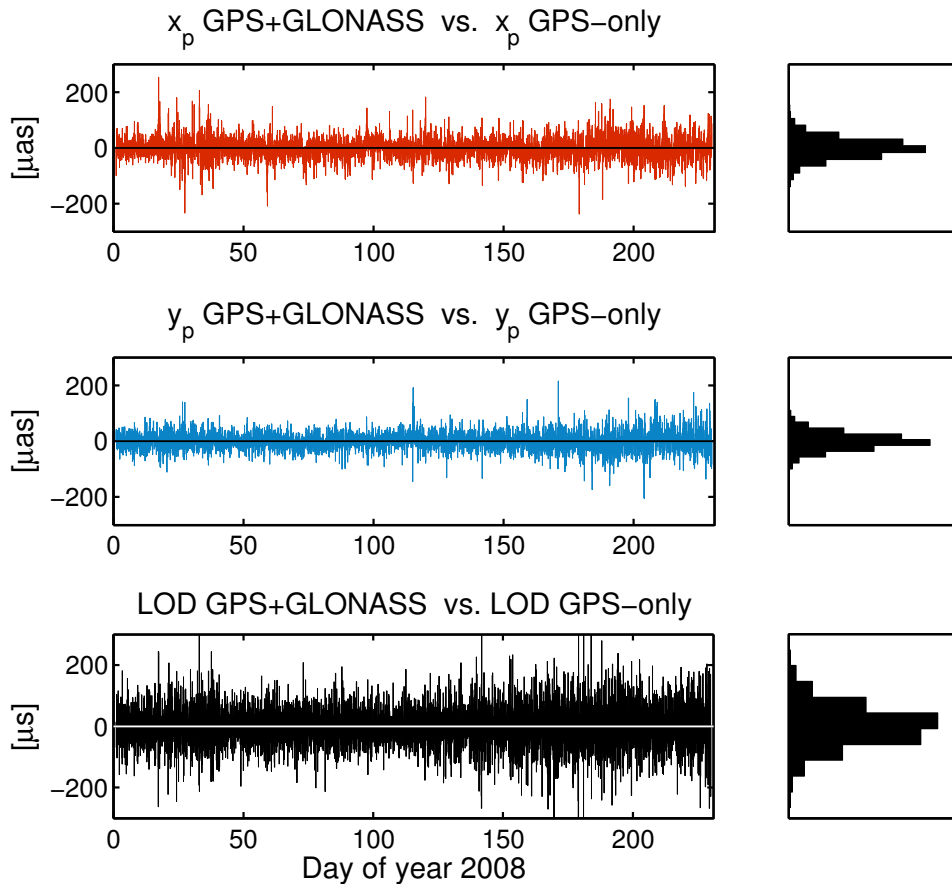


Figure 5.8: Differences in polar motion and LOD from the GPS-only compared to the GPS+GLONASS solution. Note: the LOD units refer to the nominal day.

A basic fact that should be mentioned concerning the combined approach is that the ambiguity resolution is problematic for the mixed baselines and the percentage of resolved ambiguities tends to decrease compared to the GPS stand-alone solution. Besides coordinate changes and ERP differences also the coordinate repeatabilities were examined and compared for the weekly solutions. In both approaches the coordinate repeatability is at the 2 mm level for the horizontal coordinates and at the 6 mm level for height. The differences between the repeatability RMS are at the sub-mm level only. For the horizontal components the joint approach shows generally larger repeatabilities, whereas it slightly tends to improve the height repeatabilities.

Anyhow, it should be noted in this context that the number of GLONASS observations added by the combined solution is only 7% of the total number of observation data and this is probably too small to impact the coordinate solutions essentially. That applies unfortunately as well for the determination of the subdaily tidal ERP variations, as is pointed out in the next chapter.

Table 5.1 summarizes all GPS and GNSS solutions, which are described in the present and the foregoing section.

Table 5.1: Characteristics of the GNSS solutions.

Parameter setup	GNSSlp1	GNSSsp1	GNSSsp2a	GNSSsp2b
Orbits	GPS CODE			GPS/GLONASS CODE
TRF	IGS05			
Prec./Nut.	IAU2000A			
A priori ERP	CODE			
$\delta X, \delta Y$	rates set up in 24-h int. (practically constrained to zero)			
x_p, y_p	6-h int.	1-h interval		
LOD	6 h int.	1-h interval		
Observation period	2005–2007		2008–2008.6	

Chapter 6

Modeled and observed tidal Earth rotation variations

The previous three chapters dealt with modeling of Earth rotation variations from geophysical information and its observation by means of VLBI and GNSS. This chapter strives to bring these two aspects together on the one hand and to confront them on the other hand. High-frequency and low-frequency tidal phenomena are thereby treated separately. Before the actual comparisons, the procedure to recover tidal amplitudes from ERP time series is examined for each frequency band with regard to the formalism as well as to signal preprocessing. Furthermore, a brief excursus on the determination of the zonal response coefficient is given and resulting Earth rotation variations calculated from recent ocean tide models are presented.

6.1 Time series analysis – recovery of harmonic signals

Given that tidal signals are harmonic oscillations they are appropriately investigated in the frequency domain. The transfer from time series to amplitudes and phases is accomplished predominantly by fitting sinusoidal functions to the observed variations within a least-squares adjustment. The choice of this method is mainly motivated by the fact that it is insensitive to gaps in the time series and irregular sampling. Since the majority of time series that are examined here originate from VLBI analysis this is a non-negligible issue. Aside from unequal spacing also the nature of the tidal variations which occur at well known periods suggests the application of adjustment algorithms.

Least-squares techniques are most effective and robust if the functional model properly matches the data and large outliers are eliminated before the adjustment. The derived ERP series, however, contain the full signal content (apportioned in Sections 2.3.1 and 2.3.2) and usually the import of several bad estimates cannot be avoided right within the analysis. Hence the original parameters need to be reduced to the variations of interest and screened for outliers. The first requirement does not apply for the amplitude estimation from demodulated ERP, because these are provided already split up to frequency bands.

If the examined observation period is not long enough to properly resolve side lobes to the main terms, special measures have to be taken to stabilize the adjustment. One option, proposed by Gipson (1996), is to constrain the side bands to the major terms using the ratio of the respective tidal potential amplitudes. This method is equally applicable in the short-period and in the long-period band. For diurnal and semidiurnal tides it is as well possible to employ the orthotide formalism introduced in Section 3.3.2 as an ocean tidal analysis technique. The application of this formalism for estimating tidal ERP variations is described in the last paragraph of the following section. The Hartmann & Wenzel (1995) tidal potential catalogue was used consistently throughout all applications in this work.

6.1.1 Short-period variations from highly resolved ERP

A prerequisite to harmonic signal estimation from highly resolved ERP time series is the removal of low-frequency variations inherent in the total ERP values. Especially in case of unequally spaced estimates it is straightforward to simply subtract interpolated values from smooth ERP series that do not contain subdaily variations. The selection of this smooth ERP line is actually secondary, however, for results to be compared at least the same line should be subtracted for the sake of consistency. The effect on the estimated variations is at any rate negligible. This statement was confirmed by a short test where the difference between dUT1 series reduced with the IERS C04 05 and with the IERS C04 08 was subjected to frequency analysis. The resulting amplitude spectrum shows the character of noise and is fairly below the level of $1 \mu\text{s}$ in the diurnal and subdiurnal period range. The IERS C04 05 were employed for the filtering of all high-resolution time series except for VieVSp2. This series is consistent with the direct solution VieVSp1 and the demodulated series VieVScd2 in all processing settings and these were calculated w.r.t. C04 08. Since the a priori ERP cannot be changed in post-processing in case of direct estimation and demodulated ERP, VieVSp2 is reduced as well using the C04 08 series.

Another potentially necessary preprocessing step is the harmonization of the time series concerning applied a priori high-frequency ERP models. For instance taking into account the effects of polar and spin libration was not possible in the GNSS analysis, therefore these models had to be applied to the ERP time series a posteriori.

The values obtained after reduction and screening ($\delta x_p, \delta y_p, \delta \text{UT1}$) finally serve as pseudo-observations in the least-squares adjustment. As a matter of fact, the equations to model tidal signals are presented already in Section 4.5.1. Nevertheless, a slightly different way of formulating the problem shall be given in this paragraph. This form of expression (Equation 6.1) is unconventional but it is well suited to directly visualize the relations between tidal coefficients of pro- and retrograde polar motion ($A_i^+, B_i^+, A_i^-, B_i^-$) and tidal coefficients of x_p and y_p (X^c, X^s, Y^c, Y^s). Equation (6.2) itemizes the reciprocal calculation.

$$\begin{aligned}\delta x_p(t) &= \sum_{i=1}^N \underbrace{(-A_i^+ - A_i^-)}_{X_i^c} \cos(\alpha_i(t)) + \underbrace{(B_i^+ - B_i^-)}_{X_i^s} \sin(\alpha_i(t)) , \\ \delta y_p(t) &= \sum_{i=1}^N \underbrace{(B_i^+ + B_i^-)}_{Y_i^c} \cos(\alpha_i(t)) + \underbrace{(A_i^+ - A_i^-)}_{Y_i^s} \sin(\alpha_i(t)) ,\end{aligned}\tag{6.1}$$

$$\begin{aligned}A_i^+ &= -\frac{1}{2} (X_i^c - Y_i^s) , & B_i^+ &= \frac{1}{2} (X_i^s + Y_i^c) , \\ A_i^- &= -\frac{1}{2} (X_i^c + Y_i^s) , & B_i^- &= -\frac{1}{2} (X_i^s - Y_i^c) .\end{aligned}\tag{6.2}$$

Instead of the observation equation for δUT1 , which is quoted already as Equation (4.14) in Section 4.5.1, the model for δLOD is provided here accompanied by the relations of LOD amplitudes (L_i^c, L_i^s) with UT1 amplitudes (U_i^c, U_i^s):

$$\delta\text{LOD}(t) = \sum_{i=1}^N L_i^c \cos(\alpha_i(t)) + L_i^s \sin(\alpha_i(t)) ,\tag{6.3}$$

$$U_i^c = \frac{L_i^s}{\sigma_i} \cdot \frac{1}{\text{LOD}_0} , \quad U_i^s = -\frac{L_i^c}{\sigma_i} \cdot \frac{1}{\text{LOD}_0} .\tag{6.4}$$

The notation is the same as used previously: N is the total number of considered periods, α_i is the angle argument of tide i , built according to Equation (3.15), σ_i is the corresponding angular frequency and LOD_0 denotes the nominal length of the day of 86400 s.

Estimating tidal ERP terms via orthoweights

As an alternative to a constrained solution the concept of the orthotide functions (Section 3.3.2) can be transferred to the estimation of Earth rotation variations. The advantage of this approach is the independence of the length of the observation time. The mechanism and the results are very similar to the adjustment of tidal terms with constraints, but less parameters need to be estimated and the introduction of constraints is dispensable. Instead of a sum of sinusoidal functions, the diurnal and semidiurnal variation of the respective Earth rotation parameter δERP is modeled as a sum of the orthotide functions P_ℓ^m and Q_ℓ^m provided in Equation (3.39). These are twelve functions (six diurnal, six semidiurnal) calculated from the tidal potential. In combination with twelve so-called orthoweights U_ℓ^m and V_ℓ^m they represent the variability of a tide-related quantity, with m being the order of the tidal potential and $\ell = 0, 1, 2$. The tidal variation of one ERP is represented as

$$\delta\text{ERP}(t) = \sum_{m=1}^2 \sum_{\ell=0}^2 [U_{\ell}^m P_{\ell}^m(t) + V_{\ell}^m Q_{\ell}^m(t)] . \quad (6.5)$$

Using Equation (6.5) as observation equation, the orthoweights are obtained by fitting the orthotide functions to the respective time series. In order to facilitate the comparison with the results from other approaches, the orthoweights can be very conveniently transformed to harmonic coefficients by means of the admittances, as explained in Section 3.3.2. The formal errors of these indirectly determined coefficients are assessed by applying error propagation.

6.1.2 Short-period variations from demodulated ERP

Demodulated ERP are already decomposed into frequency bands and contain only the information of the corresponding range. Hence diurnal prograde polar motion variations are retrieved from diurnal prograde demodulated polar motion parameters and so forth.

The resulting estimates from the VLBI analysis are daily values of demodulated prograde $x_{+k}(t), y_{+k}(t)$ and retrograde $x_{-k}(t), y_{-k}(t)$ polar motion and universal time $u_k^c(t), u_k^s(t)$ components for each frequency band ($k = 1, 2, 3, \dots$, is counted positive here). As stated already in Section 4.4, the demodulation procedure shifts the original frequencies $\pm\sigma_i$ to $\pm(\sigma_i - k\Omega)$, where Ω is the demodulation frequency. In terms of angle arguments tidal terms are thus estimated for $\pm(\alpha_i(t) - k\phi(t))$.

$$\begin{aligned} x_{+k}(t) &= \sum_{i=1}^{N_{+k}} -A_i^+ \cos(\alpha_i(t) - k\phi(t)) + B_i^+ \sin(\alpha_i(t) - k\phi(t)) , \\ y_{+k}(t) &= \sum_{i=1}^{N_{+k}} B_i^+ \cos(\alpha_i(t) - k\phi(t)) + A_i^+ \sin(\alpha_i(t) - k\phi(t)) , \end{aligned} \quad (6.6)$$

$$\begin{aligned} x_{-k}(t) &= \sum_{i=1}^{N_{-k}} -A_i^- \cos(-\alpha_i(t) + k\phi(t)) + B_i^- \sin(-\alpha_i(t) + k\phi(t)) , \\ y_{-k}(t) &= \sum_{i=1}^{N_{-k}} B_i^- \cos(-\alpha_i(t) + k\phi(t)) + A_i^- \sin(-\alpha_i(t) + k\phi(t)) , \end{aligned} \quad (6.7)$$

$$\begin{aligned} u_k^c(t) &= \sum_{i=1}^{N_k} U_i^c \cos(\alpha_i(t) - k\phi(t)) + U_i^s \sin(\alpha_i(t) - k\phi(t)) , \\ u_k^s(t) &= \sum_{i=1}^{N_k} U_i^s \cos(\alpha_i(t) - k\phi(t)) - U_i^c \sin(\alpha_i(t) - k\phi(t)) . \end{aligned} \quad (6.8)$$

Equations (6.6), (6.7) and (6.8) provide the functional model for the derivation of the harmonic coefficients from prograde and retrograde polar motion and universal time. $N_{\pm k}$ denotes the upper summation limit in the respective frequency band. Again retrograde arguments are represented with a minus to advert to the calculation with reversed signs. In the event of time series being too short, constraints can be imposed on the estimated terms just as for the highly resolved time series.

6.1.3 Zonal tidal variations from UT1 and LOD

Extracting zonal tidal terms from UT1 or LOD variations entails a more complicated and versatile preprocessing procedure than recovering high-frequency variations. The main reason is the presence of strong atmospheric fluctuations in the long-period range. These variations interfere with or inhibit the estimation of the zonal tidal terms, which are likewise residing in this frequency bands. Since the space geodetic techniques measure only the integral effect of all phenomena, the atmospheric excitation has to be modeled and removed using geophysical data. A smaller but still notable effect is expected from large-scale ocean circulation. Information about the geophysical fluids is provided in the form of angular momentum functions (AMF) by the Global Geophysical Fluids Center (GGFC) of the IERS. Unfortunately, the selected ocean angular momentum (OAM) data is available only from 1993 and thus does not cover the full period of VLBI observations. The benefit of reducing not only atmospheric angular momentum (AAM) but also OAM for the amplitude estimation can therefore be examined merely for the truncated time series. Figure 6.1 shows the general scheme of the signal preprocessing procedure, using the example of the UT1 case.



Figure 6.1: Signal preprocessing scheme for the calculation of zonal tidal variations from dUT1.

The first step is the re-application of the leap seconds to get a continuous time series. Before the second step, the upper limit for the periods to be estimated has to be decided on. Variations with periods exceeding this limit should then be filtered from the time series to facilitate the adjustment. Similar to the treatment of the high-frequency tidal terms, only the residual amplitudes are determined, so an a priori model is subtracted from the data. Finally, the excitation by geophysical fluids (at least AAM or AAM+OAM) needs to be considered. The resulting δUT1 values represent the pseudo-observations which are introduced to least-squares adjustment.

Preprocessing is as well necessary concerning the AMF, as it is illustrated using the example

of atmospheric AMF (AAMF) in Figure 6.2. At first the AAMF ought to be transferred to Earth rotation variations, according to Section 2.2.3. The difference from AAMF to LOD is actually only a proportionality factor, while the data has to be integrated to obtain UT1 excitation. The final atmospheric UT1 is then also filtered with the same cutoff frequency as the geodetic UT1 data to avoid the import of spurious signal when subtracting the AAM-based data. The preprocessing of OAM data for the reduction of dUT1 observations is completed accordingly. If the zonal tidal variations are to be determined from LOD observations the integration of the atmospheric or oceanic excitation is omitted. The consistent geophysical datasets employed throughout are EAMF from the NCEP/NCAR reanalysis (AAM) and EAMF (OAM) from ECCO kf080, provided by the GGFC. The provenience and attributes of the OAM dataset, ECCO kf080, are discussed in Gross (2008).

The longest time series, which are hence best suited for investigating long-period variations, are available from VLBI. VLBI directly delivers UT1, for which reason it appears appropriate to estimate the zonal tidal terms directly from the UT1 values. Yet the adjustment with UT1 series is especially sensitive to the presence of very low-frequency signal, which has to be filtered carefully in advance. It turned out that the determination of terms with periods above 35 days from preprocessed UT1 data is very instable and thus unreliable.



Figure 6.2: Signal preprocessing steps – AAMF.

Taking a look at the table of the major long-period terms (Table 3.3) reveals a rather big gap after the monthly solar term MSm . The next prominent tidal wave is the terannual Sta , followed by the dominant semiannual Ssa and the smaller but still significant annual Sa wave. By the length of the time series the estimation of constituents up to the annual period should be practicable. The inclusion of semiannual and annual term and the respective shifting of the filter cutoff frequency were examined stepwise. The cutoff was chosen with sufficient spacing to the largest estimated period, to avoid a damping of the last terms. To fit terms up to 35 days, the cutoff was taken to 48 days, for terms up to 220 days, the cutoff was 320 days and finally to fit the annual and some slightly longer periods, signal over 800 days was filtered.

In the past (e.g. Chao *et al.*, 1995) it was common practice to reduce low-frequency variations by subtracting fitted polynomials from the observed UT1 or LOD time series, which could eventually introduce unwanted artificial signal. As an alternative to that approach the UT1 time series were high-pass filtered with the desired cutoff using adapted filtering procedures to handle the unequal spacing of parameters stemming from VLBI analysis.

Concerning the integration of AAM-LOD to derive AAM-UT1 there are two options. In time domain the AAM-UT1 can be obtained by numerical integration. In frequency domain the simple relation between LOD and UT1 amplitudes (Equation 3.26) can be exploited. The results were found to be equivalent and numerical integration was subsequently applied because it is more

facile to realize. However, the integration of the atmospheric excitation is unfortunately problematic, in particular when longer periods are involved. It can be demonstrated that the coherence (correlation in frequency domain) between AAM-UT1 and UT1 with zonal tides removed changes for different filter cutoff. The upper panel of Figure 6.3 shows the magnitude squared coherence, while the lower panel displays the cross phase spectrum of the reduced UT1 and AAM-UT1 for the three tested cutoff periods.

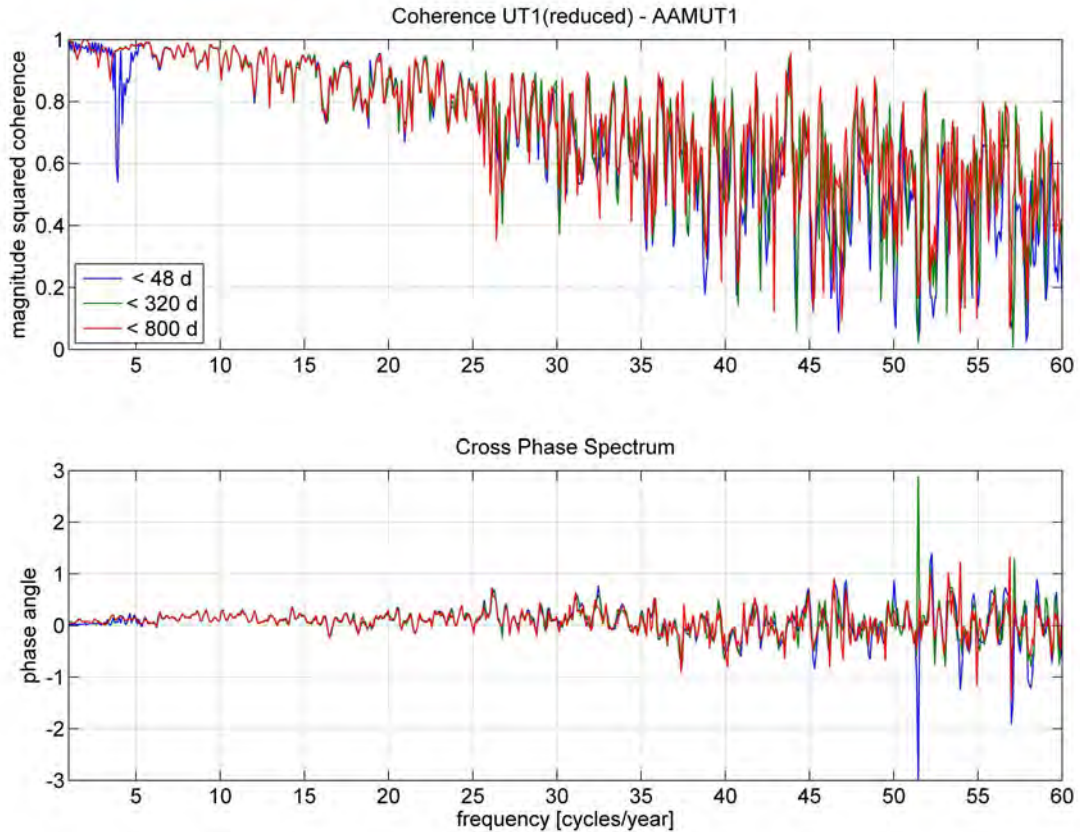


Figure 6.3: Magnitude squared coherence (top) and cross phase spectrum (bottom) between UT1 with zonal tides eliminated and AAM-UT1 for different filter cutoff periods, plotted against the frequency in cycles per year.

UT1(reduced) was calculated from the IERS C04 with the IERS2010 model for the zonal tides applied and the basis for AAM-UT1 were AAMF from the NCEP/NCAR reanalysis (Kalnay *et al.*, 1996; Salstein & Rosen, 1997). The fact that the coherence and cross phase spectrum of the two quantities are influenced by the filter boundary prompts the question whether the zonal tidal variations can be estimated reliably from observed UT1 series that are corrected by AAM-UT1. Again the C04 series were employed to investigate this issue. Zonal tidal variations are modeled, like the short period variations in UT1 or LOD, as sum of sine and cosine functions with the periods known from the tidal potential. Equations (4.14) and (6.3) are equally valid as observation equations for the adjustment of zonal tidal terms in UT1 and LOD. The only

difference is that the coefficient of $\text{GMST} + \pi$ is zero for the long-period tides and the angle argument $\alpha(t)$ consists therefore only of five components.

C04 UT1 and LOD series were preprocessed as described above and residual zonal tidal signal was estimated for the terms included in the respective model of the IERS Conventions (2010) as far as the selected filter cutoff permitted the estimation. Sets of residual coefficients (U_i^c, U_i^s) and (L_i^c, L_i^s) were determined for the three different cutoff periods. The UT1 results for scenarios with signal above 48 days and above 320 days filtered are contrasted in Figure 6.4 for the tidal terms up to 35 days. A term called *zero* is always included in the estimation as an independent measure of the noise level and accuracy. It is chosen at a period (16.63 days) where no or at least very little tidal signal is expected.

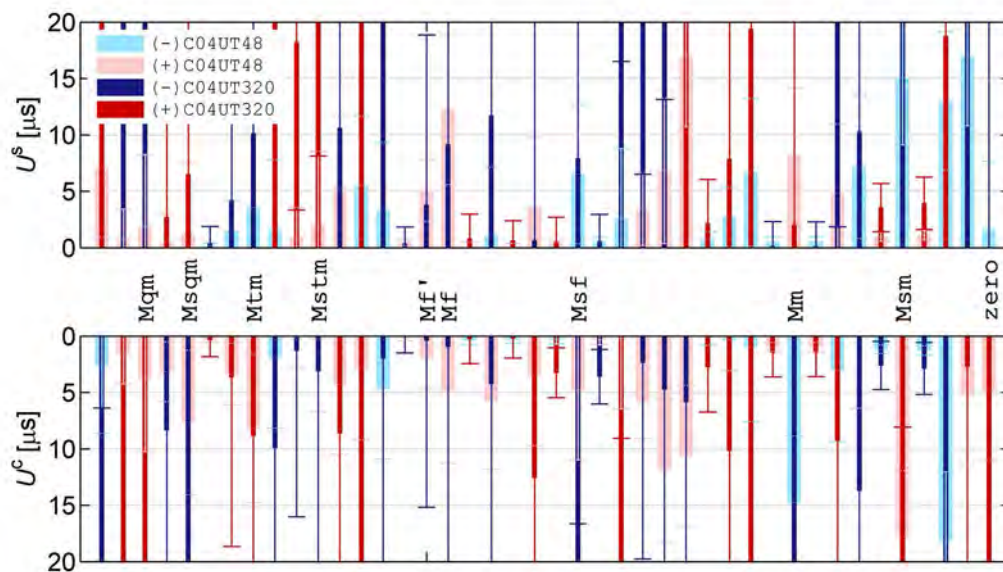


Figure 6.4: Residual zonal tidal coefficients U_i^s (top) and U_i^c (bottom) derived from C04 UT1 with 48 days filter cutoff (light colors) and 320 days filter cutoff (dark colors). The bars are plotted in light or dark red for positive values and in light or dark blue for negative values. The errorbars show the threefold formal error deriving from the adjustment.

It is obvious from the figure that the results are completely different although the series should contain the same signal at the shorter periods. Apparently the AAMF are not qualified to model UT1 excitation if variations with periods longer than 35 days are involved. From the relation of UT1 to LOD we know that UT1 amplitudes are scaled proportionally to the period. A possible explanation for this misfit at the longer periods is that the errors of the AAMF are just as well scaled with the periods due to the integration. This assumption is supported by the residual zonal tidal terms derived from LOD data. The L_i^c and L_i^s coefficients are displayed in Figure 6.5 for the shortest cutoff and the longest cutoff of 800 days. Despite the even extended period range, the results are almost identical and attest the independence of the estimated terms from the selected filter cutoff.

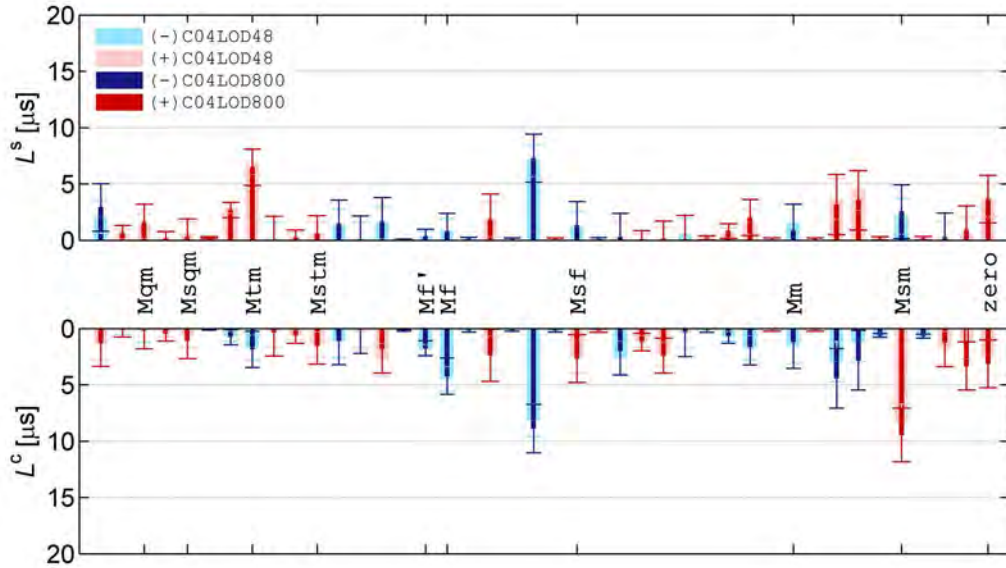


Figure 6.5: Residual zonal tidal coefficients L_i^s (top) and L_i^c (bottom) derived from C04 LOD with 48 days filter cutoff (light colors) and 800 days filter cutoff (dark colors). The bars are plotted in light or dark red for positive values and in light or dark blue for negative values. The errorbars show the threefold formal error deriving from the adjustment. Note: the LOD units refer to the nominal day.

The message of these pictures is very clear: zonal tidal variations beyond a period of 35 days cannot be safely determined directly from UT1 data. However, the important semiannual and annual terms still can be estimated in a roundabout way via LOD. The slight drawback is that in the VLBI case LOD is not the directly observed quantity but has to be derived from UT1. Nonetheless the disadvantages of deriving LOD from UT1 are negligible compared to the negative consequences of integrating AAM-LOD to AAM-UT1. The fit of zonal tidal terms below 35 days to UT1 seems to be stable, but the results should be critically cross-checked with LOD based results, bearing in mind that for example the fortnightly term Mf in UT1 is still double the magnitude of the corresponding LOD term, which is valid as well for the integrated AAM-UT1 uncertainties.

The calculations for Figures 6.4 and 6.5 were all executed with a functional model, where the side band terms were constrained to the main terms using the ratio of the tidal potential amplitudes. Variations up to 35 days could be estimated unconstrained, but if terms with higher periods are fitted the constraints are indispensable to stabilize the adjustment.

6.1.4 Estimation of the zonal response coefficient from VLBI observations

The zonal response coefficient κ , already introduced in Section 3.2.2, is a proportionality factor characterizing the reaction of the Earth-ocean-system to zonal tidal forcing. It can be also seen as a transfer function from zonal tidal potential amplitudes to zonal tidal variations in LOD or UT1. As such κ can be estimated from zonal tidal LOD or UT1 amplitudes derived as described

in the previous section or it can be estimated directly from the observed zonal tidal variations. In order to implement the latter variant, a functional model for the adjustment has to be defined accordingly. If we allow for the Earth featuring an anelastic mantle, dynamic oceans and time dependent core-mantle coupling, the coefficient κ is frequency dependent and complex. Thus for every tidal wave ℓ the coefficient is composed of a real part $\Re(\hat{\kappa}_\ell)$ and an imaginary part $\Im(\hat{\kappa}_\ell)$:

$$\hat{\kappa}_\ell = \Re(\hat{\kappa}_\ell) - i \Im(\hat{\kappa}_\ell), \quad (6.9)$$

alternatively it is expressed using the modulus $|\hat{\kappa}_\ell|$ and phase $\arg(\hat{\kappa}_\ell)$:

$$\hat{\kappa}_\ell = |\hat{\kappa}_\ell| \cdot e^{-i \arg(\hat{\kappa}_\ell)} \quad \text{where} \quad |\hat{\kappa}_\ell| = \sqrt{\Re(\hat{\kappa}_\ell)^2 + \Im(\hat{\kappa}_\ell)^2} \quad \text{and} \quad \arg(\hat{\kappa}_\ell) = \arctan \frac{\Im(\hat{\kappa}_\ell)}{\Re(\hat{\kappa}_\ell)}. \quad (6.10)$$

The negative imaginary part advises that the coefficient is modeled with a phase lag. This has consequences for the signs of the sine and cosine coefficients used in the observation equations for δLOD and δUT1 which are given in the following. Note: these equations are meant to be used with tidal potential amplitudes in Hartmann & Wenzel (1995) convention and derive from Equations (3.25), (3.26) and (6.9).

$$\delta\text{LOD}(t) = -\Re(\hat{\kappa}_\ell) \cdot \text{LOD}_0 \frac{2\sqrt{5}R^3}{3GC} A_t^{20} \cdot \cos(\alpha_\ell(t)) - \Im(\hat{\kappa}_\ell) \cdot \text{LOD}_0 \frac{2\sqrt{5}R^3}{3GC} A_t^{20} \cdot \sin(\alpha_\ell(t)), \quad (6.11)$$

$$\delta\text{UT1}(t) = -\Im(\hat{\kappa}_\ell) \cdot \frac{1}{\sigma_\ell} \frac{2\sqrt{5}R^3}{3GC} A_t^{20} \cdot \cos(\alpha_\ell(t)) + \Re(\hat{\kappa}_\ell) \cdot \frac{1}{\sigma_\ell} \frac{2\sqrt{5}R^3}{3GC} A_t^{20} \cdot \sin(\alpha_\ell(t)). \quad (6.12)$$

The input time series or rather the pseudo-observations δLOD or δUT1 are LOD or dUT1 time series preprocessed as described in the previous section, with the exception that no a priori model for the zonal tidal variations is subtracted. The pseudo-observations should instead contain the full measured zonal tidal signal in the period range of interest.

As respects a constrained adjustment, the general strategy using the ratio of the tidal potential amplitudes can be adopted for the estimation of the response coefficient as well. The amplitude ratios have to be multiplied by the same factors as the cosine and sine functions in Equations (6.11) and (6.12), though. Imposing very tight constraints effects the same magnitudes and phases for the terms which are tied together. In that way close forcing frequencies are expected to provoke the same reaction of the Earth system and thus to yield the same zonal response coefficient, which is definitely a reasonable assumption.

6.2 Derivation of ocean tidal ERP models

The theoretical foundation for calculating Earth rotation variations induced by ocean tides is provided already in Section 3.3. This section deals with the practical realization for two recent publicly available ocean tide models, TPXO7.2 (Egbert & Erofeeva, 2002) and HAMTIDE11a (Taguchi *et al.*, 2012). Both are hydrodynamic models assimilating satellite altimetry measurements and in the case of TPXO7.2 also tide gauge data. The employed parameters are tidal heights $\zeta(\sigma_i)$ and current velocities $u(\sigma_i)$, $v(\sigma_i)$ provided on global grids for the eight major diurnal and semidiurnal tidal waves ($Q_1, O_1, P_1, K_1, N_2, M_2, S_2, K_2$). The strategy of the calculation and the resulting high-frequency ocean tidal ERP models from TPXO7.2 and HAMTIDE11a are presented in the next section. TPXO7.2 additionally comprehends the fortnightly and monthly tidal constituents Mf and Mm , the Earth rotation excitation of which is examined in Section 6.2.2.

6.2.1 Diurnal and semidiurnal ocean tidal ERP models based on TPXO7.2 and HAMTIDE11a

As it is sketched in Figure 6.6 the ocean tidal heights and currents were first processed in the frequency domain. The grids were globally integrated to derive mass and motion terms of ocean tidal angular momentum (OTAM) for each frequency as described in Section 3.3.3. Ocean tidal variations in terms of polar motion $\delta\hat{p}(\sigma)$ and δLOD or δUT1 for the eight main terms were obtained according to Equations (3.50) and (3.51). Nodal corrections and minor tides were introduced in time domain and time series of 1.5 hours resolution spanning 20 years were calculated for every ERP. These time series were subsequently subjected to a least-squares adjustment in order to fit each twelve orthoweights, basically in the same manner as specified at the end of Section 6.1.1. Within the orthoweight functions the 71 tidal potential terms, that are also contained in the ocean tidal ERP model of the IERS Conventions (2010), were considered. The final 71 ERP model coefficients were generated by means of the calculation rules given in Equations (3.42)–(3.44).

The resulting major tidal constituents are displayed in polar plots (Figure 6.7) in terms of universal time and prograde and retrograde polar motion. Figure 6.7 shows the values based on

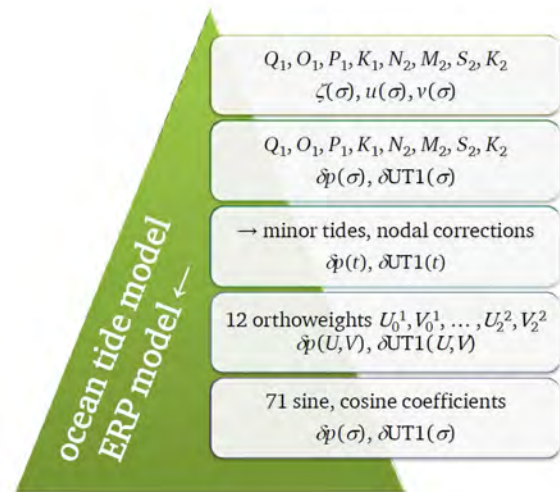


Figure 6.6: Flow diagram of ocean tidal ERP model derivation.

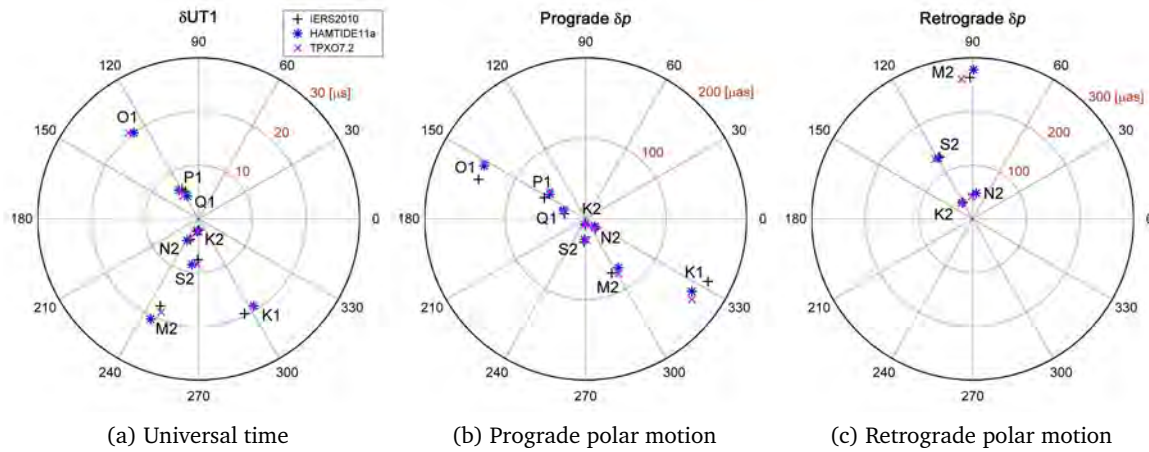


Figure 6.7: Amplitudes [$\mu\text{s}/\mu\text{as}$] and phases [degree] of the major ocean tidal ERP terms of TPXO7.2 (magenta x-marks), HAMTIDE11a (blue stars) and IERS2010 (black plus signs). The phases are referred to the fundamental arguments of the tidal constituents.

TPXO7.2 and HAMTIDE11a in comparison with the respective terms as given in the ocean tidal ERP model of the IERS Conventions (2010), named IERS2010 in the picture. There is no clear tendency of two models being closer to each other as the agreement between them varies from constituent to constituent. From the history of the IERS model, which is based on TPXO.2, one could speculate that TPXO7.2 terms should be closer to it as they share the same roots. On the other side also the two new models TPXO7.2 and HAMTIDE11a could show better agreement, since both of them assimilate recent altimetry data. In fact, there is no clear evidence for any preferred pairwise resemblance.

Table 6.1: OTAM mass and motion terms for TPXO7.2.^a

Tide	Heights						Currents					
	H_1		H_2		H_3		H_1		H_2		H_3	
	Amp	Pha	Amp	Pha	Amp	Pha	Amp	Pha	Amp	Pha	Amp	Pha
Q_1	0.114	339.3	0.259	214.6	0.073	148.7	0.058	306.9	0.071	215.9	0.138	110.0
O_1	0.457	329.9	1.154	221.8	0.207	172.7	0.253	303.7	0.393	209.6	0.606	119.3
P_1	0.144	314.0	0.435	223.7	0.029	0.4	0.150	284.0	0.206	197.3	0.238	127.5
K_1	0.460	308.4	1.367	223.9	0.149	11.6	0.506	286.9	0.727	193.4	0.768	129.6
N_2	0.129	350.0	0.038	247.5	0.043	76.0	0.132	253.4	0.249	162.4	0.289	329.7
M_2	0.522	9.2	0.365	306.5	0.576	85.4	1.023	263.0	1.803	168.4	1.535	321.9
S_2	0.127	38.9	0.290	7.2	0.244	134.6	0.575	300.0	0.982	202.2	0.773	348.8
K_2	0.035	39.2	0.086	7.3	0.071	125.8	0.162	294.5	0.282	197.0	0.228	343.2
Mm	0.005	64.3	0.005	335.1	0.219	11.2	0.009	310.9	0.005	321.4	0.005	83.5
Mf	0.013	72.0	0.028	332.2	0.380	16.6	0.017	335.1	0.015	348.6	0.037	83.6

^a Amplitude (Amp) in $10^{25} \text{ kg m}^2/\text{s}$, phase (Pha) in degrees (referred to the fundamental arguments of the tidal constituents)

Table 6.2: OTAM mass and motion terms for HAMTIDE11a.^a

Tide	Heights						Currents					
	H_1		H_2		H_3		H_1		H_2		H_3	
	Amp	Pha	Amp	Pha	Amp	Pha	Amp	Pha	Amp	Pha	Amp	Pha
Q_1	0.104	336.9	0.247	213.9	0.064	109.3	0.054	291.6	0.066	204.9	0.122	110.7
O_1	0.472	329.4	1.157	221.7	0.226	154.5	0.285	299.2	0.429	205.8	0.544	119.3
P_1	0.186	320.7	0.458	226.0	0.035	34.3	0.187	293.8	0.261	196.5	0.244	128.5
K_1	0.427	306.6	1.343	223.4	0.149	34.6	0.579	283.9	0.779	188.2	0.720	131.1
N_2	0.126	350.5	0.034	232.1	0.046	80.8	0.180	245.5	0.277	156.4	0.335	326.2
M_2	0.512	10.6	0.348	305.9	0.598	84.9	1.162	258.9	1.862	165.6	1.704	319.5
S_2	0.120	39.7	0.290	9.1	0.250	125.4	0.569	295.5	0.989	201.0	0.781	341.2
K_2	0.030	32.4	0.082	10.6	0.065	137.1	0.153	298.2	0.270	204.2	0.217	344.0

^a Amplitude (Amp) in 10^{25} kg m²/s, phase (Pha) in degrees (referred to the fundamental arguments of the tidal constituents)

The full sets of ERP terms for TPXO7.2 and HAMTIDE11a are provided for comparison in Tables A.2–A.6. A qualitative evaluation regarding the ability of the models to reflect observed Earth rotation variations is performed in Section 6.3.

As an extension from the calculation procedure, Table 6.1 and Table 6.2 display ocean tidal angular momentum split to mass (heights) and motion (currents) terms for the eight major diurnal and semidiurnal constituents as well as for the Mf and Mm tides in case of TPXO7.2. The OTAM values are presented as amplitudes and phases.

6.2.2 Monthly and fortnightly ocean tidal ERP model based on TPXO7.2

The OTAM results belonging to this section were already anticipated in the previous one by including them in Table 6.1. As to the process of deriving a monthly and fortnightly ERP model, the procedure differs only slightly from modeling the subdaily species. The orthotide formalism is not applied for the estimation of the long-period components, instead, the main terms and side lobes generated by nodal modulations are fitted directly to the time series in a least squares adjustment. In addition to the Mf term with the main period at 13.66 days four side terms with periods from 13.61 to 13.78 days were adjusted. Adjacent to Mm at 27.56 days two side lobes with the periods 27.44 and 27.67 days were estimated. The results for polar motion and UT1 are provided in Table 6.3 using the same representation with cosine and sine terms as for the diurnal and semidiurnal tidal terms.

Figure 6.8 depicts the major monthly and fortnightly UT1 constituents estimated from TPXO7.2 in comparison with the terms from three different publications, which are further explained in the figure caption.

The fortnightly terms differ by about 5% in the amplitudes and up to 4 degrees in the phases. Regarding the monthly term the differences are slightly larger, in particular the value from Desai & Wahr (1999) is fairly off. They however argue in the publication that the motion term of

Table 6.3: Ocean tidal terms of fortnightly and monthly polar motion and UT1 from TPXO7.2.^a

Tide	Fundamental arg.					Period	Polar motion [μs]				UT1 [μs]	
	l	l'	F	D	Ω		A^+	B^+	A^-	B^-	U^c	U^s
	0	0	2	0	0	13.61	0.676	3.562	-3.216	-3.526	1.757	4.151
Mf'	0	0	2	0	1	13.63	6.905	36.362	-32.835	-36.003	17.940	42.376
Mf	0	0	2	0	2	13.66	16.682	87.906	-79.387	-87.027	43.357	102.449
	2	0	0	0	-1	13.75	-0.025	0.021	-0.042	0.010	-0.025	0.032
	2	0	0	0	0	13.78	-0.034	0.014	-0.041	0.025	-0.038	0.026
Mm''	1	0	0	0	-1	27.44	-1.081	-4.140	3.997	1.059	-1.794	-7.852
Mm	1	0	0	0	0	27.56	16.638	63.688	-61.500	-16.290	27.598	120.804
Mm'	1	0	0	0	1	27.67	-1.082	-4.140	3.997	1.059	-1.794	-7.852

^a Period in days

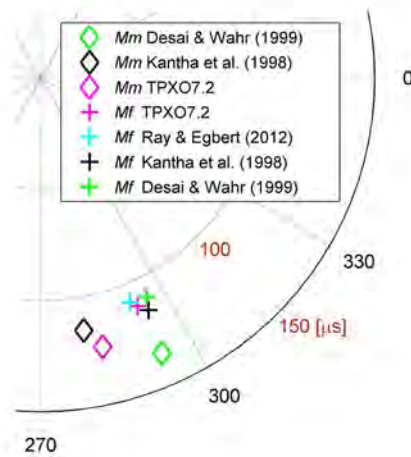


Figure 6.8: Monthly and fortnightly ocean tidal UT1 excitation from different ocean tide models. The values obtained in the frame of this work from TPXO7.2 (Egbert & Erofeeva, 2002) are plotted in magenta. The green colored markers correspond to the model T/P+SCH by Desai & Wahr (1999), which is based on an empirical ocean tide model derived from TOPEX/POSEIDON satellite altimetry data enhanced by information from the hydrodynamic Schwiderski (1980a,b) model. Black markers represent the Mf and Mm terms from a model by Kantha *et al.* (1998) which are incorporated in the present zonal tidal UT1 model of the IERS Conventions (2010). These terms are based on a hydrodynamic model assimilating altimetry data, similar to TPXO7.2. Only the fortnightly term was available from a very recent article by Ray & Egbert (2012), this is plotted in cyan. Their estimates were derived from a hydrodynamic model assimilating altimetry data which is additionally constrained to global angular momentum inferred from polar motion. The phases [degrees] are referred to the fundamental arguments of the tidal constituents.

the Mm tide seems to be overestimated by the empirical model, providing a possible explanation for the misfit. The differences between the ocean tide models and the associated Earth rotation shall not be examined any further, rather the comparison serves to substantiate the plausibility

of the calculated ERP variations induced by the TPXO7.2 model. The long-period UT1 and polar motion terms are presented here merely as results as they will not be consulted for comparison with geodetically observed tidal UT1 and polar motion.

6.3 Comparison of empirical and semi-empirical models – diurnal and subdiurnal tidal band

Various sets of diurnal and subdiurnal tidal coefficients were derived using miscellaneous approaches and different kinds of observation data, as described in Chapters 4, 5 and the present one. Certainly not all of the time series and solutions mentioned are employed to evaluate the conventional model for ocean tidal Earth rotation variations, rather subsets are consulted to demonstrate the effects of certain processing strategies and point out advantages and disadvantages in the first place. The most robust solutions are then adopted to assess deficiencies of the model currently recommended in the IERS Conventions (2010) and to validate the performance of the two ocean tidal ERP models presented in Section 6.2.1 with regard to reducing residual signal in the observed ERP.

The empirical models from VLBI and GNSS generally share the number and periods of the tidal terms. They include the 40 diurnal and 33 semidiurnal terms which constitute the present IERS Conventions (2010) model. One term of the conventional model is excluded as unresolvable, since it differs from the adjoining S_1 tide by two cycles in 20942 years only (period of the solar perigee). It is possible to calculate this term using the orthotide approach, yet it was commonly omitted for reasons of consistency and endorsed also by its anyway small amplitude. Three coefficients, denominated *zero* terms, each for the diurnal and the semidiurnal band were introduced as an additional measure of the overall noise level. These terms reside in period ranges where no significant tidal signal is expected and represent thus an independent rating of the formal errors. Additionally the terdiurnal tide M_3 was estimated in most cases.

6.3.1 Retrograde diurnal polar motion

According to the definition of the CIP (Section 2.1.3) retrograde diurnal polar motion is assigned to its celestial motion, i.e. precession-nutation. However, this is a pure convention, for which reason it is possible that retrograde diurnal signal leaks to the polar motion estimates, if the precession-nutation model is imperfect and celestial pole offsets are not estimated simultaneously or modeled inadequately. Among the presented time series of highly resolved ERP there is at least one example for insufficiently modeled celestial pole offsets: the first VLBI series termed OCCAMsp1 was computed with nutation fixed to the IAU2000 nutation model. We can therefore expect the FCN mode which is not incorporated in the nutation model to show up as retrograde diurnal polar motion around the periods of the P_1 and K_1 terms. All of the high-resolution ERP time series were estimated w.r.t. an a priori ocean tidal ERP model. Notwithstanding the fact that ocean tides do also cause retrograde diurnal polar motion terms these are not part of the

conventional ERP model, instead they are considered in the precession-nutation model due to the CIP convention. Any obtained retrograde diurnal polar motion can consequently also contain residuals to this part of the ocean tidal ERP model, but it is almost impossible to allocate such signal to certain ocean tidal terms, as it will be superimposed by the much stronger FCN signal.

In order to uncover the successful or less effective modeling of residual nutation signal, retrograde diurnal tidal polar motion terms were estimated from the highly resolved time series. The resulting values are illustrated in a phasor diagram (Figure 6.9) for five solutions emanating from time series with different processing strategies.

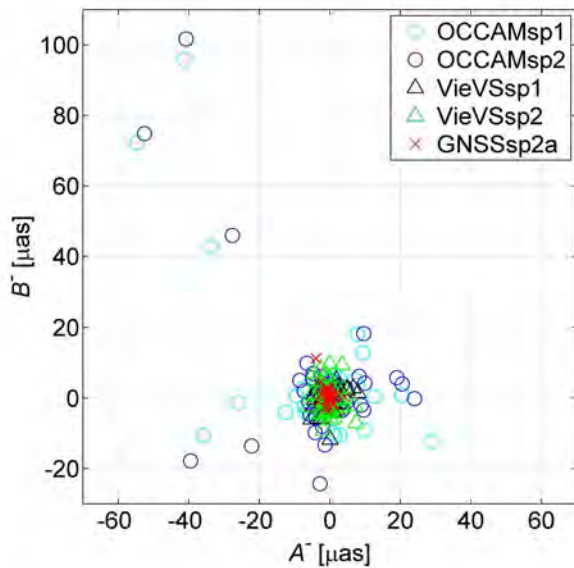


Figure 6.9: Retrograde diurnal polar motion terms estimated from two OCCAM VLBI time series (cyan and blue circles), two VieVS VLBI time series (black and green triangles) and one GPS time series (red x-marks).

50 μas this can be considered as noise leaking through to polar motion. The values from the GNSSsp2 solution are predominantly below that threshold of the VieVS solutions. In GNSS processing there is the option to block retrograde diurnal polar motion, which is compulsory if satellite orbits are estimated. Since the satellite positions were fixed to the CODE orbits for the solutions presented here, this constraint was not applied breeding small residuals as apparent in Figure 6.9.

If retrograde diurnal polar motion shall be kept in the nutation band as stipulated by the CIP frequency conventions, the re-introduction of beforehand, consistently estimated celestial pole offsets is definitely the best choice in cases where the simultaneous estimation of high-frequency polar motion variations and nutation offsets is not feasible. When using the direct or demodulation approach, celestial pole offsets are determined together with high-frequency polar motion and retrograde diurnal variations are forced into the celestial part of the CIP motion.

The OCCAMsp1 solution clearly exhibits the afore-mentioned anticipated retrograde diurnal signal spread to several tidal terms with magnitudes up to around 100 μas . The second solution OCCAMsp2 is based on time series calculated with nutation fixed to IAU2000 plus celestial pole offsets taken from the IERS C04 EOP series. Surprisingly this solution features quite as much retrograde diurnal signal as the solution with no a priori celestial pole offsets. This suggests that there were problems with the implemented C04 celestial pole offsets as they do not contribute to reduce the residuals. Both VieVS solutions were derived with consistently predetermined celestial pole offsets held fix, which obviously diminishes the residual retrograde diurnal signal to magnitudes below 10 μas . In view of the celestial pole offsets uncertainties being at a level of

For the purposes of validating the conventional ocean tidal ERP model the examination of the corresponding retrograde diurnal part would be logically consistent. Unfortunately this part is not easily accessible in terms of observations. Residuals or rather discrepancies, if present, must show up in the celestial pole offsets. However, as residuals they are comparatively small against the dominant FCN and compared with other effects, for example atmospheric tides, which can reach magnitudes of up to about $80 \mu\text{as}$. Their amplitudes are strongly enhanced by the FCN resonance like those of all retrograde quasi-diurnal variations. Since residual retrograde diurnal ocean tidal polar motion terms are only some of a variety of contributors to the nutation offsets there is currently no chance to check the validity of the ocean tidal excitation incorporated in the nutation model by means of observations.

Nevertheless, we can get an idea of possible deviations by comparing the major retrograde diurnal polar motion terms of the model by Chao *et al.* (1996), which the nutation contributions are based on (Mathews *et al.*, 2002), to the coefficients resulting from the two recent ocean tide models TPXO7.2 and HAMTIDE11a, inspected in Section 6.2.1. The respective retrograde terms are shown in Figure 6.10 separately for each diurnal constituent in terms of in-phase and quadrature coefficients, according to Equations (4.13) or (6.1). The used markers are the same as in Figure 6.7, blue stars for HAMTIDE11a and magenta x-marks for TPXO7.2. The retrograde diurnal ocean tidal contribution applied in the IAU2000 nutation model is essentially based on the same ocean tide model as the UT1 and polar motion contribution constituting the IERS2010 model. Hence the same black plus marks are used for plotting, but the legend entry is designated like the publication the values are taken from.

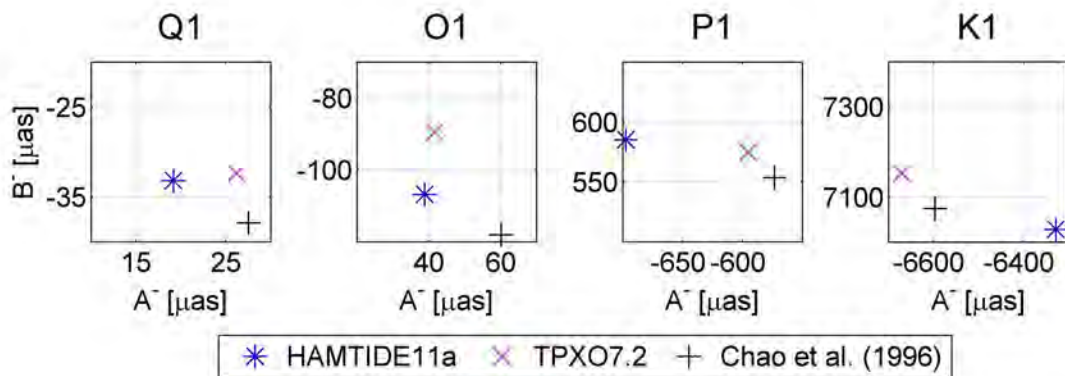


Figure 6.10: Retrograde diurnal polar motion terms, calculated from the ocean tide models HAMTIDE11a (blue stars) and TPXO7.2 (magenta x-marks) and extracted from Chao *et al.* (1996) (black plus signs).

The terms disagree by $10\text{--}20 \mu\text{as}$ in case of the Q_1 and O_1 tides and up to $100\text{--}250 \mu\text{as}$ for the periods where the amplitudes are amplified due to the vicinity to the FCN. It can be unbiasedly stated that significant discrepancies between the three models are present. These differences would be consequently mapped to observed celestial pole offsets if the ocean tidal contribution

to nutation would be accounted for by another model. Whether another model would improve the closure between modeling and observation could be proven only by exchanging this part of the nutation model and evaluating the residuals to the adapted nutation model. The celestial CIP motion is, however, not subject matter to this thesis, why investigations of that kind are attributed to future work.

6.3.2 GNSS solutions

Due to several reasons explained in Chapter 5, GNSS ERP series calculated in the frame of the present work cover a very limited time span, from eight months (GNSSsp2a, GNSSsp2b) to two years (GNSSsp1). In order to still derive the same number of tidal terms as from the longer time series and consider a most complete tidal spectrum either constraints have to be imposed on adjacent terms which would be inseparable otherwise or the terms can be obtained indirectly via orthoweights. The orthotide formalism was actually developed exactly to cope with short observation periods of tidal heights still allowing for maximum variability and seems therefore very well suited also for the purpose of representing tidal Earth rotation variations. As was stressed already in Section 6.1.1 the concept to tie the ratio of tidal amplitudes to their tidal potential ratio is inherent in both methods the constraining and the orthotide approach. By means of one exemplary GNSS time series it is demonstrated why the orthotide formalism should be eventually favored over the constraining of the amplitudes, at least for short time series.

Figure 6.11 shows a comparison of polar motion residual coefficients obtained from the orthotide and from the constrained approach. The previously mentioned *zero* terms and the ter-diurnal wave M_3 shall not be discussed comparatively here, because they are not estimated in the orthotide solution. In view of the formal errors, the differences between the two approaches of 1-2 μs are insignificant. The minor terms of the constrained solution exhibit rather consistently larger amplitude residuals accompanied by larger formal errors. If we compare these also with the magnitudes of the *zero* terms it seems most likely that those waves which are not coupled to a major term partly absorb the measurement noise. On examination of the respective residual spectra (which are not shown here) it can be stated that the approaches are virtually equivalent regarding the representation of the tidal variability. To a very small extent the orthotide approach leaves more residual signal around one and two cycles per day, indicating that the major peaks are slightly attenuated due to the expression via orthotide functions. However, this is negligible considering the advantages of a more stable constraint-free adjustment with only about a tenth of the parameters. Especially when dealing with very short time series fitting orthoweights appears to be superior to the constrained adjustment of all spectral lines. The estimation of UT1 with both methods shows a similar picture, which is not displayed here as it would present redundant information in this context only. In compliance with the above-mentioned arguments the empirical tidal models from the GNSSsp series were derived by applying the orthotide formalism.

After having appointed the principal estimation method the GNSS solutions are inspected

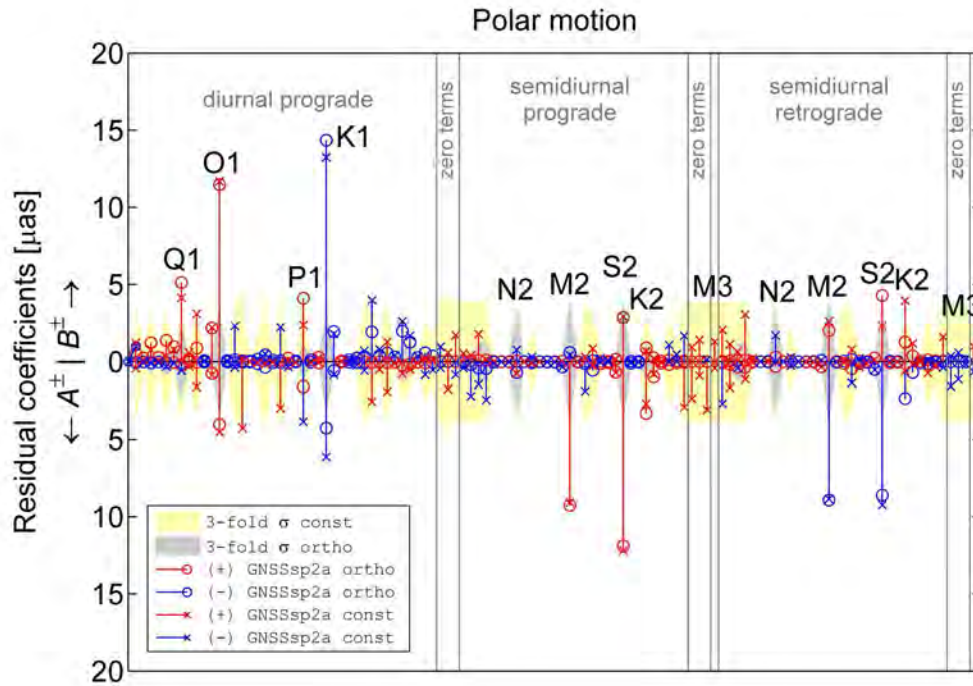


Figure 6.11: Prograde (A^+ , B^+) and retrograde (A^- , B^-) polar motion coefficients estimated from the GPS time series GNSSsp2a once using orthoweights (ortho) and once imposing constraints on the amplitude ratios (const). The coefficients are residuals w.r.t. the IERS2010 model, with circles indicating the orthotide solution and x-marks labeling the constrained solution. B terms are plotted upwards, A terms are directed downwards, with the sign of the respective estimate being specified by the color – red for positive and blue for negative values. The shaded areas in the background display the threefold formal errors of the ortho (gray) and const (yellow) solutions.

under two aspects. One aspect is the evaluation of the benefit of a combined GPS+GLONASS solution (GNSSsp2b) compared to a GPS-only scenario (GNSSsp2a). The second aspect is the agreement of the two GNSS campaigns among each other and with independent external empirical GPS models. One of the external empirical models is as well based on highly resolved (2-h intervals) ERP time series derived within a GPS reprocessing effort (Steigenberger, 2009). The underlying time series span the period 1994.0–2005.8. The second external solution was calculated via transformation of GPS normal equations containing highly resolved ERP to normal equations with tidal coefficients as parameters. The normal equations were derived in the frame of the GGOS-D project (Rothacher *et al.*, 2011) and cover the years 1994–2007. The set of terms used for comparison is one of several solutions by courtesy of N. Panafidina (personal communication, 2012), the computation of which is to some extent described in Panafidina *et al.* (2012).

As these are the most dominant and informative terms, the comparison is accomplished merely for the major diurnal and semidiurnal constituents. Phasor diagrams containing the major

polar motion and UT1 terms (w.r.t. IERS2010) of all five solutions are provided in Figure 6.12.

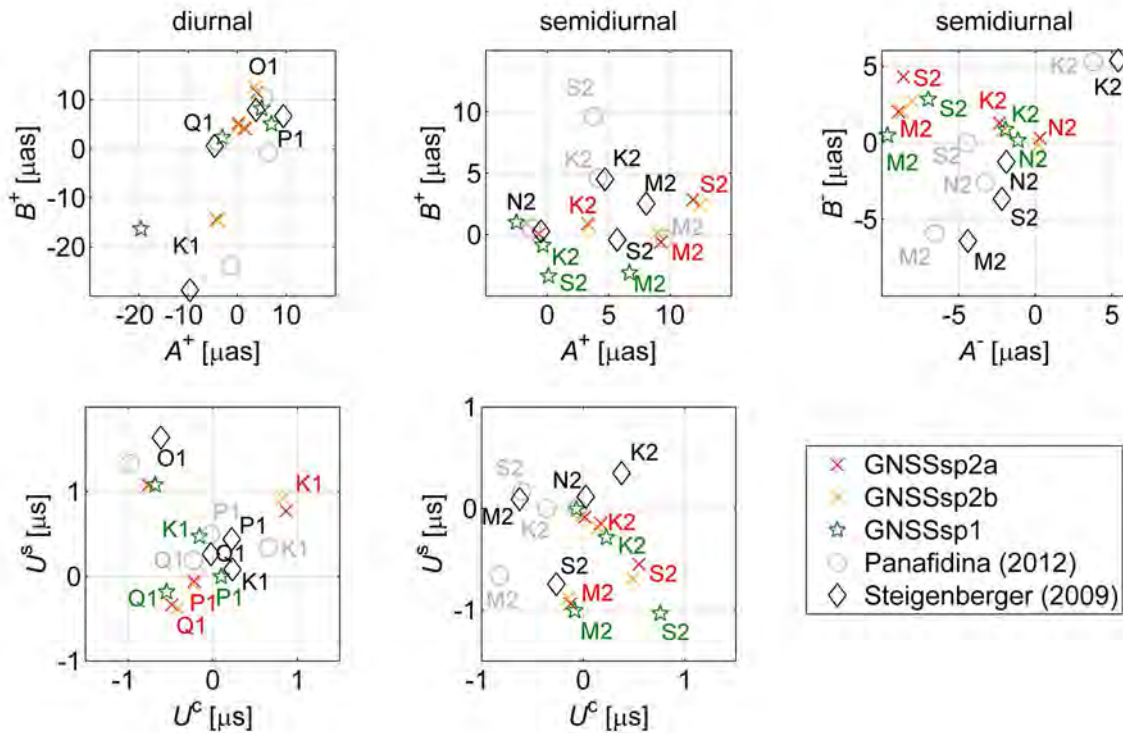


Figure 6.12: Residual polar motion (top) and UT1 (bottom) tidal coefficients w.r.t. IERS2010 from different GNSS solutions. The three upper plots show, from left to right, diurnal prograde, semidiurnal prograde and semidiurnal retrograde polar motion in μas . Diurnal and semidiurnal universal time coefficients are presented in units of μs in the two lower boxes. The internal solution from the two-years GPS campaign (GNSSsp1) is marked with green pentagrams. The x-marks represent the two sets from the eight-months campaign, with the GPS-only solution (GNSSsp2a) in red and the hybrid GPS+GLONASS solution (GNSSsp2b) in orange. If all solutions are rather unambiguously grouped together for the particular term, only the black label is retained, in all other cases each marker has a corresponding label in the same color so as to identify which constituent it belongs to. The two GNSSsp2 solutions are generally so close together that red tide names are valid for both and the GNSSsp2b solution is not labeled extra. The external solutions are depicted as gray circles (Panafidina, 2012) and black (Steigenberger, 2009) diamonds. All solutions displayed in this graph are consistently corrected for the effects of polar and spin libration according to the IERS Conventions (2010).

Regarding the first aspect touched upon before, the potential of a combined GPS+GLONASS processing, it is most evident that the differences between the combined and the GPS-only solution are insignificant. The largest deviations between GNSSsp2a and GNSSsp2b occur at the S_2 tide and amount to about $2 \mu\text{as}$ in polar motion and approximately $0.1 \mu\text{s}$ in UT1, which is fairly below the respective threefold uncertainties. These results thus confirm the presumption of Chapter 5 that the 7% of GLONASS observations contributing to the hybrid solution would fail to substantially affect the subdaily Earth rotation parameters.

The disagreement between the different other solutions, however, is well significant for several of the major tidal terms. Ample discrepancies are visible in particular for the K_1 , K_2 and S_2 tides, but also for the M_2 and the O_1 term especially in universal time. The important differences between the internal and the external solutions are first and foremost the length of the ERP observations and second the treatment of the satellite orbits. In the internal ERP calculation the orbits were fixed to the CODE solution, while both external solutions were derived with simultaneously estimated satellite positions. The tidal ERP models though were estimated directly by setting up the tidal terms as unknowns by Panafidina (2012) and in a two-step procedure similar to the internal solutions by Steigenberger (2009). The direct estimation is commonly considered as the most rigorous approach, but still particular constituents deduced from GPS are to be interpreted with caution as pointed out by Steigenberger (2009) as well as by Panafidina *et al.* (2012).

Due to the shortness of the internal time series they are not suitable to execute stability tests, i.e. to calculate a kind of repeatability for each term with a sliding window. Panafidina *et al.* (2012) presented such a study and advised that the terms P_1 , K_1 , S_2 and K_2 are notably instable. Also the O_1 term in UT1 they found to show a high root mean square for GPS solutions with different orbital arc lengths. Another unreliable term is S_1 , where the atmospheric thermal tide resides. It is not plotted in the comparison above, since it is not a major ocean tidal constituent. Yet the residual Earth rotation variations at this period are often discussed concerning the atmospheric tidal excitation. GPS based results should be, however, examined critically. In respect of the S_1 tide it should be pointed out additionally that the gravitational tidal effect at this period is very small compared to the thermal tidal effect. Consequently the thermal part of the S_1 term will not be seen when using the orthotide approach (unless an additional radiational potential is introduced) and it will be as well ruled out in a constrained adjustment if the observation period is shorter than one year.

It is recommended to exclude critical terms, such as the above-mentioned, when using tidal GNSS and especially GPS-only models for the validation of subdaily Earth rotation models, as long as the interrelations between orbit modeling and subdaily ERP harmonics are not fully resolved. Power spectra of IGS orbit discontinuities show peaks which are suspected to be low-frequency aliases due to an inadequate subdaily ERP tide model. Ray & Griffiths (2011) confirmed by simulation studies that errors in the subdaily ERP tide model can alias into orbit parameters. Since the high-frequency ERP model used a priori in the GNSS processing affects the estimated orbits and hence the estimated ERP this is a closed circuit effectively rendering an objective evaluation of the high-frequency ERP model quite intricate.

6.3.3 VLBI solutions

As there are several different empirical VLBI models at hand, a preliminary selection has to be made to reduce the number of models that will be effectively compared to the ocean tidal ERP models. The solution pairs VieVSsp1 and VieVSsp2 as well as VieVScd1b and VieVScd2 are rather similar, they differ regarding the used TRF, slightly in terms of the choice of sessions and

the solutions with the index 2 incorporate half a year of observations more. Analogously to the comparison of orthotide and constrained approach for GNSS, the quoted index 1 and index 2 VLBI solutions are contrasted in stem plots showing the coefficient residuals w.r.t. the IERS2010 model for polar motion (Figure 6.13 and Figure 6.14). The differences to the IERS2010 model shown here shall not be discussed in this section. In fact, the residuals were chosen for exposure as they facilitate the perception of differences between the solutions.

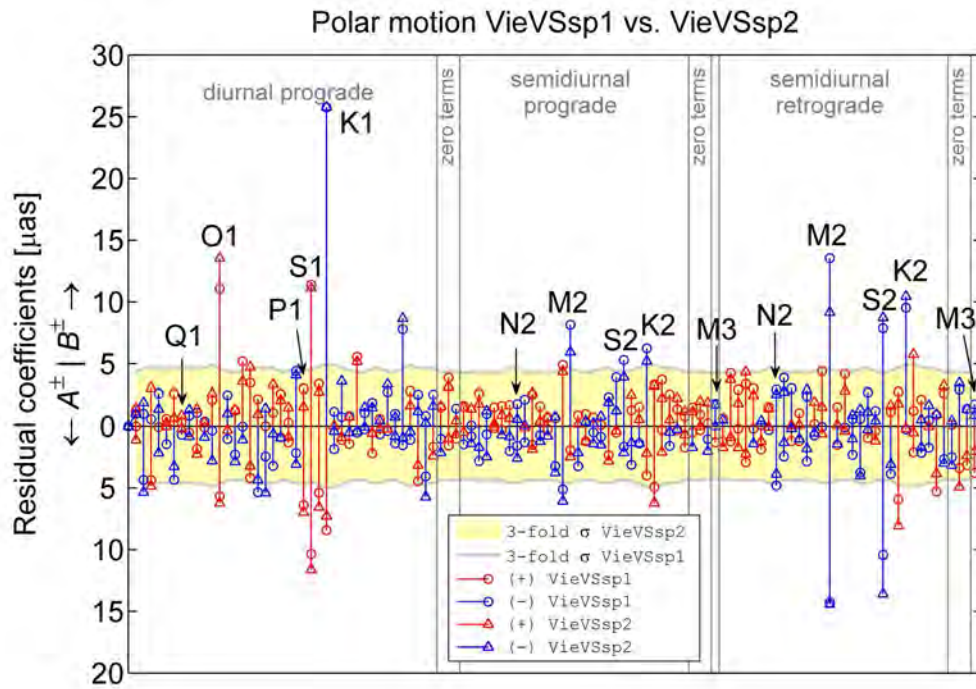


Figure 6.13: Prograde (A^+ , B^+) and retrograde (A^- , B^-) polar motion coefficients estimated from two hourly time series differing most notably in the used reference frames (VieVSsp1: VTRF2008, VieVSsp2: VieTRF10a). The coefficients are residuals w.r.t. the IERS2010 model, with circles indicating the VieVSsp1 solution and triangles labeling the VieVSsp2 solution. B terms are plotted upwards, A terms are directed downwards, with the sign of the respective estimate being specified by the color – red for positive and blue for negative values. The threefold formal errors of VieVSsp1 and VieVSsp2 are shown as thick gray line and yellow shaded area, respectively.

The plots display quite ostensively that there are no significant phase shifts between the compared models, which would appear as blue and red colored markers at the same position. Evidently, the most notable deviations are present at the M_2 and S_2 periods with a very similar magnitude in both, the highly resolved (Figure 6.13) and the demodulated ERP (Figure 6.14) cases. So this is most likely an effect of applying the NNR/NNT condition on the coordinates of two different reference frames, the VTRF2008 for the index 1 solutions and the VieTRF10a for the index 2 solutions. However, none of these discrepancies exceeds the threefold uncertainties, which is why the two solution types are considered equivalent. For further interpretation only the VieVSsp2 and VieVScd2 models are employed, because they are consistent with the unique global

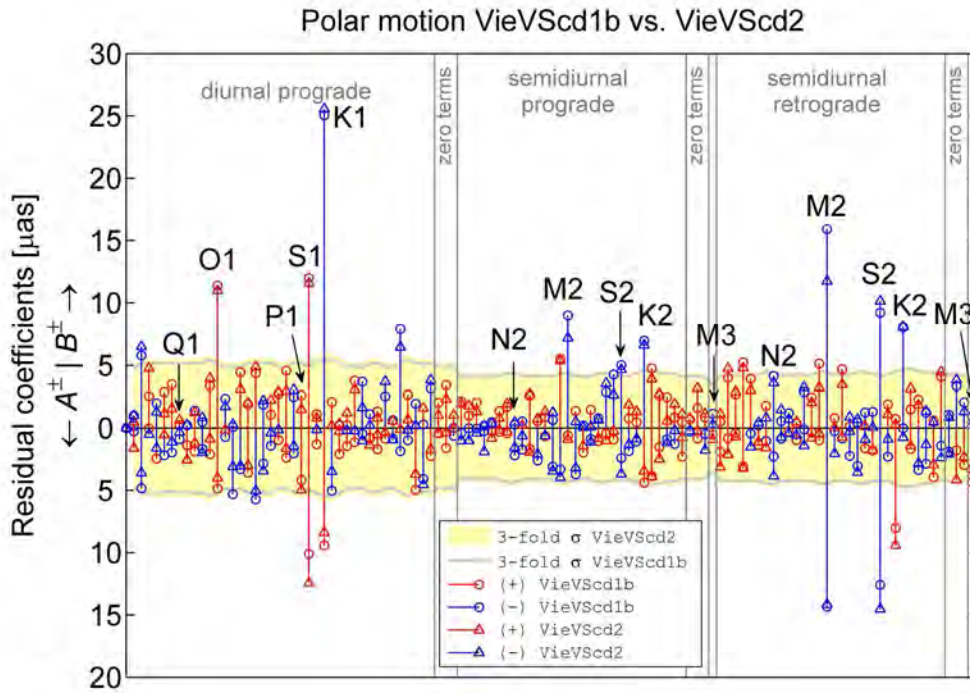


Figure 6.14: Prograde (A^+ , B^+) and retrograde (A^- , B^-) polar motion coefficients estimated from two time series of demodulated polar motion differing most notably in the used reference frames (VieVScd1b: VTRF2008, VieVScd2: VieTRF10a). The coefficients are residuals w.r.t. the IERS2010 model, with circles indicating the VieVScd1b solution and triangles labeling the VieVScd2 solution. B terms are plotted upwards, A terms are directed downwards, with the sign of the respective estimate being specified by the color – red for positive and blue for negative values. The threefold formal errors of VieVScd1b and VieVScd2 are shown as thick gray line and yellow shaded area, respectively.

solution model VieVSGs1. The corresponding pictures for universal time residuals are provided as Figure B.1 and Figure B.2 in Appendix B.

As to the other VLBI solutions, the first OCCAM model OCCAMsp1 is sorted out as well – it was inserted mainly to demonstrate the effect of introducing no a priori celestial pole offsets. The set of coefficients from OCCAMsp2 is compared to the other selected VLBI solutions for the major tidal terms later in this section to have a solution from a second software as well. Indeed, the OCCAM solutions are not optimal in terms of reference frame definition, because the station coordinates had to be fixed to the a priori TRF, which potentially affects or at least constrains the ERP.

Prior to examining the agreement of the various VLBI solutions, the temporal stability of the empirical VLBI models is scrutinized using the VieVSp2 series representatively for all. This survey follows the strategy of Panafidina *et al.* (2012) to divide the whole observation period into nine bins of 19 years each. The selected window length allows exactly for an unconstrained solution. Thus nine sets of coefficients are received with the beginning of the observation interval

shifted by one year from 1984 onwards until 1992. The development of major tidal terms plus S_1 and M_3 over time is confronted with the respective terms obtained from the whole time span from 1984–2011 in Figure 6.15 for prograde polar motion and in Figure 6.16 for UT1.

The results are given in phasor diagrams (B^+ against A^+ and U^s against U^c) and represent residuals to the IERS2010 model. Several of the model terms exhibit a kind of path starting with a larger residual amplitude in the early years which is decreasing for the later models. It is particularly noticeable that the values of the full solution are in all cases in the vicinity of the section models that are based on the more recent observation data. This leads to the conclusion that first the earlier data is more noisy yielding larger amplitudes and second the solution of the complete time span is governed predominantly by the information from the later years. Furthermore, these evolution studies demonstrate that it is safe to include the sometimes questioned early years of VLBI data, because they are obviously properly weighted by their formal errors in the adjustment. It is, however, not recommended to estimate such a tidal ERP model only from the first years, as this could bring about misinterpretations. The figures suggest that the solutions stabilize for the intervals beginning in the nineties – an observation which is congruent with the findings of Böhm *et al.* (2011) concerning the analysis of demodulated ERP.

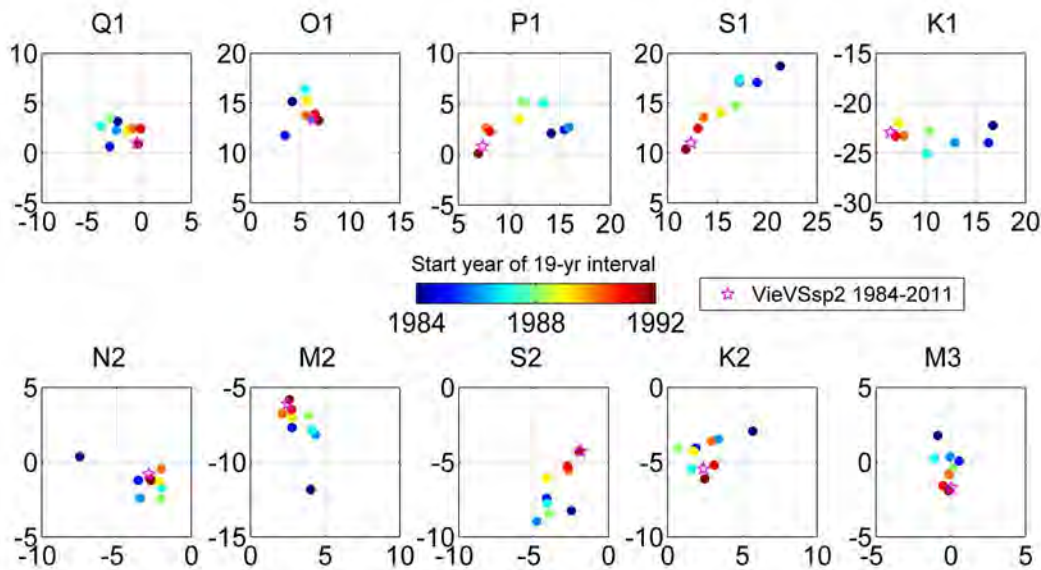


Figure 6.15: Evolution of residual prograde polar motion coefficients for the eight major tidal constituents plus S_1 and M_3 (w.r.t. IERS2010). The diagrams show B^+ against A^+ in units of μas . The nine section models are displayed as color-coded dots with the terms from the first 19-year interval in dark blue and the results from the last interval in dark red. The full solution from VieVSp2 is shown with magenta pentagrams.

Overall the diurnal terms appear to be affected stronger by the lower data quality of the first years. The maximum dispersion can be discerned for the K_1 tide for prograde polar motion as well as UT1. The evolution of the retrograde polar motion terms also shows a quite interesting

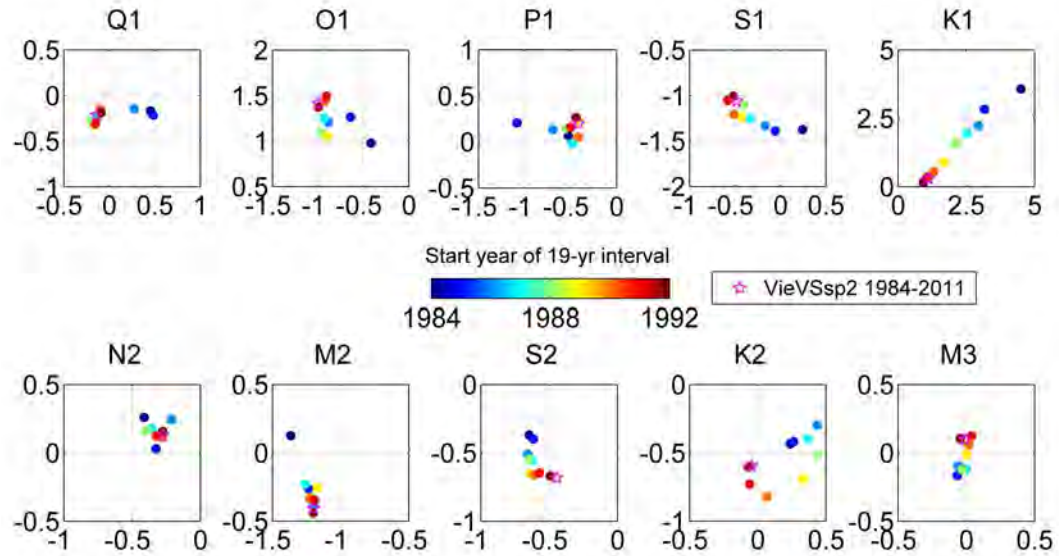


Figure 6.16: Evolution of residual universal time coefficients for the eight major tidal constituents plus S_1 and M_3 (w.r.t. IERS2010). The diagrams show U^s against U^c in units of μs . The nine section models are displayed as color-coded dots with the terms from the first 19-year interval in dark blue and the results from the last interval in dark red. The full solution from VieVSsp2 is shown with magenta pentagrams.

scatter in the diurnal band. To avoid an overloading of this section, the corresponding diagrams are provided in Appendix B in Figure B.3. If corrections to the nutation model are sufficiently accounted for hardly any retrograde diurnal polar motion should be seen. Yet, Figure 6.15 displays significant signal in that range for the models involving the older data. This is most probably due to the less precise celestial pole offsets from the early years which are re-introduced in the processing to estimate hourly ERP. It is also likely that there is a kind of intercommunication between the prograde and retrograde diurnal signal causing the more widespread scatter in the diurnal terms.

With the assurance that the incorporation of VLBI data from the eighties does not bias the results, the preselected empirical models derived from the complete observation period can be compared. As in the case of the GNSS solutions the comparison is confined to the major tidal waves, but complemented here by the S_1 term. Figure 6.17 contains residual polar motion and UT1 coefficients w.r.t. IERS2010 partitioned into diurnal and semidiurnal groups. The three VieVS solutions (VieVSsp2, VieVScd2, VieVSGs1) are juxtaposed to the OCCAMsp2 model and to an external empirical VLBI model, basically derived within a global solution by Artz *et al.* (2011).

The overall agreement between the different empirical VLBI models is quite good. Broader divergence is observed for the S_2 tide in pro- and retrograde polar motion and the M_2 tide in retrograde polar motion. In universal time we see the O_1 and M_2 coefficients obtained from de-

modulated UT1 somewhat detached from the other solutions. These tides are both demodulated to a period of 13.66 days at which a very strong zonal tidal signal is present in the long-period UT1 signal. An interference with other geophysical signals occurring naturally at the demodulated periods is definitely conceivable. The actual significance of the detected discrepancies are assessed in the following section with regard to the corresponding model uncertainties. Only the OCCAMsp2 solution will be omitted in the further inspection, because it represents a redundant model derived from highly resolved ERP time series and aside from that it is based on a not optimal processing strategy in terms of TRF definition. Moreover, it is the only solution which was still calculated w.r.t. ICRF Ext.2 instead of ICRF2 and is therefore not completely consistent with the remaining VLBI models.

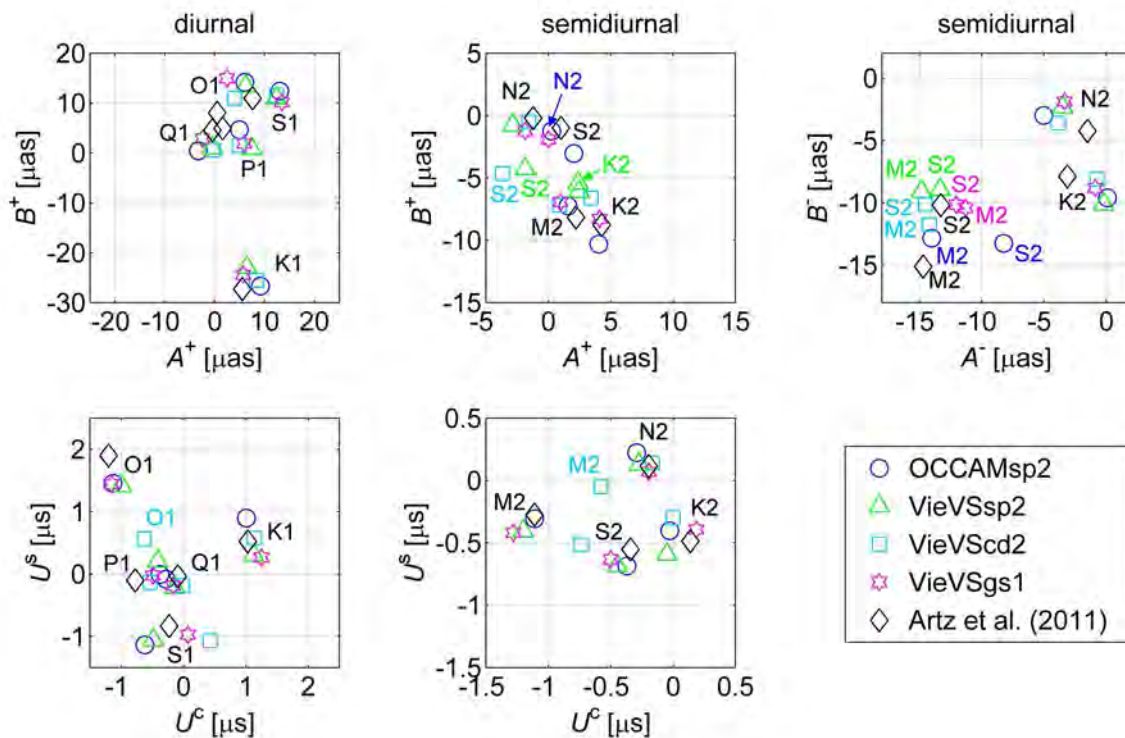


Figure 6.17: Residual polar motion (top) and UT1 (bottom) tidal coefficients w.r.t. IERS2010 from different VLBI solutions: OCCAMsp2 (blue circles), VieVSp2 (green triangles), VieVScd2 (cyan squares), VieVSGs1 (magenta hexagrams), Artz *et al.* (2011) (black diamonds). If the affiliation of markers to a special term is distinctly visible, the batches are identified only by a black label. Whenever single solutions are isolated or the terms are nested too much, the markers are additionally badged by a label in the color belonging to the respective model.

6.3.4 Assessment of ocean tidal ERP models

For the sake of visibility, most of the results so far have been presented as residuals to the ocean tidal ERP model recommended in the IERS Conventions (2010), shortly termed IERS2010.

In this section the magnitudes and significance of the residuals to the conventional model are discussed as well as the observed residuals to the two alternative ocean tidal ERP models TPXO7.2 and HAMTIDE11a derived in the course of this work. There are different ways to evaluate the agreement between tidal models. Beside the visual inspection in phasor or stem plots a more general validation can be performed by forming the root mean square (rms) of the coefficient differences, as suggested e.g. by Rothacher *et al.* (2001). The rms between the three ocean tidal ERP models, the three internal empirical VLBI models, the external VLBI model by Artz *et al.* (2011), and the external GPS model by Panafidina (2012) are assembled in Table 6.4. All compared coefficients were consistently corrected for the effects of polar and spin libration according to the IERS Conventions (2010). The values are arranged in a matrix with the upper right triangle (above the diagonal) containing the polar motion and the lower left triangle presenting the UT1 rms. The upper left and lower right separated areas show the agreement among the ocean tidal models and the geodetic models, respectively, while the upper right and lower left parts reflect the compliance of the ocean tidal models with the models from Earth rotation observation. The color-coded cells indicate best agreement in green, shading into yellow and finally into red to display worst agreement. In case of the empirical model by Artz *et al.* (2011) some coefficients were fixed to the IERS2010 model if their estimated amplitudes were below their threefold standard deviation. To ensure a consistent comparison all rms are therefore computed only from terms which were also estimated in the final model of Artz *et al.* (2011).

Table 6.4: Root mean square values of model coefficient differences.

Model	IERS2010	TPXO7.2	HAM11a	VieVSp2	VieVScd2	VieVSGs1	Artz et al.	Panafidina	ERP
IERS2010		4.0	3.5	4.6	4.7	4.6	4.9	3.9	Polar motion [µas]
TPXO7.2	0.32		3.1	4.2	4.4	4.2	4.5	3.5	
HAMTIDE11a	0.45	0.30		5.3	5.7	5.3	5.9	4.2	
VieVSp2	0.39	0.36	0.43		1.4	1.8	2.6	4.6	Universal time [µs]
VieVScd2	0.32	0.33	0.42	0.25		1.5	2.3	4.7	
VieVSGs1	0.38	0.35	0.41	0.15	0.24		2.3	4.5	
Artz et al. (2011)	0.38	0.35	0.43	0.18	0.27	0.16		4.8	
Panafidina (2012)	0.36	0.39	0.45	0.33	0.41	0.34	0.33		
ERP									

By dint of the color code it can be easily read that there is overall a better mutual agreement among each model group (ocean tidal and geodetic) than between the two groups, though with some exceptions. The VLBI empirical models show the closest accordance, whereas the GPS model is rather out-of-line especially in terms of polar motion where it exhibits better agreement with the ocean tidal ERP models. One possible reason for this is the constraining of the amplitudes to the tidal potential amplitudes, which is not applied for the VLBI models, but has to be used for the GPS solution due to the insufficient length of the observation period. If the time series and demodulation models (VieVSp2, VieVScd2) are replaced for example by their constrained counterparts, an improvement of the fit with the ocean tidal models can be observed as well. The corresponding table to confirm this statement is given in Appendix A, Table A.7. The internal GNSS solutions are not chosen for comparison here, due to the brevity of the underlying

data. Nevertheless, Table A.8 in the appendix shows the rms for the GNSSsp2b solution derived with the orthotide method. Since the ocean tidal ERP models are based on the same approach the rms of the coefficient differences are obviously even more reduced. Anyhow, it is not the pursued objective to resemble the ocean tidal ERP models, but to detect deficiencies and minimize peaks in the residual spectrum of observed high-frequency Earth rotation. Hence the rms of the coefficient differences shall be used predominantly as a global measure to estimate whether one of the more recent ocean tidal models would match the observations better than the IERS2010 model. Apparently the HAMTIDE11a does not fulfill this requirement, whereas the TPXO7.2 offers the highest level of conformity with the space geodetic ERP models. Still, the degree of improvement compared to the agreement with IERS2010 is small. In order to find out about the consistency of the models regarding single spectral components, the residual amplitudes w.r.t. IERS2010 and TPXO7.2 are examined in more detail in the following.

Figures 6.18 and 6.19 display the residual polar motion amplitudes of the three internal VLBI solutions and the two external models from VLBI and GPS w.r.t. IERS2010 and TPXO7.2, respectively. The graphs represent a kind of residual spectrum, but calculated for specified tidal frequencies only. The size of the peaks corresponds to the effective distance between the empirical and the ocean tidal phasors, i.e. the amplitude of the coefficient differences. Except for the *zero* terms which are concentrated at the end of each frequency band, the estimated spectral components are sorted by decreasing period from left to right and plotted separately for prograde and retrograde terms, if applicable.

As can be expected, the formal errors of the global solution (VieVSgs1) are the smallest since the estimation of the tidal terms is embedded in the common adjustment of many parameters and directly based on the delay observations. Both, the global solution as well as the model from demodulated ERP feature slightly larger uncertainties in the diurnal band. This is probably related to the simultaneous estimation of daily polar motion. On examination of the *zero* terms there seems to be slightly more noise in the retrograde semidiurnal band, but otherwise the terms suggest the noise level to be somewhere in between the uncertainties of the global solution and the more pessimistic errors of the demodulation and highly resolved ERP approaches. Considering these facts it is reasonable to direct closer attention merely to residuals exceeding at least the threefold formal errors of the VieVSsp2 model. This implicates at the same time that the results for the M_3 wave, which is not part of the ocean tidal models, why the given amplitudes are absolute values, have to be regarded as insignificant. Thus a distinct peak in terdiurnal retrograde polar motion as independently detected in the spectrum from the continuous VLBI CONT02 campaign by Haas (2006) and Artz *et al.* (2010) cannot be confirmed.

Being absolute values, the *zero* terms and M_3 are equivalent in Figure 6.18 and Figure 6.19. The estimates are very similar also for periods which have anyway very small amplitudes in both ocean tidal ERP models. Since minor and sideband components are controlled primarily by the magnitudes of the major constituents the focus is placed on the residuals to the latter. Apart from *zero* terms and formal errors the mutual agreement of the empirical models on certain residuals provides a clear indication of deficiencies in the ocean tidal ERP models.

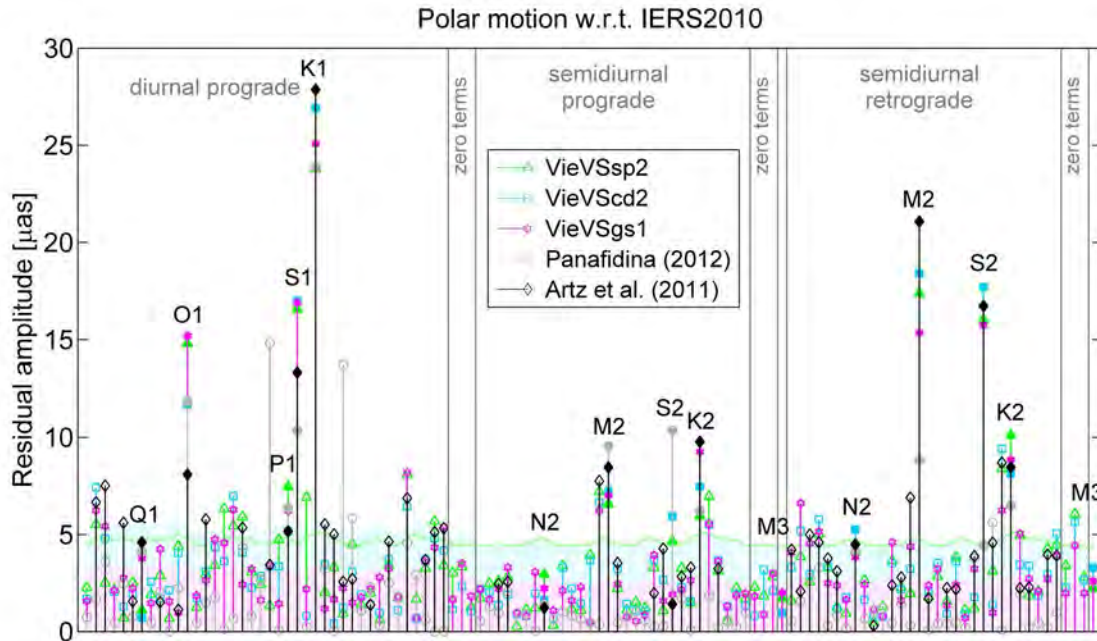


Figure 6.18: Residual amplitudes of empirical tidal models of polar motion w.r.t. IERS2010 in μas . The major constituents plus S_1 and M_3 are indicated by filled markers in addition to the corresponding label. The threefold formal errors of the internal solutions are shown as shaded areas or a thick line in the respective color itemized in the figure legend.

The most distinct misfit, unanimously seen by all geodetic models, occurs for the K_1 tide, and w.r.t. both ocean tidal models. At the O_1 period the empirical models vary in the maximum residual, the model by Artz *et al.* (2011) is closer to IERS2010, whereas the internal solutions are more consistent with TPXO7.2. For P_1 all residuals are slightly above the significance threshold without showing a clear preference for any ocean tidal model. In terms of S_1 there is an expected distinct peak varying from $10 \mu\text{as}$ to about $17 \mu\text{as}$, which is analyzed later at the end of this section together with the corresponding S_1 wave in UT1.

In the semidiurnal band significant residuals are visible in both polar motion spectra at the M_2 , S_2 and K_2 periods. The differences between the residuals to IERS2010 and TPXO7.2 are marginal in the prograde part, while a thoroughly striking improvement for the M_2 and S_2 terms with TPXO7.2 is proven in the retrograde domain.

The GPS results are actually in slight contradiction with the VLBI results for several cases. Yet, as stated earlier in Section 6.3.2, especially the GPS terms in the vicinity of one or two cycles per sidereal day have to be treated with caution, because of unexplained interactions with the orbit modeling. In spite of certain caveats the external GPS solution is retained in the comparison, because it is independent of the VLBI results and the most precise technique to determine polar motion at that.

The outstanding spike at K_1 is persistently measured in reference to all three ocean tidal ERP models. An even more striking residual is noticed with HAMTIDE11a as reference (see Figure B.4

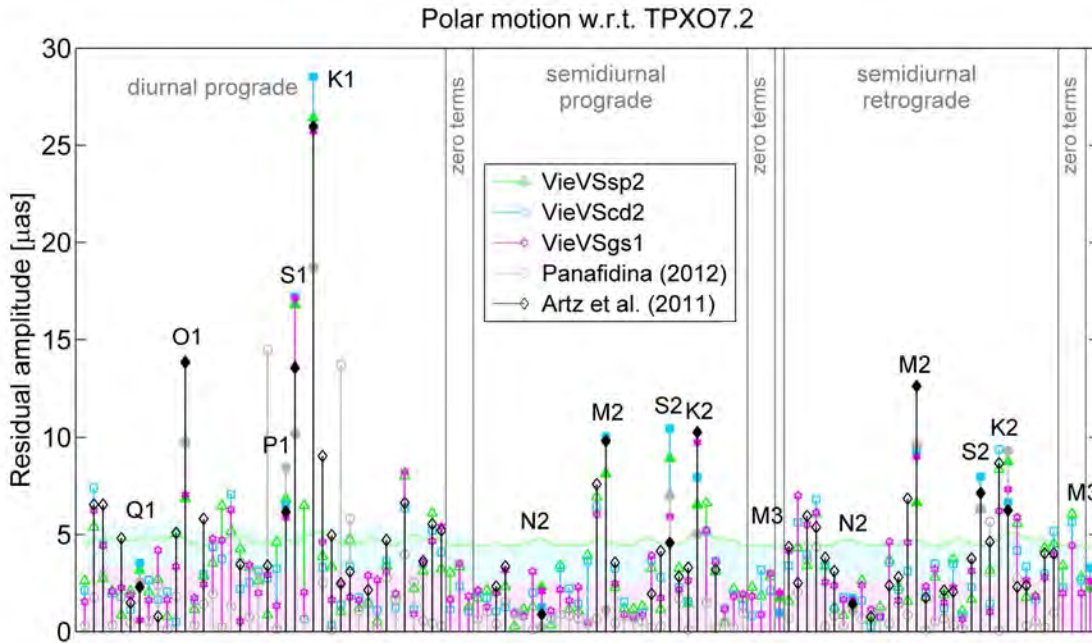


Figure 6.19: Residual amplitudes of empirical tidal models of polar motion w.r.t. TPXO7.2 in μas . The major constituents plus S_1 and M_3 are indicated by filled markers in addition to the corresponding label. The threefold formal errors of the internal solutions are shown as shaded areas or a thick line in the respective color itemized in the figure legend.

in the Appendix). This consensus among the ocean tide models prompts the question whether this is really a shortcoming of the ocean tide models. Another high-frequency ERP model that is applied already in the figures represents the effect of the lunisolar torque on the triaxial figure of the Earth, also called polar libration. The conventional model comprises corrections for

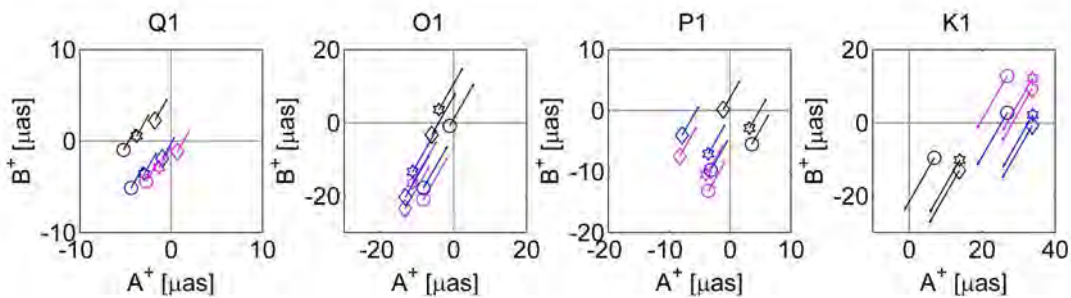


Figure 6.20: Effect of the polar libration correction on the empirical polar motion terms from VieVSgs1 (hexagrams), Artz *et al.* (2011) (diamonds) and Panafidina (2012) (circles) w.r.t. IERS2010 (black), TPXO7.2 (magenta) and HAMTIDE11a (blue). The arrows point from the uncorrected positions (indicated by markers) to the corrected positions. The starting values are thereby the pure residuals to the respective ocean tidal ERP model.

the four major diurnal constituents and some smaller terms. These corrections are illustrated

in Figure 6.20. Representatively for all empirical models, the phasor diagrams show the three rigorously estimated ensembles of tidal terms, i.e. the internal global solution VieVSgs1 and the external VLBI and GPS models. We can observe a general deterioration of the closure between the geodetic and the oceanic IERS2010 terms if the polar libration effect is added. Apart from K_1 where the tendency is not so clear, the polar libration correction definitely improves the consistency of observed ERP and the recent ocean tidal models, TPXO7.2 and HAMTIDE11a. This might be an evidence that the newer ocean tide models predict an Earth rotation contribution closer to reality. Of course a large gap remains to be explained at the K_1 constituent for all three ocean tidal ERP models. The observed residuals can most probably be attributed to deficiencies in the ocean tidal models. Imperfections in the polar libration model of such a magnitude can practically be excluded, since Brzeziński & Mathews (2003) found that differences among different libration models did not exceed $0.2 \mu\text{s}$ in terms of the individual amplitudes.

The magnitudes of the universal time residuals to IERS2010 and TPXO7.2 are shown in Figures 6.21 and 6.22. Compared empirical models as well as the notation and design of the illustrations are the same as for polar motion. Based on the size of the *zero* terms it seems that

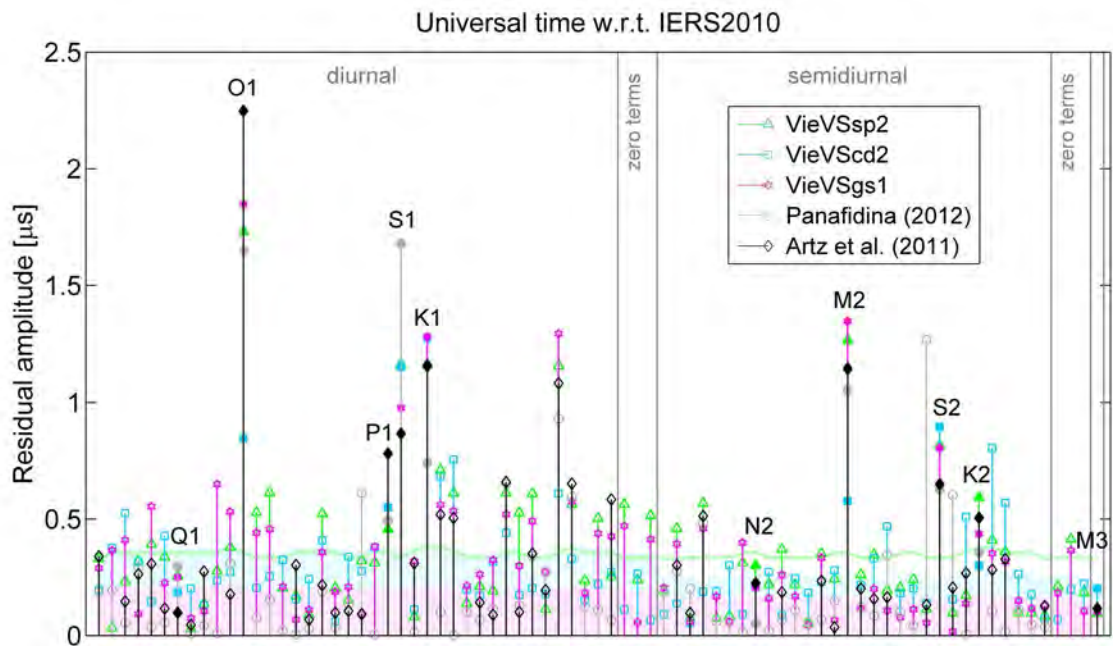


Figure 6.21: Residual amplitudes of empirical tidal models of universal time w.r.t. IERS2010 in μs . The major constituents plus S_1 and M_3 are indicated by filled markers in addition to the corresponding label. The threefold formal errors of the internal solutions are shown as shaded areas or a thick line in the respective color itemized in the figure legend.

the threefold uncertainties of the estimations are somewhat too optimistic in the case of UT1, as three terms exceed the threshold. The estimate of the terdiurnal M_3 tide is below the level of significance as in the polar motion case. The largest discrepancies to the ocean tidal ERP models arise for the O_1 and M_2 waves. Regarding O_1 the agreement is slightly better w.r.t. TPXO7.2,

while this model is slightly worse in the reduction of the M_2 residual. Also the Q_1 residual is notable in Figure 6.22, but insignificant w.r.t. IERS2010 (Figure 6.21). The deviations of all other major components, P_1 , K_1 , N_2 , S_2 and K_2 , are smaller with TPXO7.2 as reference than with IERS2010. Besides from the frequently discussed major terms, a prominent peak is spotted in the IERS2010 spectrum at the period of the OO_1 tide (near the end of the diurnal band). It is present also when TPXO7.2 is used, but the discrepancy is less pronounced. OO_1 is a constituent which is usually not explicitly estimated in ocean tide models, instead its characteristic is controlled by O_1 and K_1 . Evidently its residual is therefore scaled with the O_1 and K_1 residuals.

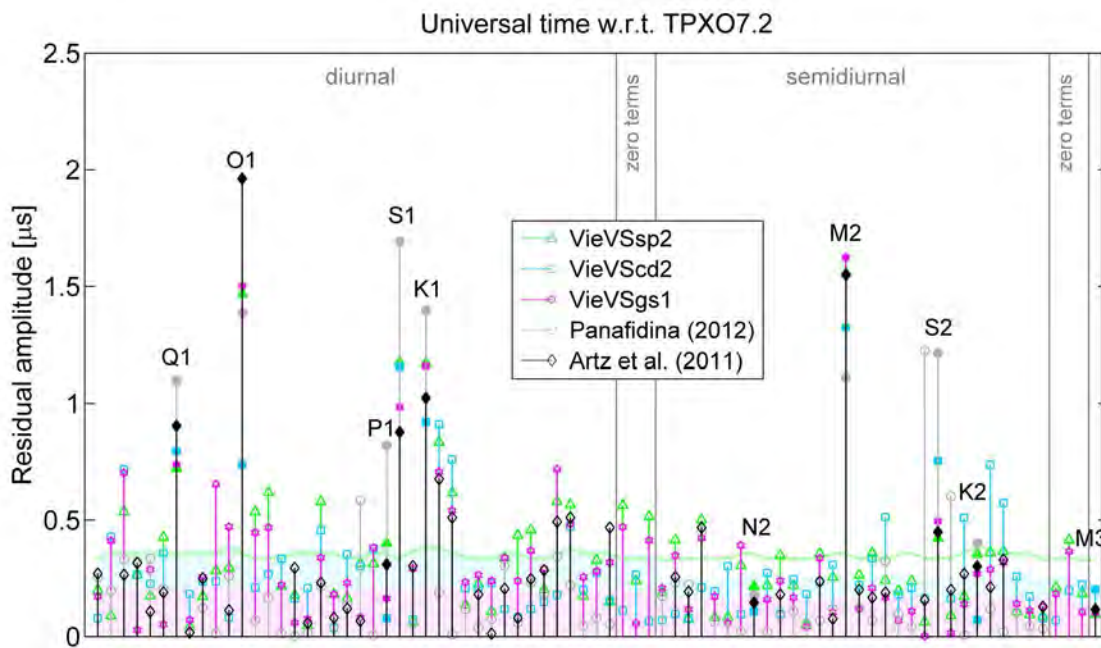


Figure 6.22: Residual amplitudes of empirical tidal models of universal time w.r.t. TPXO7.2 in μs . The major constituents plus S_1 and M_3 are indicated by filled markers in addition to the corresponding label. The threefold formal errors of the internal solutions are shown as shaded areas or a thick line in the respective color itemized in the figure legend.

In terms of universal time, the solution from demodulated ERP, VieVScd2, exhibits a rather distinctive disagreement with the other empirical tidal terms for O_1 and M_2 . As mentioned in the previous section this divergence is probably connected with the demodulated period of 13.66 days for both terms, where strong zonal tidal variations reside in universal time. Further comments on the filter-like nature of the complex demodulation which can explain some loss of power at certain frequencies can be found in Böhm *et al.* (2011). The particular strength of this technique actually relies on facilitating the investigation of irregular geophysical signal in time domain. However, the examination of the demodulated ERP time series in this respect is beyond the scope of this work. This study is confined to the exploitation of the complex demodulation as an independent method for extracting harmonic variations, even though this is not the most beneficial utilization.

Similar to the high-frequency polar motion, the effect of libration was considered also in high-frequency universal time. This means the residuals in Figures 6.21 and 6.22 are corrected already for spin libration. In contrast to polar motion, the libration affects UT1 in the semidiurnal band. The effect of applying or omitting this correction on the residuals of the measured Earth rotation variations w.r.t. the three inspected ocean tidal ERP models is demonstrated in Figure 6.23. In general, the residuals for almost all solutions w.r.t. any of the ocean tide models are decreased by application of the spin libration correction. This does not hold for the K_2 term, where the closure is improved only for the GPS model, but slightly degraded for the VLBI models.

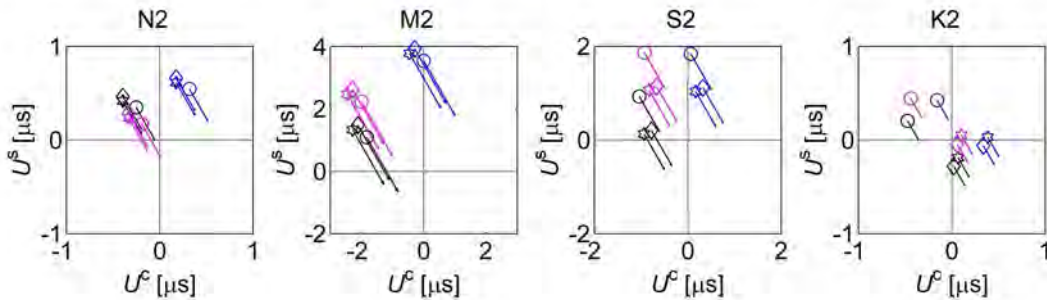


Figure 6.23: Effect of the spin libration correction on the empirical UT1 terms from VieVSgs1 (hexagrams), Artz *et al.* (2011) (diamonds) and Panafidina (2012) (circles) w.r.t. IERS2010 (black), TPXO7.2 (magenta) and HAMTIDE11a (blue). The arrows point from the uncorrected positions (indicated by markers) to the corrected positions. The starting values are thereby the pure residuals to the respective ocean tidal ERP model.

Apportioning the geophysical excitation at the period of the S_1 tide is fairly more complex than in the cases of other constituents. The gravitational excitation of the S_1 ocean tide is minor compared to the sea level oscillations induced mainly by the diurnal atmospheric pressure tide, which is in turn generated by the differential heating of the Sun. The thermal expansion of the ocean water due to the direct effects of the varying insolation is a negligible contributor to the radiational S_1 tide (Ray & Egbert, 2004). Owing to its insignificant gravitational portion, standard ocean tide models where the minor terms are inferred using admittance assumptions, do not adequately predict the S_1 tide. The missing radiational ocean tidal part of the wave should explain a fraction of the residual peak observed in Earth rotation. In addition to the forcing of the ocean, atmospheric pressure variations and wind fields also act on the surface of the solid Earth. This atmospheric, chiefly thermal S_1 tide should justify the remaining Earth rotation signal at that period. In Figure 6.24 the residuals of the VLBI solutions to TPXO7.2 are provided for the S_1 component in polar motion (a) and in universal time (b). The gravitational ocean tidal portion is therefore considered already in the VLBI estimates. In addition the picture displays predicted contributions to S_1 from different geophysical models (see figure caption).

By visual examination we detect reasonable agreement among the VLBI solutions and as well among the OAM contributions. But for the total AAM and OAM contributions there is no consensus between the geophysical models, although AAM1 and AAM3 show at least similar direction.

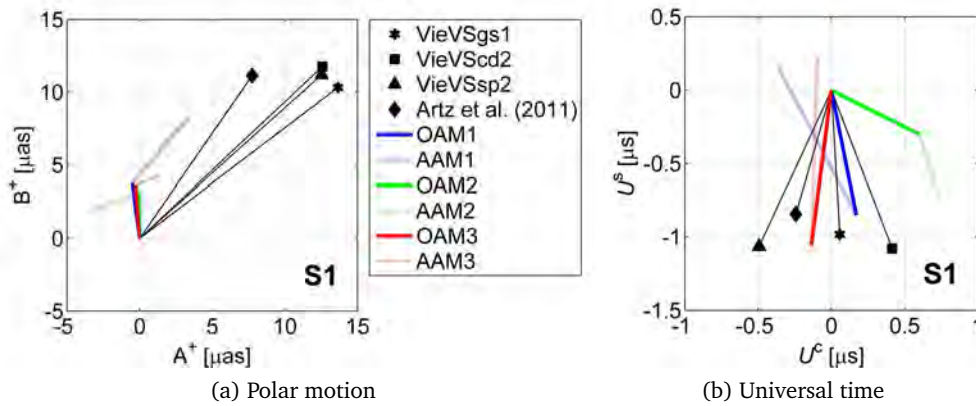


Figure 6.24: The S_1 term observed by VLBI and its Earth rotation contribution predicted from different geophysical models. The VLBI values are given w.r.t. the ocean tidal ERP model based on TPXO7.2. The ensemble termed OAM1 and AAM1 was derived by Brzeziński *et al.* (2004) from a barotropic ocean model (Ponte & Ali, 2002) and NCEP/NCAR reanalysis fields (Kalnay *et al.*, 1996; Salstein & Rosen, 1997). The second combination OAM2 and AAM2 is taken from Brzeziński (2011) and based on OMCT (Ocean Model for Circulation and Tides) and the ERA Interim reanalysis of the ECMWF (refer to Dobslaw *et al.*, 2010, and the references therein for further information about models and data). OAM3 is transferred to Earth rotation variations from S_1 OAM values provided in Ray & Egbert (2004). This harmonic S_1 component was deduced from a hydrodynamic ocean model forced by the S_1 pressure tide. A consistent AAM counterpart was not readily available for this radiational S_1 ocean contribution. Yet a reasonably consistent AAM contribution was provided by M. Schindelegger (personal communication, 2012). Atmospheric polar motion and UT1 excitation were calculated from ERA-40 reanalysis data (Uppala *et al.*, 2005) of the years 1985–2001. The resulting phasors are designated AAM3.

Moreover, we find the OAM1+AAM1 and OAM3+AAM3 combinations closer to the VLBI polar motion observations, while the situation is reversed in the case of UT1, where OAM2+AAM2 and the residuals show a better match. The solitary OAM1 or OAM3 S_1 models would actually do best in explaining the UT1 residuals seen by VLBI. However, both AAM portions propose a distinct counteraction and thus undo the agreement. At present none of the geophysical models can be fully confirmed by observations. On these grounds it should be noted that a harmonic modeling of the S_1 tide and subsequent inclusion into high-frequency ERP models would be possible, but should not be accomplished unless there is a satisfactory agreement between geophysical models.

6.4 Comparison of empirical and theoretical models – long-period tidal band

Akin to the objective in high-frequency tidal domain, the present work endeavors to uncover discrepancies between predicted and observed tidal UT1 variations also in the low-frequency band. In contrast to subdaily ERP models, models of zonal tidal variations in UT1 are less important for the processing of space geodetic observations, but primarily interesting for UT1 pre-

diction. Another aim, which is somehow embracing all studies of Earth rotation, is to close the excitation budget at least for defined period ranges to gain a better understanding of geodynamic processes.

6.4.1 Mutual agreement of empirical models

Several UT1 series are at hand to determine empirical zonal tidal models. These various empirical models serve as a measure to assess the reliability of the observed variations on the one hand and give an insight to the advantages and disadvantages of different estimation strategies on the other hand. In order to enhance the perceptibility of differences, only the residuals to the conventional zonal tidal model are displayed in the following. At present this is the model recommended in Chapter 8 of the IERS Conventions (2010), later on referred to as IERS2010. Whenever possible, the unconstrained coefficient residuals are shown. Only in cases where the time series are too short to resolve sideband terms, constrained solutions are consulted for comparisons as well. For the solutions including semiannual and annual terms, however, a constraining of the amplitudes was inevitable as mentioned in Section 6.1.3.

In fact, most of the following comparisons are related to the VieVSlp1 solution, because it is considered to be optimal in terms of observation length and processing strategy. Hence, other empirical models are essentially used to scrutinize the VieVSlp1 model, evaluate the general accuracy of such models and detect weaknesses of the estimation procedure. Figure 6.25 contains four pairs of opposed sets of zonal tidal UT1 terms. All are given w.r.t. IERS2010 and were calculated with 48 days filter cutoff and solely AAM excitation removed. The plots, therefore, comprise major and side terms with periods from 5.64 to 34.85 days, arranged in ascending order except for the *zero* term with 16.63 days which is placed at the end of the line. Plot (a) compares the VieVSlp1 solution with the corresponding terms derived from the IERS C04 05 UT1 series with its genuine sampling of one day. Some, especially smaller residual coefficients disagree in the sign and pronounced discrepancies are seen at the longer periods. From subfigure (b) it can be inferred that a couple of these differences can be attributed to the different sampling of the time series. This plot shows again the VieVSlp1 solution, but compared to a solution derived from the C04 series interpolated to the VieVSlp1 epochs. It becomes clear that many of the deviations are caused by the daily intervals of the original C04 series. The higher sampling rate seems to be advantageous for the estimation, as it yields slightly smaller uncertainties and also better decorrelation of adjacent terms (this is not demonstrated here, but was verified in the course of this work). At any rate, it should be kept in mind that the estimation of the zonal tidal signals is sensitive to the observation intervals. This sensitivity was surveyed also in terms of subdiurnal sampling by generating time series with 6-h and 5-h resolution using the OCCAM software (OCCAMlp1a, OCCAMlp1b). The resulting differences in the zonal tidal terms are minute, though. Thus only the solution from the 6-h series is compared to the VieVSlp1 solution, displayed in plot (c). The two models are in reasonable agreement within their threefold formal errors, indicated by the errorbars.

6.4 Comparison of empirical and theoretical models – long-period tidal band

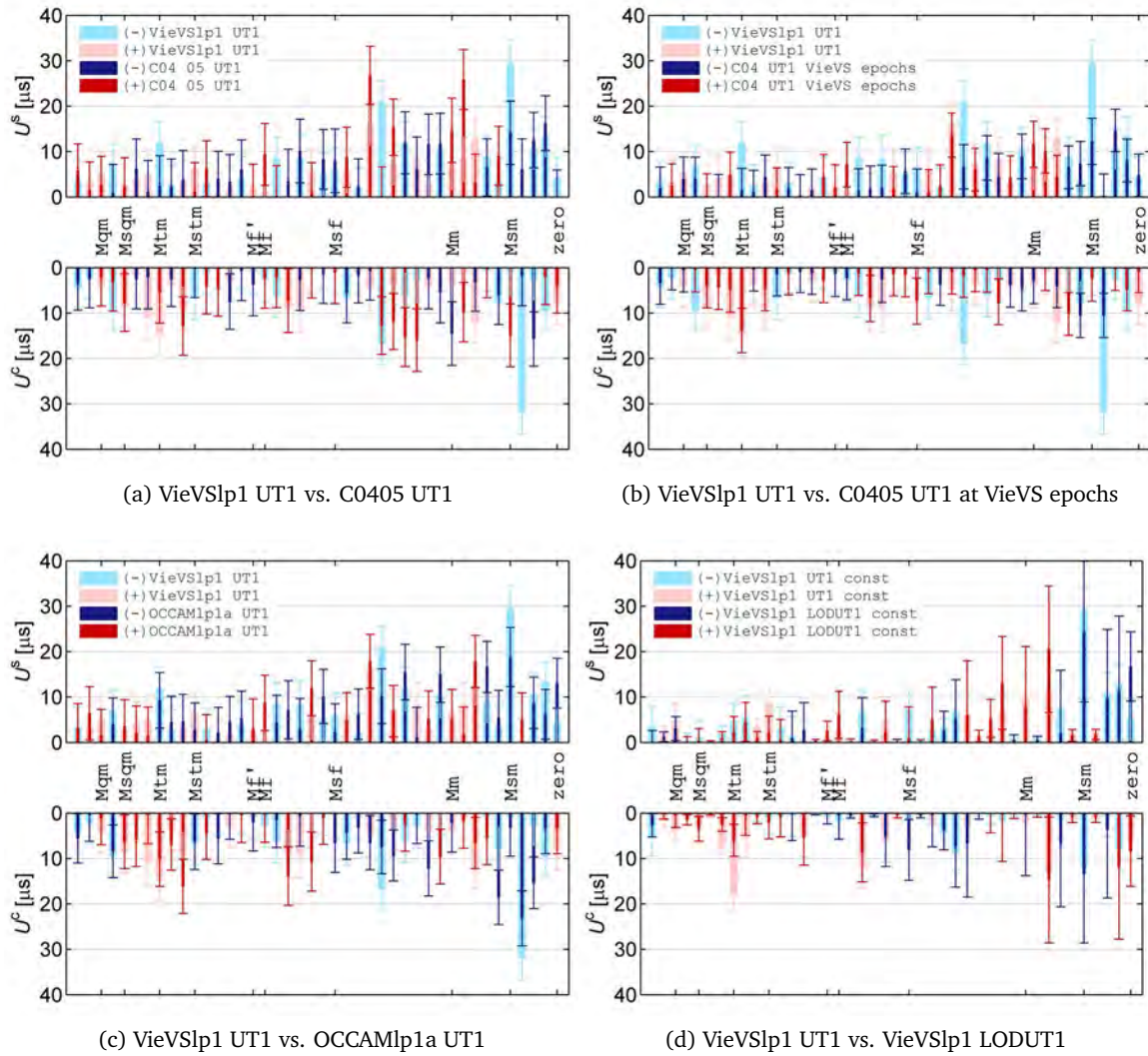


Figure 6.25: Residual zonal tidal coefficients U_i^s (top panels) and U_i^c (bottom panels) derived from each two different time series (light and dark colors) with 48 days filter cutoff and AAM contribution considered. The bars are plotted in light or dark red for positive values and in light or dark blue for negative values. The errorbars show the threefold formal error deriving from the corresponding adjustment.

It was already demonstrated in Section 6.1.3 that reducing the integrated AAM contribution from UT1 introduces spurious signal if periods longer than monthly are involved. Up to 35 days the estimation of the zonal tidal variations from UT1 is considered reliable, but there is, nevertheless, interest in variations with longer periods as well. Therefore, the investigations are continued in terms of LOD, instead of UT1 amplitudes. To this end, VLBI-based UT1 estimates were transferred to LOD using centered difference quotients. Plot (d) of Figure 6.25 presents VieVSlp1 UT1 coefficients contrasted with VieVSlp1 LOD coefficients which were converted to UT1 for the comparison. The constrained solutions are shown in this case to get a more clear picture and because these are employed in the subsequent comparisons which include terms with

periods up to the annual. According to error propagation rules, UT1 errors deduced from LOD errors are scaled proportionally to the period, which is why the LODUT1 errorbars at the longer periods are significantly larger. For ideal measurements, the results of both approaches should be almost equal. However, since geodetic and geophysical observations are affected by systematic and random errors, minor discrepancies occur, mostly due to the preprocessing differences. The overall level of agreement viewed in the different plots of Figure 6.25 suggests that model deviations below approximately $10 \mu\text{s}$ cannot be regarded as significant. This statement is supported by several of the estimated *zero* terms and obverse results around this limit are also recognized at different periods for some solutions. Of course this is valid predominantly in terms of UT1. Since zonal tidal terms have a generally smaller magnitude in LOD and formal errors are slightly smaller as well, this significance level is also somewhat lower for LOD, as we shall see later.

The only internal GPS solution intended for the study of long-period LOD variations, GNSSlp1, was finally rejected for the validation of theoretical zonal tidal models, because the observation period of two years is simply too short to obtain reliable results. Figure B.6 in the Appendix shows a comparison of the zonal tidal LOD terms up to 35 days derived from LOD of CODE and from the series GNSSlp1. For the CODE model in plot (a) the full time series (1995–2011) was used, resulting in large differences to the GNSSlp1 solution. The CODE model in plot (b) was calculated from a reduced series spanning only 2005–2007, like the GNSSlp1 solution, and is in good accordance with the corresponding empirical model. Thus, the disagreement is fully attributed to the short observation period and not to a putative bad data quality. The impact of the time series length was supplementary examined using the example of the VieVslp1 LOD series. The tidal terms, deduced from the full period, were compared to single models calculated from reduced time series successively extended by one year. The length of the starting series was two years spanning 2009–2011. Interestingly, the biggest differences occur between models spanning two years and three years. A real stabilization of the coefficient magnitudes, however, arises only with an observation period of ten years and more.

All residual coefficient results presented so far were computed from time series which were reduced by taking into account atmospheric excitation only. In view of a best possible cleaning of the original UT1 or LOD series from irregular geophysical fluctuations, oceanic influences should be considered as well. As mentioned previously, the OAM data (consistent with the used AAM data) is available only after 1993. However, constraints have to be introduced either way if periods up to the annual are estimated, and the VLBI data of the early years is more noisy at that. A comparison of terms estimated from the full period with those derived using only data as of 1993 proved that the differences are insignificant. By checking an LOD model with only AAM considered against one with AAM+OAM reduced (Figure 6.26), we can assert that minor changes are present for some terms such as *Msm* or *Sa*. Yet it cannot be affirmed that one solution is more correct than the other. The justification to consider OAM as well is found by means of juxtaposing the coherence of LOD (with zonal tides removed) with LOD from AAM and with LOD from AAM+OAM.

The magnitude squared coherence for these two pairs is displayed in Figure 6.27. Apparently,

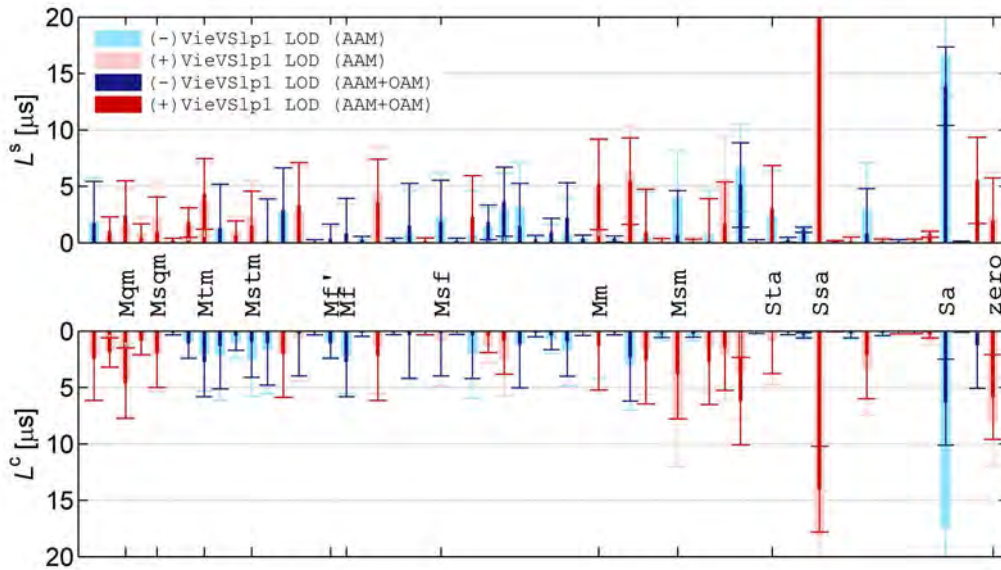


Figure 6.26: Residual zonal tidal coefficients L_i^s (top) and L_i^c (bottom) derived from VieVSlp1 LOD with AAM reduced (light colors) and VieVSlp1 LOD with AAM+OAM reduced (dark colors); 800 days filter cutoff. The bars are plotted in light or dark red for positive values and in light or dark blue for negative values. The errorbars show the threefold formal error deriving from the corresponding adjustment.

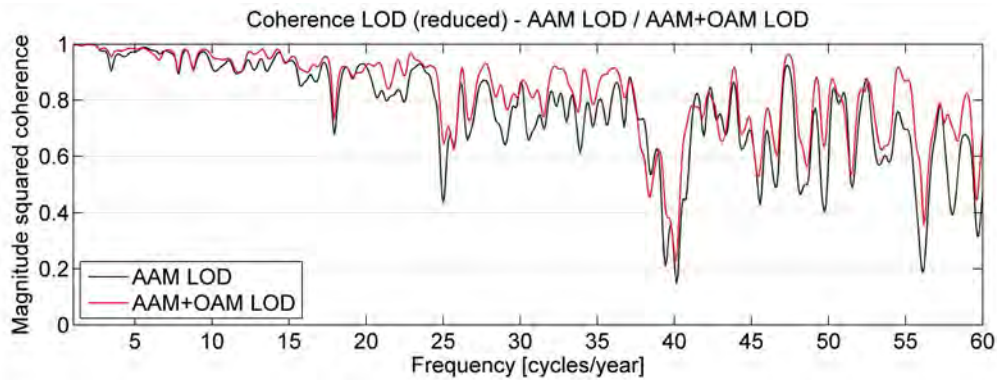


Figure 6.27: Magnitude squared coherence between LOD with zonal tides eliminated and AAM LOD (black), and between LOD (reduced) and AAM+OAM LOD (red), plotted against the frequency in cycles per year.

the coherence with the geodetic excitation is improved if the sum of AAM and OAM is used. This implies that subtracting the aggregated AAM+OAM contribution yields an LOD signal which is less corrupted by aperiodic variations. On grounds of this evident benefit and considering the marginal weight of the early observations, it was decided to shorten the time series and utilize the sum of AAM and OAM in the signal preprocessing.

6.4.2 Assessment of zonal tidal UT1/LOD models

It was already announced in Section 3.2.3 that there are two different theoretical models of zonal tidal variations in UT1 or LOD which are validated in the frame of this dissertation. These two models were consecutively published in the Conventions of the IERS. As a matter of fact, a study conducted as part of the present work (Englich *et al.*, 2009) contributed to confirm certain deficiencies of the older model (IERS2003) and supported the decision to switch to the model which is currently the conventional one (IERS2010). In the following both models are compared with the VieVSlp1 LOD solution and a set of terms derived from C04 LOD, interpolated to six-hourly epochs. The assessment of the model terms is executed up to a side term of the annual period, which was the longest period fitted to the LOD observations. The variation with the longest period incorporated in the IERS models, at 18.6 years, is inaccessible with present observation time spans and in addition superposed by unpredictable decadal fluctuations due to core-mantle interactions. The magnitudes of the residual coefficients w.r.t. IERS2003 and IERS2010 are shown in Figure 6.28a and 6.28b, respectively.

Except for some minor constituents, the VLBI-observed values and the terms derived from the C04 series agree well within the threefold uncertainties of the VieVSlp1 terms. The formal errors of the solution from C04 LOD (with six-hourly sampling) are distinctly smaller, because a much larger number of pseudo-observations is subjected to the least-squares adjustment.

Conspicuous and significant peaks are present in the spectrum relative to IERS2003 at the fortnightly (Mf' , Mf), the monthly (Mm), the semiannual (Ssa) and the annual (Sa) period. The observed amplitudes w.r.t. the IERS2010 model show a reduction of these deviations for the fortnightly and the monthly tidal constituent. All other residuals are practically unaffected by the transition from IERS2003 to IERS2010. Although the underlying solid Earth tide models are also different, the only difference which can actually be well identified arises from the diverging treatment of the ocean tidal contribution. IERS2003 incorporates only an equilibrium ocean tidal portion, whereas a dynamical ocean tidal contribution was considered in IERS2010 for the fortnightly and the monthly tide (see Section 3.2.3). The introduction of the dynamical tides imports in particular a significant out-of-phase part. By examining the phasor diagram of the VieVSlp1 residual coefficients (Figure 6.29) we can clearly discern that the major part of the Mf and Mm residuals w.r.t. IERS2003 is constituted by the out-of-phase terms. The residual terms to IERS2003 are shown as green plus signs and the terms w.r.t. IERS2010 are displayed as blue circles. The magnitude of the *zero* term is provided as red circle and the maximum threefold uncertainty of the VieVSlp1 terms is shown by the gray circle. In the case of LOD the out-of-phase part, also called quadrature, is established by the sine coefficient L_i^s , because cosine is the base function in the utilized phase convention. It is vice versa for the zonal tidal variations in UT1, where sine is the base function and U_i^s is the in-phase coefficient.

As a further interesting fact, Figure 6.29 demonstrates that the out-of-phase component as well dominates the Ssa and Sa residuals w.r.t. both theoretical models. In view of the *zero* term size as significance level, the semiannual and annual terms represent the only significant devia-

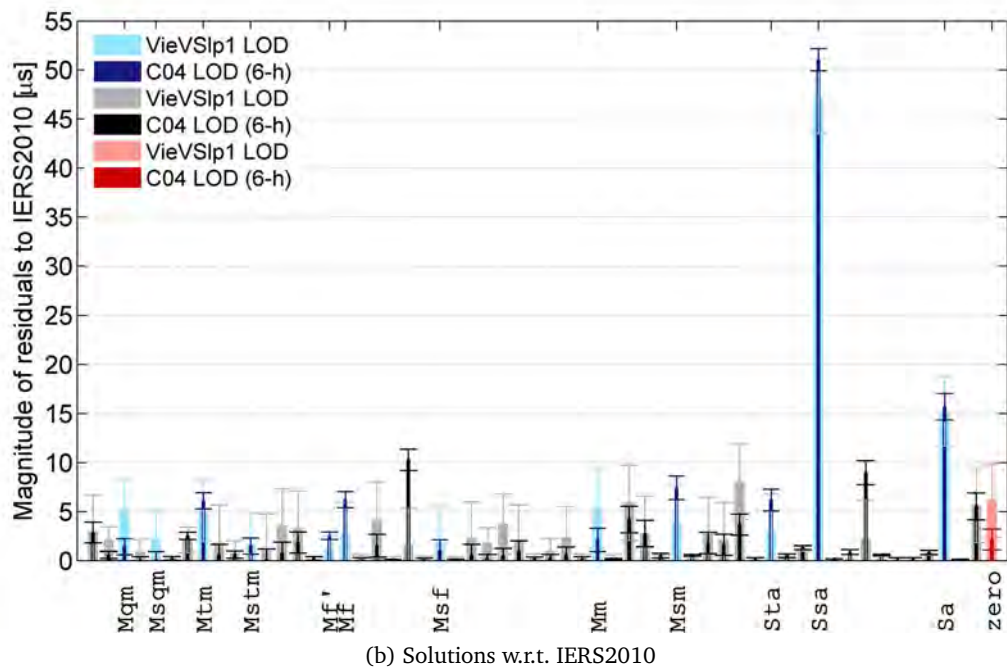
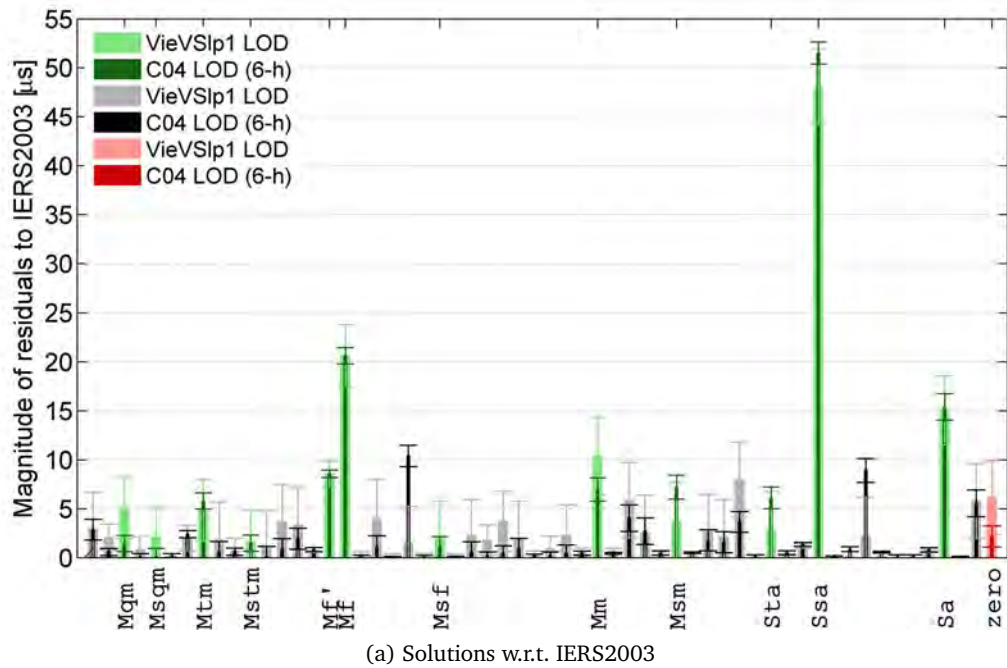


Figure 6.28: Magnitude of the residuals to the IERS2003 and IERS2010 models for zonal tidal variations in LOD based on VieVSlp1 LOD (light colors) and C04 LOD at 6-h intervals (dark colors); 800 days filter cutoff, AAM+OAM considered. Green and blue colors indicate the corresponding major constituents, while side terms are plotted in gray and black and the *zero* term is displayed in red colors. The errorbars show the threefold formal error deriving from the corresponding adjustment. Note: the LOD units refer to the nominal day.

tions (among the major tides) to the IERS2010 model. The sizes of these discrepancies are remarkable however. The out-of-phase parts of the theoretical model terms are much smaller than the in-phase parts if existent at all. Elastic body tides generate only in-phase signal, out-of-phase contributions arise either from mantle anelasticity (to a very small extent) or from ocean tides departing from equilibrium. Yet there is no ocean tide model suggesting that these long-period tides exhibit a significant dynamic behavior. Incorporating for example the Sa and Ssa effects of Weis (2006) into the theoretical models would result in a difference of merely a few microseconds. Underestimated ocean tidal excitation, therefore, drops out as a reason for the observed discrepancies. The most reasonable explanation for these extraordinary peaks is an insufficiently removed atmospheric or non-tidal oceanic input, connected with seasonal variations.

In order to substantiate this assumption, the residuals of VieVS1p1 w.r.t. IERS2010 were additionally evaluated utilizing spectral analysis. Since the VLBI-based data is unequally spaced, the so-called CLEAN algorithm, which is designed for the analysis of data with gaps, was employed following Baisch & Bokelmann (1999). The residual spectrum in μs is given in Figure 6.30 along with the frequencies of the major tidal terms indicated by vertical lines.

The most striking features of the CLEAN spectrum are the two peaks at one and two cycles per year, i.e. around the annual and semiannual tidal line. The higher frequency range suggests an overall noise floor of the residuals of 5–10 μs . This is partly attributable to VLBI measurement errors, but to some extent it is presumably atmospheric or oceanic signal which is not accurately represented by AAM and OAM. Somewhat larger residual signal can be seen around 60 days and also around 17 days. These periods are very far from any tidal variations, but can be found among fluctuations of the atmosphere, so they suggest again that there are remains of geophysical fluids signal included in the LOD residuals.

In a review on atmospheric and oceanic excitation of LOD variations Gross *et al.* (2004) stressed the importance of upper atmospheric winds at seasonal time scales. They estimated the AAM contribution of zonal winds above 10 hPa to overtop the oceanic mass and motion terms. Since the employed AAM from NCEP is computed from data up to this pressure level only, the thus neglected impact of the upper zonal winds could eventually account for the observed residuals at the semiannual and annual period. The uppermost layer of the ECMWF numerical weather models is the 1 hPa pressure level. So AAM based on ECMWF data includes the excitation due to high atmospheric winds.

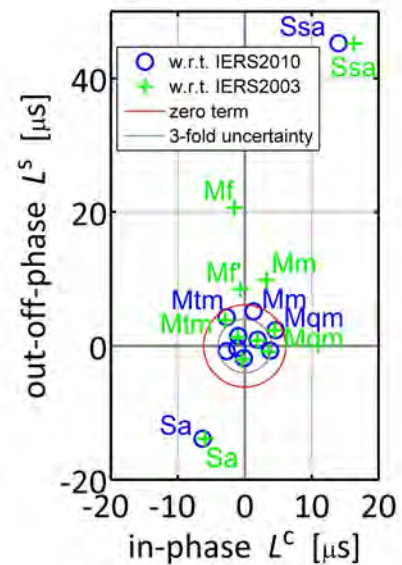


Figure 6.29: Residual zonal tidal LOD terms (solution VieVS1p1) w.r.t. IERS2003 and IERS2010. Note: the LOD units refer to the nominal day.

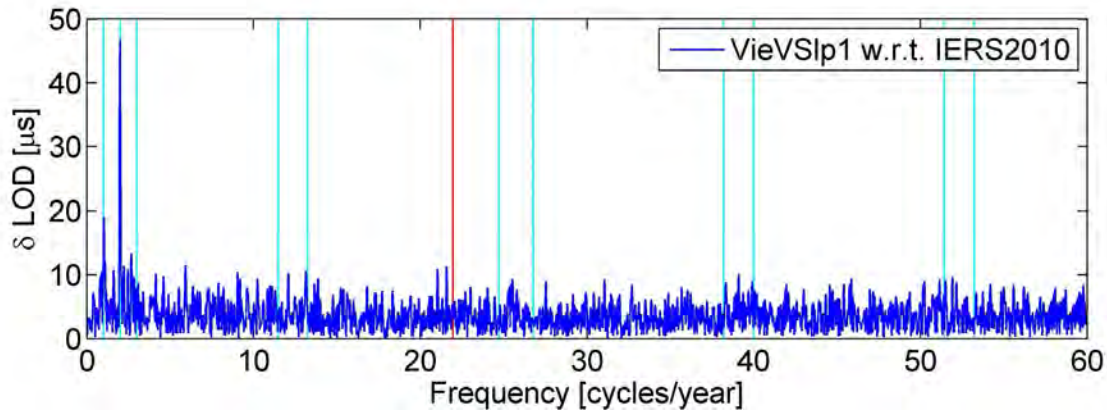


Figure 6.30: Amplitude spectrum of δLOD VieVSlp1 w.r.t. IERS2010 (blue line). The cyan vertical lines are placed at the frequencies of the major tidal constituents, the line of the *zero* term is printed in red. Note: the LOD units refer to the nominal day.

This issue was investigated in a quick-look study by means of an alternative set of consistently processed excitation functions, involving AAM from ECMWF. These datasets are publicly available at the GGFC and are calculated by a team at GFZ (GeoForschungsZentrum) in Potsdam (Dobslaw *et al.*, 2010). The excitation values utilized here were AAM from ECMWF ERA Interim reanalysis and corresponding OAM from OMCT and HAM (Hydrologic Angular Momentum) from LSDM (Land Surface Discharge Model). The VieVSlp1 LOD data with 800 days filter cutoff was preprocessed using the GFZ models, for the same truncated time span as previously (1993–2010.5). Subsequently, the IERS2010 model was removed and residual zonal tidal terms up to annual were estimated for three scenarios. Starting with only AAM considered, the preprocessing was successively completed by accounting for OAM and then HAM as well. These were compared to the estimated zonal tidal residuals derived from VieVSlp1 LOD with the NCEP and ECCO models removed.

The outcome of the short study strongly corroborates the assumption that the upper atmospheric winds are the dominant source for the spurious semiannual and annual signal that we saw in the residual tidal spectrum. When using AAM based on ECMWF for the data cleaning, these peaks are reduced almost below the level of significance. However, if the consistent OAM contribution from OMCT is removed too, the residual in the annual term is again distinctly enhanced. Accounting for the complete GFZ geophysical fluid perturbation (AAM+OAM+HAM) yields a reasonable residual in the semiannual term, but a considerably larger residual in the annual term than was achieved with the NCEP+ECCO model combination. A graphical presentation of the comparisons is provided in the Appendix, Figure B.7.

The smallest residuals would probably be obtained by removing the contribution of a combined AAM(ECMWF)+OAM(ECCO) model, unfortunately, these datasets are not consistent. Having in mind a geophysical interpretation of zonal tidal residuals it is, however, crucial to separate different effects in a clear and consistent way. Otherwise the results could be corrupted leading to

interpretation of spurious signal. By reason of these inconsistencies and disagreements between geophysical fluid datasets, the GFZ EAMF were exploited merely to evaluate the meaning of the residual seasonal peaks. Apart from that, the results based on this data set were not interpreted further.

6.4.3 Results for the zonal response coefficient

As a last addendum to the topic of zonal tidal variations, selected results for the zonal tidal response coefficient κ are provided in this section. It is not the intention to give a geophysical interpretation, such as inferring mantle anelasticity or core-mantle coupling from the κ magnitudes and phases. Rather, the values of different solutions shall be compared to rate the sensitivity of the estimated zonal response coefficient to varying processing schemes.

There are actually two possibilities to calculate κ : either it is estimated from the reduced LOD or UT1 time series directly within a least-squares adjustment, or the previously estimated zonal tidal terms are converted to κ using the proportionality relations (3.23) or (3.24). For this study it was decided to apply the rigorous approach, using the corresponding observation equations derived in Section 6.1.4 (Equations 6.11 and 6.12). Furthermore, tidal terms which differ by one cycle in 18.6 years were assumed to have a common response function. The reliability of estimated κ values increases significantly with the size of the potential amplitude. The estimation of response coefficients for spectral components with a bad signal-to-noise ratio is problematic therefore. The same applies for periods at which the reduced time series are evidently contaminated by fragments of atmospheric signal, such as the annual and semiannual. Residual non-tidal signal which is large in relation to the total zonal tidal amplitude would severely corrupt the results. For this reasons κ estimates are presented only for periods below 35 days with a signal-to-noise ratio of at least 3:1 in terms of LOD. The noise or uncertainty of the UT1 or LOD series was pessimistically adopted to 10 μ s for this rough estimation. Five major constituents meet this criteria: the termensual (Mtm), the fortnightly (Mf , Msf) and the monthly (Mm , Msm) terms.

Figure 6.31 displays magnitudes and phases of κ , for the five selected frequencies, estimated from VieVSlp1 UT1 and VieVSlp1 LOD series with 48 days filter cutoff and AAM+OAM considered. The values are compared to the corresponding estimates of Chao *et al.* (1995) and kind of baseline values converted to κ magnitudes and phases from the zonal tidal coefficients of the IERS2010 model. The smallest uncertainties and closest estimates are seen for the terms with the largest amplitudes (Mf , Mm), as can be expected. At the other periods significant differences are noted, which are probably an effect of the slightly diverging preprocessing of UT1 and LOD data. Ocularly, the precision of UT1-based estimates at longer periods is higher than the one of the LOD values. This is a consequence of the increase of the zonal tidal UT1 amplitudes with the period. We could, hence, infer that UT1 allows for a more accurate estimation of the zonal response coefficient. On the other hand we know that errors of the AAM functions used for reduction of UT1 are also scaled upon integration. Consequently, it is impossible to ascertain which of the values

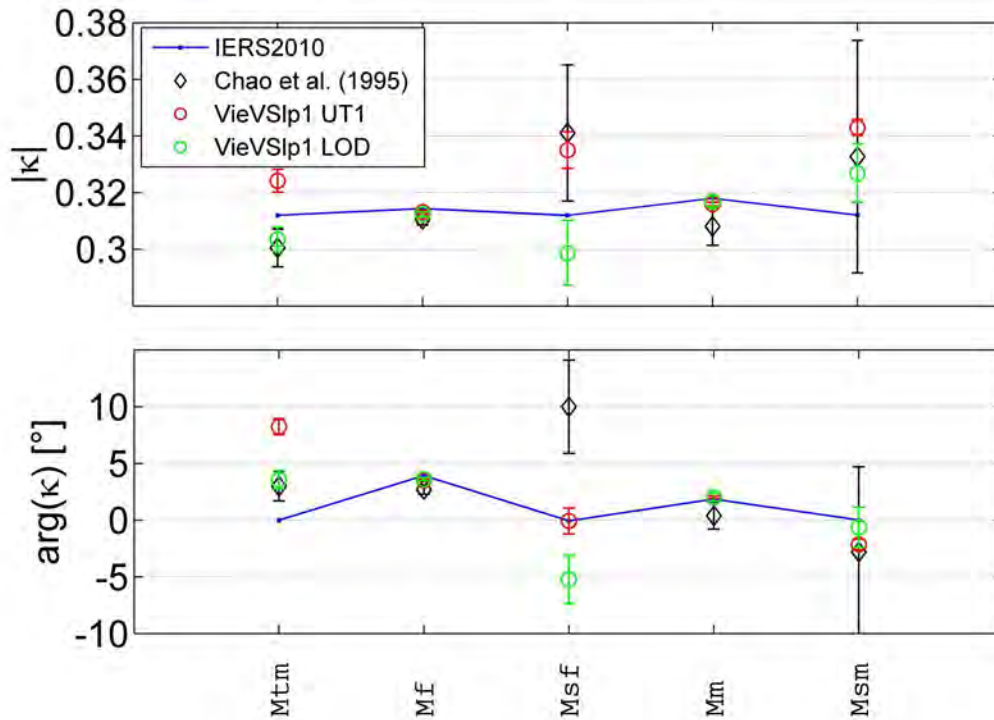


Figure 6.31: Magnitudes (top) and phases (bottom) of the zonal tidal response coefficient from different solutions for selected tidal frequencies. The errorbars indicate the plane standard deviations resulting from the adjustment.

(UT1- or LOD-based) are correct. The estimates from LOD are apparently closer to the baseline of IERS2010, but for example not necessarily closer to Chao *et al.* (1995). Of course, it should be added that Chao *et al.* (1995) determined their coefficients from observations of 13 years only, which were additionally less precise. This is reflected by the relatively large errorbars as well.

The magnitudes and phases shown in Figure 6.31 are provided numerically in Table 6.5 and Table 6.6, respectively. The numbers are complemented with a very recent estimate of the Mf response coefficient published by Ray & Egbert (2012), which agrees very well with the findings of this section in terms of magnitude as well as phase. In general, the results for Mf and Mm are considered reliable, with the magnitudes being precise to about 0.3%.

Table 6.5: Magnitudes of the zonal response coefficient $|\kappa|$ from various solutions.^a

Tide	Period	Chao <i>et al.</i> (1995)	VieVSlp1 UT1	VieVSlp1 LOD	IERS2010	Ray & Egbert (2012)
<i>Mtm</i>	9.13	0.301 ± 0.007	0.324 ± 0.004	0.304 ± 0.004	0.312	
<i>Mf</i>	13.66	0.311 ± 0.002	0.313 ± 0.001	0.312 ± 0.001	0.316	0.313 ± 0.001
<i>Msf</i>	14.77	0.341 ± 0.024	0.335 ± 0.006	0.299 ± 0.011	0.312	
<i>Mm</i>	27.56	0.308 ± 0.007	0.316 ± 0.001	0.317 ± 0.002	0.318	
<i>Msm</i>	31.81	0.333 ± 0.041	0.343 ± 0.003	0.327 ± 0.010	0.312	

^a Period in daysTable 6.6: Phases of the zonal response coefficient $\arg(\kappa)$ from various solutions.^a

Tide	Period	Chao <i>et al.</i> (1995)	VieVSlp1 UT1	VieVSlp1 LOD	IERS2010	Ray & Egbert (2012)
<i>Mtm</i>	9.13	3.0 ± 1.3	8.3 ± 0.7	3.6 ± 0.8	0.0	
<i>Mf</i>	13.66	2.7 ± 0.4	3.5 ± 0.1	3.6 ± 0.2	3.9	3.5 ± 0.1
<i>Msf</i>	14.77	10.0 ± 4.1	-0.1 ± 1.1	-5.2 ± 2.1	0.0	
<i>Mm</i>	27.56	0.4 ± 1.2	2.0 ± 0.1	2.0 ± 0.4	1.7	
<i>Msm</i>	31.81	-2.8 ± 7.5	-2.1 ± 0.5	-0.6 ± 1.8	0.0	

^a Period in days, phase in degrees (referred to the fundamental arguments of the tidal constituents)

Chapter 7

Summary, conclusions, and future prospects

Accurate models of Earth rotation variations induced by tides are of vital importance not only for the analysis of space geodetic observations and the prediction of Earth rotation parameters, but also for the decomposition of this integral quantities according to driving geophysical mechanisms. The present thesis is therefore centered around two primary objectives. The first is to assess the quality of available models for short-period ocean tidal ERP variations and long-period effects of zonal tidal deformations on UT1 by means of VLBI- and GNSS-based observations. The second aim is the inquiry for and allocation of alternatives if the conventional models fail to account for the total observed variability – thus the investigation and improvement of geophysical modeling and the closure of the corresponding excitation budgets.

Various ensembles of tidal terms in the high-frequency as well as in the low-frequency band are determined from VLBI and GNSS, with the two frequency ranges being treated separately. While the tidal ERP variations from GNSS are estimated solely by least-squares adjustment of time series with appropriate resolution, two other approaches are additionally applied in the case of VLBI.

The interval of VLBI observations consulted in this work spans 1984–2011. The length of the observation period entails the advantage that side lobes to major constituents (which differ by only one cycle in 18.6 years) can be estimated free of constraints, i.e. free of any hypothesis concerning their amplitude ratios. For that reason, a re-assessment of tidal phenomena based on VLBI-derived Earth rotation variations becomes particularly effective in the recent years. Long-time series of polar motion and universal time with hourly and six-hourly resolution are computed using two different VLBI software packages, OCCAM and VieVS. The latter is also employed to implement two alternative methods for the investigation of subdaily ERP variations: First, the so-called complex demodulation is applied that demands for a modification of the ERP parameterization and delivers demodulated ERP, with the high-frequency signal transferred to long periods. Second, the parameters of harmonic functions are formulated directly in the observation equations and retrieved within a global adjustment.

The era of high-quality GPS observations starts with the year 1995. However, the utilization of the complete time span for the investigation of tidal Earth rotation excitation is not feasible in the frame of this thesis. Since processing of GNSS data is very time consuming and necessitates advanced computing capacities, the related efforts had to be confined to two short campaigns. One GPS campaign of two years length (2005–2007), and a double processed eight-months campaign (2008–2008.6) designed to evaluate the potential benefit of a combined GPS+GLONASS solution for estimating diurnal and subdiurnal tidal effects. The campaigns are not adjacent, as the modernization of the GLONASS system just started to take effect in 2008. The processing of GNSS measurements is conducted using the BERNESE GNSS Software.

A combined analysis of GNSS and VLBI observations, for instance on the normal equation level, is not carried out due to the limited length of the GNSS time series on the one hand and because of known caveats of GPS analysis on the other hand: There are unresolved interrelations between orbit modeling and deficiencies in subdaily ERP models, probably causing associated aliased signal at longer tidal periods. The independent treatment of VLBI and GNSS is therefore favored in the present case.

7.1 Discussion of short-period polar motion and UT1 variations

In view of a most robust review of the conventional model for ocean tidal Earth rotation variations, the internally derived empirical high-frequency models are carefully cross-checked and also compared to corresponding external solutions (GPS: N. Panafidina, personal communication, 2012; Steigenberger, 2009; VLBI: Artz *et al.*, 2011). Based on these examinations several solutions are sorted out for being redundant or inadequate.

In terms of GNSS, the internal solutions are rejected entirely due to the shortness of the underlying observation period. Nevertheless, the impact of a hybrid GPS+GLONASS solution is investigated, though without examining the detected discrepancies to the ocean tidal model. Inclusion of GLONASS data into a combined GNSS solution is assumed to mitigate negative effects of the GPS orbits' resonance with Earth rotation. However, this benefit or at least a distinct change cannot be proved here. The differences between the GPS-only and the GPS+GLONASS tidal terms turn out to be insignificant, most probably owing to the fact that the contingent of contributing GLONASS observations is only 7% for the selected time interval. Because of the disadvantageous resonance effects and associated problems in orbit determination, GPS-based tidal terms in the vicinity of one and two cycles per sidereal day should be interpreted with reservation.

To examine the reliability and stability of VLBI-derived tidal models an evolution study is performed. Nine independent sets of terms are calculated from 19-year bins, each shifted by one year, starting with the interval 1984–2003 and ending with the interval 1992–2011. The comparison of the nine section models with the model estimated from the complete time span show, that the full solution is governed by information of the more recent observation data. It is

thereby demonstrated that it is absolutely safe to include the sometimes questioned early years of VLBI data, as the effects of possibly lower data quality can be apparently compensated by proper weighting within the adjustment procedure.

The present IERS Conventions (2010) model for ocean tidal ERP variations is based on a data assimilative hydrodynamic ocean tide model from 1994 (TPXO.2). Since then a large number of observations of satellite altimetry has been collected and was used as input for several new and precise assimilation and empirical ocean tide models. Two such recent models, which publicly provide the tidal elevations and current velocities, are TPXO7.2 (Egbert & Erofeeva, 2002) and HAMTIDE11a (Taguchi *et al.*, 2012). Both models are employed to derive two new high-frequency ocean tidal ERP models, applying standard procedures of excitation modeling. Fortnightly and monthly polar motion and UT1 variations are supplementary computed from the respective constituents available for TPXO7.2.

All three ocean tidal ERP models (IERS2010, TPXO7.2, HAMTIDE11a) are assessed with three different internal VLBI solutions: estimated from highly resolved time series, from demodulated ERP, and within a global solution. The VLBI solution by Artz *et al.* (2011) and the GPS model by Panafidina (personal communication, 2012) serve as independent references. The evaluation of the root mean square values of the coefficient differences between all possible model pairs reveals that TPXO7.2 is in better agreement with the geodetic models than IERS2010, as regards polar motion and also UT1. A term-by-term inspection of the observed residuals to TPXO7.2 pinpoints a clear improvement for several terms, such as the M_2 and S_2 in polar motion and the O_1 , S_2 and K_2 in UT1. However, other tides experience a slight degradation compared to IERS2010 and, furthermore, various significant residuals remain w.r.t. all three validated ocean tidal ERP models. A closer look at the effects of polar and spin libration illustrates that the application of the corresponding corrections tends to improve the closure between observed ERP and the recent ocean tidal ERP models from TPXO7.2 and HAMTIDE11a, whereas they increase the deviations to IERS2010 in many terms. Whether observed gaps are to be attributed entirely to deficiencies in the ocean tidal ERP models or partly also to shortcomings of the libration models is impossible to ascertain.

Clearly, the budget of diurnal and subdiurnal Earth rotation variations is still not closed. There are unsettled discrepancies on the part of gravitational tidal effects as well as of thermal tidal effects. In order to verify the last statement, the S_1 residuals observed by VLBI are opposed to different models of geophysical excitation (atmospheric and non-tidal oceanic). These model combinations do not agree among each other and moreover none is capable of explaining the amplitude and phase of the observed S_1 signal.

Regarding the actually irregular thermal S_1 tide it is rather questionable if it will be possible in future to adequately represent it in terms of a time dependent function, which could be used in a priori models for space geodetic data processing.

The development of a better ocean tidal ERP model still persists as an open task of crucial importance for unbiased GNSS orbit determination and other processing issues, particularly with

regard to accomplishing the ambitious GGOS target accuracy. As is exposed in the present work, the utilization of updated ocean tide models alone does not yield a satisfying product. Future strategies for improving the subdaily ERP model could involve a revision of the transfer functions or the provision of more than the eight major constituents on the part of ocean tide modelers. In any case, the use of empirical models, based on geodetic observations, within the analysis process cannot be recommended. The application of such models might help to reduce aliased signal in the data processing, but bears the danger of just covering other errors in the subdiurnal domain and besides disables the study and separation of geophysical effects. Nonetheless, a further empirical examination of high-frequency Earth rotation, for example by means of SLR observations would be worthwhile. The potential of a combined GPS+GLONASS solution should be re-evaluated in future as well, since the GLONASS system has again reached the status of full operability and the quality of GLONASS orbits and clocks is continuously increasing.

Ocean tides also induce considerable retrograde diurnal polar motion, which is considered in the nutation model according to the CIP frequency conventions. The observed discrepancies in the ERP, and additionally remarkable differences between the retrograde diurnal terms calculated from the ocean tide models (up to 250 μas), inspire the future amendment of the respective contribution incorporated in the nutation model.

7.2 Discussion of long-period UT1 and LOD variations

The extraction of the zonal tidal signal from UT1 or LOD necessitates the thorough removal of non-harmonic geophysical fluctuations inferred by angular momentum changes of respective subsystems (AAM, OAM, HAM). This required data reduction poses the problem that the estimation of zonal tidal terms directly from reduced UT1 becomes extremely instable if periods longer than 35 days are involved. The most reasonable explanation is that errors of the geophysical fluids data are increasingly amplified with the period upon integration. Hence, the derivation of tidal signal from UT1 is recommended only for variations below 35 days. In order to obtain the terms with periods beyond that limit, the time derivative – LOD – should be utilized.

The analysis of the mutual agreement between zonal tidal solutions obtained from internally and externally (IERS C04) computed time series is employed to quantify the level of significance to about 5 μs . The estimates of a term at a non-tidal period, as well as the spectrum of LOD residuals (with a model for zonal tides and AAM+OAM removed), suggest a general noise level of 5–10 μs . A test on the sensitivity of the estimated terms on the length of the introduced time series points out that the internal GNSS time series of two years is too short to provide reliable results. Most striking changes in the resulting terms are observed at the transition from a two-year to a three-year solution, yet, substantial stabilization is attained only after using ten years of observations.

In the course of the present thesis two conventional models for zonal tidal variations in UT1/LOD are validated. These models were consecutively published in the IERS Conventions

(2003) and IERS Conventions (2010). The results presented here, derived from VLBI LOD, confirm a study conducted as part of this work (Englich *et al.*, 2009) in terms of UT1 as well as the findings by Gross (2009), who actually suggested the replacement of the IERS2003 model. The main deficit of this model is that it is lacking the contribution of a dynamic ocean tide at the fortnightly Mf and the monthly Mm constituents. At the other tidal periods a significant difference in the performance of the 2003 and the 2010 conventional models cannot be detected. Unlike the previous studies, the validation of the model terms is extended up to annual variations, revealing thereby conspicuous peaks at the semiannual Ssa and the annual Sa period. The also seasonal character of these periods arouses the suspicion that atmospheric or oceanic oscillations are not completely removed with the employed AAM+OAM combination based on NCEP and ECCO data. A rapid inspection of another consistent data set, including AAM, OAM and HAM based on ECMWF, OMCT and LSDM, indicates that the spurious seasonal peaks in the residual spectrum can be explained by the contribution of zonal winds in the upper atmosphere, which is not contained in AAM from NCEP. The application of the full set of alternative geophysical fluid models considerably improves the closure at the semiannual term, but results in explicitly larger residuals at the annual term.

Since there is evidently no consensus between the output of general circulation models at seasonal time scales, the determination of the zonal response coefficient of the Earth-ocean system κ is confined to periods below 35 days. Among the estimated frequency dependent coefficients, those at the fortnightly and monthly periods are considered reliable, with the magnitudes being precise to about 0.3%. According to Ray & Egbert (2012), who recently determined a $\kappa(Mf)$ equal in magnitude, phase, and precision to the solutions presented here, such estimates start to become valuable for imposing new constraints on mantle anelasticity.

A future task, supporting the research on elastic and anelastic body tides, as well as dynamic ocean tides, is the refinement of the calculation methods. In the course of this dissertation one step towards a more rigorous estimation of zonal tidal variations in UT1 has been taken by implementing the option to solve for corresponding parameters to the global solution of the Vienna VLBI Software. Final results are, however, not yet available for integration to this work.

Another mission will be the update of the current zonal tidal model of the IERS Conventions (2010), although the observational evidence presently does not imply the need for a revision. After all, the accuracy of space geodetic measurements is steadily increasing and geophysical fluids models are permanently improved as well. With a view to close the LOD excitation budget at least for certain periods an up-to-date model for the effect of solid Earth tides should be fostered. The dynamic ocean tidal contribution could be replaced as well, as there are more recent ocean tide models at hand, e.g. for Mf from Ray & Egbert (2012) or for Mf and Mm from TPXO7.2 (Egbert & Erofeeva, 2002).

Last but not least, we can be optimistic that a consistent combination of appropriate geophysical models will enable the investigation of mantle anelasticity even from observed tidal LOD variations at semiannual and annual periods in the near future.

Appendix A

Tables

A.1 Orthotide formalism

Table A.1: Orthotide coefficients (Matsumoto *et al.*, 1995).

	Diurnal $nm = 21$	Semidiurnal $nm = 22$
p_{00}	0.0298	0.0200
p_{10}	0.1408	0.0905
p_{11}	0.0805	0.0638
p_{20}	0.6002	0.3476
p_{21}	0.3025	0.1645
q_{21}	0.1517	0.0923

A.2 Tidal ERP coefficients

Table A.2: Ocean tidal terms of diurnal prograde polar motion.^a

Tide	Fundamental arguments						Period	TPX07.2		HAMTIDE11a	
	l	l'	F	D	Ω	GMST+ π		A^+	B^+	A^+	B^+
	-1	0	-2	-2	-2	1	29.0727	-1.4	0.0	-1.2	0.1
$2Q'_1$	-2	0	-2	0	-1	1	28.0110	-0.8	0.1	-0.7	0.2
$2Q_1$	-2	0	-2	0	-2	1	28.0062	-4.4	0.6	-3.9	0.9
	0	0	-2	-2	-1	1	27.8531	-1.0	0.2	-0.9	0.2
σ_1	0	0	-2	-2	-2	1	27.8484	-5.2	0.9	-4.7	1.2
Q'_1	-1	0	-2	0	-1	1	26.8728	-5.4	1.8	-5.1	2.0
Q_1	-1	0	-2	0	-2	1	26.8684	-28.8	9.7	-27.1	10.4
RO'_1	1	0	-2	-2	-1	1	26.7274	-1.0	0.4	-1.0	0.4
RO_1	1	0	-2	-2	-2	1	26.7231	-5.3	2.0	-5.1	2.0
	0	0	-2	0	0	1	25.8275	0.7	-0.4	0.7	-0.4
O'_1	0	0	-2	0	-1	1	25.8234	-23.7	13.0	-23.7	12.4
O_1	0	0	-2	0	-2	1	25.8193	-125.7	69.0	-125.7	65.8
	-2	0	0	0	0	1	25.8022	0.8	-0.4	0.8	-0.4
TO_1	0	0	0	-2	0	1	25.6681	1.6	-0.9	1.6	-0.9
	-1	0	-2	2	-2	1	24.9748	0.8	-0.6	0.8	-0.5
	1	0	-2	0	-1	1	24.8529	0.6	-0.4	0.6	-0.4
	1	0	-2	0	-2	1	24.8492	3.0	-2.2	3.1	-2.0
M_1	-1	0	0	0	0	1	24.8332	8.3	-6.0	8.5	-5.5
M'_1	-1	0	0	0	-1	1	24.8295	1.7	-1.2	1.7	-1.1
χ_1	1	0	0	-2	0	1	24.7091	1.5	-1.1	1.6	-1.0
π_1	0	-1	-2	2	-2	1	24.1321	-2.6	2.0	-2.6	1.8
P'_1	0	0	-2	2	-1	1	24.0694	0.5	-0.4	0.5	-0.3
P_1	0	0	-2	2	-2	1	24.0659	-44.1	33.8	-44.5	30.4
	0	1	-2	2	-2	1	24.0000	0.4	-0.3	0.4	-0.3
S_1	0	-1	0	0	0	1	23.9999	1.0	-0.8	1.0	-0.7
K''_1	0	0	0	0	1	1	23.9380	-2.6	2.0	-2.6	1.8
K_1	0	0	0	0	0	1	23.9345	131.8	-99.9	131.7	-89.8
K'_1	0	0	0	0	-1	1	23.9310	17.9	-13.5	17.9	-12.2
	0	0	0	0	-2	1	23.9275	-0.4	0.3	-0.4	0.3
ψ_1	0	1	0	0	0	1	23.8693	1.0	-0.8	1.0	-0.7
ϕ_1	0	0	2	-2	2	1	23.8045	1.9	-1.4	1.8	-1.2
TT_1	-1	0	0	2	0	1	23.2070	1.4	-0.9	1.3	-0.8
J_1	1	0	0	0	0	1	23.0985	7.3	-4.3	6.6	-4.0
J'_1	1	0	0	0	-1	1	23.0952	1.5	-0.8	1.3	-0.8
SO_1	0	0	0	2	0	1	22.4202	1.3	-0.4	1.1	-0.5
	2	0	0	0	0	1	22.3189	0.7	-0.2	0.5	-0.2
OO_1	0	0	2	0	2	1	22.3061	4.5	-1.3	3.6	-1.4
OO'_1	0	0	2	0	1	1	22.3030	2.9	-0.8	2.3	-0.9
	0	0	2	0	0	1	22.3000	0.6	-0.2	0.5	-0.2
ν_1	1	0	2	0	2	1	21.5782	1.0	-0.0	0.7	-0.1
ν'_1	1	0	2	0	1	1	21.5754	0.7	-0.0	0.5	-0.1

^a Amplitudes in μas , period in hours

Table A.3: Ocean tidal terms of semidiurnal prograde polar motion.^a

Tide	Fundamental arguments						Period	TPXO7.2		HAMTIDE11a	
	l	l'	F	D	Ω	GMST+ π		A^+	B^+	A^+	B^+
	-3	0	-2	0	-2	2	13.1622	0.2	-0.1	0.2	-0.0
	-1	0	-2	-2	-2	2	13.1273	0.5	-0.2	0.5	-0.1
$2N_2$	-2	0	-2	0	-2	2	12.9054	1.7	-1.1	1.7	-0.8
η_2	0	0	-2	-2	-2	2	12.8718	2.0	-1.4	2.1	-1.1
	0	1	-2	-2	-2	2	12.8529	0.1	-0.1	0.1	-0.1
	-1	-1	-2	0	-2	2	12.6767	-0.1	0.1	-0.1	0.1
N_2'	-1	0	-2	0	-1	2	12.6593	-0.4	0.4	-0.4	0.4
N_2	-1	0	-2	0	-2	2	12.6583	11.0	-11.3	11.3	-9.6
	-1	1	-2	0	-2	2	12.6401	0.1	-0.1	0.1	-0.1
ν_2	1	0	-2	-2	-2	2	12.6260	2.0	-2.2	2.1	-1.9
	1	1	-2	-2	-2	2	12.6078	0.1	-0.1	0.1	-0.1
	-2	0	-2	2	-2	2	12.4519	-0.1	0.2	-0.1	0.2
	0	-1	-2	0	-2	2	12.4382	-0.1	0.2	-0.1	0.2
M_2'	0	0	-2	0	-1	2	12.4215	-1.5	2.5	-1.5	2.3
M_2	0	0	-2	0	-2	2	12.4206	40.7	-67.7	40.6	-60.6
	0	1	-2	0	-2	2	12.4030	0.1	-0.2	0.1	-0.2
λ_2	-1	0	-2	2	-2	2	12.2218	-0.2	0.5	-0.2	0.5
L_2	1	0	-2	0	-2	2	12.1916	-0.6	1.9	-0.5	1.7
	-1	0	0	0	0	2	12.1878	0.1	-0.5	0.1	-0.4
	-1	0	0	0	-1	2	12.1869	0.1	-0.2	0.1	-0.2
T_2	0	-1	-2	2	-2	2	12.0164	0.1	-1.6	-0.0	-1.5
S_2	0	0	-2	2	-2	2	12.0000	1.6	-26.1	-1.2	-25.5
R_2	0	1	-2	2	-2	2	11.9836	-0.0	0.2	0.0	0.2
K_2''	0	0	0	0	1	2	11.9681	-0.0	0.1	0.0	0.1
K_2	0	0	0	0	0	2	11.9672	0.1	-6.8	-0.7	-6.7
K_2'	0	0	0	0	-1	2	11.9664	0.0	-2.0	-0.2	-2.0
	0	0	0	0	-2	2	11.9655	0.0	-0.2	-0.0	-0.2
	1	0	0	0	0	2	11.7545	-0.1	-0.2	-0.2	-0.3
	1	0	0	0	-1	2	11.7537	-0.0	-0.1	-0.1	-0.1
	0	0	2	0	2	2	11.5458	-0.0	-0.0	-0.1	-0.0

^a Amplitudes in μas , period in hours

Table A.4: Ocean tidal terms of semidiurnal retrograde polar motion.^a

Tide	Fundamental arguments						Period	TPXO7.2		HAMTIDE11a	
	l	l'	F	D	Ω	GMST+ π		A^-	B^-	A^-	B^-
	3	0	2	0	2	-2	13.1622	-0.3	0.2	-0.0	0.3
	1	0	2	2	2	-2	13.1273	-0.7	0.6	-0.1	1.0
$2N_2$	2	0	2	0	2	-2	12.9054	-1.0	3.8	0.7	4.9
η_2	-0	0	2	2	2	-2	12.8718	-1.0	4.9	1.0	6.1
	-0	-1	2	2	2	-2	12.8529	-0.1	0.3	0.1	0.4
	1	1	2	0	2	-2	12.6767	0.0	-0.3	-0.1	-0.4
N_2'	1	0	2	0	1	-2	12.6593	0.0	-1.6	-0.2	-1.8
N_2	1	0	2	0	2	-2	12.6583	-1.3	41.9	6.7	47.6
	1	-1	2	0	2	-2	12.6401	-0.0	0.4	0.1	0.5
ν_2	-1	0	2	2	2	-2	12.6260	-0.2	8.2	1.2	9.3
	-1	-1	2	2	2	-2	12.6078	-0.0	0.4	0.1	0.4
	2	0	2	-2	2	-2	12.4519	0.0	-0.8	-0.0	-0.8
	0	1	2	0	2	-2	12.4382	0.1	-0.9	-0.0	-1.0
M_2'	0	0	2	0	1	-2	12.4215	0.8	-9.7	-0.1	-10.4
M_2	0	0	2	0	2	-2	12.4206	-20.8	260.5	1.7	277.9
	0	-1	2	0	2	-2	12.4030	-0.1	0.8	-0.0	0.8
λ_2	1	0	2	-2	2	-2	12.2218	0.5	-2.0	0.4	-2.0
L_2	-1	0	2	0	2	-2	12.1916	2.2	-7.5	1.8	-7.7
	1	0	0	0	0	-2	12.1878	-0.6	1.9	-0.5	1.9
	1	0	0	0	1	-2	12.1869	-0.2	0.8	-0.2	0.9
T_2	0	1	2	-2	2	-2	12.0164	-3.9	6.6	-3.6	6.7
S_2	0	0	2	-2	2	-2	12.0000	-70.0	110.6	-64.4	112.8
R_2	0	-1	2	-2	2	-2	11.9836	0.6	-0.9	0.6	-0.9
K_2''	0	0	0	0	-1	-2	11.9681	0.3	-0.4	0.2	-0.4
K_2	0	0	0	0	0	-2	11.9672	-20.9	29.1	-19.2	29.7
K_2'	0	0	0	0	1	-2	11.9664	-6.2	8.7	-5.7	8.8
	0	0	0	0	2	-2	11.9655	-0.7	0.9	-0.6	1.0
	-1	0	0	0	0	-2	11.7545	-1.9	1.2	-1.7	1.2
	-1	0	0	0	1	-2	11.7537	-0.8	0.5	-0.7	0.5
	0	0	-2	0	-2	-2	11.5458	-0.7	0.1	-0.6	0.2

^a Amplitudes in μas , period in hours

Table A.5: Ocean tidal terms of diurnal UT1 variations.^a

Tide	Fundamental arg.						Period	TPXO7.2		HAMTIDE11a	
	l	l'	F	D	Ω	GMST+ π		U^c	U^s	U^c	U^s
	-1	0	-2	-2	-2	1	29.0727	-0.11	0.26	-0.03	0.25
$2Q'_1$	-2	0	-2	0	-1	1	28.0110	-0.07	0.14	-0.04	0.14
$2Q_1$	-2	0	-2	0	-2	1	28.0062	-0.39	0.74	-0.19	0.73
	0	0	-2	-2	-1	1	27.8531	-0.09	0.16	-0.05	0.16
σ_1	0	0	-2	-2	-2	1	27.8484	-0.48	0.86	-0.25	0.85
Q'_1	-1	0	-2	0	-1	1	26.8728	-0.54	0.80	-0.39	0.79
Q_1	-1	0	-2	0	-2	1	26.8684	-2.87	4.22	-2.09	4.19
RO'_1	1	0	-2	-2	-1	1	26.7274	-0.10	0.15	-0.08	0.14
RO_1	1	0	-2	-2	-2	1	26.7231	-0.54	0.77	-0.41	0.76
	0	0	-2	0	0	1	25.8275	0.08	-0.09	0.07	-0.09
O'_1	0	0	-2	0	-1	1	25.8234	-2.47	3.01	-2.28	3.02
O_1	0	0	-2	0	-2	1	25.8193	-13.10	15.97	-12.10	16.00
	-2	0	0	0	0	1	25.8022	0.08	-0.10	0.08	-0.10
TO_1	0	0	0	-2	0	1	25.6681	0.17	-0.20	0.16	-0.20
	-1	0	-2	2	-2	1	24.9748	0.08	-0.09	0.08	-0.09
	1	0	-2	0	-1	1	24.8529	0.05	-0.06	0.06	-0.06
	1	0	-2	0	-2	1	24.8492	0.29	-0.35	0.31	-0.35
M_1	-1	0	0	0	0	1	24.8332	0.81	-0.96	0.85	-0.96
M'_1	-1	0	0	0	-1	1	24.8295	0.16	-0.19	0.17	-0.19
χ_1	1	0	0	-2	0	1	24.7091	0.15	-0.18	0.16	-0.18
π_1	0	-1	-2	2	-2	1	24.1321	-0.22	0.31	-0.22	0.31
P'_1	0	0	-2	2	-1	1	24.0694	0.04	-0.06	0.04	-0.06
P_1	0	0	-2	2	-2	1	24.0659	-3.57	5.32	-3.69	5.31
	0	1	-2	2	-2	1	24.0000	0.03	-0.04	0.03	-0.04
S_1	0	-1	0	0	0	1	23.9999	0.08	-0.13	0.08	-0.13
K''_1	0	0	0	0	1	1	23.9380	-0.20	0.32	-0.20	0.32
K_1	0	0	0	0	0	1	23.9345	10.15	-16.25	10.26	-16.16
K'_1	0	0	0	0	-1	1	23.9310	1.37	-2.20	1.39	-2.19
	0	0	0	0	-2	1	23.9275	-0.03	0.05	-0.03	0.05
ψ_1	0	1	0	0	0	1	23.8693	0.08	-0.13	0.08	-0.13
ϕ_1	0	0	2	-2	2	1	23.8045	0.14	-0.24	0.13	-0.23
TT_1	-1	0	0	2	0	1	23.2070	0.07	-0.21	0.05	-0.20
J_1	1	0	0	0	0	1	23.0985	0.35	-1.11	0.19	-1.09
J'_1	1	0	0	0	-1	1	23.0952	0.07	-0.22	0.04	-0.22
SO_1	0	0	0	2	0	1	22.4202	0.04	-0.24	-0.03	-0.23
	2	0	0	0	0	1	22.3189	0.02	-0.13	-0.02	-0.12
OO_1	0	0	2	0	2	1	22.3061	0.11	-0.84	-0.13	-0.81
OO'_1	0	0	2	0	1	1	22.3030	0.07	-0.54	-0.09	-0.52
	0	0	2	0	0	1	22.3000	0.01	-0.11	-0.02	-0.11
ν_1	1	0	2	0	2	1	21.5782	0.02	-0.22	-0.06	-0.21
ν'_1	1	0	2	0	1	1	21.5754	0.01	-0.14	-0.04	-0.13

^a Amplitudes in μs , period in hours

Table A.6: Ocean tidal terms of semidiurnal UT1 variations.^a

Tide	Fundamental arg.						Period	TPXO7.2		HAMTIDE11a	
	l	l'	F	D	Ω	GMST+ π		U^c	U^s	U^c	U^s
	-3	0	-2	0	-2	2	13.1622	-0.02	-0.07	-0.03	-0.08
	-1	0	-2	-2	-2	2	13.1273	-0.05	-0.18	-0.08	-0.20
$2N_2$	-2	0	-2	0	-2	2	12.9054	-0.21	-0.55	-0.30	-0.61
η_2	0	0	-2	-2	-2	2	12.8718	-0.25	-0.65	-0.36	-0.72
	0	1	-2	-2	-2	2	12.8529	-0.02	-0.04	-0.02	-0.05
	-1	-1	-2	0	-2	2	12.6767	0.01	0.03	0.02	0.03
N'_2	-1	0	-2	0	-1	2	12.6593	0.06	0.13	0.08	0.15
N_2	-1	0	-2	0	-2	2	12.6583	-1.62	-3.62	-2.13	-3.99
	-1	1	-2	0	-2	2	12.6401	-0.02	-0.03	-0.02	-0.04
ν_2	1	0	-2	-2	-2	2	12.6260	-0.30	-0.68	-0.40	-0.75
	1	1	-2	-2	-2	2	12.6078	-0.01	-0.03	-0.02	-0.03
	-2	0	-2	2	-2	2	12.4519	0.02	0.05	0.03	0.06
	0	-1	-2	0	-2	2	12.4382	0.02	0.06	0.03	0.06
M'_2	0	0	-2	0	-1	2	12.4215	0.26	0.65	0.34	0.70
M_2	0	0	-2	0	-2	2	12.4206	-6.96	-17.34	-8.97	-18.64
	0	1	-2	0	-2	2	12.4030	-0.02	-0.05	-0.03	-0.06
λ_2	-1	0	-2	2	-2	2	12.2218	0.03	0.13	0.05	0.13
L_2	1	0	-2	0	-2	2	12.1916	0.11	0.49	0.16	0.50
	-1	0	0	0	0	2	12.1878	-0.03	-0.12	-0.04	-0.13
	-1	0	0	0	-1	2	12.1869	-0.01	-0.05	-0.02	-0.06
T_2	0	-1	-2	2	-2	2	12.0164	-0.02	-0.49	-0.08	-0.49
S_2	0	0	-2	2	-2	2	12.0000	-0.27	-8.48	-1.26	-8.46
R_2	0	1	-2	2	-2	2	11.9836	0.00	0.07	0.01	0.07
K''_2	0	0	0	0	1	2	11.9681	-0.00	0.03	0.00	0.03
K_2	0	0	0	0	0	2	11.9672	0.01	-2.34	-0.28	-2.32
K'_2	0	0	0	0	-1	2	11.9664	0.00	-0.70	-0.08	-0.69
	0	0	0	0	-2	2	11.9655	0.00	-0.08	-0.01	-0.08
	1	0	0	0	0	2	11.7545	0.03	-0.15	0.01	-0.14
	1	0	0	0	-1	2	11.7537	0.01	-0.06	0.00	-0.06
	0	0	2	0	2	2	11.5458	0.01	-0.04	0.01	-0.04

^a Amplitudes in μs , period in hours

A.3 Root mean square of tidal coefficients differences

Table A.7: Root mean square values of model coefficient differences with constrained versions of VieVSp2 and VieVScd2.

Model	IERS2010	TPXO7.2	HAM11a	VieVSp2c	VieVScd2c	VieVSgs1	Artz et al.	Panafidina	ERP	
IERS2010		4.0	3.5	4.2	4.2	4.6	4.9	3.9	Polar motion [μs]	
TPXO7.2	0.32		3.1	3.9	3.9	4.2	4.5	3.5		
HAM11a	0.45	0.30		5.1	5.2	5.3	5.9	4.2		
VieVSp2 const	0.36	0.34	0.41		0.9	2.2	2.9	4.1		
VieVScd2 const	0.32	0.33	0.42	0.22		2.1	2.8	4.2		
VieVSgs1	0.38	0.35	0.41	0.17	0.25		2.3	4.5		
Artz et al. (2011)	0.38	0.35	0.43	0.18	0.27	0.16		4.8		
Panafidina (2012)	0.36	0.39	0.45	0.33	0.37	0.34	0.33			
ERP	Universal time [μs]									

Table A.8: Root mean square values of model coefficient differences including the orthotide version of GNSSp2 instead of VieVSp2.

Model	IERS2010	TPXO7.2	HAM11a	GNSSp2b	VieVScd2	VieVSgs1	Artz et al.	Panafidina	ERP	
IERS2010		4.0	3.5	2.7	4.7	4.6	4.9	3.9	Polar motion [μs]	
TPXO7.2	0.32		3.1	2.4	4.4	4.2	4.5	3.5		
HAM11a	0.45	0.30		2.9	5.7	5.3	5.9	4.2		
GNSSp2 ortho	0.24	0.19	0.36		4.3	4.0	4.4	3.1		
VieVScd2	0.32	0.33	0.42	0.31		1.5	2.3	4.7		
VieVSgs1	0.38	0.35	0.41	0.30	0.24		2.3	4.5		
Artz et al. (2011)	0.38	0.35	0.43	0.28	0.27	0.16		4.8		
Panafidina (2012)	0.36	0.39	0.45	0.33	0.41	0.34	0.33			
ERP	Universal time [μs]									

Appendix B

Figures

B.1 Empirical high-frequency ERP terms

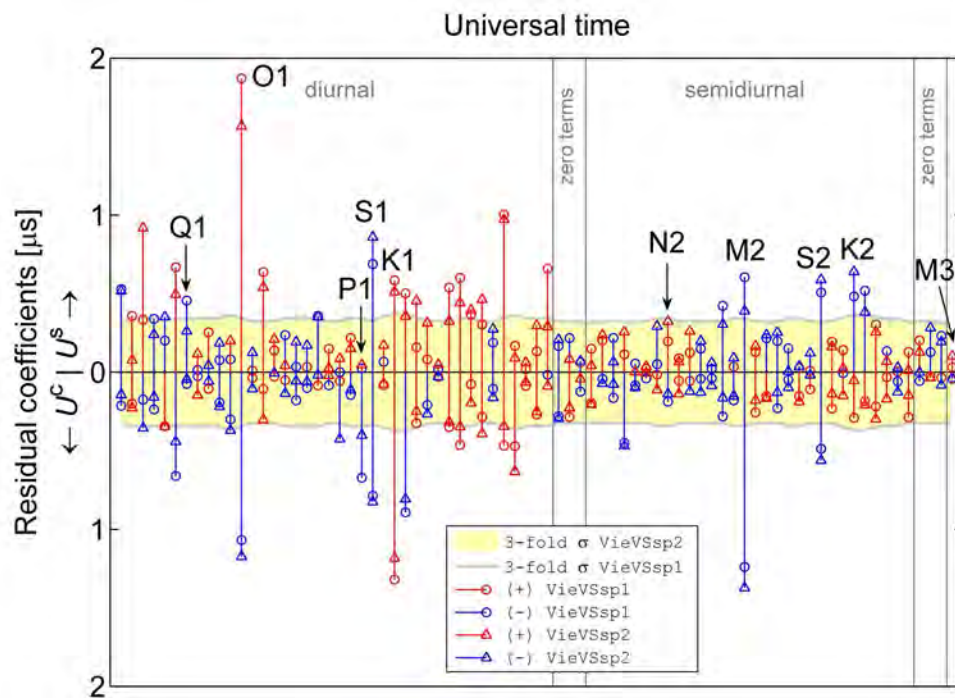


Figure B.1: Universal time coefficients (U^s , U^c) estimated from two hourly UT1 time series differing most notably in the used reference frames (VieVSsp1: VTRF2008, VieVSsp2: VieTRF10a). The coefficients are residuals w.r.t. the IERS2010 model, with circles indicating the VieVSsp1 solution and triangles labeling the VieVSsp2 solution. U^s terms are plotted upwards, U^c terms are directed downwards, with the sign of the respective estimate being specified by the color – red for positive and blue for negative values. The threefold formal errors of VieVSsp1 and VieVSsp2 are shown as thick gray line and yellow shaded area, respectively.

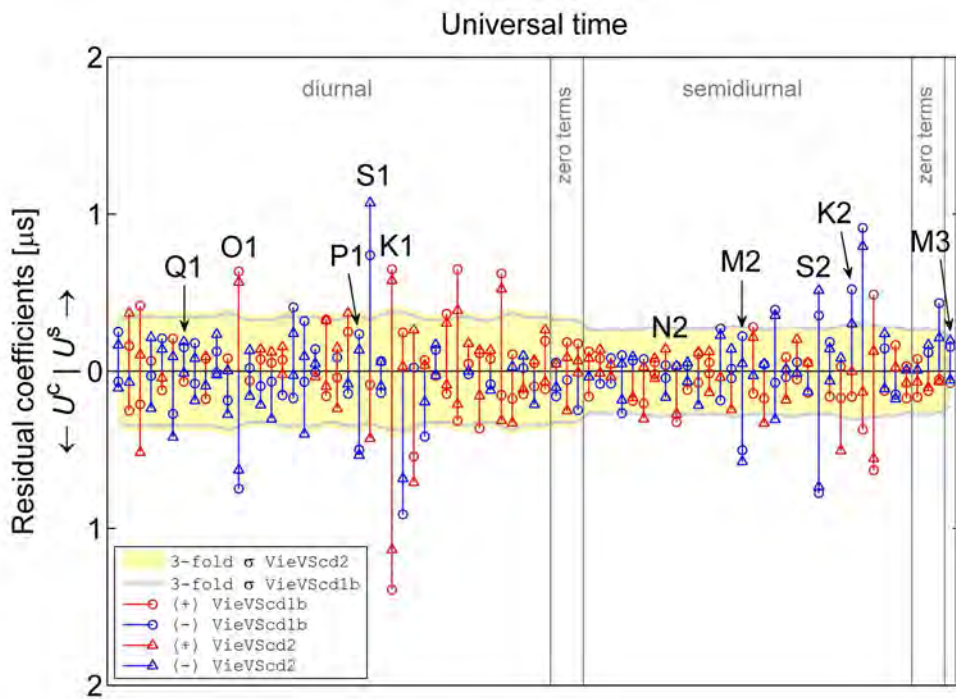


Figure B.2: Universal time coefficients (U^s , U^c) estimated from two time series of demodulated UT1 differing most notably in the used reference frames (VieVScd1b: VTRF2008, VieVScd2: VieTRF10a). The coefficients are residuals w.r.t. the IERS2010 model, with circles indicating the VieVScd1b solution and triangles labeling the VieVScd2 solution. U^s terms are plotted upwards, U^c terms are directed downwards, with the sign of the respective estimate being specified by the color – red for positive and blue for negative values. The threefold formal errors of VieVScd1b and VieVScd2 are shown as thick gray line and yellow shaded area, respectively.

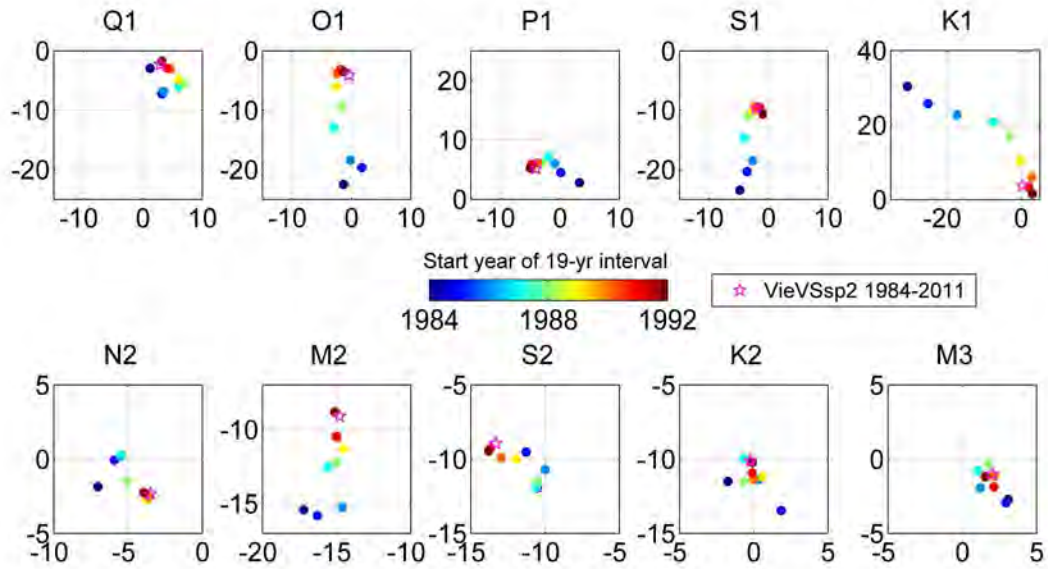


Figure B.3: Evolution of residual retrograde polar motion coefficients for the eight major tidal constituents plus S_1 and M_3 (w.r.t. IERS2010). The diagrams show B^- against A^- in units of μas .

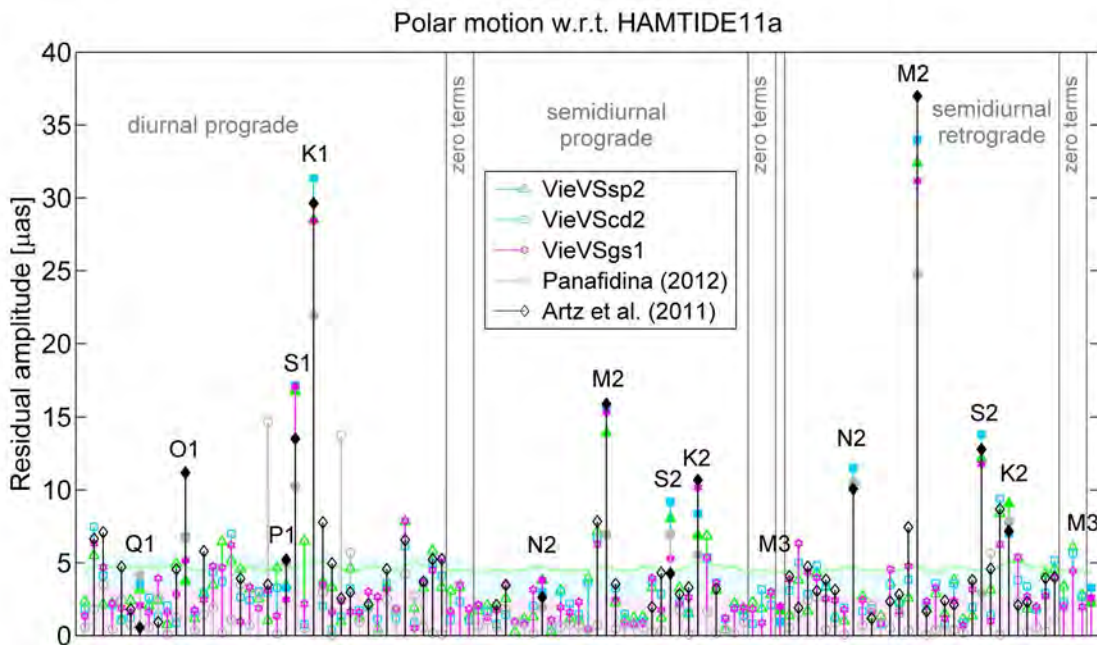


Figure B.4: Residual amplitudes of empirical tidal models of polar motion w.r.t. HAMTIDE11a in μas . The threefold formal errors of the internal solutions are shown as shaded areas or a thick line in the respective color itemized in the figure legend.

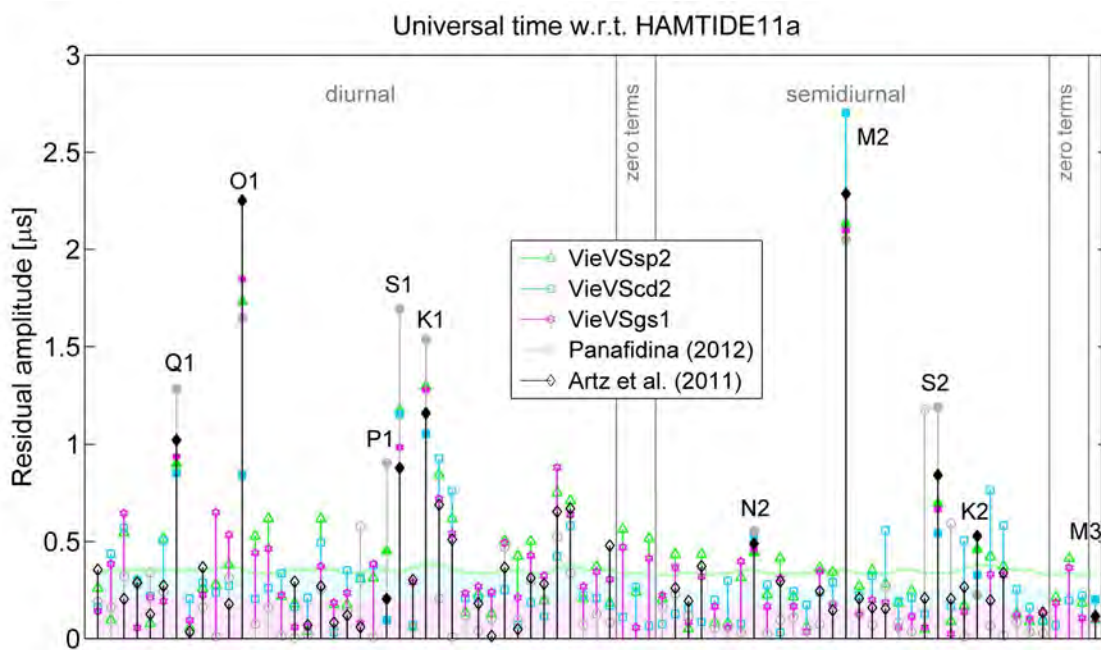


Figure B.5: Residual amplitudes of empirical tidal models of universal time w.r.t. HAMTIDE11a in μs . The threefold formal errors of the internal solutions are shown as shaded areas or a thick line in the respective color itemized in the figure legend.

B.2 Empirical zonal tidal UT1/LOD terms

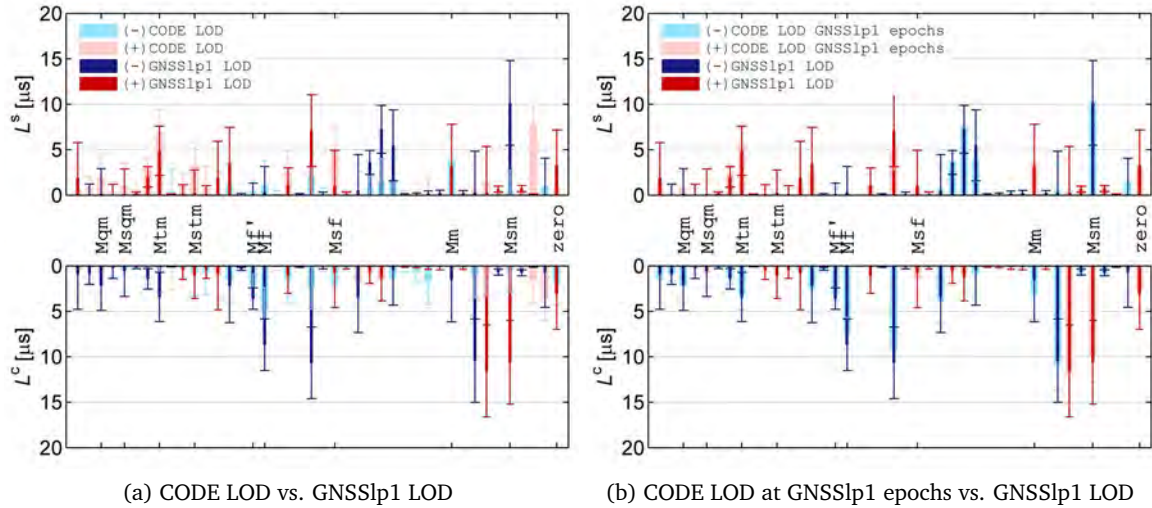
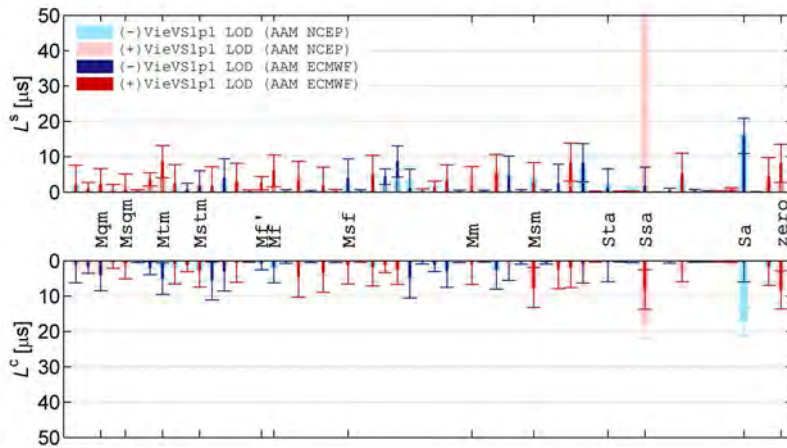
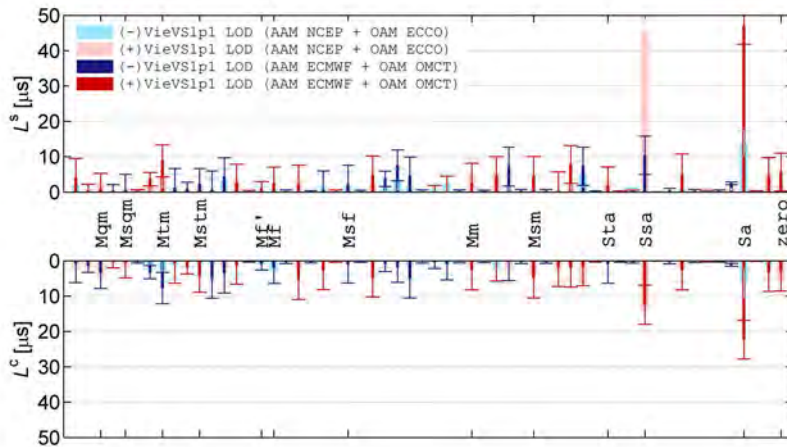


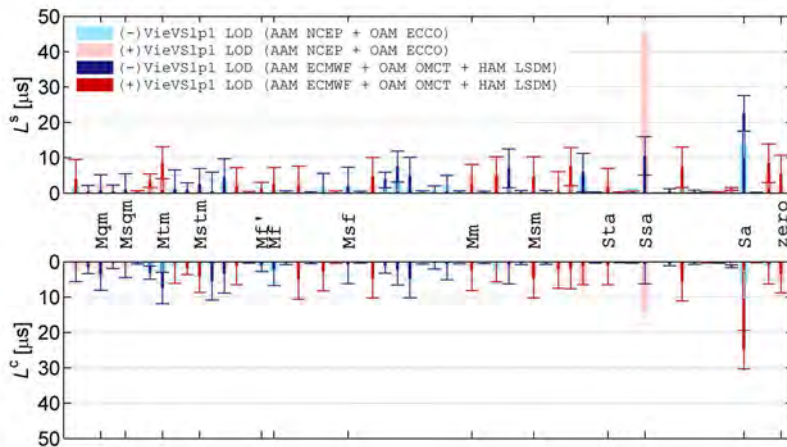
Figure B.6: Residual zonal tidal coefficients L_i^s (top) and L_i^c (bottom) derived from each two different time series (light and dark colors) with 48 days filter cutoff and AAM contribution considered. The bars are plotted in light or dark red for positive values and in light or dark blue for negative values. The errorbars show the threefold formal error deriving from the corresponding adjustment. Note: the LOD units refer to the nominal day.



(a) AAM contribution



(b) AAM+OAM contribution



(c) AAM+OAM(+HAM) contribution

Figure B.7: Residual zonal tidal coefficients L_i^s (top) and L_i^c (bottom) derived from each two different time series (light and dark colors) with 800 days filter cutoff and various EAMF contributions considered. Note: the LOD units refer to the nominal day.

List of Figures

2.1	CIP frequency convention	10
2.2	Signal components of polar motion	18
2.3	Signal components of universal time	19
3.1	Tidal force	22
3.2	Spherical triangle	23
3.3	Zonal, tesseral and sectorial deformation of degree two	28
3.4	Toroidal oscillation of degree one	32
3.5	Seismic velocity and density in the Earth – PREM	33
3.6	Ocean tide heights and volume transports TPXO7.1	37
3.7	Orthotide functions	40
3.8	Ocean tide model \Rightarrow ERP variations	42
4.1	Basic principle of VLBI observation	48
4.2	Setup of time dependent parameters in OCCAM and VieVS	54
4.3	Networks and correlations of VLBI sessions 08FEB06XA and 08AUG04XA	56
4.4	Polyhedra and volumina of the station networks	56
4.5	Correlation matrices of 08AUG04XA for different processing settings	57
4.6	Global map of processed baselines (1984–2009)	59
4.7	High resolution ERP time series	62
4.8	EOP correlation matrix for session 08AUG04XA – demodulation approach	65
4.9	Smoothed demodulated diurnal dUT1 parameters (2005–2010)	66
5.1	Network configuration, GPS-only campaign	78
5.2	Polar motion biases between different GPS solutions	79
5.3	LOD biases between different GPS solutions	79
5.4	Prograde diurnal polar motion versus satellite revolution period	80
5.5	Network configuration, GPS+GLONASS campaign	81
5.6	Coordinate differences NMF versus GMF	82
5.7	Coordinate differences GPS-only versus GPS+GLONASS	82
5.8	ERP differences GPS-only versus GPS+GLONASS	83

6.1	Signal preprocessing steps – dUT1	89
6.2	Signal preprocessing steps – AAMF	90
6.3	Coherence and cross phase spectrum UT1(reduced) and AAM-UT1	91
6.4	Residual zonal tidal coefficients from C04 UT1	92
6.5	Residual zonal tidal coefficients from C04 LOD	93
6.6	Flow diagram of ocean tidal ERP model derivation	95
6.7	Major ocean tidal ERP terms of TPXO7.2, HAMTIDE11a and IERS2010	96
6.8	Monthly and fortnightly ocean tidal UT1 excitation	98
6.9	Retrograde diurnal polar motion in VLBI and GNSS solutions	100
6.10	Retrograde diurnal polar motion from ocean tide models	101
6.11	Residual polar motion coefficients GNSSsp2a – orthotide versus constrained approach	103
6.12	GNSS based polar motion and UT1 residual coefficients w.r.t. IERS2010	104
6.13	Residual polar motion coefficients – VieVSp1 versus VieVSp2	106
6.14	Residual polar motion coefficients – VieVScd1b versus VieVScd2	107
6.15	Evolution of residual prograde polar motion coefficients	108
6.16	Evolution of residual universal time coefficients	109
6.17	VLBI-based polar motion and UT1 residual coefficients w.r.t. IERS2010	110
6.18	Residual amplitudes of empirical tidal models of polar motion w.r.t. IERS2010	113
6.19	Residual amplitudes of empirical tidal models of polar motion w.r.t. TPXO7.2	114
6.20	Effect of the polar libration correction on residual empirical tidal terms	114
6.21	Residual amplitudes of empirical tidal models of universal time w.r.t. IERS2010	115
6.22	Residual amplitudes of empirical tidal models of universal time w.r.t. TPXO7.2	116
6.23	Effect of the spin libration correction on residual empirical tidal terms	117
6.24	Prediction of S_1 from VLBI and geophysical models	118
6.25	Residual zonal tidal coefficients from different UT1 series	120
6.26	Residual zonal tidal LOD – AAM reduced versus AAM+OAM reduced	122
6.27	Coherence of LOD (reduced) with AAM LOD and AAM+OAM LOD	122
6.28	Magnitude of zonal tidal LOD residuals to IERS2003 and IERS2010	124
6.29	Phasor plot of residual zonal tidal LOD terms w.r.t. IERS2003 and IERS2010	125
6.30	Amplitude spectrum of δ LOD VieVSp1 w.r.t. IERS2010	126
6.31	Magnitude and phase of the zonal tidal response coefficient	128
B.1	Residual universal time coefficients – VieVSp1 versus VieVSp2	145
B.2	Residual universal time coefficients – VieVScd1b versus VieVScd2	146
B.3	Evolution of residual retrograde polar motion coefficients	147
B.4	Residual amplitudes of empirical tidal models of polar motion w.r.t. HAMTIDE11a	147
B.5	Residual amplitudes of empirical tidal models of universal time w.r.t. HAMTIDE11a	148
B.6	Residual zonal tidal coefficients from different GNSS LOD series	149
B.7	Residual zonal tidal coefficients from differently pretreated VieVS LOD series	150

List of Tables

3.1	Doodson variables	25
3.2	Delaunay variables	25
3.3	Selected tidal waves – long-period components	26
3.4	Selected tidal waves – short-period components	27
4.1	Characteristics of the OCCAM solutions	60
4.2	Characteristics of the VieVS solutions	61
4.3	Characteristics of the demodulated ERP solutions	66
4.4	Characteristics of the VieVS global solution	69
5.1	Characteristics of the GNSS solutions	84
6.1	OTAM mass and motion terms for TPXO7.2	96
6.2	OTAM mass and motion terms for HAMTIDE11a	97
6.3	Ocean tidal terms of fortnightly and monthly polar motion and UT1 from TPXO7.2	98
6.4	Root mean square values of model coefficient differences	111
6.5	Magnitude of the zonal response coefficient κ	129
6.6	Phase of the zonal response coefficient $\arg(\kappa)$	129
A.1	Orthotide coefficients	137
A.2	Ocean tidal terms of diurnal prograde polar motion	138
A.3	Ocean tidal terms of semidiurnal prograde polar motion	139
A.4	Ocean tidal terms of semidiurnal retrograde polar motion	140
A.5	Ocean tidal terms of diurnal UT1 variations	141
A.6	Ocean tidal terms of semidiurnal UT1 variations	142
A.7	Root mean square values of model coefficient differences	143
A.8	Root mean square values of model coefficient differences	143

Acronyms

AAMF	Atmospheric Angular Momentum Function
AAM	Atmospheric Angular Momentum
AMF	Angular Momentum Function
BVSS	Bonn-VLBI-Software-System
CIO	Celestial Intermediate Origin
CIP	Celestial Intermediate Pole
CODE	Center for Orbit Determination in Europe
CRF	Celestial Reference Frame
CW	Chandler Wobble
DORIS	Doppler Orbitography and Radiopositioning Integrated by Satellite
EAMF	Effective Angular Momentum Function
ECMWF	European Centre for Medium-Range Weather Forecasts
EOP	Earth Orientation Parameter
ERA	Earth Rotation Angle
ERP	Earth Rotation Parameter
FCN	Free Core Nutation
GCRS	Geocentric Celestial Reference System
GEBCO	General Bathymetric Chart of the Oceans
GFZ	Deutsches GeoForschungsZentrum
GGFC	Global Geophysical Fluids Center
GGOS	Global Geodetic Observing System
GIM	Global Ionospheric Model
GLONASS	Globalnaja Nawigazionnaja Sputnikowaja Sistema
GMF	Global Mapping Function
GMST	Greenwich mean sidereal time
GNSS	Global Navigation Satellite System
GPS	Global Positioning System
HAM	Hydrologic Angular Momentum
IAG	International Association of Geodesy
IAU	International Astronomical Union
IB	Inverted Barometer

ICRF	International Celestial Reference Frame
ICRS	International Celestial Reference System
IERS	International Earth Rotation and Reference System Service
IGG	Institute of Geodesy and Geophysics
IGS	International GNSS Service
ITRF	International Terrestrial Reference Frame
ITRS	International Terrestrial Reference System
IVS	International VLBI Service for Geodesy and Astrometry
JPL	Jet Propulsion Laboratory
LLR	Lunar Laser Ranging
LOD	Length of Day
LSDM	Land Surface Discharge Model
NCEP	United States National Center for Environmental Predictions
NDFW	Nearly Diurnal Free Wobble
NMF	Niell Mapping Function
NNR	No-Net-Rotation
NNT	No-Net-Translation
NRO	Non-Rotating Origin
OAM	Ocean Angular Momentum
OMCT	Ocean Model for Circulation and Tides
OTAM	Ocean Tidal Angular Momentum
PREM	Preliminary Reference Earth Model
QIF	Quasi Ionosphere-Free
SLR	Satellite Laser Ranging
SSB	Solar System Barycentric
TCB	Barycentric Coordinate Time
TIO	Terrestrial Intermediate Origin
TRF	Terrestrial Reference Frame
TT	Terrestrial Time
UT1	Universal Time 1
UTC	Universal Time Coordinated
VieVS	Vienna VLBI Software
VLBI	Very Long Baseline Interferometry
VMF1	Vienna Mapping Function 1

Bibliography

- AGNEW, D. (2007). Earth tides. In T.A. Herring, ed., *Geodesy*, Vol. 3 of *Treatise on Geophysics*, 163–195, Elsevier, Amsterdam.
- AGNEW, D. AND FARRELL, W. (1978). Self-consistent equilibrium ocean tides. *Geophys. J. R. Astron. Soc.*, 55, 171–181.
- ALTAMIMI, Z., COLLILIEUX, X. AND MÉTIVIER, L. (2011). ITRF2008: an improved solution of the international terrestrial reference frame. *J. Geod.*, 85, 457–473.
- ARIAS, E.F., CHARLOT, P., FEISSEL, M. AND LESTRADE, J.F. (1995). The extragalactic reference system of the International Earth Rotation Service, ICRS. *Astron. Astrophys.*, 303, 604–608.
- ARTZ, T., BÖCKMANN, S., NOTHNAGEL, A. AND STEIGENBERGER, P. (2010). Subdiurnal variations in the Earth's rotation from continuous Very Long Baseline Interferometry campaigns. *J. Geophys. Res.*, 115, doi:10.1029/2009JB006834.
- ARTZ, T., TESMER NÉE BÖCKMANN, S. AND NOTHNAGEL, A. (2011). Assessment of periodic sub-diurnal Earth rotation variations at tidal frequencies through transformation of VLBI normal equation systems. *J. Geod.*, 85, 565–584.
- BAADER, H.R., BROSCHE, P. AND HÖVEL, W. (1983). Ocean Tides and Periodic Variations of the Earth's Rotation. *J. Geophys.*, 52, 140–142.
- BAISCH, S. AND BOKELMANN, G. (1999). Spectral analysis with incomplete time series: an example from seismology. *Comput. Geosci.*, 25, 739–750.
- BARNES, R.T.H., HIDE, R., WHITE, A.A. AND WILSON, C.A. (1983). Atmospheric Angular Momentum Fluctuations, Length-of-Day Changes and Polar Motion. *Proc. R. Soc. Lond. A*, 387, 31–73.
- BEUTLER, G., MERVART, L. AND VERDUN, A. (2005). *Application to Planetary System, Geodynamics and Satellite Geodesy*, Vol. II of *Methods of Celestial Mechanics*. Springer, Astronomy and Astrophysics Library.
- BÖCKMANN, S., ARTZ, T. AND NOTHNAGEL, A. (2010). VLBI terrestrial reference frame contributions to ITRF2008. *J. Geod.*, 84, 201–219.

- BÖHM, J. AND SCHUH, H. (2004). Vienna mapping functions in VLBI analyses. *Geophys. Res. Lett.*, 31, doi:10.1029/2003GL018984.
- BÖHM, J. AND SCHUH, H. (2007). Troposphere gradients from the ECMWF in VLBI analysis. *J. Geod.*, 81, 403–408.
- BÖHM, J., NIELL, A., TREGONING, P. AND SCHUH, H. (2006a). Global Mapping Function (GMF): A new empirical mapping function based on numerical weather model data. *Geophys. Res. Lett.*, 33.
- BÖHM, J., WERL, B. AND SCHUH, H. (2006b). Troposphere mapping functions for GPS and very long baseline interferometry from European Centre for Medium-Range Weather Forecasts operational analysis data. *J. Geophys. Res.*, 111, doi:10.1029/2005JB003629.
- BÖHM, J., NIELL, A.E., SCHUH, H., TESMER, V. AND TREGONING, P. (2008). Mapping functions for atmospheric delay modelling in GNSS analysis. In *Proceedings of the IGS Analysis Workshop in Darmstadt*, only available on CD-ROM.
- BÖHM, J., SPICAKOVA, H., PLANK, L., TEKE, K., PANY, A., WRESNIK, J., ENGLISH, S., NILSSON, T., SCHUH, H., HOBIGER, T., ICHIKAWA, R., KOYAMA, Y., GOTOH, T., KUBOOKA, T. AND OTSUBO, T. (2009). Plans for the Vienna VLBI Software VieVS. In G. Bourda, P. Charlot and A. Collioud, eds., *Proceedings of the 19th European VLBI for Geodesy and Astrometry Working Meeting*, 161–164.
- BÖHM, S., BRZEZIŃSKI, A. AND SCHUH, H. (2011). Complex demodulation in VLBI estimation of high frequency Earth rotation components. *J. Geodyn.*, 10.1016/j.jog.2011.10.002.
- BROSCHÉ, P., SEILER, U., SÜNDERMANN, J. AND WÜNSCH, J. (1989). Periodic changes in Earth's rotation due to oceanic tides. *Astron. Astrophys.*, 220, 318–320.
- BRZEZIŃSKI, A. (1992). Polar motion excitation by variations of the effective angular momentum function: considerations concerning the deconvolution problem. *Manuscripta Geodaetica*, 17, 3–20.
- BRZEZIŃSKI, A. (1994). Polar motion excitation by variations of the effective angular momentum function, II: extended-model. *Manuscripta Geodaetica*, 19, 157–171.
- BRZEZIŃSKI, A. (2011). Diurnal excitation of Earth rotation estimated from recent geophysical models. In N. Capitaine, ed., *Proceedings of the Journées 2010 “Systèmes de Référence Spatio-Temporels”*, 131–136.
- BRZEZIŃSKI, A. (2012). On estimation of high frequency geophysical signals in Earth rotation by complex demodulation. *J. Geodyn.*, 10.1016/j.jog.2012.01.008.

- BRZEZIŃSKI, A. AND CAPITAIN, N. (1993). The Use of the Precise Observations of the Celestial Ephemeris Pole in the Analysis of Geophysical Excitation of Earth Rotation. *J. Geophys. Res.*, 98, 6667–6675.
- BRZEZIŃSKI, A. AND MATHEWS, P. (2003). Recent advances in modeling the lunisolar perturbation in polar motion corresponding to high frequency nutation: report on the discussion of the IAU Commission 19 WG on nutation. In N. Capitaine and M. Stavinschi, eds., *Proceedings of the Journées 2002 “Systèmes de Référence Spatio-Temporels”*, 101–108.
- BRZEZIŃSKI, A., BIZOUARD, C. AND PETROV, S.D. (2002). Influence of the atmosphere on Earth rotation: what new can be learned from the recent atmospheric angular momentum estimates? *Surv. Geophys.*, 23, 33–69.
- BRZEZIŃSKI, A., PONTE, R.M. AND ALI, A.H. (2004). Nontidal oceanic excitation of nutation and diurnal/semidiurnal polar motion revisited. *J. Geophys. Res.*, 109, doi: 10.1029/2004JB003054.
- BÜLLESFELD, F.J. (1985). Ein Beitrag zur harmonischen Darstellung des gezeitenerzeugenden Potentials. DGK, Reihe C 314, Verlag der Bayerischen Akademie der Wissenschaften.
- CAPITAIN, N., GUINOT, B. AND SOUCHAY, J. (1986). A Non-rotating Origin on the Instantaneous Equator: Definition, Properties and Use. *Celest. Mech.*, 39, 283–307.
- CARTWRIGHT, D.E. (1977). Oceanic Tides. *Rep. Prog. Phys.*, 40, 665–708.
- CARTWRIGHT, D.E. AND RAY, R.D. (1990). Oceanic Tides From Geosat Altimetry. *J. Geophys. Res.*, 95, 3069–3090.
- CARTWRIGHT, D.E. AND TAYLER, R.J. (1971). New Computations of the Tide-generating Potential. *Geophys. J. R. Astron. Soc.*, 23, 45–73.
- CHAO, B.F. AND RAY, R.D. (1997). Oceanic tidal angular momentum and Earth’s rotation variations. *Prog. Oceanog.*, 40, 399–421.
- CHAO, B.F., DONG, D.N., LIU, H.S. AND HERRING, T.A. (1991). Libration in the Earth’s rotation. *Geophys. Res. Lett.*, 18, 2007–2010.
- CHAO, B.F., MERRIAM, J.B. AND TAMURA, Y. (1995). Geophysical analysis of zonal tidal signals in length of day. *Geophys. J. Int.*, 122, 765–775.
- CHAO, B.F., RAY, R.D., GIPSON, J.M., EGBERT, G.D. AND MA, C. (1996). Diurnal/semidiurnal polar motion excited by oceanic tidal angular momentum. *J. Geophys. Res.*, 101, 20151–20163.
- DACH, R., HUGENTOBLE, U., FRIDEZ, P. AND MEINDL, M. (2007). *User Manual of the Bernese GPS Software Version 5.0*. Astronomical Institute, University of Bern, Bern, Switzerland.
- DAHLEN, F.A. (1976). The passive influence of the oceans upon the rotation of the earth. *Geophys. J. R. Astron. Soc.*, 46, 363–406.

- DEFRAIGNE, P. AND SMITS, I. (1999). Length of day variations due to zonal tides for an inelastic earth in non-hydrostatic equilibrium. *Gephys. J. Int.*, 139, 563–572.
- DESAI, S. AND WAHR, J. (1999). Monthly and fortnightly tidal variations of the Earth's rotation rate predicted by a TOPEX/POSEIDON empirical ocean tide model. *Geophys. Res. Lett.*, 26, 1035–1038.
- DICKMAN, S.R. AND NAM, Y.S. (1995). Revised predictions of long-period ocean tidal effects on Earth's rotation rate. *J. Geophys. Res.*, 100, 8233–8243.
- DICKMAN, S.R. AND NAM, Y.S. (1998). Constraints on Q at long periods from Earth's rotation. *Geophys. Res. Lett.*, 25, 211–214.
- DOBRAWA, H., DILL, R., GRÖTZSCH, A., BRZEZIŃSKI, A. AND THOMAS, M. (2010). Seasonal polar motion excitation from numerical models of atmosphere, ocean, and continental hydrosphere. *J. Geophys. Res.*, 115, doi:10.1029/2009JB007127.
- DOODSON, A.T. (1921). The Harmonic Development of the Tide-Generating Potential. *Proc. R. Soc. A*, 100, 305–329.
- DOODSON, A.T. AND WARBURG, H.D. (1941). *Admiralty Manual of Tides*. His Majesty's Stationery Office, London.
- DZIEWONSKI, A.D. AND ANDERSON, D.L. (1981). Preliminary reference earth model. *Phys. Earth Planet. Inter.*, 25, 297–356.
- EGBERT, G.D. AND EROFEEVA, S.Y. (2002). Efficient inverse modeling of barotropic ocean tides. *J. Atmos. Oceanic Technol.*, 19, 183–204.
- EGBERT, G.D., BENNET, A.F. AND FOREMAN, M.G.G. (1994). TOPEX/Poseidon tides estimated using a global inverse model. *J. Geophys. Res.*, 99, 24821–24852.
- ENGLISH, S., SCHUH, H. AND WEBER, R. (2009). Short-term tidal variations in UT1: compliance between modelling and observation. In I.F. Corbett, ed., *Proceedings of the International Astronomical Union*, Vol. 5, Highlights of Astronomy H15, 215.
- EUBANKS, T.M. (1993). Variations in the Orientation of the Earth. In D.E. Smith and D.L. Turcotte, eds., *Contributions of Space Geodesy to Geodynamics: Earth Dynamics*, Vol. 24 of *Geodynamic Series*, American Geophysical Union.
- FEY, A.L., GORDON, D. AND JACOBS, C.S., eds. (2009). The Second Realization of the International Celestial Reference Frame by Very Long Baseline Interferometry. IERS Technical Note; 35, Frankfurt am Main: Verlag des Bundesamtes für Kartographie und Geodäsie.
- FOLKNER, W.M., WILLIAMS, J.G. AND BOGGS, D.H. (2009). The Planetary and Lunar Ephemeris DE 421. IPN (Interplanetary Network) Progress Report 42-178, Jet Propulsion Laboratory, Pasadena, California.

- GILBERT, F. AND DZIEWONSKI, A.M. (1975). An application of normal mode theory to the retrieval of structure parameters and source mechanisms for seismic spectra. *Phil. Trans. R. Soc. Lond.*, A278, 187–269.
- GILL, A.E., ed. (1982). Atmosphere–ocean dynamics. Vol. 30 of *International Geophysics*, Academic Press.
- GIPSON, J.M. (1996). Very long baseline interferometry determination of neglected tidal terms in high-frequency Earth orientation variation. *J. Geophys. Res.*, 101, 28051–28064.
- GROSS, R.S. (1992). Correspondence between theory and observations of polar motion. *Geophys. J. Int.*, 109, 162–170.
- GROSS, R.S. (1993). The effect of ocean tides on the Earth’s rotation as predicted by the results of an ocean tide model. *Geophys. Res. Lett.*, 20, 293–296.
- GROSS, R.S. (2007). Earth rotation variations - long period. In T.A. Herring, ed., *Geodesy*, Vol. 3 of *Treatise on Geophysics*, 239–294, Elsevier, Amsterdam.
- GROSS, R.S. (2008). An improved empirical model for the effect of long-period ocean tides on polar motion. *J. Geod.*, 83, 635–644.
- GROSS, R.S. (2009). Ocean tidal effects on earth rotation. *J. Geodyn.*, 48, 219–225.
- GROSS, R.S., FUKUMORI, I., MENEMENLIS, D. AND GEGOUT, P. (2004). Atmospheric and oceanic excitation of length-of-day variations during 1980–2000. *J. Geophys. Res.*, 109, doi:10.1007/s00190-008-0277-y.
- GROVES, G.W. AND REYNOLDS, R.W. (1975). An Orthogonalized Convolution Method of Tide Prediction. *J. Geophys. Res.*, 80, 4131–4138.
- HAAS, R. (2006). Investigating high frequency Earth orientation variations with continuous geodetic VLBI campaigns. In D. Behrend and K.D. Baver, eds., *International VLBI Service for Geodesy and Astrometry 2006 General Meeting Proceedings*, 316–319.
- HARTMANN, T. AND WENZEL, G. (1995). The HW95 Tidal Potential Catalogue. *Geophys. Res. Lett.*, 22, 3553–3556.
- HEFTY, J. (1982). Love number k determined from astronomical observations of the Earth’s rotation. *Bulletin of the Astronomical Institutes of Czechoslovakia*, 33, 84–88.
- HEFTY, J. AND CAPITAIN, N. (1990). The fortnightly and monthly zonal tides in the Earth’s rotation from 1962 to 1988. *Geophys. J. Int.*, 103, 219–231.
- HEINKELMANN, R., BÖHM, J., SCHUH, H. AND TESMER, V. (2006). Global VLBI Solution IGG05R01. In D. Behrend and K.D. Baver, eds., *International VLBI Service for Geodesy and Astrometry 2006 General Meeting Proceedings*, 42–51.

- HERRING, T.A. AND DONG, D.N. (1994). Measurement of diurnal and semidiurnal rotational variations and tidal parameters of Earth. *J. Geophys. Res.*, 99, 18051–18071.
- HOFMANN-WELLENHOF, B. AND MORITZ, H. (2005). *Physical Geodesy*. Springer, Wien, New York.
- HOFMANN-WELLENHOF, B., LICHTENEGGER, H. AND WASLE, E. (2008). *GNSS - Global Navigation Satellite Systems. GPS, GLONASS, Galileo, and more*. Springer, Wien, New York, 1st edn.
- IERS CONVENTIONS (1996). D. D. McCarthy (ed.). IERS Technical Note; 21, Paris: Central Bureau of IERS - Observatoire de Paris.
- IERS CONVENTIONS (2003). D. D. McCarthy and G. Petit (eds.). IERS Technical Note; 32, Frankfurt am Main: Verlag des Bundesamtes für Kartographie und Geodäsie.
- IERS CONVENTIONS (2010). G. Petit and B. Luzum (eds.). IERS Technical Note; 36, Frankfurt am Main: Verlag des Bundesamtes für Kartographie und Geodäsie, in print.
- IERS STANDARDS (1989). D. D. McCarthy (ed.). IERS Technical Note; 3, Paris: Central Bureau of IERS - Observatoire de Paris.
- KALNAY, E., KANAMITSU, M., KISTLER, R., COLLINS, W., DEAVEN, D., GANDIN, L., IREDELL, M., SAHA, S., WHITE, G., WOOLLEN, J., ZHU, Y., LEETMAA, A., REYNOLDS, R., CHELLIAH, M., EBISUZAKI, W., HIGGINS, W., JANOWIAK, J., MO, K.C., ROPELEWSKI, C., WANG, J., JENNE, R. AND JOSEPH, D. (1996). The NCEP/NCAR 40-year reanalysis project. *Bull. Amer. Meteor. Soc.*, 77, 437–471.
- KANTHA, L.H., STEWART, J.S. AND DESAI, S.D. (1998). Long-period lunar fortnightly and monthly ocean tides. *J. Geophys. Res.*, 103, 12639–12647.
- KEDAR, S., HAJJ, G.A., WILSON, B.D. AND HEFLIN, M.B. (2003). The effect of the second order GPS ionospheric correction on receiver positions. *Geophys. Res. Lett.*, 30, 1829–1832.
- KERTZ, W. (1995). *Einführung in die Geophysik I*. Spektrum Hochschultaschenbuch, Spektrum Akademischer Verlag, Heidelberg.
- KRÁSNÁ, H., BÖHM, J., PLANK, L., NILSSON, T. AND SCHUH, H. (2012). Atmospheric Effects on VLBI-derived Terrestrial and Celestial Reference Frames. In C. Rizos, ed., *International Association of Geodesy Symposia Series*, accepted for publication.
- LAMBECK, K. (1980). *The Earth's Variable Rotation - Geophysical causes and consequences*. Cambridge Monographs on Mechanics and Applied Mathematics, Cambridge University Press.
- LETELLIER, T. (2004). *Etude des ondes de marée sur les plateaux continentaux*. Ph.D. thesis, Université de Toulouse III, Ecole Doctorale des Sciences de l'Univers, de l'Environnement et de l'Espace.

- LIESKE, J.H., LEDERLE, T., FRICKE, W. AND MORANDO, B. (1977). Expressions for the precession quantities based upon the IAU 1976 system of astronomical constants. *Astron. Astrophys.*, 58, 1–16.
- MA, C., ARIAS, E.F., EUBANKS, T.M., FEY, A.L., GONTIER, A.M., JACOBS, C.S., SOVERS, O.J., ARCHINAL, B.A. AND CHARLOT, P. (1998). The international celestial reference frame as realized by very long baseline interferometry. *Astron. J.*, 116, 516–546.
- MALKIN, Z. (2009). On comparison of the Earth orientation parameters obtained from different VLBI networks and observing programs. *J. Geod.*, 83, 547–556.
- MATHEWS, P.M., HERRING, T.A. AND BUFFETT, B.A. (2002). Modeling of nutation and precession: New nutation series for nonrigid Earth and insights into the Earth’s interior. *J. Geophys. Res.*, 107, doi:10.1029/2001JB000390.
- MATSUMOTO, K., OOE, M., SATO, T. AND SEGAWA, J. (1995). Ocean tide model obtained from TOPEX/POSEIDON altimetry data. *J. Geophys. Res.*, 100, 25319–25330.
- MELCHIOR, P. (1983). *The tides of the planet earth*. Pergamon Press, Oxford, 2nd edn.
- MERRIAM, J. (1984). Tidal terms in universal time: effects of zonal winds and mantle Q. *J. Geophys. Res.*, 89, 10109–10114.
- MORITZ, H. AND MUELLER, I.I. (1987). *Earth Rotation – Theory and Observation*. Ungar Publishing Company, New York.
- MORRISON, L.V. AND STEVENSON, F.R. (2001). Historical eclipses and the variability of the Earth’s rotation. *J. Geodyn.*, 32, 247–265.
- MUNK, W.H. AND CARTWRIGHT, D.E. (1966). Tidal Spectroscopy and Prediction. *Phil. Trans. R. Soc. Lond.*, A259, 533–581.
- MUNK, W.H. AND MACDONALD, G.J.F. (1975). *The Rotation of the Earth - A Geophysical Discussion*. Cambridge Monographs on Mechanics and Applied Mathematics, Cambridge University Press.
- NAM, Y.S. AND DICKMAN, S.R. (1990). Effects of Dynamic Long-Period Ocean Tides on Changes in Earth’s Rotation Rate. *J. Geophys. Res.*, 95, 6751–6757.
- NIELL, A. (1996). Global mapping functions for the atmosphere delay at radio wavelengths. *Journal of Geophysical Research*, 101, 3227–3246.
- NIEMEIER, W. (2008). *Ausgleichsrechnung*. Walter de Gruyter, Berlin.
- PANAFIDINA, N., KURDUBOV, S. AND ROTHACHER, M. (2012). Empirical model of subdaily variations in the Earth rotation from GPS and its stability. In H. Schuh, S. Böhm, T. Nilsson and N. Capitaine, eds., *Proceedings of the Journées 2011 “Systèmes de Référence Spatio-Temporels”*, accepted for publication.

- PLAG, H.P AND PEARLMAN, M., eds. (2009). *Global Geodetic Observing System: Meeting the Requirements of a Global Society on a Changing Planet in 2020*. Springer, Berlin, Heidelberg.
- PONTE, R. AND ALI, A. (2002). Rapid ocean signals in polar motion and length of day. *Geophys. Res. Lett.*, 29, 1711–1714.
- PUGH, D.T. (1996). *Tides, Surges and Mean Sea-Level*. John Wiley & Sons, Chichester.
- RAY, J. AND GRIFFITHS, J. (2011). Status of IGS orbit modeling and areas for improvement. *Geophys. Res. Abstr.*, 13, EGU2011 – 3774, oral presentation at EGU General Assembly 2011.
- RAY, R. AND EGBERT, G. (2004). The Global S_1 tide. *J. Phys. Oceanogr.*, 34, 1922–1935.
- RAY, R. AND EGBERT, G. (2012). Fortnightly Earth rotation, ocean tides and mantle anelasticity. *Geophys. J. Int.*, 189, 400–413.
- RAY, R.D., STEINBERG, D., CHAO, B. AND CARTWRIGHT, D. (1994). Diurnal and semidiurnal variations in the Earth's rotation rate induced by oceanic tides. *Science*, 264, 830–832.
- ROBERTSON, D.S., RAY, J.R. AND CARTER, W.E. (1994). Tidal variations in UT1 observed with very long baseline interferometry. *J. Geophys. Res.*, 99, 621–636.
- ROOSBEEK, F. (1996). RATGP95: a harmonic development of the tide-generating potential using an analytical method. *Geophys. J. Int.*, 126, 197–204.
- ROTHACHER, M., HERRING, T.A. AND WEBER, R. (1999). Estimation of nutation using the Global Positioning System. *J. Geophys. Res.*, 104, 4835–4859.
- ROTHACHER, M., BEUTLER, G., WEBER, R. AND HEFTY, J. (2001). High-frequency variations in Earth rotation from Global Positioning System data. *J. Geophys. Res.*, 106, 13711–13738.
- ROTHACHER, M., ANGERMANN, D., ARTZ, T., BOSCH, W., DREWES, H., GERSTL, M., KELM, R., KOENIG, D., KOENIG, R., MEISEL, B., MUELLER, H., NOTHNAGEL, A., PANAFIDINA, N., RICHTER, B., RUDENKO, S., SCHWEGMANN, W., SEITZ, M., STEIGENBERGER, P., TESMER, S., TESMER, V. AND THALLER, D. (2011). GGOS-D: homogeneous reprocessing and rigorous combination of space geodetic observations. *J. Geod.*, 85, 679–705.
- SALSTEIN, D.A. AND ROSEN, R.D. (1997). Global momentum and energy signals from reanalysis systems. *Preprints, 7th Conf. on Climate Variations*, 344–348.
- SCHINDELEGGER, M., BÖHM, J., SALSTEIN, D. AND SCHUH, H. (2011). High-resolution atmospheric angular momentum functions related to Earth rotation parameters during CONT08. *J. Geod.*, 85, 425–433.
- SCHINDELEGGER, M., BÖHM, S., BÖHM, J. AND SCHUH, H. (2013). Atmospheric effects on Earth rotation. In J. Böhm and H. Schuh, eds., *Atmospheric effects in space geodesy*, Springer, in press.

- SCHUH, H. (1987). Die Radiointerferometrie auf langen Basen zur Bestimmung von Punktverschiebungen und Erdrotationsparametern. DGK, Reihe C 328, Verlag der Bayerischen Akademie der Wissenschaften.
- SCHUH, H. (2000). Geodetic Analysis Overview. In N.R. Vandenberg and K.D. Baver, eds., *International VLBI Service for Geodesy and Astrometry 2000 General Meeting Proceedings*, 219–229.
- SCHUH, H. AND BEHREND, D. (2012). VLBI: A fascinating technique for geodesy and astrometry. *J. Geodyn.*, 61, 68–80.
- SCHUH, H. AND BÖHM, J. (2013). Very Long Baseline Interferometry for Geodesy and Astrometry. In G. Xu, ed., *Sciences of Geodesy II: Innovations and Future Developments*, 339–376, Springer, in press.
- SCHUH, H. AND BÖHM, S. (2011). Earth rotation. In H. Gupta, ed., *Encyclopedia of Solid Earth Geophysics*, Encyclopedia of Earth sciences series, 123–129, Springer.
- SCHUH, H., CHARLOT, P., HASE, H., HIMWICH, E., KINGHAM, K., KLATT, C., MA, C., MALKIN, Z., NIELL, A., NOTHNAGEL, A., SCHLÜTER, W., TAKASHIMA, K. AND VANDENBERG, N. (2002). Final Report of the IVS Working Group 2 for Product Specification and Observing Programs. In N.R. Vandenberg and K.D. Baver, eds., *International VLBI Service for Geodesy and Astrometry 2001 Annual Report*, NASA/TP–2002–210001.
- SCHWIDERSKI, E. (1980a). Ocean tides, I; Global ocean tide equations. *Mar. Geod.*, 3, 161–217.
- SCHWIDERSKI, E. (1980b). Ocean tides, II; A hydrodynamical interpolation model. *Mar. Geod.*, 3, 219–255.
- SEEBER, G. (2003). *Satellite Geodesy*. Walter de Gruyter, Berlin, 2nd edn.
- SEIDELMANN, P.K. (1982). 1980 IAU theory of nutation - The final report of the IAU Working Group on Nutation. *Celest. Mech.*, 27, 79–106.
- SEILER, U. (1991). Periodic changes of the angular momentum budget due to the tides of the world ocean. *J. Geophys. Res.*, 96, 10287–10300.
- SEITZ, F. (2004). Atmosphärische und ozeanische Einflüsse auf die Rotation der Erde - Numerische Untersuchungen mit einem dynamischen Erdsystemmodell. DGK, Reihe C 578, Verlag der Bayerischen Akademie der Wissenschaften.
- SEITZ, F. AND SCHUH, H. (2010). Earth rotation. In G. Xu, ed., *Sciences of Geodesy I: Advances and Future Directions*, 185–227, Springer.
- SEITZ, F., STUCK, J. AND THOMAS, M. (2004). Consistent atmospheric and oceanic excitation of the Earth's free polar motion. *Geophys. J. Int.*, 157, 25–35.

- SIMON, J.L., BRETAGNON, P., CHAPRONT, J., CHAPRONT-TOUZE, M., FRANCOU, G. AND LASKAR, J. (1994). Numerical expressions for precession formulae and mean elements for the Moon and the planets. *Astron. Astrophys.*, 282, 663–683.
- SOVERS, O.J., FANSELOW, J.L. AND JACOBS, C.S. (1998). Astrometry and geodesy with radio interferometry: experiments, models, results. *Reviews of Modern Physics*, 70, 1393–1454.
- STEIGENBERGER, P. (2009). Reprocessing of a Global GPS Network. DGK, Reihe C 640, Verlag der Bayerischen Akademie der Wissenschaften.
- STEWART, R.H. (2008). *Introduction to physical oceanography*. Department of Oceanography, Texas A & M University, open Source textbook.
- TAGUCHI, E., STAMMER, D. AND ZAHHEL, W. (2012). Estimation of deep ocean tidal energy dissipation based on the high-resolution data-assimilative HAMTIDE model. In preparation.
- TAMURA, Y. (1987). A harmonic development of the tide-generating potential. *Bulletin D'Informations Marées Terrestres*, 99, 6813–6855.
- TEKE, K., TANIR KAYIKCI, E., BÖHM, J. AND SCHUH, H. (2012). Modelling Very Long Baseline Interferometry (VLBI) observations. *Journal of Geodesy and Geoinformation*, 1, 17–26.
- TESMER, V. (2004). Das stochastische Modell bei der VLBI-Auswertung. DGK, Reihe C 573, Verlag der Bayerischen Akademie der Wissenschaften.
- TESMER, V., KUTTERER, H., RICHTER, B. AND SCHUH, H. (2001). Reassessment of highly resolved EOP determined with VLBI. In A. Rius and D. Behrend, eds., *Proceedings of the 15th Working Meeting on European VLBI for Geodesy and Astrometry*, 83–90.
- TISSERAND, F. (1891). *Théorie de la figure des corps célestes et de leur mouvement de rotation*, Vol. II of *Traité de mécanique céleste*. Paris: Gauthier-Villars et Fils.
- TITOV, O., TESMER, V. AND BÖHM, J. (2004). OCCAM v.6.0 Software for VLBI Data Analysis. In N.R. Vandenberg and K.D. Baver, eds., *International VLBI Service for Geodesy and Astrometry 2004 General Meeting Proceedings*, 267–271.
- TORGE, W. (2001). *Geodesy*. Walter de Gruyter, Berlin.
- UPPALA, S.M., KÄLLBERG, P.W., SIMMONS, A.J., ANDRAE, U., BECHTOLD, V.D.C., FIORINO, M., GIBSON, J.K., HASELER, J., HERNANDEZ, A., KELLY, G.A., LI, X., ONOGI, K., SAARINEN, S., SOKKA, N., ALLAN, R.P., ANDERSSON, E., ARPE, K., BALMASEDA, M.A., BELJAARS, A.C.M., BERG, L.V.D., BIDLOT, J., BORMANN, N., CAIRES, S., CHEVALLIER, F., DETHOF, A., DRAGOSAVAC, M., FISHER, M., FUENTES, M., HAGEMANN, S., HÓLM, E., HOSKINS, B.J., ISAKSEN, L., JANSSEN, P.A.E.M., JENNE, R., MCNALLY, A.P., MAHFOUF, J.F., MORCRETTE, J.J., RAYNER, N.A., SAUNDERS, R.W., SIMON, P., STERL, A., TRENBERTH, K.E., UNTCH, A., VASILJEVIC, D., VITERBO, P. AND WOOLLEN, J. (2005). The ERA-40 re-analysis. *Quarterly Journal of the Royal Meteorological Society*, 131, 2961–3012.

-
- WAHR, J.M. AND BERGEN, Z. (1986). The effects of mantle anelasticity on nutations, Earth tides, and tidal variations of rotation rate. *Geophys. J. R. Astron. Soc.*, 87, 633–668.
- WEIS, P. (2006). *Ocean Tides and the Earth's Rotation – Results of a High-Resolving Ocean Model forced by the Lunisolar Tidal Potential*. Ph.D. thesis, Universität Hamburg.
- WILHELM, H., ZÜRN, W. AND WENZEL, H.G., eds. (1997). *Tidal Phenomena*, Vol. 66 of *Lecture Notes in Earth Sciences*. Springer.
- WILSON, C. AND VICENTE, R. (1990). Maximum Likelihood Estimates of Polar Motion Parameters. In D. McCarthy and W. Carter, eds., *Variations in Earth Rotation*, Geophysical Monograph Series 59, 151–155, American Geophysical Union.
- WOOLARD, E.W. (1959). Inequalities in mean solar time from tidal variations in the rotation of the Earth. *Astron. J.*, 64, 140–141.
- WÜNSCH, J. AND SEILER, U. (1992). Theoretical amplitudes and phases of the periodic polar motion terms caused by ocean tides. *Astron. Astrophys.*, 266, 581–587.
- XI, Q. (1989). A new complete development of the tide-generating potential for the epoch J2000.0. *Bulletin D'Informations Marées Terrestres*, 99, 6766–6812.
- YODER, C.F., WILLIAMS, J.G. AND PARKE, M.E. (1981). Tidal Variations of Earth Rotation. *J. Geophys. Res.*, 86, 881–891.
- ZHARKOV, V.N., MOLODENSKY, S.M., BRZEZIŃSKI, A., GROTEN, E. AND VARGA, P. (1996). *The Earth and its Rotation – Low Frequency Geodynamics*. Wichman, Heidelberg.

Curriculum vitae

Name: Sigrid Böhm
E-mail: sigrid.boehm@tuwien.ac.at
Date of birth: April 19, 1980
Place of birth: Klagenfurt, Austria
Nationality: Austria
Marital status: married

Academic Education

10/2005 – 10/2012 Vienna University of Technology, Doctoral program
Technical Sciences – Geodesy
10/1998 – 04/2005 Vienna University of Technology, Master program
Surveying and Geoinformation – Geodesy and Geophysics

Employment

11/2012 – present University assistant at the Vienna University of Technology,
Department of Geodesy and Geoinformation, Advanced Geodesy
10/2011 – 10/2012 Scientific research assistant at the Vienna University of Technology,
Institute of Geodesy and Geophysics, Advanced Geodesy
10/2007 – 09/2011 University assistant at the Vienna University of Technology,
Institute of Geodesy and Geophysics, Advanced Geodesy
11/2005 – 09/2007 PhD Stipendiary of the Austrian Academy of Sciences
07/2005 – 10/2005 Scientific research assistant at the Vienna University of Technology,
Institute of Geodesy and Geophysics, Advanced Geodesy
04/2003 – 10/2005 Occasional work as a technical surveyor for
Geodata Ziviltechnikergesellschaft mbH, Vienna
07/2002 Assistance in the international Project 'ALP 2002'
(geophysical research)
07/2001; 02/2002; Employee of surveying company,
07/2002; 07/2003 Korschineck & Partner, Vienna

Teaching

Lecture Earth rotation and global dynamic processes
Exercises Earth gravity field and Earth rotation
Exercises Satellite Geodesy

GEOWISSENSCHAFTLICHE MITTEILUNGEN

Bisher erschienen:

- Heft 1 Kolloquium der Assistenten der Studienrichtung Vermessungswesen. 1970 - 1973, Dezember 1973.
- Heft 2 EGGER-PERDICH-PLACH-WAGENSOMMERER, Taschenrechner HP 45 und HP 65, Programme und Anwendungen im Vermessungswesen. 1. Auflage, März 1974, Special Edition in English, Juli 1974, 2. verbesserte Auflage, November 1974.
- Heft 3 Kolloquium der Assistenten der Studienrichtung Vermessungswesen 1973 - 1974, September 1974.
- Heft 4 EGGER-PALFINGER-PERDICH-PLACH-WAGENSOMMERER, Tektronix-Tischrechner TEK 31, Programmbibliothek für den Einsatz im Vermessungswesen, November 1974.
- Heft 5 K. LEDERSTEGGER, Die horizontale Isostasie und das isostatische Geoid, Februar 1975.
- Heft 6 F. REINHART, Katalog von FK4 Horrebow-Paaren für Breiten von +30 bis +60, Oktober 1975.
- Heft 7 Arbeiten aus dem Institut für Höhere Geodäsie, Wien, Dezember 1975.
- Heft 8 Veröffentlichungen des Instituts für Photogrammetrie zum XIII. Internationalen Kongreß für Photogrammetrie in Helsinki 1976, Wien, Juli 1976.
- Heft 9 W. PILLEWIZER, Felsdarstellung aus Orthophotos, Wien, Juni 1976.
- Heft 10 PERDICH-PLACH-WAGENSOMMERER, Der Einsatz des programmierbaren Taschenrechners Texas Instruments SR-52 mit Drucker PC100 in ingenieurgeodätischen Rechentechnik, Wien, Mai 1976.
- Heft 11 Kolloquium der Assistenten der Studienrichtung Vermessungswesen 1974 - 1976, November 1976.
- Heft 12 Kartographische Vorträge der Geodätischen Informationstage 1976, Wien, Mai 1977.
- Heft 13 Veröffentlichung des Instituts für Photogrammetrie anlässlich des 80. Geburtstages von Prof. Dr.h.c. K. Neumaier, Wien, Januar 1978.
- Heft 14 L. MOLNAR, Self Checking Analytical Relative Orientation and Strip Formation, Wien, Dezember 1978.
- Heft 15 Veröffentlichung des Instituts für Landesvermessung anlässlich des 80. Geburtstages von Prof. Dr. Alois Bavir, Wien, Januar 1979.
- Heft 16 Kolloquium der Assistenten der Studienrichtung Vermessungswesen 1976 - 1978, Wien, November 1979.
- Heft 17 E. VOZIKIS, Die photographische Differentialumbildung gekrümmter Flächen mit Beispielen aus der Architekturbildmessung, Wien, Dezember 1979.
- Heft 18 Veröffentlichung des Instituts für Allgemeine Geodäsie anlässlich des 75. Geburtstages von Prof. Dipl.-Ing. Dr. F. Hauer, Die Höhe des Großglockners, Wien, 1981.

- Heft 19 H. KAGER, Bündeltriangulation mit indirekt beobachteten Kreiszentren, Wien, April 1981.
- Heft 20 Kartographische Vorträge der Geodätischen Informationstage 1980, Wien, Mai 1982.
- Heft 21 Veröffentlichung des Instituts für Kartographie anlässlich des 70. Geburtstages von Prof. Dr. Wolfgang Pillewizer: Glaziologie und Kartographie, Wien, Dezember 1982.
- Heft 22 K. TEMPFLI, Genauigkeitsschätzung digitaler Höhenmodelle mittels Spektralanalyse, Wien, Mai 1982.
- Heft 23 E. CSAPLOVICS, Interpretation von Farbinfrarotbildern, Wien, November 1982.
- Heft 24 J. JANSKA, Rektifizierung von Multispektral-Scanneraufnahmen - Entwicklung und Erprobung eines EDV-Programms, Wien, Mai 1983.
- Heft 25 Zusammenfassung der Diplomarbeiten, Dissertationen und Habilitationen an den geodätischen Instituten der TU Wien, Wien, November 1984.
- Heft 26 T. WUNDERLICH, Die voraussetzungsfreie Bestimmung von Refraktionswinkeln, Wien, August 1985.
- Heft 27 G. GERSTBACH (Hrsg.), Geowissenschaftliche/geotechnische Daten in Landinformationssystemen - Bedarf und Möglichkeiten in Österreich, Juni 1986.
- Heft 28 K. NOVAK, Orientierung von Amateuraufnahmen ohne Paßpunkte, Wien, August 1986.
- Heft 29 Veröffentlichung des Instituts für Landesvermessung und Ingenieurgeodäsie, Abt. Ingenieurgeodäsie, anlässlich des 80. Geburtstages von Prof. Dipl.-Ing. Dr. F. Hauer, Wien, Oktober 1986.
- Heft 30 K.-H. ROCH, Über die Bedeutung dynamisch ermittelter Parameter für die Bestimmung von Gesteins- und Gebirgseigenschaften, Wien, Februar 1987.
- Heft 31 G. HE, Bildverbesserung mittels digitaler Filterung, Wien, April 1989.
- Heft 32 F. SCHLÖGELHOFER, Qualitäts- und Wirtschaftlichkeitsmodelle für die Ingenieurphotogrammetrie, Wien, April 1989.
- Heft 33 G. GERSTBACH (Hrsg.), Geowissenschaftliche/geotechnische Daten in Landinformationssystemen - Datenbestände und Datenaustausch in Österreich, Wien, Juni 1989.
- Heft 34 F. HOCHSTÖGER, Ein Beitrag zur Anwendung und Visualisierung digitaler Geländemodelle, Wien, Dezember 1989.
- Heft 35 R. WEBER, Lokale Schwerefeldmodellierung unter Berücksichtigung spektraler Methoden zur Geländereduktion, Wien, April 1990.
- Heft 36 o.Prof. Dr. Hans Schmid zum 70. Geburtstag. Veröffentlichung der Abteilung für Landesvermessung, Wien, Oktober 1990.
- Heft 37 G. GERSTBACH, H. P. HÖLLRIEGL und R. WEBER, Geowissenschaftliche Informationsbörse - Eine Nachlese zu GeOLIS II, Wien, Oktober 1990.
- Heft 38 R. ECKER, Rastergraphische Visualisierungen mittels digitaler Geländemodelle, Wien, August 1991.

- Heft 39 Kartographische Forschungen und Anwendungsorientierte Entwicklungen, herausgegeben von W. Stams und F. Kelnhofer zum 80. Geburtstag von Prof. Dr. W. Pillewizer, Wien, Juli 1991.
- Heft 39a W. RIEGER, Hydrologische Anwendungen des digitalen Geländemodelles, Wien, Juli 1992.
- Heft 40 K. STEINNOCHER, Methodische Erweiterungen der Landnutzungsklassifikation und Implementierung auf einem Transputernetzwerk, Wien, Juli 1994.
- Heft 41 G. FORKERT, Die Lösung photogrammetrischer Orientierungs- und Rekonstruktionsaufgaben mittels allgemeiner kurvenförmiger Elemente, Wien, Juli 1994.
- Heft 42 M. SCHÖNER, W. SCHÖNER, Photogrammetrische und glaziologische Untersuchungen am Gäsbre (Ergebnisse der Spitzbergenexpedition 1991), Wien, Mai 1996.
- Heft 43 M. ROIC. Erfassung von nicht signalisierten 3D-Strukturen mit Videotheodoliten, Wien, April 1996.
- Heft 44 G. RETSCHER, 3D-Gleiserfassung mit einem Multisensorsystem und linearen Filterverfahren, Wien, April 1996.
- Heft 45 W. DAXINGER, Astrogravimetrische Geoidbestimmung für Ingenieurprojekte, Wien, Juli 1996.
- Heft 46 M. PLONER, CCD-Astrometrie von Objekten des geostationären Ringes, Wien, November 1996.
- Heft 47 Zum Gedenken an Karl Killian "Ingenieur" und "Geodät" 1903-1991, Veröffentlichung der Fachgruppe Geowissenschaften, Wien, Februar 1997.
- Heft 48 A. SINDHUBER, Ergänzung und Fortführung eines digitalen Landschaftsmodelles mit multispektralen und hochauflösenden Fernerkundungsaufnahmen, Wien, Mai 1998.
- Heft 49 W. WAGNER, Soil Moisture Retrieval from ERS Scatterometer Data, Wien, Dezember 1998.
- Heft 50 R. WEBER, E. FRAGNER (Editoren), Prof. Bretterbauer, Festschrift zum 70. Geburtstag, Wien, Juli 1999.
- Heft 51 Ch. ÖHRENER, A Similarity Measure for Global Image Matching Based on The Forward Modeling Principle, Wien, April 1999.
- Heft 52 M. LECHTHALER, G. GARTNER, Per Aspera ad Astra, Festschrift für Fritz Kelnhofer zum 60. Geburtstag, Wien, Jänner 2000.
- Heft 53 F. KELNHOFER, M. LECHTHALER, Interaktive Karten (Atlanten) und Multimedia – Applikationen, Wien, März 2000.
- Heft 54 A. MISCHKE, Entwicklung eines Videotheodolit-Meßsystems zur automatischen Richtungsmessung von nicht signalisierten Objektpunkten, Wien, Mai 2000.
- Heft 55 Veröffentlichung des I.P.F. anlässlich der Emeritierung von Prof. Dr. Peter Waldhäusl, Wien.
- Heft 56 F. ROTTENSTEINER, Semi-automatic Extraction of Buildings Based on Hybrid Adjustment Using 3D Surface Models and Management of Building Data in a TIS, Wien, Juni 2001.

- Heft 57 D. LEGENSTEIN, Objektrekonstruktion aus perspektiven Bildern unter Einbeziehung von Umrisslinien, Wien, Mai 2001.
- Heft 58 F. KELNHOFER, M. LECHTHALER und K. BRUNNER (Hrsg.), Telekartographie und Location Based Services, Wien, Jänner 2002.
- Heft 59 K. BRETTERBAUER, Die runde Erde eben dargestellt: Abbildungslehre und sphärische Kartennetzentwürfe, Wien, 2002.
- Heft 60 G. GARTNER, Maps and the Internet 2002, Wien 2002.
- Heft 61 L. DORFFNER, Erzeugung von qualitativ hochwertigen 3D Photomodellen für Internetbasierte Anwendungen mit besonderem Augenmerk auf Objekte der Nahbereichsphotogrammetrie, Wien, Jänner 2002.
- Heft 62 K. CHMELINA, Wissensbasierte Analyse von Verschiebungsdaten im Tunnelbau, Wien 2002.
- Heft 63 A. NIESSNER, Qualitative Deformationsanalyse unter Ausnutzung der Farbinformation, Wien 2002.
- Heft 64 K. BRETTERBAUER, R. WEBER, A Primer of Geodesy for GIS-Users, Wien 2003.
- Heft 65 N. PFEIFER, 3D Terrain Models on the basis of a triangulation, Wien, Jänner 2002.
- Heft 66 G. GARTNER (Hrsg), Location Based Services & Telecartography, Wien 2004.
- Heft 67 I. KABASHI, Gleichzeitig-gegenseitige Zenitwinkelmessung über größere Entfernungen mit automatischen Zielsystemen, Wien 2004.
- Heft 68 J. BÖHM, Troposphärische Laufzeitverzögerungen in der VLBI, Wien 2004.
- Heft 69 R. WEBER, W. SCHLÜTER, U. SCHREIBER, O. TITOV Evolving Space Geodesy Techniques (EGS XXVII General Assembly, Nice, France, 2002), Wien 2004.
- Heft 70 G. WEINWURM, Amalthea's Gravity Field and its Impact on a Spacecraft Trajectory, Wien 2004.
- Heft 71 Forschungsgruppe Ingenieurgeodäsie, Festschrift anlässlich des 65. Geburtstages von Herrn o.Univ. Prof. Dr.-Ing. Heribert Kahmen, Wien 2005.
- Heft 72 A. REITERER, A Knowledge-Based Decision System for an On-Line Video-Theodolite-Based Multisensor System, Wien 2005.
- Heft 73 M. HABERLER, Einsatz von Fuzzy Methoden zur Detektion konsistenter Punktbewegungen, Wien 2005.
- Heft 74 G. GARTNER, Location Based Services & Telecartography, Proceedings of the Symposium 2005, Wien 2005.
- Heft 75 Th. HOBIGER, VLBI as a tool to probe the ionosphere, Wien 2006.
- Heft 76 E. KLAFFENBÖCK, Troposphärische Laufzeitverzögerung von GNSS-Signalen – Nutzen aktiver Referenzstationsnetze für die Meteorologie, Wien 2006.
- Heft 76a P. J. MENDES-CERVEIRA, Tidal and non-tidal contributions to surface loading processes on station coordinates, Wien 2006.

- Heft 78 G. KOSTOV, G. BOURDA, L. FERNANDEZ, T. KONDO, Research Projects at IGG Reports, Wien 2007.
- Heft 79 J. BÖHM, A. PANY, H. SCHUH (Editors), Proceedings of the 18th European VLBI for Geodesy and Astrometry Working Meeting, 12-13 April 2007, Wien 2007.
- Heft 80 J. BÖHM, Tropospheric Delay Modelling at Radio Wavelengths for Space Geodetic Techniques, Wien 2007.
- Heft 81 G. Retscher, Mobile Multi-sensor Systems for Personal Navigation and Location-based Services, Wien 2007.
- Heft 82 R. HEINKELMANN, Bestimmung des atmosphärischen Wasserdampfes mittels VLBI als Beitrag zur Klimaforschung, Wien 2008.
- Heft 83 F. ROTTENSTEINER, Automatic extraction of buildings from airborne laserscanner data and aerial images, Wien 2008.
- Heft 84 S. TODOROVA, Kombination geodätischer Weltraumverfahren für globale Karten der Ionosphäre, Wien 2009.
- Heft 85 J. WRESNIK, Simulationen für die neue Generation von VLBI-Systemen, Wien 2009.
- Heft 86 A. KARABATIC, Precise Point Positioning (PPP). An alternative technique for ground based GNSS troposphere monitoring, Wien 2011.
- Heft 87 K. TEKE, Sub-daily Parameter Estimation in VLBI Data Analysis, Wien 2011.
- Heft 88 G. THALER, Echtzeit Bahn- und Uhrberechnung der GPS-Satellitenkonstellation basierend auf Beobachtungsdaten des RTIGS-Stationsnetzwerkes, Wien 2013.
- Heft 89 P. SWATSCHINA, Dynamic and Reduced-Dynamic Precise Orbit Determination of Satellites in Low Earth Orbits, Wien 2012.
- Heft 90 S. BÖHM, Tidal excitation of Earth rotation observed by VLBI and GNSS, Wien 2012.